Nuclear Quantum Effects in Aqueous Systems

David M. Wilkins

St. Edmund Hall

University of Oxford

A thesis submitted for the degree of Doctor of Philosophy

April 2016

Nuclear Quantum Effects in Aqueous Systems

David M. Wilkins

St. Edmund Hall, University of Oxford

A thesis submitted for the degree of Doctor of Philosophy

Hilary Term 2016

Abstract

This thesis is concerned with the influence of nuclear quantum effects (NQEs) on the properties of aqueous systems. Although such systems have been studied ever since methods to account for NQEs within atomistic simulations were first developed, it has been shown in recent years that a full accounting for the flexibility of O–H bonds leads to a cancellation between intermolecular and intramolecular quantum effects, meaning that the total effect is often much smaller than was originally believed to be the case. Several examples of systems are studied in which NQEs give rise to a small, though detectable, effect.

Path integral molecular dynamics simulations are used to explain the results of sum-frequency generation spectroscopy experiments that observe a small preference for hydrogen over deuterium atoms in the dangling O–H bonds at the surface of isotopically substituted liquid water. These simulations are able to give a free energy of isotope fractionation that agrees quite well with that obtained from experiments.

The effect of quantum mechanics on dynamical properties is studied by using ring polymer molecular dynamics to look at two types of process: the exchange of water around monatomic, monovalent ions and the reorientation of hydrogen bonds in the pure liquid. In both cases, NQEs speed up the process by a small degree, but leave the mechanism of the process unchanged. This suggests that a classical treatment of these processes will give an excellent qualitative description, and will give a quantitatively reasonable result.

The results of second-harmonic generation scattering experiments on aqueous solutions of ions are also considered: the ions are shown to give rise to long-ranged orientational correlations between solvent molecules. Replacement of light water with heavy water causes a significant change in the scattered signal intensity, a hallmark of NQEs. A preliminary, classical study is performed using both Debye-Hückel theory and molecular dynamics simulations to explain the microscopic origin of these effects.

Acknowledgements

Firstly, I would like to thank my supervisor David Manolopoulos for all of his help and guidance: his ability to get intuitively to the heart of a physics problem and to explain science clearly have been a particular inspiration to me.

I am also very grateful to Michele Ceriotti, whose support and patience throughout my D.Phil was invaluable, and who has been a great role model to me from the beginning of my research career.

I have been fortunate enough to be a part of a wonderful research group, full of intelligent and kind people who have all helped make my degree a happy and productive one. In particular, I would like to thank Josh, whose sense of humour and knowledge of path integrals made him great company. I also thank Alan L., Peter, Jake, Joe, Jonathan, Tom, Lachlan and Mariana. I also spent a very enjoyable three months in EPFL and am grateful to the Ceriotti group, Gabriele, Bingqing, Piero, Daniele, Chungwen and Sandip, who were all extremely warm and welcoming.

Throughout my degree I have worked with several collaborators, who taught me a great deal: I thank Jian Liu, Liem Dang (who hosted me for an enjoyable two weeks at PNNL), Damien Laage, Silvio Pipolo, Casey Hynes, Yixing Chen and Sylvie Roke.

My friends were kind enough to distract me from work whenever necessary, whether with coffee, dinner or conversation. In particular, I would like to acknowledge Karolis, Jed, Jonny, Owen, Alan C., Michael, Emma, Richard, David R., Oliy, Max, Kathryn and Iain.

I am also very grateful to Drs. Cheetham and Miller for the resolution of my knee problems towards the end of my D.Phil.

Ich bedanke mich bei Andrea und Thoralf, weil sie haben in ihre Familie mich aufgenommen.

I am greatly indebted to my wonderful parents, who have always encouraged and supported me, and to whom I owe much. I would also like to thank my grandparents, my great aunt and my brother Nicholas.

Finally, I would like to dedicate this thesis to my wife, Anne, who helped keep me (reasonably) sane through the last few years. I am more grateful for your support than I could possibly put into words here, so will say simply: thank you for everything.

Contents

Chapter 1

Introduction

1.1 Nuclear Quantum Effects in Water

It seems easy to take water for granted: this liquid is abundant in chemistry, and indeed throughout everyday life. As a common solvent, it might appear to be simply a backdrop to the chemical reactions of its solutes. However, to make this assumption would be to ignore the unusual properties of aqueous systems [1]. The key to these properties is a complex networks of hydrogen bonds (H-bonds), as illustrated in Fig. 1.1. A water molecule is capable of accepting and of donating two H-bonds, whose strength is responsible for the fact that water persists in a liquid state over a fairly large temperature range. Water interacts strongly not only with like molecules, but with others; this is the reason, for example, that it has such a high propensity for forming ionic solutions.

Given its pivotal role in many chemical systems, water has been an extremely popular target for atomistic simulations over the last few decades. Barker and Watts [2] used a simple potential model to calculate the structure, energy and heat capacity of pure water with the Monte Carlo method in 1969, and in 1971 Rahman

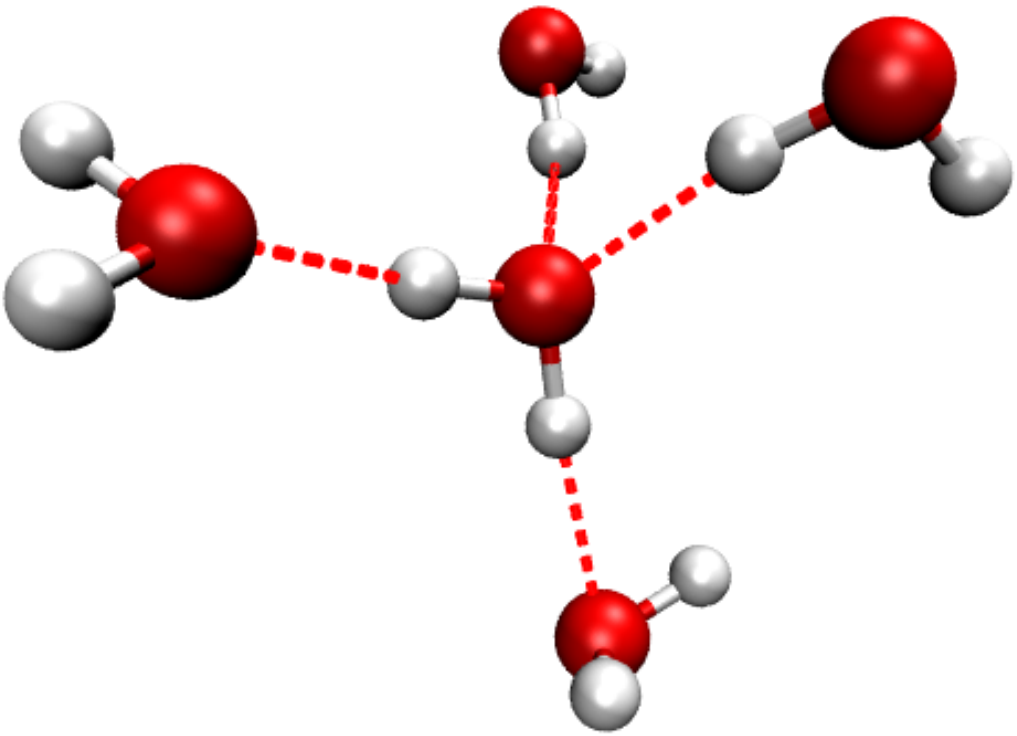

Figure 1.1: The structure of liquid water: in aqueous systems water molecules are able to accept and to donate two H-bonds (shown here as red dotted lines).

and Stillinger [3] used molecular dynamics to compute several static and dynamical properties.

Since then, the complexity and scope of these simulations has increased. The effect of dissolved electrolytes on the structure and dynamics of the solvent has been elucidated for several ions [4–8]. Computational studies of processes at the surface of water have also been carried out, including the evaporation of water [9, 10], the propensity of an ion to adsorb on the surface [11,12] and the formation of a premelted

layer on the surface of ice [13–15].

Many interaction potentials have been developed to describe the interactions between water molecules, from rigid-body models such as SPC/E [16] and TIP4P [17] to more complex models such as TTM3-F [18], which takes into account the flexibility and polarizability of the water molecules. Although simpler models can often perform quite well, giving reasonable agreement with a number of experiments [19], the description they give of a water system is still not perfect; for example, including the molecular polarizability can double the relaxation time of hydrogen bonds [20].

A more advanced description of the interactions between water molecules is given by using *ab initio* molecular dynamics simulations [21, 22]; electronic structure calculations for the forces have allowed the study of a wide variety of systems, including protonated water [23] and the solvation of very highly charged ions such as Zr^{4+} [24]. At present, molecular simulations thus allow us to investigate a wide variety of aqueous systems.

A problem that has been studied since quite early on in the history of simulations of water is the extent to which nuclear quantum effects influence the properties of aqueous systems [25–33]. Perhaps a better way to cast this question is to ask: to what degree would these properties change if we assumed that the nuclear motion obeyed the laws of classical mechanics?

Within classical mechanics, a system evolves deterministically through time according to Hamilton's equations. Although a classical treatment can often be quite accurate, particularly in describing the macroscopic world, it is ultimately just an

approximation to quantum mechanics, in which Schrödinger's equation describes the time-evolution of a system's wavefunction. As we consider objects of smaller and smaller masses and the microscopic world is approached, it becomes more important to treat a system quantum-mechanically. To gauge how appropriate the classical approximation is for the motion of nuclei, we can consider the vibrational modes of a system, since it is vibrations for which quantization will have the largest effect. A general rule of thumb is that if the thermal energy $k_{\mathrm{B}}T = \beta^{-1}$ is much larger than the vibrational level spacing $\hbar\omega$, or $\beta\hbar\omega \ll 1$, then this vibration will behave classically. At 300 K, this translates to $\omega \ll 1300$ cm^{-1}.

In Table 1.1 we show the largest vibrational frequency ω_{max} of a few molecules. All of the molecules shown have large enough ω_{max} that quantum mechanics may have an appreciable effect on their properties, but this is most pronounced for those containing hydrogen, the lightest element.

Table 1.1: Maximum vibrational frequencies ω_{max} for some small inorganic molecules. These data were obtained from Ref. [34].

Molecule	ω_{max} [cm^{-1}]	Molecule	ω_{max} [cm^{-1}]
SO_3	1391	CH_4	3019
O_2	1580	NH_3	3444
N_2	2359	H_2	4401
CO_2	2349	H_2O	3756

Example of nuclear quantum effects (NQEs) are tunnelling and zero-point energy

(ZPE). The tunnelling of a system through the energy barrier of a chemical reaction leads to an increase in the rate; this can be observed experimentally as non-Arrhenius behaviour, with a plot of $\ln k$ vs. $1/T$ (where k the reaction's rate constant) showing a positive deviation from linearity at small T [35]. This behaviour has been observed particularly for reactions involving H, such as hydrogen transfer reactions [36] and C–H activation [37]. It has been suggested that tunnelling is important in the formation of small molecules in the interstellar medium [38].

ZPE in a coordinate destabilizes it. A difference in a static property upon isotopic substitution suggests that NQEs are present. In the Born-Oppenheimer approximation, changing the isotope used does not change the underlying potential surface, and the isotope effect can be attributed to quantum fluctuations; ZPE decreases with increasing mass, so that a lighter isotope will have more ZPE. Examples of isotope effects that suggest a NQE include the fractionation of light and heavy water between liquid and vapour [39] and the isotope dependence of hydrogen solubility in palladium [40,41], as well as the experimental observations described in Chapters 3 and 5. The explanations for these experiments will rest on the fact that in water, ZPE leads to weaker hydrogen-bonding [25–31].

The inclusion of NQEs in atomistic simulations was made possible by the development of techniques based on the imaginary time path integral formulation of statistical mechanics [42]; an isomorphism exists between a quantum-mechanical system and a system containing classical ring polymers of several replicas of the atoms, connected by harmonic springs [43]. Path integral molecular dynamics [44], described in Section 7, and Path Integral Monte Carlo [25], provided a starting point

for the investigation of quantum effects in water.

The quantum-mechanical disruption of the H-bonding network was observed by Kuharski and Rossky [25], and by Wallqvist and Berne [26], who found a broadening of peaks in pair correlation functions (particularly in those involving hydrogen atoms). Several studies were carried out following these, including an investigation of the decrease in structure of H_2O compared to D_2O [45], the model-dependence of quantum effects [46] and the NQEs that are operative in a polarizable water model [47].

In recent years, the development of approximate path integral techniques such as centroid molecular dynamics [48, 49] and ring polymer molecular dynamics [50, 51], which will be discussed further in Section 2.3, has meant that time correlation functions can be calculated with a reasonable degree of accuracy. The effects of quantum mechanics on the dynamical properties of aqueous systems have thus been found. These are also subject to the weakening of the H-bonds: diffusion coefficients are increased [28, 30, 31], and orientational relaxation times are decreased [28, 29, 31, 52]. The peaks in infrared absorption spectra corresponding to H-bonds are red-shifted, indicating lower-frequency vibrations [27, 31, 53, 54].

Although water models parametrized in classical simulations have been used in studies of NQEs [25, 26, 29, 55], if such models were fitted to experiments (in which NQEs are implicitly accounted for), then to use these potentials for path integral simulations can lead to "double counting" of quantum effects. It is thus important to use models which have been parametrized in simulations that take nuclear quantum fluctuations into account. The first such model was based on

the flexible SPC/F potential and reparametrized to give structural and dynamical properties quite well [27].

Another model that was parametrized using path integral simulations is the q-TIP4P/F model [32], which we will discuss in Section 2.4. There, we will also discuss the fact that the quantum-mechanical disruption of the H-bonding network is not the full story of NQEs in water. The total quantum effect for several properties is the result of a competition between two effects [32, 33]: ZPE in the water bending and librational coordinates tends to weaken H-bonds, but ZPE in the anharmonic O–H stretching coordinate increases the bond length (and thus the molecular dipole moment) and strengthens the interactions between neighbouring molecules, mitigating against the weakening effect. The fact that both of these effects must be taken into account in order to fully understand the effect of quantum fluctuations on aqueous systems will be vital in explaining the effects observed in Chapters 3 and 4.

Even more recently, the MB-pol potential has been developed by Paesani and coworkers [56–58]. This potential contains many-body interactions and is fairly expensive to evaluate. However, MB-pol predicts experimental data well in the liquid phase and in small clusters, suggesting that it is a very good all-round model for water.

For some applications, it is desirable to treat not just the nuclei, but also the electrons quantum-mechanically. The combination of path integral methods with *ab initio* electronic structure calculations is well-established [59, 60]. As originally implemented, quantization of both electrons and nuclei led to even more computa-

tional expense than quantization of either one alone, but this combination has been successfully used to study many systems in which neither effect can be neglected if an accurate description of the system is desired: excess protons and electrons in water [61, 62], as well as low-temperature hydrogen [63] and several hydrogen-bonding clusters [33]. The general effect in these simulations is the same as noted earlier: the hydrogen-bonding network is weakened by quantum mechanics.

Several methodological developments have allowed path integral calculations to be made much more efficient. Among these is the ring polymer contraction [64, 65], which we will describe further in Section 2.2. This makes use of the observation that long-distance forces (such as electrostatics) vary slowly over the length scale of a ring polymer, meaning that these forces can be evaluated instead on a contracted ring polymer with fewer replicas. Since the calculation of these forces is generally the most computationally demanding part of a simulation, this leads to a large speed-up. A very recent development is a contraction scheme that works for *ab initio* path integral molecular dynamics [66]. A thermostat algorithm [67, 68] based on the generalized Langevin equation allows for a frequency-dependent coupling to the vibrational modes of the system. This thermostat can be tuned so that it couples to the system in such a way as to give appropriate quantum fluctuations, allowing the results to converge with fewer beads than would otherwise be needed [69]. With these advances, it is now possible to account for NQEs with very little effort above that of a classical simulation.

1.2 Summary

In this Thesis, we will consider aqueous systems in which either the experimental observation of isotope effects has suggested the presence of NQEs or their influence has otherwise been proposed. We begin in Chapter 2 by discussing the computational methods used throughout this work: path integral molecular dynamics (PIMD) [44] (which is an exact method used to incorporate nuclear quantum effects into the calculation of static properties) and ring polymer molecular dynamics (RPMD) [51] (an approximate method used to include nuclear quantum effects when calculating dynamical properties), both of which involve running classical molecular dynamics simulations in an extended phase space in which several replicas of a particle are joined by harmonic springs to form a ring polymer. We will also describe in more detail the concept of competing quantum effects [32, 33], as well as the potential model used for most of this thesis.

In Chapter 3 we perform a joint investigation with an experimental group into the preference for hydrogen over deuterium in the free O–H bonds at the surface of liquid water, as measured by sum-frequency generation spectroscopy (a nonlinear spectroscopy with high surface specificity). Using a dividing surface based on the microscopic nature of the system [70] to locate the air-water interface, and thus to identify the O–H bonds pointing out of the surface, we were able to observe this preference and to attribute it to the decrease of confinement of an H or D atom on going from the bulk to the surface.

Chapter 4 focuses on the effect on quantum fluctuations on the dynamics of water

exchange around the Li^+ and F^- ions; we calculate the mean residence time of a water molecule in their first hydration shells and find that this time is decreased by a small amount for both ions when quantum effects are accounted for. The decrease for F^- is even smaller than for Li^+, which is attributed to a combination of effects: the stronger binding of water molecules to Li^+ than to F^-, the larger mass of F^-, and the presence of a competing quantum effect in water exchange around the anion that is not present in exchange around the cation. We also calculate the mechanism of exchange, and find that this is essentially unchanged by quantum effects.

In Chapter 5 we again conduct a joint experimental-theoretical study, looking into second-harmonic generation scattering experiments (once again, a nonlinear optical effect) on ionic solutions at varying ionic strengths. There are two particularly interesting results of these experiments: firstly, at large ionic strength the intensity of scattered light reaches a plateau, and secondly, the observed results are independent of the identity of the ions used. We derive a theory for this scattering, and show that it qualitatively accounts for both of these observations, but that it fails to quantitatively predict the scattering intensity. This is followed by classical molecular dynamics simulations in which we look at the correlations between water molecules and suggest that the quantitative failure of the theory is due to its omission of interactions between water molecules.

We return to the dynamics of water molecules in Chapter 6, which is concerned with nuclear quantum effects on the extended jump mechanism of O–H bond reorientation in pure water. In this model, there are two methods by which these bonds reorient: large angular jumps in which hydrogen bond donors change between two

acceptors, and rotational diffusion of the hydrogen-bonded O$\cdots$O bonds. We begin by extending the model to account for the distribution of jump angles, and use this improved model to fit the Legendre relaxation times of the O–H bonds, from which we can find the quantum effect on the rate of water jumps and on the rotational diffusion constant. Both of these effects are quite small, and are once again accompanied by a negligible change in jump mechanism. Finally, Chapter 7 concludes.

Chapter 2

Theory

2.1 Classical Atomistic Simulations

In a thermodynamic system with constant number of atoms N, volume V and temperature T, the equilibrium average of some observable A is given quantum-mechanically by [71],

$$\langle A \rangle = \frac{1}{Z} \mathrm{tr} \left[\hat{A} e^{-\beta \hat{H}} \right], \tag{2.1}$$

in which $\hat{A}$ is the operator corresponding to this observable, $\hat{H}$ is the Hamiltonian operator, $\beta = 1/k_{\mathrm{B}}T$ is the reciprocal temperature, $\mathrm{tr}\left[\cdots\right]$ is a quantum-mechanical trace, and $Z = \mathrm{tr}\left[e^{-\beta \hat{H}}\right]$ is the partition function. In principle, we can obtain any average using this expression.

In practice, however, the trace in Eqn. (2.1) is effectively impossible to calculate for the kinds of complex systems that are relevant to Chemistry. We can circumvent this problem by using classical mechanics to approximate $\langle A \rangle$.

Within the Born-Oppenheimer approximation [72], the motions of electrons and nuclei are uncoupled, and the nuclei experience a mean-field due to the much lighter electrons. These electrons thus determine the potential energy surface (PES) on

which the nuclei move. We begin by assuming that the motion of the nuclei on this PES is governed by classical mechanics. As described in Chapter 1, this assumption is reasonable for a wide range of systems of interest, and it has been used in an enormous body of work [73, 74].

We need also to decide how to deal with the motion of the electrons. They are at least three orders of magnitude lighter than the atomic nucleus, and classical mechanics cannot be expected to accurately describe their motion. One way to calculate the PES is to use *ab initio* electronic structure methods to compute the energy of a given nuclear configuration, as well as the forces on the nuclei – which are used to generate the dynamics of the system [59, 75–77].

An alternative method is to ignore the motion of the electrons altogether, and simply represent the PES by a relatively simple functional form. The parameters in this force-field are tuned so that the results of simulations agree either with the results of experiment or those of *ab initio* simulations.

While this method is computationally much cheaper it does suffer from a number of downsides. Being described only by a relatively small number of parameters compared to the number of degrees of freedom of the system, a model parametrized to give certain experimental properties correctly may describe others less well. For example, the extended simple point charge (SPC/E) model for water [16], one of the most popular water potentials in the literature, gives a very good description of the experimental density and self-diffusion constant within classical simulations, but predicts a melting point of 215 K [78].

Ultimately, no potential model is perfect, but so long as we are working un-

der thermodynamic conditions reasonably close to those in which the model was parametrized and have found it to be reliable for properties of interest under these conditions, this represents a cheap and efficient way of gathering statistics – a task that is much harder when using *ab initio* methods.

A classical system of N atoms is described completely by their coordinates $\boldsymbol{q}$ and momenta $\boldsymbol{p}$. For an observable $A(\boldsymbol{q}, \boldsymbol{p})$, the classical equilibrium average is [71],

$$\langle A \rangle_{\mathrm{cl}} = \frac{1}{(2\pi\hbar)^{3N} Z_{\mathrm{cl}}} \int \mathrm{d}\boldsymbol{q} \int \mathrm{d}\boldsymbol{p}\ A(\boldsymbol{q}, \boldsymbol{p}) e^{-\beta \mathcal{H}(\boldsymbol{q}, \boldsymbol{p})}, \tag{2.2}$$

with the classical partition function defined,

$$Z_{\mathrm{cl}} = \frac{1}{(2\pi\hbar)^{3N}} \int \mathrm{d}\boldsymbol{q} \int \mathrm{d}\boldsymbol{p}\ e^{-\beta \mathcal{H}(\boldsymbol{q}, \boldsymbol{p})}, \tag{2.3}$$

and $\mathcal{H}(\boldsymbol{q}, \boldsymbol{p})$ the Hamiltonian, which can be written as a sum of kinetic energy $\mathcal{T}(\boldsymbol{p})$ and potential energy $\mathcal{V}(\boldsymbol{q})$,

$$\mathcal{H}(\boldsymbol{q}, \boldsymbol{p}) = \mathcal{T}(\boldsymbol{p}) + \mathcal{V}(\boldsymbol{q}). \tag{2.4}$$

We are now faced with a $6N$-dimensional integral – which, it should be noted, also cannot be solved analytically for systems of chemical interest. However, it is possible to carry out the integration numerically with far less effort than is needed to evaluate Eqn. (2.1). The two most popular methods for doing so are molecular dynamics (MD) [79] and Monte Carlo (MC) [80]. Of these two, MD will feature heavily in this thesis, although in Chapter 3 MC will be used to augment MD simulations of the surface of water. Since a number of excellent references exist that deal with molecular simulations [73, 74], only a brief description of molecular dynamics will follow.

The basic principle underlying MD is the ergodic hypothesis [71]: in a system described by the microcanonical ensemble, in which N, V and total energy E are constant, the equilibrium average of a quantity can be replaced by a time average, since over a long enough period of time the system will visit all available microstates. That is,

$$\langle A \rangle_{\mathrm{NVE}} = \lim_{\tau \to \infty} \frac{1}{\tau} \int_{t}^{t+\tau} A(\boldsymbol{q}_{t'}, \boldsymbol{p}_{t'}) \, \mathrm{d}t', \tag{2.5}$$

with $\boldsymbol{q}_{t'}$ the configuration of the system, and $\boldsymbol{p}_{t'}$ its momentum, at time t'. To implement Eqn. (2.5), we take a system with suitable initial conditions, and evolve it through time using the dynamics derived from the Hamiltonian $\mathcal{H}(\boldsymbol{q}, \boldsymbol{p})$ for N_t discrete timesteps. The time-averaged quantity we seek is then calculated as,

$$\langle A \rangle_{\mathrm{NVE}} = \lim_{N_t \to \infty} \frac{1}{N_t} \sum_{t'=1}^{N_t} A(\boldsymbol{q}_{t'}, \boldsymbol{p}_{t'}). \tag{2.6}$$

This method will give the microcanonical average of $A(\boldsymbol{q}, \boldsymbol{p})$. In order to calculate a canonical average such as in Eqn. (2.2), a thermostat is applied to the system to ensure that rather than a single energy the system visits volumes of phase space with many energies, each with a probability determined by the Boltzmann distribution.

There are many types of thermostat algorithm available for use in MD simulations [73, 74, 81, 82]. Of particular relevance to the work that follows are those based on the Langevin equation [83–85]. In the remainder of this thesis, we will use the thermostat described in Ref. [85] to generate canonical average quantities in classical MD simulations, unless stated otherwise. To run molecular dynamics with Langevin thermostatting, the following procedure is used to evolve the positions $\boldsymbol{q}$ and momenta $\boldsymbol{p}$ of a particle from their values at time t to their values at time $t+\Delta t$,

with m the mass of the particle and $\boldsymbol{f}(t)$ the force acting on it at time t:

1. $\boldsymbol{p}^*(t) = c_1\boldsymbol{p}(t) + c_2\boldsymbol{R_1}$,

2. $\boldsymbol{q}(t+\Delta t) = \boldsymbol{q}(t) + \frac{\Delta t}{m}\boldsymbol{p}^*(t) + \frac{\Delta t^2}{2m}\boldsymbol{q}(t)$,

3. $\boldsymbol{p}^*(t+\Delta t) = \boldsymbol{p}^*(t) + \frac{\Delta t}{2}\left[\boldsymbol{f}(t) + \boldsymbol{f}(t+\Delta t)\right]$,

4. $\boldsymbol{p}(t+\Delta t) = c_1\boldsymbol{p}^*(t+\Delta t) + c_2\boldsymbol{R_2}$,

where,

$$c_1 = e^{-\gamma\Delta t/2}, \tag{2.7a}$$

and,

$$c_2 = \left[\left(1 - e^{-\gamma\Delta t}\right) m/\beta\right]^{1/2}, \tag{2.7b}$$

with γ a friction coefficient. $\boldsymbol{R_1}$ and $\boldsymbol{R_2}$ are two vectors whose elements are random numbers drawn from a normal distribution (with a mean of zero and variance of unity). This thermostat will serve as the basis for the path integral Langevin equation (PILE) thermostat [67], described in the following section.

2.2 Path Integral Molecular Dynamics

The classical approximation is not always valid. For systems in which high-frequency vibrations are involved (such as bonds involving light atoms), zero-point energy (ZPE) in these motions can destabilize these coordinates, and narrow potential barriers allow tunnelling, which can speed up reaction rates; this latter effect is particularly important at low temperatures, where the barrier height is much greater

than the thermal energy and can be surmounted only by tunnelling. It has been suggested that these effects contribute to properties of many systems, including the rates of chemical reactions on the surface of cosmic dust [38, 86] and the dynamics of enzymatic reactions [87, 88].

One can go beyond the classical approximation by using the path integral formulation of quantum mechanics [42, 89]. As is shown in Appendix A, there is an isomorphism between a quantum-mechanical system and an extended system consisting of n classical replicas of the original, with each copy of a particle connected by harmonic springs to two other copies of this particle such that a "ring polymer" is formed [43, 90]. This isomorphism is exact in the limit of an infinite number of replicas. That is, for a configuration-dependent variable $A(\boldsymbol{q})$,

$$\langle A \rangle = \lim_{n\to\infty} \langle A \rangle_n \,, \tag{2.8}$$

where $\langle A \rangle_n$ is the average calculated using a ring polymer with n replicas (or "beads"),

$$\langle A \rangle_n = \frac{1}{(2\pi\hbar)^{3Nn} Z_n} \int \mathrm{d}\boldsymbol{q}_1 \cdots \int \mathrm{d}\boldsymbol{q}_n \int \mathrm{d}\boldsymbol{p}_1 \cdots \int \mathrm{d}\boldsymbol{p}_n \; A_n(\boldsymbol{q}) e^{-\beta_n \mathcal{H}_n(\boldsymbol{q},\boldsymbol{p})}. \tag{2.9}$$

In this expression $\beta_n = \beta/n$,[1] $\boldsymbol{q} = (\boldsymbol{q}_1, \ldots, \boldsymbol{q}_n)$ contains all of the coordinates of all of the replicas, and similarly for the momenta, $\boldsymbol{p} = (\boldsymbol{p}_1, \ldots, \boldsymbol{p}_n)$. $\mathcal{H}_n(\boldsymbol{q}, \boldsymbol{p})$ is the Hamiltonian for this ring polymer,

$$\mathcal{H}_n(\boldsymbol{q}, \boldsymbol{p}) = \sum_{k=1}^{n} \sum_{i=1}^{N} \frac{\left|\boldsymbol{o}_k^i\right|^2}{2m_i} + \sum_{k=1}^{n} \mathcal{V}(\boldsymbol{q}_k) + \sum_{k=1}^{n} \sum_{i=1}^{N} \frac{1}{2} m_i \omega_n^2 \left|\boldsymbol{q}_k^i - \boldsymbol{q}_{k+1}^i\right|^2 , \tag{2.10}$$

[1] That is, the extended system at n times the physical temperature gives the equilibrium properties of the quantum system.

where $\omega_n = 1/\beta_n\hbar$, $\boldsymbol{p}_k^i$ is the momentum of the k^{th} replica of the i^{th} atom, $\boldsymbol{q}_k^i$ is its position, and the index k has cyclic symmetry, such that $\boldsymbol{q}_{n+1}^i \equiv \boldsymbol{q}_1^i$. Z_n is the ring-polymer partition function, which is defined as,

$$Z_n = \frac{1}{(2\pi\hbar)^{3Nn}} \int \mathrm{d}\boldsymbol{q}_1 \cdots \int \mathrm{d}\boldsymbol{q}_n \int \mathrm{d}\boldsymbol{p}_1 \cdots \int \mathrm{d}\boldsymbol{p}_n \; e^{-\beta_n \mathcal{H}_n(\boldsymbol{q},\boldsymbol{p})}. \tag{2.11}$$

$A_n(\boldsymbol{q})$ is the average over replicas,

$$A_n(\boldsymbol{q}) = \frac{1}{n}\sum_{k=1}^{n} A(\boldsymbol{q}_k), \tag{2.12}$$

an important special case of which is the ring-polymer centroid,

$$\bar{\boldsymbol{q}} = \frac{1}{n}\sum_{k=1}^{n} \boldsymbol{q}_k. \tag{2.13}$$

In Eqn. (2.10), the first term is the kinetic energy of all of the replicas of the system (a sum of individual system kinetic energies), the second term is the sum of the potential energies of the individual systems, and the third term is a "spring term" connecting each atom in one system with its analogues in the two neighbouring systems. This isomorphism is illustrated in Fig. 2.1. When $n = 1$, a ring polymer collapses to a single replica and the system becomes classical.

Two points remain to be discussed: the first of these is that, as described in Appendix A, the masses in the kinetic energy term of the Hamiltonian (the first term in Eqn. (2.10)) are arbitrary; any other masses could just as easily be chosen. In Section 2.3 we will discuss why we have chosen to use the physical masses of the particles in generating the dynamics. The second point is that, rather comfortingly, it is not necessary to use an infinite number of replicas to converge upon the exact, quantum-mechanical average. A general rule of thumb for choosing a number of

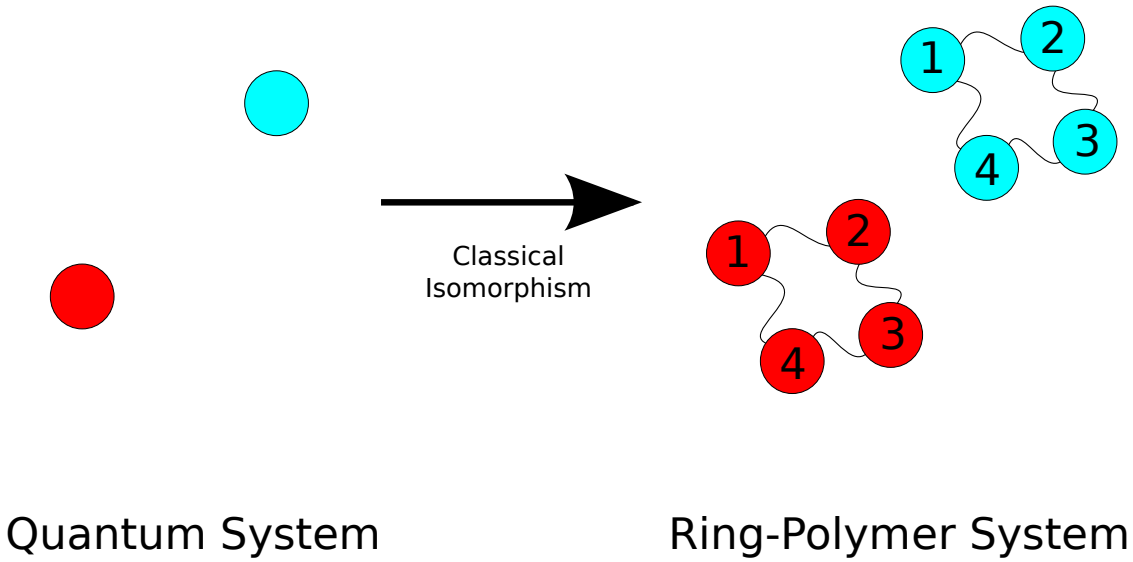

Figure 2.1: Illustration of the ring polymer isomorphism [43, 90]: the left-hand side shows a system described by quantum mechanics. The right-hand side shows a classical system of ring polymers, each with four replicas (or beads); the only direct interactions between ring polymers are between replicas with the same label (i.e., replica 1 in the red ring polymer interacts directly with replica 1 of the blue ring polymer); intra-ring polymer interactions are brought about by the harmonic springs linking neighbouring replicas. The thermodynamic properties of the extended classical system can be used, in the limit of an infinite number of replicas, to obtain the corresponding properties of the quantum system.

replicas is that if $\omega_{\max}$ is the highest frequency involved in the system of interest, then $n > \beta\hbar\omega_{\max}$ is required for convergence [25,64]. This is in accord with the idea that at low temperatures or for larger frequencies, the system is "more quantum-mechanical", and more ring polymer replicas are required to capture its properties.

Eqn. (2.9) is an average over a classical phase space, and so can be evaluated using molecular dynamics. This is referred to as path integral molecular dynamics (PIMD) [44]. In a PIMD simulation, a ring polymer system is evolved through time under the dynamics obtained from the Hamiltonian of Eqn. (2.10), and an average over the visited configurations will give the equilibrium average $\langle A \rangle_n$.

A number of modifications are made to standard molecular dynamics algorithms in order to efficiently carry out PIMD simulations. For example, specialized thermostats exist for controlling the temperature in PIMD. Of these, the most relevant to this work is the path integral Langevin equation (PILE) thermostat [67], based on the Langevin thermostat of Ref. [85]. Rather than acting on the momenta of the ring-polymer beads, the harmonic springs of the ring polymer are decomposed into their normal modes, and the PILE thermostat is coupled to these modes. The k^{th} normal mode has a frequency $\omega_k = 2\omega_n \sin\left(\frac{k\pi}{n}\right)$, and a friction coeffcient $\gamma_k = 2\omega_k$ is found to optimize the sampling of all of the non-centroid ($k > 0$) modes. For the centroid ($k = 0$), $\omega_0 = 0$ and γ_0 is treated as an adjustable parameter that can be tuned to improve the sampling. When evolving the system through time we must change between the bead representation and the normal mode representation in order to apply the thermostat, but the existence of highly efficient code libraries for carrying out discrete Fourier transformation means that this adds no significant

overhead to the PIMD calculation.

In principle, a PIMD simulation with n replicas requires n times as much computational effort as the corresponding classical simulation with a single replica. One development that can be used to speed up PIMD simulations is the ring-polymer contraction [64]; this is based on the observation that the most expensive part of the force to calculate is generally the long-range part (in particular, the electrostatic force). These forces vary relatively slowly with distance, so that they are very similar on different beads of the same ring polymer. Rather than evaluating this force on every bead, the ring polymer is contracted to a smaller one, on each bead of which the force is evaluated, and the chain rule is used to calculate the forces on the beads of the original ring polymer.

An improvement to this method [65] allows the ring polymer to be contracted to a single bead (which is equivalent to using the centroid to evaluate the long-range forces), with the addition of a short-ranged correction term giving excellent agreement with the results of PIMD calculations where the full ring polymer was used.

In all PIMD simulations in this thesis, we will use the PILE thermostat to control temperature, along with the improved ring-polymer contraction scheme to speed up collection of statistics.

2.3 Ring Polymer Molecular Dynamics

The time correlation function for two variables A and B is defined quantum-mechanically as,

$$\begin{aligned} C_{AB}(t) &= \frac{1}{Z}\mathrm{tr}\left[e^{-\beta\hat{H}}\hat{A}(0)\hat{B}(t)\right], \\ &= \frac{1}{Z}\mathrm{tr}\left[e^{-\beta\hat{H}}\hat{A}e^{+i\hat{H}t/\hbar}\hat{B}e^{-i\hat{H}t/\hbar}\right]. \end{aligned} \tag{2.14}$$

$C_{AB}(t)$ measures the degree of correlation of two variables A and B at different times. Time correlation functions of molecular properties can be used [91] to obtain macroscopic observables, such as diffusion coefficients [92,93], reaction rate constants [94, 95], neutron diffraction cross-sections [96] and frequency-dependent dielectric constants [97]; this makes their computation particularly useful.

Given a time correlation function, we will often wish to extract from it a characteristic time taken for decorrelation. The relaxation time, τ_{AB}, is obtained by fitting $C_{AB}(t)$ to an exponential decay at long time,

$$C_{AB}(t) \simeq ae^{-t/\tau_{AB}}. \tag{2.15}$$

Another characteristic quantity, the correlation time,

$$\bar{\tau}_{AB} = \int_0^\infty C_{AB}(t)\,\mathrm{d}t, \tag{2.16}$$

is equal to τ_{AB} if $C_{AB}(t)$ is exponentially decaying over the entire time range. When we wish to characterize a time correlation function in this thesis we will use the relaxation time, since this has the advantage that it ignores the short-time transient behaviour of $C_{AB}(t)$ [98].

While the equilibrium properties of a quantum-mechanical system can be calculated exactly using PIMD, the same is not true for dynamical properties: there is no reason *a priori* that the dynamics obtained from the Hamiltonian $\mathcal{H}_n(\boldsymbol{q}, \boldsymbol{p})$ of Eqn. (2.10) should reflect the true dynamics of the system. Instead, approximate methods are used to calculate time correlation functions.

Two such methods, which are conceptually quite similar, are centroid molecular dynamics (CMD) [48, 49] and ring polymer molecular dynamics (RPMD) [50, 51]. Both of these are based on path integrals (and both can be derived from the more general Matsubara dynamics technique [99, 100]): in CMD, time correlation functions are calculated by evolving the centroids of the ring polymers through time as classical particles, with the equations of motion generated from the centroid potential of mean force, and in RPMD the dynamics of the ring polymer itself are used to compute these time correlation functions.

Rather than the time correlation function of Eqn. (2.14), these methods aim to calculate the so-called Kubo-transformed correlation function [92],

$$\begin{aligned}\tilde{C}_{AB}(t) &= \frac{1}{\beta Z}\int_0^\beta \mathrm{tr}\left[e^{-(\beta-\lambda)\hat{H}}\hat{A}(0)e^{-\lambda\hat{H}}\hat{B}(t)\right]\,\mathrm{d}\lambda, \\ &\equiv \frac{1}{\beta}\int_0^\beta \left\langle \hat{A}(-i\lambda\hbar)\hat{B}(t)\right\rangle \,\mathrm{d}\lambda. \end{aligned} \tag{2.17}$$

Such a function has the same symmetries as a classical time correlation function, and its Fourier transform $\tilde{C}_{AB}[\omega]$ is straightforwardly related to that of $C_{AB}(t)$ [50].

We will be using ring polymer molecular dynamics in this thesis, and so will spend some time explaining the advantages of this method. RPMD gives the exact Kubo-transformed correlation function in a number of limits [50]. The first of these

is the classical ($n = 1$) limit, in which RPMD gives the classical time correlation function [50]. Secondly, for a system subject to a harmonic potential RPMD gives exact results as $n \to \infty$ for time correlation functions where at least one of $\hat{A}$ or $\hat{B}$ is a linear function of position [50]. Finally, for $n \to \infty$ RPMD is correct in the short-time limit, with a leading error of at least $\mathcal{O}(t^3)$ [101, 102].

RPMD rate theory [103, 104] also has a number of advantages: as well as giving the exact result for the high-temperature (classical) limit and for parabolic reaction barriers [51], it has been shown [105] to agree very well in the low-temperature (deep-tunnelling) limit with the semiclassical instanton theory, which is known to be accurate at low temperatures. Furthermore, Hele and Althorpe found [106–108] that the transition state theory (TST) rate constant obtained from RPMD rate theory is the unique quantum TST rate constant that gives a non-zero result with the correct statistics. These factors make RPMD particularly suitable for calculating quantum-mechanical rate constants.

RPMD is not without problems. As originally developed, an RPMD simulation was run by taking a system equilibrated using PIMD and allowing it to evolve without a thermostat. Since unthermostatted ring polymer systems suffer from non-ergodicity due to inefficient energy exchange between their high-frequency normal modes [109], it was necessary to resample the momenta periodically. The standard practice was thus to calculate a time correlation function by running a large number of short simulations, with the momenta drawn from a Boltzmann distribution before each run. This method is relatively computationally inefficient: if the same simulation time could be used as one uninterrupted block, there would be much more

information about time-correlation.

A further downside to RPMD is brought about by the harmonic springs of the ring polymer. When using RPMD to calculate vibrational spectra, spurious peaks are observed due to the normal modes of the ring polymer [53,110]. One way to avoid these unphysical features is to decrease the effective masses of the ring polymer's "internal" (i.e., non-centroid) modes [32], as is done in partially adiabatic CMD (PA-CMD) [111]; this will increase the normal mode frequencies so that they are out of the spectral range in which we are interested. One other possible issue is that the effects of quantum coherence are completely neglected by RPMD, but in the condensed-phase systems for which it is used these effects are expected to be quite small.

Recently, a modification of RPMD has been developed in which a thermostat is attached to the internal modes of the ring polymer, while the centroid mode remains unthermostatted [110]. This thermostatted RPMD (TRPMD) method is an improvement over the original RPMD: its results are just as accurate, and there is no longer a problem with non-ergodicity, so that it is possible to run one long TRPMD simulation to calculate time correlation functions, rather than many short ones. This thermostat also damps the high-frequency normal modes that cause spurious frequencies in infrared spectra, making RPMD more reliable for their calculation. However, these frequencies are not completely removed from the spectrum, causing peaks to broaden as temperature is lowered. TRPMD is intermediate between RPMD and CMD (in which the internal modes of a ring polymer are thermostatted, but their masses are made much smaller), and has been shown to perform better than

either for the calculation of spectra [110]. The PILE thermostat is used in RPMD, with the friction coefficients for the normal modes chosen to be half their values in PIMD (that is, $\gamma_k = \omega_k$); this was found to give optimum sampling efficiency [110].

The final point to be discussed is the choice of masses for the ring polymer beads. While they can be chosen arbitrarily in PIMD without affecting the equilibrium properties, they do influence the dynamical properties calculated in RPMD. In fact, there are several reasons to use the appropriate physical masses: this gives a more accurate result at short times than any other choice of mass [101], and Richardson and Althorpe have shown that in a rate theory calculation these masses are required in order for the rate constant to be well-approximated in the deep-tunnelling regime, without the need to choose a particular transition-state dividing surface [105].

We will use TRPMD in future chapters when computing dynamical quantities. When the two operators to be correlated are functions only of the coordinates, the RPMD approximation to a Kubo-transformed correlation function is found using the formula [50],

$$\tilde{C}_{AB}^{\mathrm{RPMD}}(t) = \langle A_n(\boldsymbol{q}_0) B_n(\boldsymbol{q}_t) \rangle_n \,, \tag{2.18}$$

with the averages over replicas $A_n(\boldsymbol{q}_0)$ and $B_n(\boldsymbol{q}_t)$ defined as in Eqn. (2.12), $\boldsymbol{q}_t$ denoting the configuration of the ring-polymer system at time t and $\langle \cdots \rangle_n$ defined as in Eqn. (2.9). Explicitly,

$$\langle A_n(\boldsymbol{q}_0) B_n(\boldsymbol{q}_t) \rangle_n = \frac{1}{(2\pi\hbar)^{3Nn} Z_n} \int \mathrm{d}\boldsymbol{q}_0 \mathrm{d}\boldsymbol{p}_0 \; A_n(\boldsymbol{q}_0) B_n(\boldsymbol{q}_t) e^{-\beta_n \mathcal{H}_n(\boldsymbol{q}_0, \boldsymbol{p}_0)}, \tag{2.19}$$

where $\mathrm{d}\boldsymbol{q}_0 \mathrm{d}\boldsymbol{p}_0$ is the initial phase-space volume element for the ring polymer.

2.4 Competing Quantum Effects

Isotopic substitution experiments can provide some information on the magnitude of quantum effects operating in a system; within the Born-Oppenheimer approximation, this is expected to leave the PES of the system unchanged. A change in a static property of the system can be attributed to nuclear quantum effects. For a dynamical property an isotope effect does not necessarily point to a nuclear quantum effect, since isotopic substitution will change dynamical variables even within classical mechanics.[2] Because ZPE scales with mass m as $m^{-1/2}$, static properties tend to their classical values in the $m \to \infty$ limit; substituting hydrogen for deuterium, for example, takes us some of the way towards this limit, from which we can infer what would happen if we replaced our quantum world with a classical one.

However, quite a number of the properties of H_2O change only a little on going to D_2O: for example, the melting point increases by 4 K and the boiling point by 1 K, and the surface tension increases by at most 1% [34, 114]. These small changes are at odds with computational studies in which significant changes were found upon quantization [25–31].

These studies often did not fully account for the stretching of the O–H bond. In particular, the anharmonicity of the potential energy in this coordinate may be ignored [25, 27–30]. In this case, the only quantum effect that influences hydrogen bond strengths is that of zero point energy in the coordinates orthogonal to the O–H

[2] Methods, such as that of Swain *et al.* [112], do exist for finding the extent to which an isotope effect in a reaction rate is quantum-mechanical in nature, but these can often be quite ambiguous [113].

bond, which will disrupt the hydrogen-bonding structure. There is also ZPE in the O–H stretch, but for a harmonic bond this will neither weaken nor strengthen the H-bonds.

When an anharmonic O–H bond is included, there will be a competing effect in operation [32, 33]: the anharmonicity in this bond means that ZPE will cause the bond length to increase. In turn, a longer O–H bond length means a larger dipole moment and thus stronger intermolecular attractions. This will mitigate the weakening of hydrogen bonds due to the ZPE in the orthogonal coordinates. The net hydrogen bond disruption will then be less than for rigid water. An example of this is given by the self-diffusion constant D: while rigid water models lead to an increase of up to $\sim$50% in D on quantization [28,29,31,32,64], a flexible model with an anharmonic O–H stretch leads to an increase of only 15% [32].

Competing quantum effects can be observed in a wide range of materials, and unsurprisingly, the net effect of quantum fluctuations on hydrogen-bond strength depends on the nature of the system under study. Using *ab initio* molecular dynamics, Li *et al.* found that when the strength of a hydrogen bond is strong enough, it is strengthened by quantum effects, and otherwise it is weakened [33]. Whereas the hydrogen bonds of water are weak enough to be further weakened by quantum effects, clusters of at least four HF molecules have strong enough hydrogen bonds that upon quantization, H–F bond stretching wins out and they are strengthened.

In order to account for these competing quantum effects in a simulation of water, we will use the flexible and anharmonic q-TIP4P/F potential [32]. This model has the following features:

- long-ranged Coulombic interactions between charge sites on different molecules (there are three charge sites on each molecule: a positive charge on each hydrogen atom, and a negative charge displaced from the oxygen atom along the dipole moment axis),
- shorter-ranged Lennard-Jones interactions between oxygen atoms on different molecules,
- a harmonic H–O–H bend,
- an O–H bond stretch, modelled as a Morse oscillator expanded to fourth order in the displacement of the bond length from its equilibrium value.

It is this latter term that is crucial to describe the interplay between quantum effects. The q-TIP4P/F model was parametrized using path integral calculations to give good agreement with the experimental structure of water (i.e., the O$\cdots$O, O$\cdots$H and H$\cdots$H radial distribution functions), its self-diffusion coefficient and the absorption frequencies in infrared spectra. It has also been successfully used to describe the isotope fractionation of light and heavy water between liquid and vapour [39], as well as being applied to the dynamics of water relaxation following a sudden jump in solute charge [115], and to the properties of hexagonal [116,117] and amorphous [118] ice. Furthermore, the fact that the model was parametrized using simulations that took quantum fluctuations into account means that there will be no "double counting" of quantum effects, as discussed in Chapter 1.

Given this model, perhaps the simplest way to observe the competition of effects is to switch off the anharmonicity of the O–H bond; by running two path integral

simulations, one with the full q-TIP4P/F model and one with the bond stretching term in the potential energy truncated at the harmonic term, the difference between the results of the two will give an idea of the effect of anharmonic bond stretching. While this can provide a qualitative understanding of the result of competing quantum effects, however, it is more useful to quantify the contribution of zero-point energies in various coordinates in a full, anharmonic simulation.

This can be achieved using the quantum kinetic energy. For a single atom, the quantum-mechanical expectation value of kinetic energy is $\langle \mathcal{T} \rangle = \langle p^2/2m \rangle$. The classical equipartition value is $\frac{3}{2} k_\mathrm{B} T$, and any deviation from this is due to quantum effects. A larger $\langle \mathcal{T} \rangle$ corresponds to a smaller uncertainty in position, and thus to a more confined atom. Kinetic energy is not a configurational property so as discussed in Appendix A it cannot be calculated with Eqn. (2.9). Instead, we must use an estimator, a variable that depends on the atomic configurations and whose average value is the same as that of $\mathcal{T}$. The most commonly used estimator for the kinetic energy of an atom is the centroid virial estimator [119, 120],

$$\mathcal{T}_\mathrm{CV} = \frac{3}{2} k_\mathrm{B} T + \frac{1}{2n} \sum_{k=1}^{n} \left(\boldsymbol{q}_k - \bar{\boldsymbol{q}} \right) \cdot \boldsymbol{\nabla} \mathcal{V} \left(\boldsymbol{q}_k \right) . \tag{2.20}$$

The fluctuations in this estimator are reasonably independent of the number of replicas n, and for this reason is widely used. It is also possible to decompose $\mathcal{T}_\mathrm{CV}$ into contributions from three orthogonal types of motion. An element of the quantum kinetic energy tensor is $\langle \mathcal{T}_{\alpha\beta} \rangle = \langle p_\alpha p_\beta / 2m \rangle$, and the centroid virial estimator for this element is [69],

$$\mathcal{T}_{\alpha\beta} = \frac{1}{2} \delta_{\alpha\beta} k_\mathrm{B} T + \frac{1}{4n} \sum_{k=1}^{n} \left\{ \left(q_{k,\alpha} - \bar{q}_\alpha \right) \frac{\partial \mathcal{V}}{\partial q_{k,\beta}} + \left(q_{k,\beta} - \bar{q}_\beta \right) \frac{\partial \mathcal{V}}{\partial q_{k,\alpha}} \right\} , \tag{2.21}$$

with $q_{k,\alpha}$ the α^{th} cartesian component of $\boldsymbol{q}_k$ and $\bar{q}_\alpha$ the centroid of this component. The trace of $\langle \mathcal{T}_{\alpha\beta} \rangle$ is equal to the total kinetic energy, and a diagonal element $\langle \mathcal{T}_{\alpha\alpha} \rangle$ gives the contribution from motion in the α^{th} direction; it is this that allows us to find out how quantum effects due to the O–H stretch compete with effects due to orthogonal motion.

To compare kinetic energy tensors, we seek the average $\langle \mathcal{T}_{\alpha\beta} \rangle$ for certain types of atom (these types might be, for example, "all H atoms" or "H atoms in the first hydration shell of an ion"). The rotational motion of water molecules and the differing orientations of different molecules in systems of chemical interest mean, however, that we cannot simply calculate the tensor in some space-fixed coordinate system for all atoms of each type, as the result would be completely isotropic and we would lose all directional information [69].

One way to overcome this hurdle is to use the mean-square displacement (MSD) method [121, 122]. Kabsch's algorithm [123, 124] is used to find the rotation that, when applied to each molecule, minimizes the mean-square difference between the molecule and a reference water molecule. The rotation thus found is then applied to the kinetic energy tensor of the molecule, giving $\mathcal{T}_{\alpha\beta}$ in a frame defined by the reference molecule. Such tensors are then averaged to give $\langle \mathcal{T}_{\alpha\beta} \rangle$.

Finally, this tensor is diagonalized; the eigenvalues give the contributions to $\langle \mathcal{T} \rangle$ due to motion in three mutually orthogonal directions parallel to the three eigenvectors. Fig. 2.2 illustrates this tensor, for an H atom in a bulk water molecule from a PIMD simulation, as an ellipsoid whose principal components are the eigenvectors of $\langle \mathcal{T}_{\alpha\beta} \rangle$ and whose principal values are the respective eigenvalues. The eigenvector

corresponding to $\langle T_1 \rangle$ is roughly in the direction of the O–H bond, the $\langle T_2 \rangle$ eigenvector is orthogonal to the $\langle T_1 \rangle$ in the plane of the molecule, and the $\langle T_3 \rangle$ eigenvector is normal to this plane. The eigenvalues are around 3.9 $k_{\mathrm{B}}T$, 1.3 $k_{\mathrm{B}}T$ and 0.8 $k_{\mathrm{B}}T$ respectively. Comparing these with the classical value of 0.5 $k_{\mathrm{B}}T$, we see that the greatest amount of ZPE is in the direction of the O–H stretch, in accord with the fact that the frequency of this stretching mode is greater than that of the bending and libration modes (which are due to motion in directions orthogonal to the bond) [125].

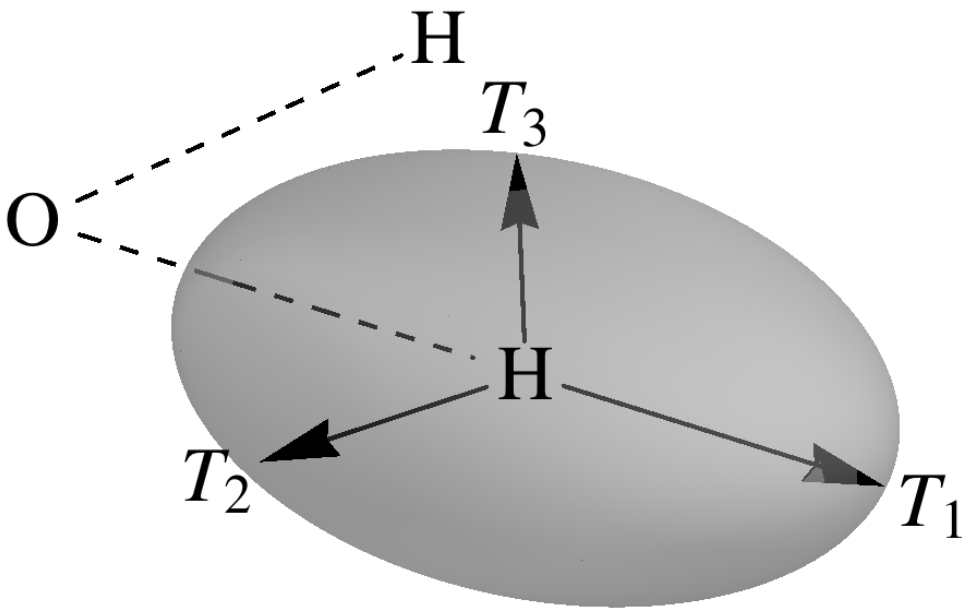

Figure 2.2: Kinetic energy tensor for an H atom in bulk H_2O: the vectors T_1, T_2 and T_3 show the directions of the principal axes, and their lengths are proportional to the corresponding principal values.

Very recently, competing quantum effects have been observed experimentally

[122]: deep inelastic neutron scattering (DINS) is able to measure the average components of the kinetic energy tensor in a molecule-fixed axis. Comparing these components for D_2O in the liquid and the solid state, it can be seen that upon melting, the $\langle T_3 \rangle$ component decreases, and the $\langle T_1 \rangle$ component increases, while the $\langle T_2 \rangle$ component is relatively unchanged. Within the experimental error, the total kinetic energy is not changed by melting, and a set of simulations carried out alongside these experiments gave similar results.

As we shall see in Chapter 3, the quantum kinetic energy can also be used to calculate the free energy of isotope fractionation between the bulk of liquid water and its surface, allowing us to find the competing quantum effects responsible for this fractionation. Chapter 4 will also use an analysis similar to the one described in the current section to help explain the very small change in water exchange rate around the fluoride ion when competing quantum effects are accounted for.

Chapter 3

An Isotope Effect at the Surface of Liquid Water[1]

3.1 Introduction

3.1.1 Isotope Fractionation at the Air-Water Interface

The air-water interface is a desirable, yet challenging, target for both computational and experimental study. It is desirable because this surface is the site of fascinating physical chemistry: it is from here that evaporation occurs [9, 10, 126–129], and heterogeneous reactions between gases and liquid water take place at the interface [130–133]. It is challenging because it is a 2-dimensional subsystem of a 3-dimensional sample: experimental techniques must be highly surface specific in order to measure only the interface. Even in simulations, in which the surface atoms can be clearly defined, larger systems and longer simulation times are needed to gather better statistics than in the study of the bulk. However, such studies of surfaces are quite feasible with modern computational power, and experimental

[1]The work described in this Chapter appears in Ref. [121]. All experiments were carried out by members of the Chen group.

techniques such as those based on nonlinear spectroscopy [134–136] make it possible to study the interface in exquisite detail.

The fractionation of light and heavy water between the liquid and its vapour is of interest in environmental chemistry: lighter isotopes are more likely than heavier ones to be found in the vapour [126, 137–139], and an investigation of the isotopic composition of a sample of water can reveal its origin [140–142]. This isotope effect was studied computationally by Markland and Berne [39] using PIMD with the q-TIP4P/F potential, and accounted for by considering the quantum kinetic energies of H and D atoms in the bulk and in the vapour.

The liquid-vapour fractionation is not purely an equilibrium effect; experiments on irreversible evaporation from liquid microjets show that the rate of evaporation of light water is greater than that of heavy water [127, 128]. Since this is due to the solvation environment at the surface [10, 128], an in-depth study of this environment is needed to better understand the effect.

In this Chapter, we will model the isotope fractionation between hydrogen and deuterium in free O–H bonds at the surface of liquid water: sum-frequency generation spectroscopy [134, 136] experiments carried out in conjunction with this work, performed by members of the Chen group, show that there is a small preference for hydrogen over deuterium in these sites [121]. The molecules with these broken hydrogen bonds are the precursors to evaporation, and so this enrichment of H over D could help to explain why lighter isotopes of water evaporate more readily.

3.1.2 Sum-Frequency Generation Spectroscopy

Sum-frequency generation spectroscopy (SFGS) is a nonlinear optical technique. The best way to explain this is by comparison with linear optics [143], in which an oscillating electric field $\boldsymbol{E}(\omega)$ of frequency ω impinging on a medium gives rise to an oscillatory polarization $\boldsymbol{P}^{(1)}(\omega)$, whose i^{th} Cartesian component is,

$$P_i^{(1)}(\omega) = \sum_j \chi_{ij}^{(1)}(\omega) E_j(\omega), \tag{3.1}$$

in which $E_j(\omega)$ is the j^{th} component of the applied electric field and $\chi_{ij}^{(1)}(\omega)$ is a component of $\boldsymbol{\chi}^{(1)}(\omega)$, the linear susceptibility tensor. This first-order response to an applied field is the basis of Rayleigh and Raman scattering [144].

However, a linear dependence of the induced polarization on the applied field is only an approximation. As field strengths increase, terms in higher powers of the electric field will become more important. If only a single field is applied, then this can lead to optical effects such as second harmonic generation and hyper-Rayleigh scattering, which are discussed in Chapter 5.

Nonlinear effects can also arise if there are two fields, $\boldsymbol{E}(\omega_1)$ and $\boldsymbol{E}(\omega_2)$, incident on a sample. In this case, there will be a polarization induced which oscillates at the sum-frequency, $\omega_1 + \omega_2$,

$$P_i^{(2)}(\omega_1 + \omega_2) = \sum_{j,k} \chi_{ijk}^{(2)}(\omega_1, \omega_2) E_j(\omega_1) E_k(\omega_2), \tag{3.2}$$

where $\chi_{ijk}^{(2)}(\omega_1, \omega_2)$ is a component of $\boldsymbol{\chi}^{(2)}(\omega_1, \omega_2)$, the second-order susceptibility tensor. There will also be a polarization induced at the difference frequency, $\omega_1 - \omega_2$; we will ignore this term because it is the sum-frequency that is probed experimentally.

In Eqn. (3.2), it can be seen that a second-order polarization can be observed at the frequency $\omega_1 + \omega_2$ only from a medium without inversion symmetry. In a system with this symmetry, the reversal of the directions of both fields will reverse the direction of the induced polarization. However, reversing the sign of all three of these terms in this equation gives the condition $P_i^{(2)}(\omega_1 + \omega_2) = -P_i^{(2)}(\omega_1 + \omega_2)$, which requires that $\boldsymbol{\chi}^{(2)}(\omega_1, \omega_2) = 0$. Essentially, this means that in the bulk of an isotropic liquid, such as water, there will be no such polarization induced.

$\boldsymbol{\chi}^{(2)}(\omega_1, \omega_2)$ is only nonzero in environments which have no inversion symmetry. For this reason, it is exquisitely sensitive to the surface of a material (even more so than a number of popular techniques for surface spectroscopy [136]). Happily, this can be used as the basis of a spectroscopic technique: if one of the two incident frequencies is resonant with a vibrational mode of the medium, then $\boldsymbol{\chi}^{(2)}(\omega_1, \omega_2)$ will be enhanced.

The setup of an SFGS experiment is shown in Fig. 3.1: two beams of light, one at the optical frequency ω_{vis} and one in the infrared, ω_{IR}, are incident on a sample, and the signal at $\omega_{\text{SFG}} = \omega_{\text{vis}} + \omega_{\text{IR}}$ is detected. By tuning ω_{IR}, a vibrational spectrum can be produced. The choice of a visible frequency ω_{vis} means that ω_{SFG} will also be in the visible region, and a photomultiplier can be used for detection [134].

The intensity of emitted light is proportional to the square modulus of the second-order polarization [134], and thus depends on the second-order susceptibility $\boldsymbol{\chi}^{(2)}$. Using perturbation theory calculations, it has been shown that this susceptibility

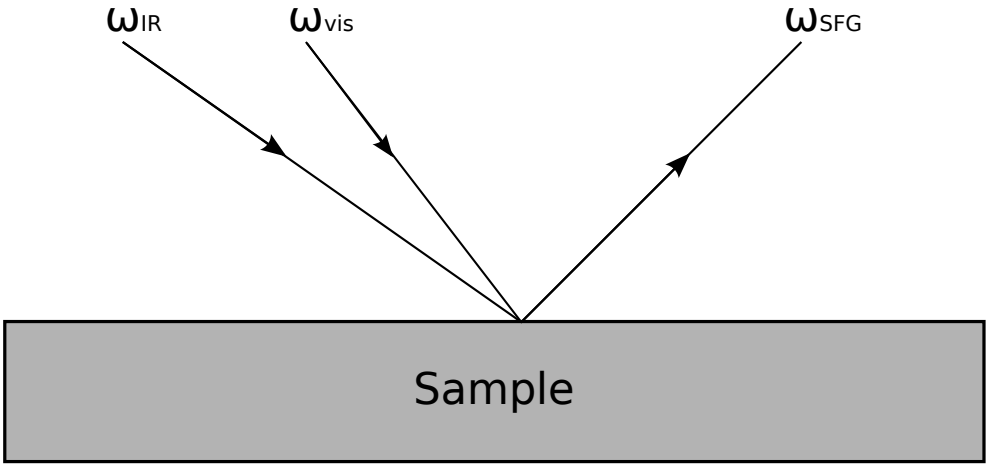

Figure 3.1: Setup of sum-frequency generation spectroscopy used for the experiments described in this Chapter. Infrared light of frequency ω_{IR} and visible light of frequency ω_{vis} are incident on a sample, and light of frequency $\omega_{\mathrm{SFG}} = \omega_{\mathrm{IR}} + \omega_{\mathrm{vis}}$ is detected.

can be written in the form [145],

$$\boldsymbol{\chi}^{(2)} = \boldsymbol{\chi}^{(2)}_{\mathrm{NR}} e^{\mathrm{i}\theta} + \sum_{q=1}^{N_m} \frac{\boldsymbol{A}_q}{(\omega_{\mathrm{IR}} - \omega_q) + \mathrm{i}\Gamma_q}, \tag{3.3}$$

with $\boldsymbol{\chi}^{(2)}_{\mathrm{NR}}$ due to non-resonant scattering and the second term due to resonance between ω_{IR} and the vibrational frequencies ω_q. N_m is the number of vibrational modes, Γ_q a damping coefficient, θ describes the phase difference between the reso-

nant and non-resonant terms and $\boldsymbol{A}_q$ is the strength of a mode. $\boldsymbol{A}_q$ is proportional to the square of the transition dipole moment for the vibrational transition, and to the spatial derivatives of both the polarizability of a molecule and its polarizability during this vibration. This product enforces both the infrared and Raman selection rules for the vibration, ensuring that there is no spectrum from a region with inversion symmetry. Depending on the polarization of the incoming and the detected light, an SFG experiment will probe a particular combination of components of the susceptibility tensor [135, 146, 147], and thus of the $\boldsymbol{A}_q$ tensors.

The SFG signal is then fitted to the expression,

$$I(\omega_{\mathrm{IR}}) \propto \left| \chi^{(2)}_{\mathrm{NR}} e^{\mathrm{i}\theta} + \sum_{q=1}^{N_m} \frac{A_q}{(\omega_{\mathrm{IR}} - \omega_q) + \mathrm{i}\Gamma_q} \right|^2 , \tag{3.4}$$

allowing the frequencies and intensities of peaks to be found. Here, $\chi^{(2)}_{\mathrm{NR}}$ and A_q represent the combinations of elements appropriate to the polarizations used.

Sum-frequency generation spectroscopy has been applied to a wide range of aqueous systems, including the air-water interface [136, 148–154], the premelted layer on ice close to the melting point [155, 156], and the interface with hydrophobic [149, 157–160] and hydrophilic [161–164] species.

When SFG spectroscopy is applied to the surface of liquid H_2O, there are two important features: a broad band in the 3100–3500 cm^{-1} range assigned to bond stretching of hydrogen-bonded O–H bonds and a much sharper peak at 3690 cm^{-1} due to the stretching of free O–H bonds [136, 147–150, 157, 165]. This assignment can be made by comparison with the infrared spectra of water dimers, which contain two peaks due to free O–H bonds, one at 3600 cm^{-1} due to the symmetric stretching

mode and one at 3722 cm^{-1} due to the antisymmetric stretch [166]. The presence of only one peak indicates that there is only one free O–H bond at the surface [148], which we will describe from here onwards as a dangling bond.

By looking at the dangling O–H bond peak in aqueous solutions of methanol, it is possible to infer the structure of the water surface [167]. As the concentration of methanol is increased, the intensity of this peak decreases, up to a bulk concentration of 11% MeOH, at which the peak disappears altogether. This corresponds to a 25% surface concentration of the solute [168], and assuming that each methanol molecule hydrogen-bonds to a dangling O–H bond, this suggests that 25% of the water molecules at the surface are originators of a dangling bond. The surface of liquid water is thus similar to that of hexagonal ice, for which a free surface would lead to one free O–H bond for every four water molecules [136, 167].

SFG experiments have also been performed on isotopically dilute samples in which some fraction of the hydrogen atoms have been replaced by deuterium. When the entirety of the sample is D_2O, the spectrum is qualitatively similar to that of H_2O, though quantitatively different: there are two peaks due to hydrogen-bonded O–D, at 2400 and 2500 cm^{-1}, and one peak due to dangling O–D bonds at 2740 cm^{-1} [153,154]. In mixtures of H_2O, D_2O and HOD, it has been shown that the frequency of the dangling O–H stretch changes little with the concentration of deuterium in the sample, suggesting that the surface environment in which these bonds are found is very similar to that of pure H_2O [169, 170].

3.1.3 Experimental Details

When isotopically diluted water is studied with SFG spectroscopy, there will be peaks due to dangling O–H and dangling O–D bonds. The intensities of these peaks are proportional to the surface concentration of the types of bonds and thus to the surface mole fractions s_{H} and s_{D}, where $s_{\mathrm{H}} + s_{\mathrm{D}} = 1$. The corresponding bulk mole fractions are x_i, with $x_{\mathrm{H}} + x_{\mathrm{D}} = 1$. In order to find a theoretical model for this isotope fractionation we consider the chemical equilibrium,

$$\mathrm{H_b} + \mathrm{D_s} \overset{\mathrm{K}}{\rightleftharpoons} \mathrm{H_s} + \mathrm{D_b}, \tag{3.5}$$

in which the subscript "b" stands for an atom in the bulk, and "s" for an atom at the surface (i.e., in a dangling bond).

By treating the problem in a similar way to Langmuir adsorption, we can find a relationship between the surface and bulk concentrations of a species. We assume that all dangling bond sites are equivalent, and that K does not depend on the surface H:D ratio. Then, the equilibrium constant can be related to the surface and bulk mole fractions of the two atom types as,

$$K = \frac{s_{\mathrm{H}} x_{\mathrm{D}}}{x_{\mathrm{H}} s_{\mathrm{D}}} = \frac{s_{\mathrm{H}} \left(1 - x_{\mathrm{H}}\right)}{x_{\mathrm{H}} \left(1 - s_{\mathrm{H}}\right)}. \tag{3.6}$$

Rearranging this equation gives,

$$x_{\mathrm{H}} = \frac{s_{\mathrm{H}}}{s_{\mathrm{H}} + K \left(1 - s_{\mathrm{H}}\right)}. \tag{3.7}$$

In the experiments performed in tandem with the work of this Chapter, the SFG spectra of samples of water with bulk H:D ratios of 0:100, 25:75, 50:50, 75:25 and 100:0 were recorded; for each ratio the experiment was performed three times.

Details of the experimental setup are given in the Supplementary Information of Ref. [121].

For each experiment, the spectra were fitted to Eqn. (3.4). For X an isotope of hydrogen, s_{X} was found by dividing the intensity of the dangling O–X bond peak by its intensity when the bulk is pure X_2O. Because this is done independently for H and D atoms, the sum of surface mole fractions need not be unity for each experiment. Fitting the surface and bulk mole fraction of hydrogen to Eqn. (3.7) then gave an equilibrium constant, from which the free energy change for substitution of bulk hydrogen with surface deuterium is,

$$\Delta G_{\mathrm{H/D}} = -RT \ln K. \tag{3.8}$$

Fig. 3.2 shows the SFG spectra in the dangling O–H and dangling O–D regions for the five different bulk concentrations. In each case, the peaks have been fitted with two Lorentzians (i.e., $N_m = 2$ in Eqn. (3.4)) [154]. This is necessary because there are two types of O–H bonds (due to HOH and HOD molecules) and two types of O–D bonds (due to DOD and DOH molecules). These four types of dangling bonds are labelled ***D***OD, ***D***OH, ***H***OH, ***H***OD, where the atom in bold italics is the dangling one.

The reason that, for example, ***D***OD and ***D***OH have different stretching frequencies is due to coupling between the dangling bond and the other bond in the molecule [154]. In fact, in Fig. 3.2 it is difficult to discern by eye that there are two Lorentzian terms in each peak, except for the O–D peak in the 50:50 H:D mixture: for the O–D region the two terms are separated by 18 cm^{-1}, and for the O–H region

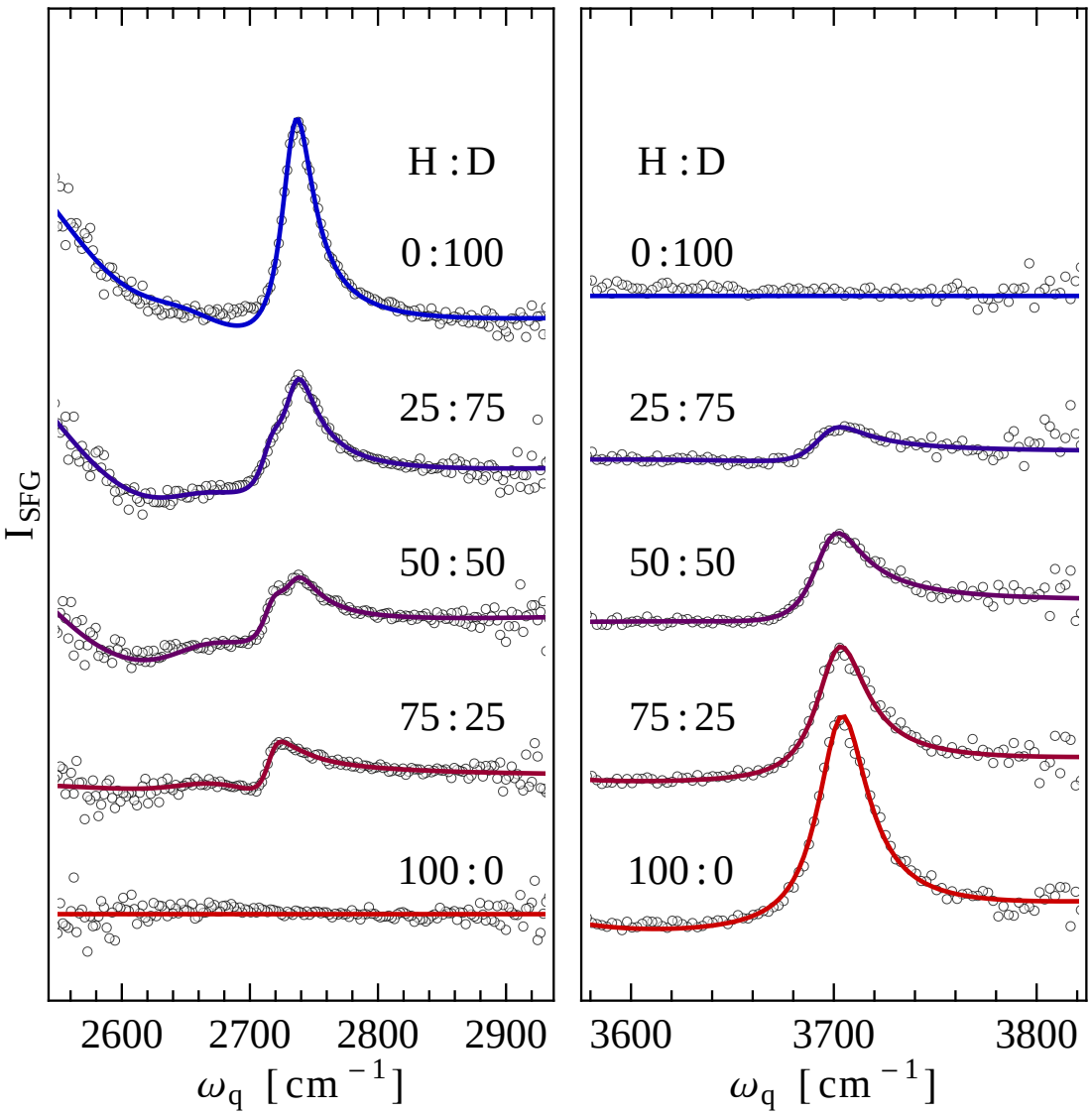

Figure 3.2: SFG spectra of the dangling O–D (left-hand panel) and O–H (right-hand panel) bonds at the surface of isotopically dilute water with several ratios of H:D atoms in the bulk. Open circles show the experimental results and solid lines are obtained by fitting to Eqn. (3.4). This figure was produced by Jian Liu [121].

they are separated by only 9 cm^{-1}, with this latter smaller than the width of the peak [121].

Fig 3.3 shows the surface mole fractions of hydrogen and of deuterium from the three experiments on each mixture, along with the results of fitting Eqn. (3.7) to these populations. These results are widely scattered, indicative of significant experimental errors; the surface represents a very small sample, making it very difficult to gather statistics. This problem is exacerbated by the fact that the effect itself is so small: at a 50:50 bulk ratio of H:D, the surface ratio is 52:48. Nevertheless, there is a measurable preference for H over D atoms in dangling bond sites that the surface.

Because $s_H + s_D \neq 1$ for each experiment, there are 18 independent data points used for fitting. The resulting free energy difference is $\Delta G_{H/D} = (-2.3 \pm 0.7)$ meV. The uncertainty in this number is quite large ($\sim$30%), a result of the widely scattered experimental results. Nevertheless, there is a measurable preference for H over D atoms in dangling bond sites at the surface. In order to observe this preference in simulations, we cannot use classical MD, but will need to turn instead to PIMD.

3.2 Simulation Details

3.2.1 PIMD Simulations

There have been a number of computational studies aimed at interpreting SFG spectra of water surfaces; of particular relevance to this Chapter is the work of Nagata *et al.* [171], who used PIMD to show that HOD molecules at the surface

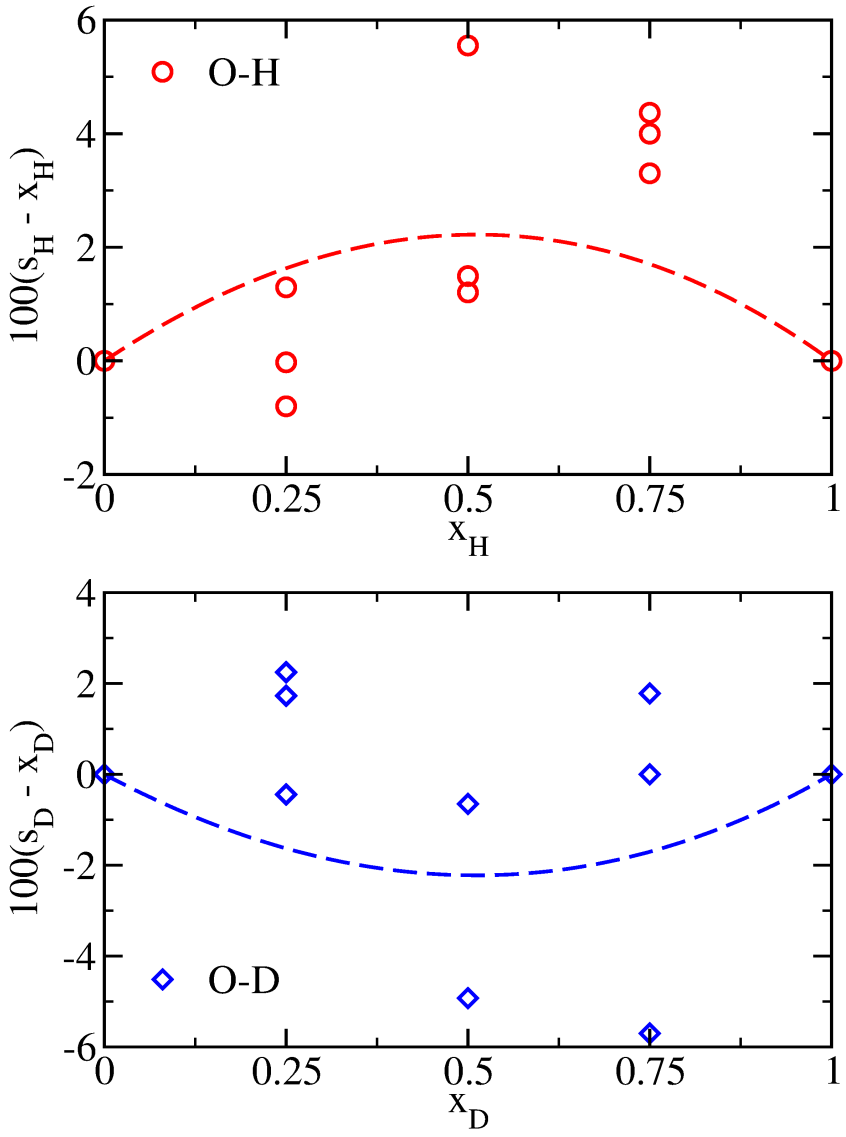

Figure 3.3: Surface mole fractions ($s_{\mathrm{H/D}}$) of hydrogen (upper panel) and deuterium (lower panel) in dangling bond sites, relative to the bulk mole fractions ($x_{\mathrm{H/D}}$). Open symbols represent the results of three different experiments performed on three different days for each bulk mole fraction, and dashed lines show the fit to the functional form of Eqn. (3.7) for s_{H}, or its equivalent for s_{D}. These data are as shown in Fig. 5 of Ref. [121]. The fairly large spread of these data is discussed in the main text.

prefer to be oriented with the O–H bond in the dangling position. Ref. [171] is similar in essence to the work here, but does not give quantitative agreement between the results of simulation and of experiment.

Techniques for calculating the SFG spectrum of water have been used in the literature to give a quantitative comparison between experiment and simulations [170, 172–179]. Since we are interested here in the relative populations of hydrogen and deuterium in dangling bond sites rather than the shapes of the SFG spectra, we will forego a calculation of the spectra and simply find the surface populations of these species in this Chapter.

In order to model the experimental situation, we ran PIMD simulations with a so-called "slab" geometry: a cubic simulation box of 1331 water molecules at the experimental density was extended by around 23 Å in the positive and negative z directions, creating two air-water interfaces, one above and one below the water sample. The q-TIP4P/F potential was used to describe water. The fact that this model is non-polarizable means that some care should be taken in using it in an electrostatically inhomogeneous environment such as the interface [11, 180]; however, the good quality of agreement between the liquid-vapour fractionation ratios predicted by the q-TIP4P/F and the experimental results [39] lends us confidence in the ability of this model to reproduce the experimental results.

These simulations were carried out with H:D ratios of 0.125, 0.25, 0.375, 0.5, 0.625 and 0.875. For each H:D ratio, the system was evolved in the NVT ensemble for 1.2 ns, except for the 50:50 mixture, which was evolved for 4.8 ns. In order to allow the system to reach equilibrium with respect to the bulk concentrations of

H_2O, D_2O and HOD molecules and, more importantly, the surface concentrations of dangling O–H and O–D bonds, we supplemented our PIMD simulations with Monte Carlo trial moves. One hydrogen and one deuterium atom are chosen per trial move, and their momenta and masses swapped. This move is accepted if a chosen random number is less than or equal to $e^{-\beta\Delta\mathcal{H}}$, where the change in energy is,

$$\Delta\mathcal{H} = \frac{\omega_n^2}{2n}\left(m_\mathrm{D} - m_\mathrm{H}\right)\sum_{k=0}^{n-1}\left[\left(\boldsymbol{q}_k^\mathrm{H} - \boldsymbol{q}_{k+1}^\mathrm{H}\right)^2 - \left(\boldsymbol{q}_k^\mathrm{D} - \boldsymbol{q}_{k+1}^\mathrm{D}\right)^2\right], \tag{3.9}$$

with $\boldsymbol{q}_k^\mathrm{H}$ the coordinate of the k^th replica of the H atom and $\boldsymbol{q}_k^\mathrm{D}$ that of the k^th replica of the D atom. Although the probability of accepting such a move is quite small, the calculation of the energy change is computationally extremely cheap, meaning that these moves can be tried tens of thousands of times per PIMD step. During a 20 ps simulation with a 50:50 H:D ratio, there are around 360 000 successful moves, but this represents an acceptance rate of only 0.2%.

The benefit of carrying out these trial moves is shown by calculating the surface hydrogen concentration time correlation function,

$$C_\mathrm{conc}(r) = \frac{\langle \delta s_\mathrm{H}(0)\delta s_\mathrm{H}(t)\rangle}{\langle \delta s_\mathrm{H}(0)\delta s_\mathrm{H}(0)\rangle}, \tag{3.10}$$

where $\delta s_\mathrm{H}(t) = s_\mathrm{H}(t) - \langle s_\mathrm{H}\rangle$, with $\langle s_\mathrm{H}\rangle$ the mean surface mole fraction of H and $s_\mathrm{H}(t)$ the mole fraction at time t. Because the trial moves are so cheap to perform, we treat them as though they take no time: t is then proportional to the number of molecular dynamics timesteps and $C_\mathrm{conc}(t)$ thus shows how much these "free" actions decorrelate the surface environment in the same amount of simulation time.

Fig. 3.4 shows $C_\mathrm{conc}(t)$ for PIMD simulations both with and without these trial

moves. In both cases, starting configurations were used in which the concentrations of H_2O, HOD and D_2O had been equilibrated using simulations with these moves included. Using the moves leads to a much faster decorrelation; fitting the long-time decay to $C_{\rm conc}(t) \simeq Ae^{-t/\tau_{\rm conc}}$ we find $\tau_{\rm conc} = 470$ fs without the moves and 40 fs with them. This means that the PIMD simulations with the trial moves can much more quickly reach equilibrium.

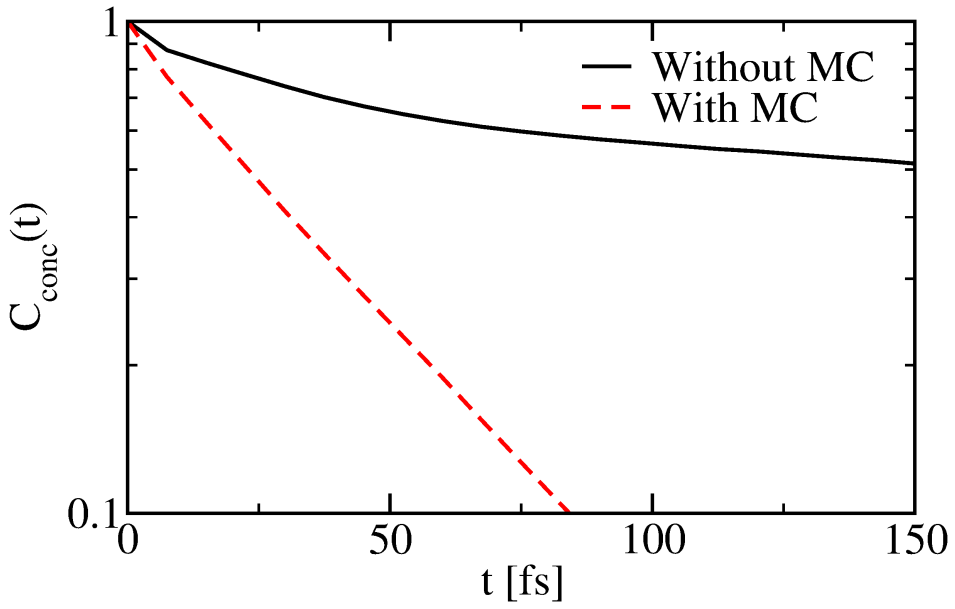

Figure 3.4: Surface hydrogen concentration time correlation function $C_{\rm conc}(t)$ from PIMD for 50:50 bulk ratios of H:D. Solid black lines show the function without Monte Carlo hydrogen-deuterium exchanges, and dashed red lines show the function in the case where these moves are included.

3.2.2 Definition of the Air-Water Interface

The dangling O–H and O–D bonds must be identified from the results of our simulations; this requires that we define the surface of the liquid. The classic way to do this [10, 11, 171, 173] is to employ a Gibbs dividing surface: that is, to calculate the density profile for a slab in the z direction by averaging over many configurations, and to take the interface to be the plane normal to z on which the density reaches half its bulk value. The left-hand panel of Fig. 3.5 illustrates the Gibbs surface.

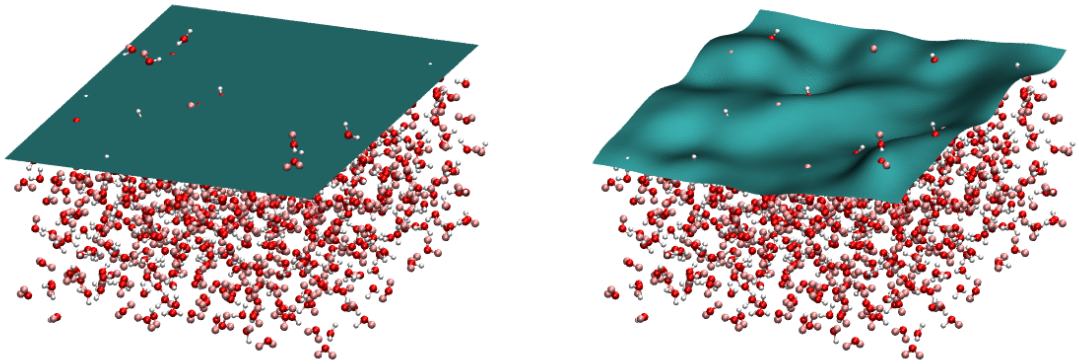

Figure 3.5: Left-hand panel: Gibbs dividing surface for a slab configuration of water (only the upper surface is shown). Right-hand panel: Willard-Chandler dividing surface for the same configuration.

However, by defining the interface in this way, we are ignoring the microscopic detail of the water: its surface is not flat and infinitesimally thin, instead supporting capillary waves [181, 182]. This detail can be recovered by defining the surface in terms of microscopic, rather than macroscopic, variables. The method we used was that of Willard and Chandler [70]. For a given configuration the density at a point

$\boldsymbol{r}$ is defined,

$$\rho(\boldsymbol{r}) = \frac{1}{(2\pi\xi^2)^{3/2}} \sum_{i=1}^{N_\mathrm{O}} e^{-|\boldsymbol{r}-\boldsymbol{r}_i|^2/2\xi^2}, \tag{3.11}$$

where N_O is the number of oxygen atoms, $\boldsymbol{r}_i$ is the position of the i^{th} oxygen atom, and ξ is the width of the Gaussian functions. Following Ref. [70], we used $\xi = 2.4$ Å. Each water molecule is then the source of a Gaussian density, such that the value of $\rho(\boldsymbol{r})$ at some point is a measure of the microscopic density of the system at that point. The air-water interfaces are then defined to be the 2-dimensional surfaces on which $\rho(\boldsymbol{r})$ is equal to half its value ρ_bulk at the centre of the slab. The right-hand panel of Fig. 3.5 illustrates this dividing surface.

In detail, the algorithm we used for finding the Willard-Chandler dividing surface for a configuration of a water slab was as follows:

- Starting at $x = x_0$ and $y = y_0$, the two roots of the equation,

$$\rho(x_0, y_0, z) = \frac{1}{2}\rho_\mathrm{bulk}, \tag{3.12}$$

  are found. These are the z positions of the surface at this (x, y) combination.

- Spreading outwards from (x_0, y_0) the xy plane is divided into a grid on whose points the z position of the surface is found. In order to minimize computational effort, the z values already found are used to narrow down the search for the surface: the root of Eqn. (3.12) is found within lower and upper bounds that are chosen based on where the surface is already known to be.

- As well as the z position of the surface at every pair of (x, y) values on the grid, we also calculate the surface normal, which is parallel to the vector $\boldsymbol{\nabla}\rho(\boldsymbol{r})$.

- For each H or D atom in this configuration, we interpolated from the values at the nearby grid points to find the z position of the dividing surface for the (x, y) coordinate of the atom, and the direction of the surface normal at this point.

To find a straightforward criterion for identifying dangling bonds, we ran classical simulations on isotopically pure H_2O and analyzed these systems using both types of dividing surface. For every O–H bond, the distance (z) of the H atom from the interface and the angle (θ) made with the surface normal at the interface directly above it were recorded and used to build histograms showing the joint probability distribution for $\cos\theta$ and z.

These histograms are shown in Fig. 3.6; the most striking observation to be made in this Figure is that using the Willard-Chandler dividing surface the dangling bonds, which are found at the surface pointing outwards, are clearly identifiable (region a), being separated from all other types of bond by a saddle point in the probability distribution. Two other types of bond at the surface can also be identified: those that are tangential to the surface (region b) and those pointing into the bulk (region c). A suitable definition for a dangling O–H bond is that $z/\text{Å} > 0.410 - 1.011\cos\theta$. On the other hand, the Gibbs dividing surface provides no such definition; there are no distinct regions, and so a dangling bond cannot be identified.

For a given bulk H:D ratio, the number of dangling O–H and O–D bonds at the surface can be counted and averaged over configurations to give the surface H:D ratio. By fitting to Eqn. (3.7), we can then extract an equilibrium constant K, and thus a free energy change $\Delta G_{\text{H/D}}$, for comparison with the experimental value.

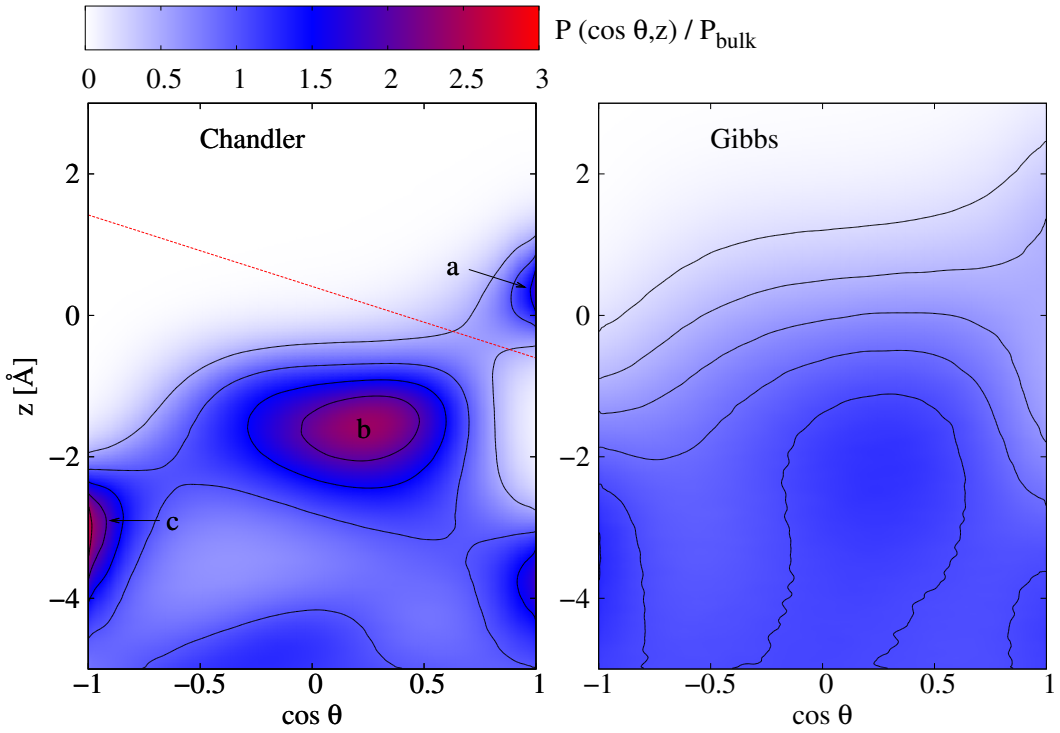

Figure 3.6: Joint probability distribution $P(\cos\theta, z)$ for H atoms near the surface, normalized by the value in the bulk, for the Willard-Chandler (left-hand panel) and Gibbs (right-hand panel) dividing surfaces, as calculated by classical simulations at 298 K. In the left-hand panel, region a describes the dangling O–H bonds, region b the atoms for which the O–H bond is tangential to the surface, and region c the atoms for which the O–H bond points into the bulk. Any H atom with $\cos\theta$ and z values that place it above the red line was counted as a dangling bond.

3.2.3 Competing Quantum Effects

The free energy change for reaction (3.5) can be written as the integral [121, 183],

$$\Delta G_{\mathrm{H/D}} = \int_{m_{\mathrm{H}}}^{m_{\mathrm{D}}} \frac{\langle T_{\mathrm{s}}(m)\rangle - \langle T_{\mathrm{b}}(m)\rangle}{m}\,\mathrm{d}m, \tag{3.13}$$

where $\langle T_{\mathrm{s}}(m)\rangle$ and $\langle T_{\mathrm{b}}(m)\rangle$ are respectively the average quantum kinetic energies for a hydrogen atom of mass m in surface (dangling bond) sites and in the bulk.

Following Ref. [183] we change the variable of integration to $1/\sqrt{m}$ to give,

$$\Delta G_{\mathrm{H/D}} = -2\int_{1/\sqrt{m_{\mathrm{H}}}}^{1/\sqrt{m_{\mathrm{D}}}} \frac{\langle T_{\mathrm{s}}(m)\rangle - \langle T_{\mathrm{b}}(m)\rangle}{1/\sqrt{m}}\,\mathrm{d}\left(1/\sqrt{m}\right). \tag{3.14}$$

This substitution is used because in the limit where the vibrations of the system are harmonic, $\langle T(m)\rangle \propto 1/\sqrt{m}$, so that it renders the integrand almost constant and the integral can be approximated quite well using only the two end points as,

$$\Delta G_{\mathrm{H/D}} \simeq -\left[\frac{1}{\sqrt{m_{\mathrm{D}}}} - \frac{1}{\sqrt{m_{\mathrm{H}}}}\right]\left[\frac{\langle T_{\mathrm{s}}(m_{\mathrm{H}})\rangle - \langle T_{\mathrm{b}}(m_{\mathrm{H}})\rangle}{1/\sqrt{m_{\mathrm{H}}}} + \frac{\langle T_{\mathrm{s}}(m_{\mathrm{D}})\rangle - \langle T_{\mathrm{b}}(m_{\mathrm{D}})\rangle}{1/\sqrt{m_{\mathrm{D}}}}\right]. \tag{3.15}$$

Furthermore, the relationship $\langle T_{\mathrm{E}}(m)\rangle = c_{\mathrm{E}}/\sqrt{m}$ for atoms of mass m in environment E means that the kinetic energy at one end point can be written in terms of that at the other, and a compact approximation for the free energy difference is given by,

$$\Delta G_{\mathrm{H/D}} \simeq 2\left(1 - \sqrt{\frac{m_{\mathrm{H}}}{m_{\mathrm{D}}}}\right)\left(\langle T_{\mathrm{s}}(m_{\mathrm{H}})\rangle - \langle T_{\mathrm{b}}(m_{\mathrm{H}})\rangle\right). \tag{3.16}$$

Eqn. (3.16) shows that we can obtain an approximation to the free energy of isotope fractionation by looking at the kinetic energy of H atoms in dangling bonds

and in the bulk. We can also ascertain the contribution of motion in three orthogonal directions to $\Delta G_{\mathrm{H/D}}$ by calculating the average kinetic energy tensor $\langle T_{\alpha\beta} \rangle$ and finding its eigenvalues and eigenvectors, as explained in Section 2.4. A similar approach was used in Ref. [39] to explain the competing quantum effects responsible for liquid-vapour isotope fractionation.

Thus, in order to rationalize the free energy difference found by fitting our results to Eqn. (3.7), we will find $\langle T_{\alpha\beta} \rangle$ for the four types of dangling bonds (***H***OH, ***H***OD, ***D***OD and ***D***OH) in systems with a 50:50 bulk ratio of H:D, and will also find the average kinetic energy tensors for these species in the bulk by repeating the simulations of Sec. 3.2.1 without extending the simulation box. By comparing the average kinetic energies in bulk and surface sites, we hope to understand the microscopic driving forces for the observed preference of surface sites for hydrogen over deuterium.

3.3 Results and Discussion

3.3.1 Surface Isotope Ratios

Fig. 3.7 shows the surface mole fractions of hydrogen from our PIMD simulations at different bulk H:D ratios, along with the results of fitting Eqn. (3.7) to the results of the simulation and of the experiments, for comparison. Because $s_{\mathrm{H}} + s_{\mathrm{D}} = 1$ in our simulations, $s_{\mathrm{H}} - x_{\mathrm{H}}$ uniquely determines $s_{\mathrm{D}} - x_{\mathrm{D}}$, and so we have not shown this latter. The surface mole fraction of H was calculated as described in Sec. 3.2.2, and the bulk mole fraction was calculated using a section of the bulk 8 Å from the

surface.

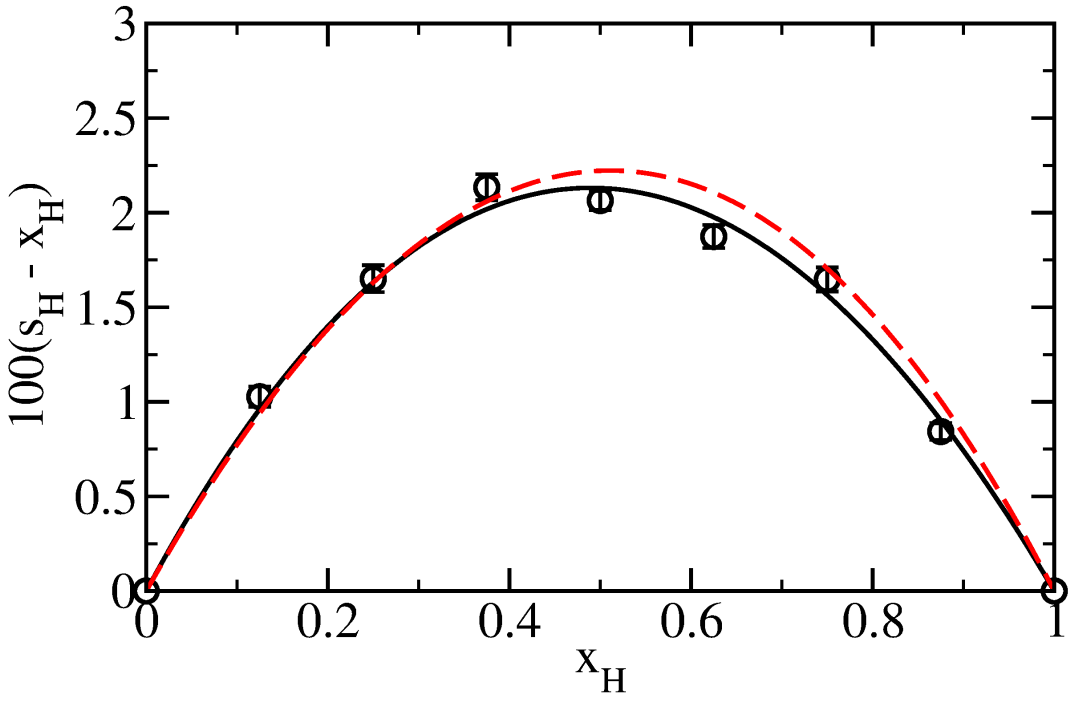

Figure 3.7: Surface mole fraction s_{H} of hydrogen in dangling bond sites, relative to the bulk mole fraction x_{H}. Open symbols represent the results of simulations, and the solid line shows the fit to the functional form of Eqn. (3.7) for s_{H}. The dashed red line is the line fitted to the experimental data, as shown in Fig. 3.3.

The line fitted from simulations is remarkably close to that fitted from experiments, despite the large spread in the experimental results, and the free energy that results is $\Delta G_{\mathrm{H/D}} = (-2.19 \pm 0.04)$ meV. Compared with the value of (-2.3 ± 0.7) meV from experiments, we can see that the agreement is good. The simulation results fit quite well to the Langmuir equation, which helps to justify its use in our

analysis.

Using the results of our simulations, we are able to further validate the use of a Langmuir adsorption equation; the histogram in the left-hand panel of Fig. 3.6 is unchanged both when PIMD is used and when the concentration of D is varied. This means that the structure of the surface (and thus the equilibrium constant K) is unaffected by the surface concentration, as assumed in Sec. 3.1.3.

The question remains: to what extent is this effect specific to the surface? Fig. 3.8 shows how the local concentration of H atoms differs from the bulk concentration for a 50:50 bulk ratio of H:D, as a function of z and $\cos\theta$. There is a clear accretion of H atoms in the dangling bond sites, but only in these sites: elsewhere, the local concentration of H is the same as in the bulk. This means that the effect is extremely surface-specific – to further understand it we need only look at H atoms in dangling bond sites and in the bulk liquid.

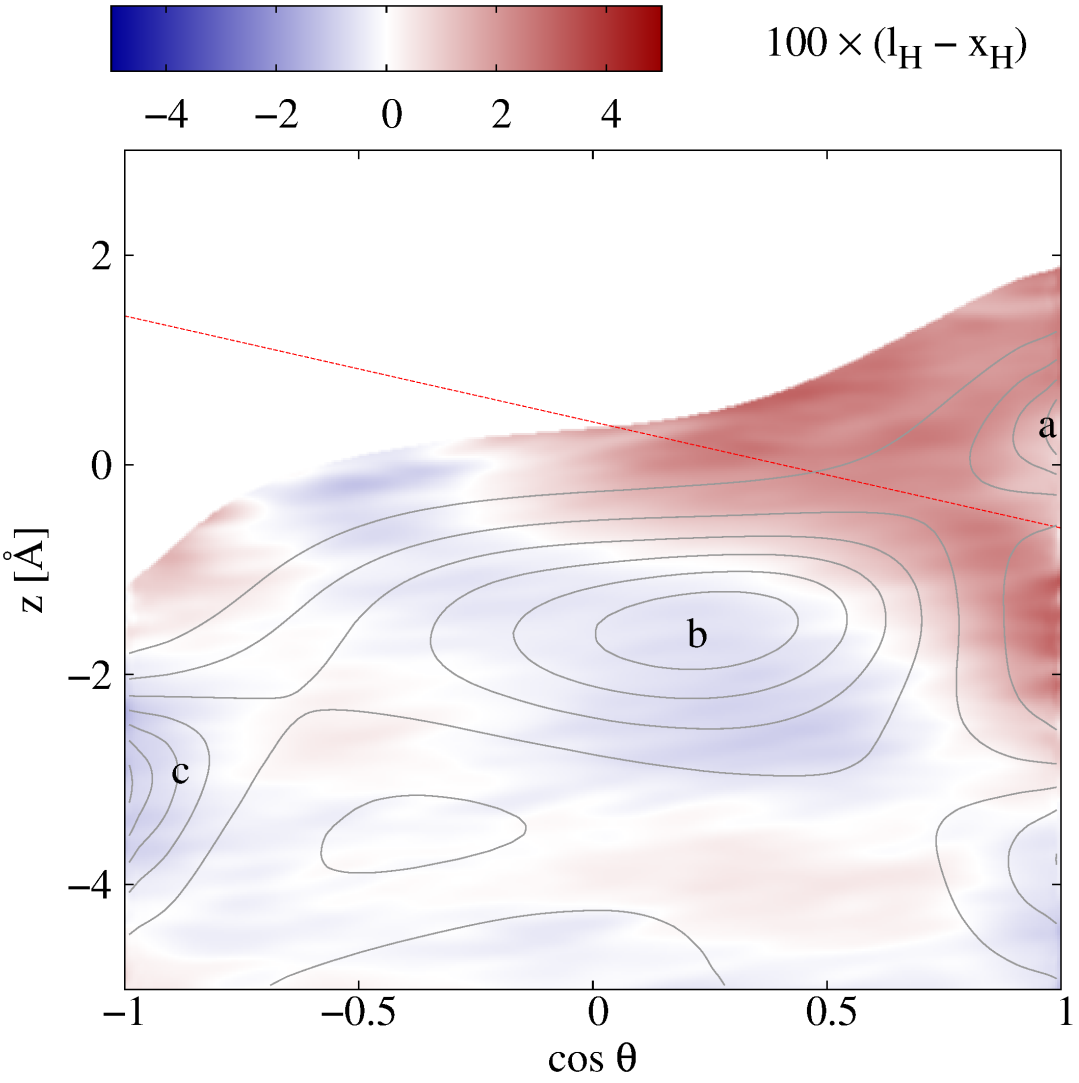

Figure 3.8: Difference between the local mole fraction l_{H} and the bulk mole fraction x_{H} for a 50:50 bulk ratio of H:D, as a function of z and $\cos\theta$, defined by the Willard-Chandler dividing surface. The contours are the same as those in the left-hand panel of Fig. 3.6. O–H and O–D bonds with values of z and $\cos\theta$ that put them above the dashed red line are dangling bonds. The three distinct regions are labelled as in Fig. 3.6: (a) dangling O–H bonds, (b) O–H bonds parallel to the surface, (c) O–H bonds at the surface pointing inwards.

3.3.2 Competing Quantum Effects

The experimental results can now be understood in more depth by considering the kinetic energy tensor. As described in Sec. 3.2.3, the free energy of isotope fractionation can be written as a thermodynamic integral in terms of the surface and bulk kinetic energies. Alternatively, using the approximation of Eqn. (3.16) and the fact that $\langle T \rangle = \langle T_1 \rangle + \langle T_2 \rangle + \langle T_3 \rangle$ we can write $\Delta G_{\mathrm{H/D}}$ as a sum of contributions from motion in three orthogonal directions as,

$$\Delta G_{\mathrm{H/D}} \simeq \sum_{i=1}^{3} \Delta G_i, \tag{3.17a}$$

where,

$$\Delta G_i = 2\left(1 - \sqrt{\frac{m_{\mathrm{H}}}{m_{\mathrm{D}}}}\right)\left(\langle T_{i,\mathrm{s}}(m_{\mathrm{H}})\rangle - \langle T_{i,\mathrm{b}}(m_{\mathrm{H}})\rangle\right), \tag{3.17b}$$

with $\langle T_{i,\mathrm{s}}(m_{\mathrm{H}})\rangle$ the average of the i^{th} eigenvalue of the kinetic energy tensor for an H atom in a dangling bond site, and $\langle T_{i,\mathrm{b}}(m_{\mathrm{H}})\rangle$ the same in the bulk.

Table 3.1 shows the average tensor eigenvalues in the bulk and at the surface, for hydrogen and deuterium atoms in the four possible types of water molecule. The key result in this Table is that on going from the bulk to the surface $\langle T_1 \rangle$ increases, while $\langle T_2 \rangle$ and $\langle T_3 \rangle$ decrease. The eigenvector corresponding to $\langle T_1 \rangle$ is in the direction of the O–H bond, and this increase shows that the H atom is more confined in this direction at the surface, since the O–H bond is unable to stretch and form hydrogen bonds with neighbouring molecules. The eigenvectors corresponding to $\langle T_2 \rangle$ and $\langle T_3 \rangle$ are orthogonal to the O–H bond, and their decrease means that the H atom is less confined in these directions at the surface; molecules are more freely able to librate because there are fewer neighbours to hinder them and no hydrogen bonds

that would be broken by their libration.

These results are qualitatively the same as in Ref. [39], and are illustrated in Fig. 3.9. The total change in $\langle T \rangle$ on going to the surface is negative: the decrease in confinement due to motion orthogonal to the O–H bond is the dominant effect.

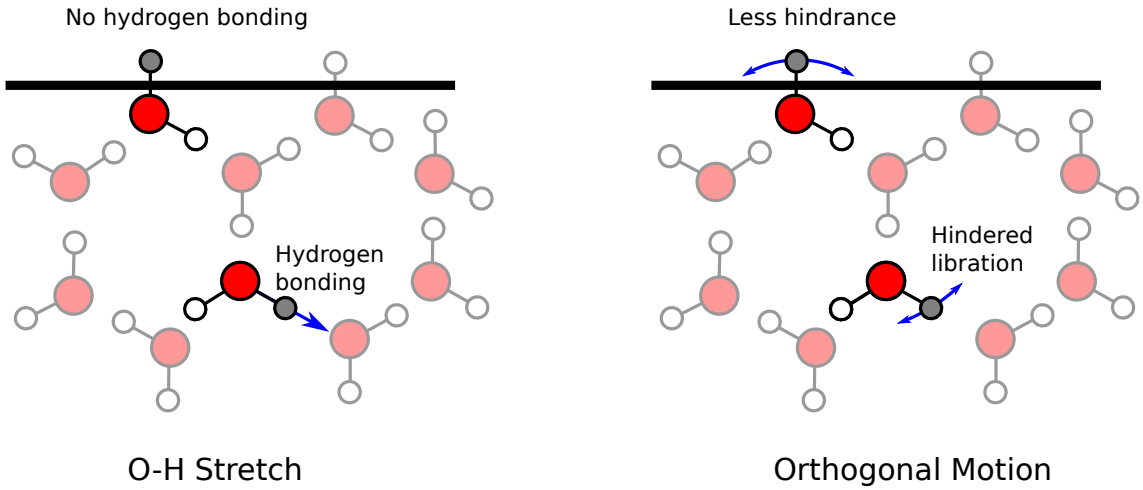

Figure 3.9: Competing quantum effects in hydrogen isotope fractionation at the surface of liquid water. Left panel: the hydrogen atom is more confined at the surface in the direction of the O–H bond, since it is unable to stretch to form hydrogen bonds as it can in the bulk. Right panel: the atom is less confined at the surface in directions parallel to the O–H bond, since the lack of neighbours and of a hydrogen bond allow the bond to librate more easily.

From the values of Table 3.1, ΔG_1, ΔG_2 and ΔG_3 can be calculated, as shown in Table 3.2. Although the resulting approximate $\Delta G_{\mathrm{H/D}}$ does not agree with the results of our simulations within their error bars, it does for the experimental results, and gives a reasonable idea of the contributions of the three different types of motion

Table 3.1: The eigenvalues of the kinetic energy tensor for H and D atoms in bulk water and in dangling bond sites at the surface, as well as for an isolated molecule. These values are obtained from PIMD simulations with a 50:50 bulk H:D ratio at 298 K. The bold font indicates which atom's kinetic energy is shown, and bold italics denote an atom dangling from the surface. As in Fig. 2.2, the T_1 direction is parallel to the O–H bond, the T_2 direction is perpendicular to the O–H bond in the plane of the water molecule, and T_3 is normal to both. $\langle T \rangle$ is the sum of the eigenvalues.

[meV]	$\langle T_1 \rangle$	$\langle T_2 \rangle$	$\langle T_3 \rangle$	$\langle T \rangle$
Bulk				
HOH	99.2	33.7	21.6	154.5
HOD	99.3	34.7	21.6	155.6
DOH	70.8	24.7	17.6	113.0
DOD	70.8	25.4	17.6	113.7
Surface				
HOH	104.9	29.9	15.2	150.0
HOD	104.5	31.2	15.3	151.0
DOH	75.1	22.3	14.0	111.4
DOD	75.0	23.0	14.0	112.0
Isolated Molecule				
HOH	105.3	29.6	13.6	148.5
HOD	105.3	31.0	13.6	150.0
DOH	75.6	21.9	13.1	110.6
DOD	75.6	22.9	13.1	111.6

to the free energy of isotope substitution. All of these contributions are reasonably small (the largest is about $k_{\mathrm{B}}T/7$), and their sum produces an extremely subtle effect.

Table 3.2: Contributions to the free energy of isotope substitution from motion in three orthogonal directions, as approximated in Eqns. (3.17) using the kinetic energy components of Table 3.1, along with total approximate total free energy. Also included for reference are the results from our simulations and from the experiments. The uncertainties in the final digits are shown in brackets.

[meV]	ΔG_1	ΔG_2	ΔG_3	$\Delta G_{\mathrm{H/D}}$
Eqn. (3.17)	3.19	-2.14	3.72	-2.66
			Simulations	-2.19(4)
			Experiment	-2.3(7)

3.4 Conclusions

In the broken hydrogen bonds at the surface of isotopically diluted water, there is a preference for H over D atoms, as seen in the results of sum-frequency generation spectroscopy experiments. Using path integral molecular dynamics, we have been able to observe this effect and to shed light on the microscopic driving forces responsible: both H and D atoms are able to lower their kinetic energy by going from the bulk to the surface, where they are less confined. Because this decrease is greater for

H than for D, the replacement of a dangling O–D bond by an O–H is accompanied by a decrease in free energy.

The average kinetic energy components in the gas phase are also included in Table 3.1. From the point of view of the kinetic energy, the dangling atom is much more similar to an atom in the gas phase than to one in the bulk, as we might expect for an atom not participating in a hydrogen bond. This is also in accord with the fact [128] that molecules at the surface are precursors to evaporation into the vapour phase. The surface preference for H over D helps to account for the fact that light water (which is more likely to be in these precursor sites) evaporates more quickly than heavy water, a phenomenon that provides the basis for the geochemical analysis of water samples.

Chapter 4

Quantum Effects in Water Exchange Around Ions[1]

4.1 Introduction

4.1.1 Ionic Solutions

A very common role for water within chemistry is as the solvent in an ionic solution. These solutions have been studied experimentally for a very long time: it was first recognized in 1887 that ionic compounds dissociate when dissolved in water [185]. Since then, the diverse range of fields of study in which aqueous solvation plays a role include protein folding [186,187], organometallic catalysis [188–190] and electrochemical sensors [191–193]. Water has a great propensity to solvate ionic compounds, as evidenced by free energies of hydration several orders of magnitude larger than $k_{\mathrm{B}}T$ [194].

One of the simplest theoretical models of ionic hydration treats the ion as a charged sphere immersed in a continuous dielectric medium [195]. From this model,

[1]The work described in this Chapter appears in Ref. [184].

one can obtain quantities to be compared with experiment, such as the free energy of hydration [195] and the ionic diffusion constant [196–198]. However, such models are not without problems. For example, since they completely neglect the molecular nature of water, they predict that the hydration free energy of an ion is independent of the sign of its charge.

To account for the asymmetric solvation of cations and anions, as well as other omissions in the continuum model, requires atomistic simulation. Indeed, the results of simulations have been used to improve upon the predictions of continuum theories for several properties. The assumption [199–201] that two oppositely charged ions of the same size will have the same free energy of hydration is fully justified in a continuum theory. However, an analysis of this assumption [202] found that for two large, oppositely charged ions commonly used as reference standards for thermodynamic solvation properties, the cation was more strongly hydrated than the anion, leading to an asymmetry in the free energies. The ion's diffusion constant has also been shown to depend not only on its size, but also on the sign of its charge [7, 203]; the charge asymmetry of hydration is clearly key to the properties of solutions.

Among the details not accessible to a continuum model are the dynamics of water molecules in solvation shells. The simulation of water exchange between the first and second shells has recently garnered interest [6, 8, 24, 204–216], and the effect of nuclear quantization on this reaction is the focus of this Chapter.

4.1.2 Water Exchange

In an aqueous solution of ions $I^{z\pm}$, the water exchange reaction is,

$$\mathrm{I}^{z\pm}\left(\mathrm{H_2O}\right)_n + \left(\mathrm{H_2O}\right)^* \overset{k_{\mathrm{ex}}}{\rightleftharpoons} \mathrm{I}^{z\pm}\left(\mathrm{H_2O}\right)_{n-1}\left(\mathrm{H_2O}\right)^* + \mathrm{H_2O},$$

where k_{ex} is the exchange rate constant. While this reaction is conceptually quite simple, it is a vital step in several processes in organic chemistry (nucleophilic substitution of a neutral molecule by an anion requires the nucleophile to shed its solvent shell before the reaction can occur; it has been suggested that for some such reactions this may be the rate-limiting step [217]), geochemistry (the immobilization of contaminants by metals in soils requires exchange of these contaminants with the water ligands of the metal [218]) and biochemistry (for a reaction to occur at a protein surface, some of the hydrating water molecules must leave [219, 220]). The simplicity of this reaction thus hides a wealth of chemistry, and it is well worth understanding as fully as possible.

The exchange rate or its reciprocal, the mean residence time (MRT), $\tau_{\mathrm{ex}} = 1/k_{\mathrm{ex}}$, is amenable to experimental observation; one viable method for slow enough exchange is nuclear magnetic resonance (NMR) [221–224]. However, if k_{ex} is too high (as is the case for the monovalent ions) then rather than water in the first hydration shell and that in the bulk giving separate NMR signals, they will be indistinguishable by this method, and all that can be deduced is an upper bound to the MRT based on the resolution of the experimental apparatus. Quasi-elastic neutron scattering (QENS) experiments have been used to provide upper bounds of 100 ps for τ_{ex} around several monatomic ions [225–227]. Very recently, 2-dimensional infrared spectroscopy has been able to measure mean residence times below 10 ps for the $\mathrm{BF_4^-}$ [228] and $\mathrm{ClO_4^-}$ [229, 230] anions.

In addition to the exchange rate, another informative quantity is the volume of activation, $\Delta V^{\ddagger}$, which is the difference in volume between the reactant and the transition state. This can be obtained using measurements of the rate constant at multiple pressures p as,

$$\Delta V^{\ddagger} = -k_{\mathrm{B}}T \left(\frac{\partial \ln k_{\mathrm{ex}}}{\partial p} \right)_{T}. \tag{4.1}$$

A negative $\Delta V^{\ddagger}$ indicates that the transition state has a smaller volume than the reactant, which suggests an associative reaction in which the first step is the attachment of a water molecule, and similarly a positive $\Delta V^{\ddagger}$ suggests a dissociative reaction in which the first step is the detachment of a molecule [231].

Although it cannot be used for monatomic ions, whose MRTs are too short, variable-pressure NMR [224, 232] has been used to find volumes of activation for several multivalent ions, including monatomic transition metals [233, 234] and lanthanides [235, 236] as well as transition metal clusters [224, 237–239].

The mean residence time can be calculated by atomistic simulation. Two popular methods for doing so, which we will apply in this Chapter, involve the calculation of time correlation functions: τ_{ex} is calculated either as the decay time of a residence correlation function [4], or as the reciprocal of k_{ex}, found using reaction rate theory [6, 206]. These two methods will be described in detail in Sec. 4.3, along with their strengths and weaknesses and possible alternatives.

$\Delta V^{\ddagger}$ can also be calculated from the results of simulations: using Eqn. (4.1), the rate constant is found at several pressures, and numerical differentiation gives the activation volume. This method was first used by Rustad and Stack [210] to look at the Li^{+} cation, and has been applied since then to several other monatomic and

diatomic ions [8,213,214]. $\Delta V^{\ddagger}$ was also calculated for Li^+ and Na^+ by Hermansson *et al.* by using Voronoi polyhedra to extract the partial molar volumes of species involved in the exchange reactions [204, 205].

Perhaps an even more attractive computational route to understanding the mechanism of a water exchange reaction is that employed in Ref. [206], in which individual exchange events were analyzed to find that the water exchange mechanism around Li^+ was associative, a conclusion that is verified by later work [210, 213]. This method does not require explicit calculations of $\Delta V^{\ddagger}$, and can also be used to provide more information on the mechanism than just its associativity or dissociativity. We will apply it in this Chapter to find the effect of quantum fluctuations on the exchange mechanism.

4.1.3 Nuclear Quantum Effects

Nuclear quantum effects in ion hydration dynamics have been studied previously: Videla *et al.* used RPMD to look at the relaxation of solvent after an instantaneous jump in the charge of a neutral solute atom (a model for a proton or electron transfer, which is very fast compared to nuclear motion) [115]. They found that quantum-mechanical water relaxed more quickly than classical water. Even more recently, Habershon used RPMD to look at how quantum fluctuations affect the mean residence time of water in the first hydration shell of the halide ions [216]. In this paper, the ratio of quantum to classical mean residence times was found to be as large as 1.4 for F^-, with smaller values for larger halogens. However, these simulations used the rigid SPC/E model of water [16], and so did not include

the competition of quantum effects we would expect to see using a flexible and anharmonic model.

These competing effects are particularly interesting in the context of the work of Li *et al.* [33]: a number of the hydrogen fluoride clusters investigated exhibited "strong" hydrogen-bonding, which was thus strengthened by quantum effects. If the hydrogen bond between the F^- ion and the surrounding water molecules were strong enough, quantum effects would strengthen it. In turn, this would mean that it was more difficult for a water molecule to leave the first shell of the fluoride ion than would be the case classically, leading to a quantum MRT that was longer than the classical one. For this reason, it is important to fully account for the flexibility of the O–H bond.

This Chapter will look at the quantum effect on the mean residence time of water around the Li^+ cation and the F^- anion. There are several reasons for choosing these two ions:

- Cations and anions interact differently with their first hydration shell: Li^+ interacts directly with the O atoms of its first-shell water molecules and F^- interacts directly with their H atoms. The competing quantum effect suggested for F^- will not be in operation for Li^+, so that by comparing our results for both ions we can find the extent to which this effect operates.

- Li^+ and F^- have the strongest interactions, in their respective groups, with surrounding water molecules; this is evidenced by their enthalpies and free energies of solvation, which are the most negative in their groups [194]. As

noted by Habershon [216], stronger ion-water interactions lead to larger nuclear quantum effects, and so by looking at Li^+ and F^- we will get an idea of the largest effects for monovalent, monatomic ions.

- Since they are small and monovalent ions, they have small polarizabilities [240,241]. This means that the use of a non-polarizable interaction potential to model these systems should be more reasonable than for other ions. However, as we will note in Section 4.2.1, we are still likely to miss out on some of the physics of the problem by treating the water molecules as non-polarizable.

Because no potential models previously existed for the interaction of ions with q-TIP4P/F water, we will begin by deriving such models for these two ions.

4.2 Parameterization of Ion-Water Potentials

4.2.1 Simulation Details

Since the q-TIP4P/F model gives a good description of the properties of water and accounts for the competition between intra- and intermolecular quantum effects, we will use this for the water-water interactions. The q-TIP4P/F potential is non-polarizable; while it is likely that an explicitly polarizable model would better account for experimental observations [20], the main goal of this work is to look at the effects of quantum fluctuations on hydration properties. It is thus preferable to use a simpler model that treats polarization in a mean-field way, allowing a large amount of data to be collected.

As we are using a non-polarizable water model, we chose to treat the ions in the same way. Because both Li^+ and F^- have small polarizabilities [240, 241], this should be reasonable. For larger halide ions it would likely be necessary to account explicitly for their polarizability.

The longer-range part of the ion-water potential is due to Coulomb interactions between the ion and the charge sites on the water molecules, for which there are no adjustable parameters. There is also a shorter-range part, accounting for van der Waals attraction and Pauli repulsion between the ion and the oxygen atoms. The most common form chosen for this interaction is the Lennard-Jones model,

$$V_{\mathrm{LJ}}(r) = 4\varepsilon_{\mathrm{IO}}\left[\left(\frac{\sigma_{\mathrm{IO}}}{r}\right)^{12} - \left(\frac{\sigma_{\mathrm{IO}}}{r}\right)^{6}\right], \tag{4.2}$$

for which there are two adjustable parameters, $\varepsilon_{\mathrm{IO}}$ and σ_{IO}. For Li^+, this potential was sufficient to give a good description of the solution. For F^-, however, we could not find a combination of parameters that provided as good-quality a description. Since the form of the hard-wall term (the r^{-12} term in Eqn. (4.2)) is arbitrary, we also varied its r-dependence, finding that with an r^{-9} term instead,

$$V_{6\text{-}9}(r) = \frac{27}{4}\varepsilon_{\mathrm{IO}}\left[\left(\frac{\sigma_{\mathrm{IO}}}{r}\right)^{9} - \left(\frac{\sigma_{\mathrm{IO}}}{r}\right)^{6}\right], \tag{4.3}$$

it was possible to get much better agreement with the experimental properties of the solution (as discussed below). In both Eqns. (4.2) and (4.3), $\varepsilon_{\mathrm{IO}}$ is the depth of the potential well. By using $V_{6\text{-}9}(r)$ instead of $V_{\mathrm{LJ}}(r)$, we are able to have a softer ion-oxygen potential while retaining the same well depth and position of the potential minimum.

To find the values of the two parameters $\varepsilon_{\mathrm{IO}}$ and σ_{IO}, we compared the results of simulations to experimental data. We chose to compare to $\Delta G^{\ominus}_{\mathrm{hyd}}$, the standard free energy of hydration, and r^*, the first maximum of the ion-oxygen radial distribution function $g_{\mathrm{IO}}(r)$. These data have been used previously by Jensen and Jorgensen [242] to fit the Lennard-Jones parameters. Alternative target data that have been used in the literature include the enthalpy of hydration [243, 244], ion-water cluster binding energies [243, 245, 246], and properties of the solid salts such as lattice energy and lattice constants [247].

In order to calculate $g_{\mathrm{IO}}(r)$, we ran both classical MD and PIMD simulations in the canonical ensemble. For the Li^+ ion, 25 MD simulations of length 2 ns and 25 PIMD simulations of length 2.6 ns were used, and for F^-, 20 simulations of length 250 ps were carried out in each case. We also used these calculations to find $g_{\mathrm{IH}}(r)$, the ion-hydrogen radial distribution function, and the coordination number n_{coord} of water molecules around each ion,

$$n_{\mathrm{coord}} = 4\pi\rho \int_0^{r_{\mathrm{min}}} r^2 g_{\mathrm{IO}}(r)\, dr, \tag{4.4}$$

ρ being the number density of oxygen atoms and r_{min} the position of the first minimum in $g_{\mathrm{IO}}(r)$. While $g_{\mathrm{IH}}(r)$ and n_{coord} were not used in the parametrization of the potential models, they did allow more insight into the coordination structure of the ions, as well as the effect of quantum fluctuations on this structure.

The free energy difference ΔG_{hyd} was calculated using thermodynamic integration [74]. The scheme we used for doing so was based on those of Refs. [8, 248], with the total ion-water interaction potential written in terms of two variable parameters

λ_1 and λ_2,

$$V(\lambda_1, \lambda_2) = \sum_{i=1}^{N_\mathrm{O}} \left[1 - (1-\lambda_1)^6\right] V_{\mathrm{IO}}(r_{\mathrm{I}i}) + \lambda_2 \sum_{j=1}^{N_\mathrm{C}} \frac{q_\mathrm{I} q_j}{4\pi\epsilon r_{\mathrm{I}j}}, \tag{4.5}$$

with the first sum over all oxygen atoms, and the second over all charge sites on the water molecules. q_I is the charge of the ion and q_j the charge of site j, and $r_{\mathrm{I}j}$ the distance between the ion and site j. $V_{\mathrm{IO}}(r)$ is the short-range ion-water interaction.

The hydration process was broken up into two steps: in the first, $\lambda_2 = 0$ and λ_1 was increased from 0 to 1, corresponding to the growing of an uncharged atom in a box containing 215 water molecules. In the second, $\lambda_1 = 1$ and λ_2 was increased from 0 to 1, as this atom was charged. For each stage, a Gaussian quadrature with 12 points was used to calculate the free energy change. 24 simulations were thus carried out for the free energy of hydration of an ion; during each simulation, the system was evolved for 200 ps at constant temperature and pressure (in order to keep the pressure constant, we used the barostat proposed in Ref. [249]).

To the total free energy thus calculated, we added two correction terms:

- The first of these terms is due to the potential difference incurred on crossing the air-water interface [246,250] due to the orientational ordering of molecules near the surface [251]. This leads to a contribution of $N_\mathrm{A} q_\mathrm{I} \phi$ to the free energy due to an ion of charge q_I crossing the potential difference ϕ between points infinitely far from the surface in the air and water phases [252].

  To calculate this potential difference, we carried out an analysis similar to that of Wilson *et al.* [253]. Using the PIMD simulations of pure water slabs carried out in Sec. 3.2 at 298 K, and classical simulations with the same system size

and simulation time, we calculated the mean electric field $E(z)$ as,

$$E(z) = \frac{2\pi}{A} \langle q_-(z) - q_+(z) \rangle \,, \tag{4.6}$$

where a bulk simulation box has been extended along the z axis to give a slab, $q_+(z)$ is the net charge above the height z and $q_-(z)$ is the net charge below this height. In a simulation of bulk water, these quantities would vanish on average for all z.

The electric field can then be used to calculate the electrostatic potential as,

$$\phi(z) = \phi(z^*) - \int_{z^*}^{z} E(z')\,\mathrm{d}z'. \tag{4.7}$$

z^* was chosen to be in the vacuum, around 50 Å from the centre of the slab, and we took $\phi(z^*) = 0$ V. The potential thus calculated is shown in Fig. 4.1, where we see that the vacuum phase is at a potential $\Delta\phi = +576$ mV compared to bulk water in PIMD simulations and $\Delta\phi = +512$ mV in classical MD simulations. This leads to a correction of ± 13.3 kcal/mol to the free energy quantum-mechanically and ± 11.9 kcal/mol classically, where the positive sign corresponds to the F^- ion and the negative sign to Li^+. Although the potential differences on crossing the surface are quite small in both cases, there is a clear 13% increase in the quantum $\Delta\phi$ over the classical one. The O–H bond in quantum-mechanical q-TIP4P/F water is longer than when this model is used in classical simulations, leading to a larger dipole moment [32]; the larger surface dipole moment that results will give rise to a larger electric field.

- The addition of a second term gives us the standard free energy of hydration

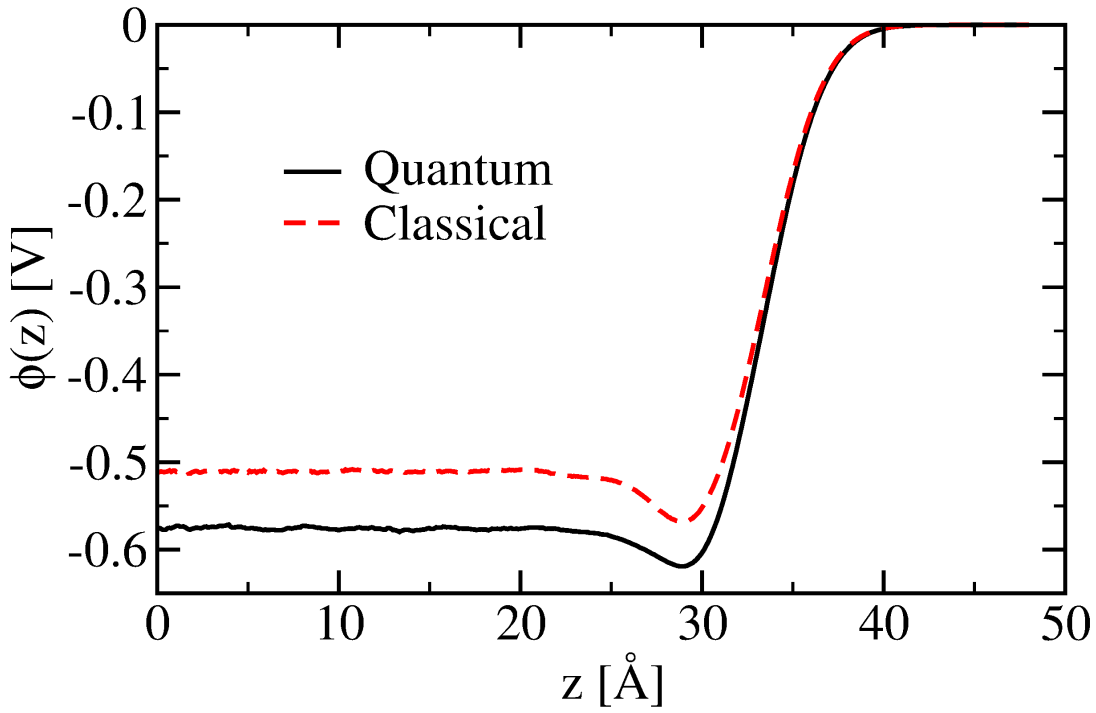

Figure 4.1: Mean electric potential $\phi(z)$ as a function of the height z from the centre of a slab of water molecules from PIMD simulations (solid black lines) and classical MD simulations (dashed red lines) at 298 K.

$\Delta G^{\ominus}_{\mathrm{hyd}}$. This is the free energy difference between an ideal gas of ions at standard pressure ($p^{\ominus} = 1$ bar) and a solution at standard molality ($b^{\ominus} = 1$ mol kg^{-1}). The correction, equal to 1.9 kcal/mol, is the free energy change when a mole of ideal gas at $p^{\ominus}$ is compressed to the molar volume of the solution [246].

For the Li^+ ion, we took as a starting point for our parametrization the parameters of Peng *et al.* [244], using the Lorentz-Berthelot combination rules [73] to convert from parameters appropriate to the TIP4P-Ew water model to those for

the q-TIP4P/F model. For F^-, we started with the Lennard-Jones parameters of Jensen and Jorgensen [242], using the same ε_{IO} as they did and a value of σ_{IO} that gave the same position of the minimum in $V(r)$.

4.2.2 Results

Table 4.1 gives the potential parameters we used to describe the interactions of the Li^+ and F^- ions with the oxygen atoms in the surrounding solvent, and Table 4.2 compares the hydration free energy, first maximum in the ion-oxygen RDF, and coordination number, with experimental values.

The parameters used for Li^+ are unchanged from those derived from Ref. [244], since we found that agreement with experiment was quite good, and could not be improved by altering the parameters. There were two reasons for this:

- As discussed by Jensen and Jorgensen [242], r^* is positively correlated with σ_{IO} and ε_{IO}, and $\left|\Delta G^{\ominus}_{hyd}\right|$ is negatively correlated with both of these. This means that both pieces of data cannot be fitted perfectly.

- It is possible to alter both σ_{IO} and ε_{IO} to fit one piece of data perfectly and the other piece reasonably well, but in doing so the coordination number was drastically altered, decreasing the quality of the model.

On the other hand, when we used a set of parameters based on Ref. [242] for F^- with a standard Lennard-Jones potential, the fit to both pieces of data was much poorer. Even after varying σ_{IO} and ε_{IO}, we could not find a good enough set of parameters. It is for this reason that we decided to use the 6–9 potential of Eqn. (4.3),

with which we could obtain perfect agreement with r^*, while simultaneously fitting $\Delta G^{\ominus}_{\mathrm{hyd}}$ to the same quality as for Li^+, and with a reasonable coordination number. This potential model has not previously been used in modelling ionic solutions, but it is justified by its success in doing so here. In fact, other potentials besides the Lennard-Jones have previously been used to study a range of different ions [4, 206].

Table 4.1: Parameters for the ion-water potentials.

Ion	$\varepsilon_{\mathrm{IO}}$ [kcal/mol]	σ_{IO} [Å]	Potential
Li^+	0.136	2.297	V_{LJ} [Eqn. (4.2)]
F^-	0.054	3.791	$V_{6\text{–}9}$ [Eqn. (4.3)]

Looking at Table 4.2, the static properties we have simulated change only by a very small amount when nuclear quantum effects are accounted for: none of these properties changes by more than 0.5%. However, this does not mean that quantization of the system has no effect at all: Figs. 4.2 and 4.3 show the ion-oxygen and ion-hydrogen RDFs for Li^+ and F^- solutions, respectively, where we see that although the quantum-mechanical and classical RDFs have their first peak at the same position (and the same coordination number), this peak is smaller and broader in the quantum case.

As described in Sec. 2.4, this de-structuring on quantization is expected, being due to ZPE in the coordinates responsible for hydrogen-bond breaking [25, 26]. The effect is larger for Li^+. While we will discuss the causes of this difference in detail

Table 4.2: Comparison of static properties of the ion-water potential models, obtained using classical MD and PIMD, with experimental results. $\Delta G^{\ominus}_{\text{hyd}}$ is the standard free energy of hydration, r^* is the position of the first minimum in the ion-oxygen RDF $g_{\text{IO}}(r)$, and n_{coord} is the ion's coordination number. The uncertainty in the final digits of a quantity are given in parentheses.

Property	Classical	PIMD/RPMD	Experiment
	Li^+ Ion		
$-\Delta G^{\ominus}_{\text{hyd}}$ [kcal/mol]	123.0(1)	123.2(1)	126.5(1)[a]
r^* [Å]	1.92	1.93	2.08[b]
n_{coord}	4.03	4.05	4[c]
	F^- Ion		
$-\Delta G^{\ominus}_{\text{hyd}}$ [kcal/mol]	106.6(1)	106.0(1)	102.5(1)[a]
r^* [Å]	2.63	2.63	2.63[b]
n_{coord}	5.67	5.68	4–6[d]

[a]Ref. [194]
[b]Ref. [254]
[c]Ref. [255]
[d]Ref. [5]

in Sec. 4.5, one possible reason for this is that in the exchange of water around F^-, there are two competing effects: ZPE in the stretching coordinate of the O–H donating a hydrogen bond to F^- will mitigate the structure weakening due to ZPE in the orthogonal coordinates.

Another factor is that water molecules are more tightly bound in the first hydration shell of Li^+ than in that of F^-. This is apparent on looking at $g_{IO}(r)$ for the two ions in Figs. 4.2 and 4.3, in which the lithium-oxygen RDF has a much sharper first peak than that of the fluoride-oxygen RDF. In the case of Li^+, there will thus be more ZPE in the coordinates involved in water exchange. As pointed out by Habershon [216], this ZPE is not solely in the $Li^+ \cdots O$ coordinate; it is made up of contributions from the many coordinates involved in the exchange.

The hydration shell structures described by the RDFs of Figs. 4.2 and 4.3 are further illustrated in Fig. 4.4, which shows snapshots from classical MD simulations. Around Li^+, the first solvation shell consists of four water molecules arranged tetrahedrally, with their oxygen atoms pointing towards the ion. Around F^-, the shell consists of six molecules arranged octahedrally, donating hydrogen bonds to the ion.

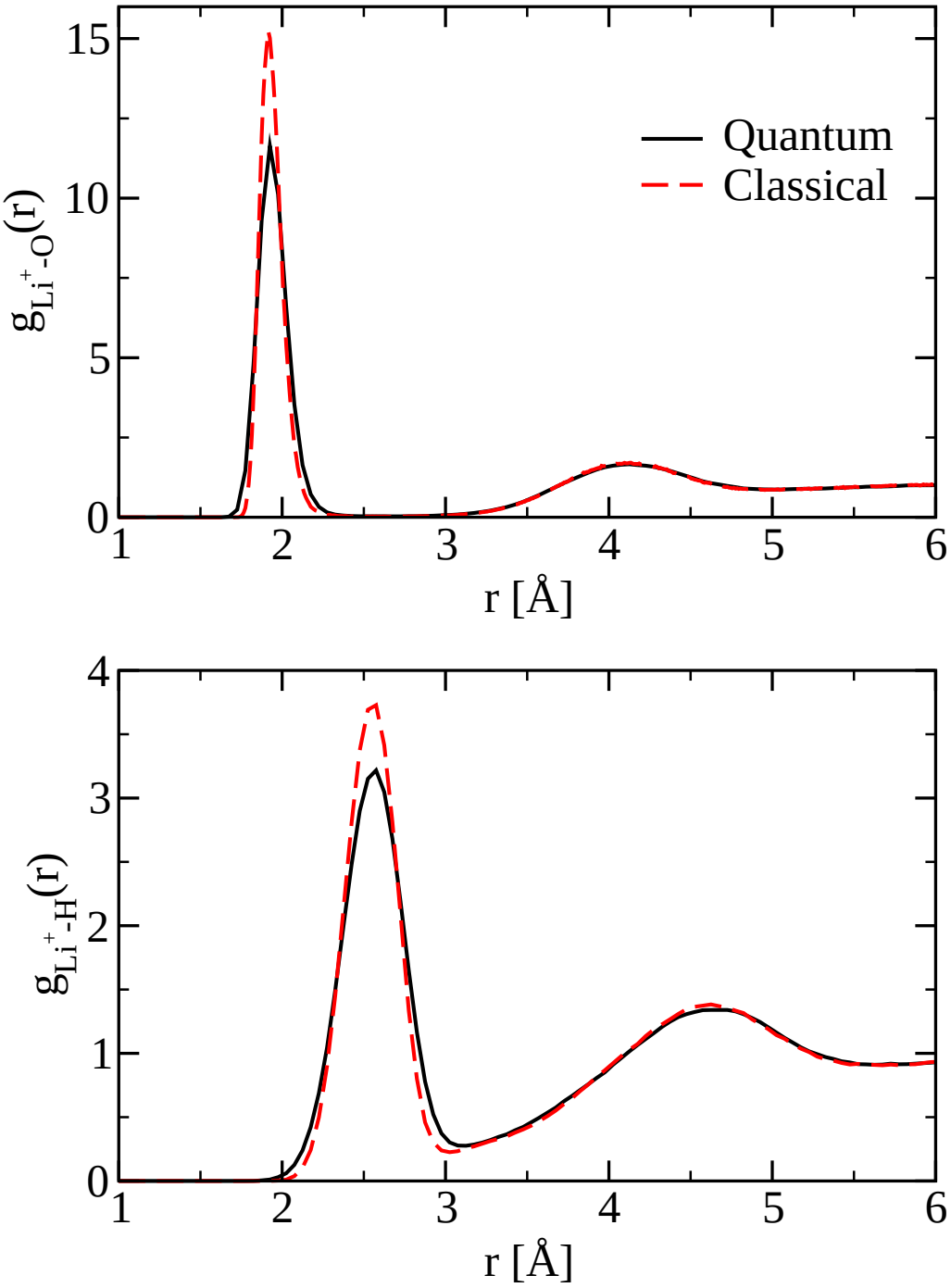

Figure 4.2: Ion-oxygen RDFs (top panel) and ion-hydrogen RDFs (bottom panel) for Li^+ from PIMD simulations (solid black lines) and classical MD simulations (dashed red lines) at 298 K.

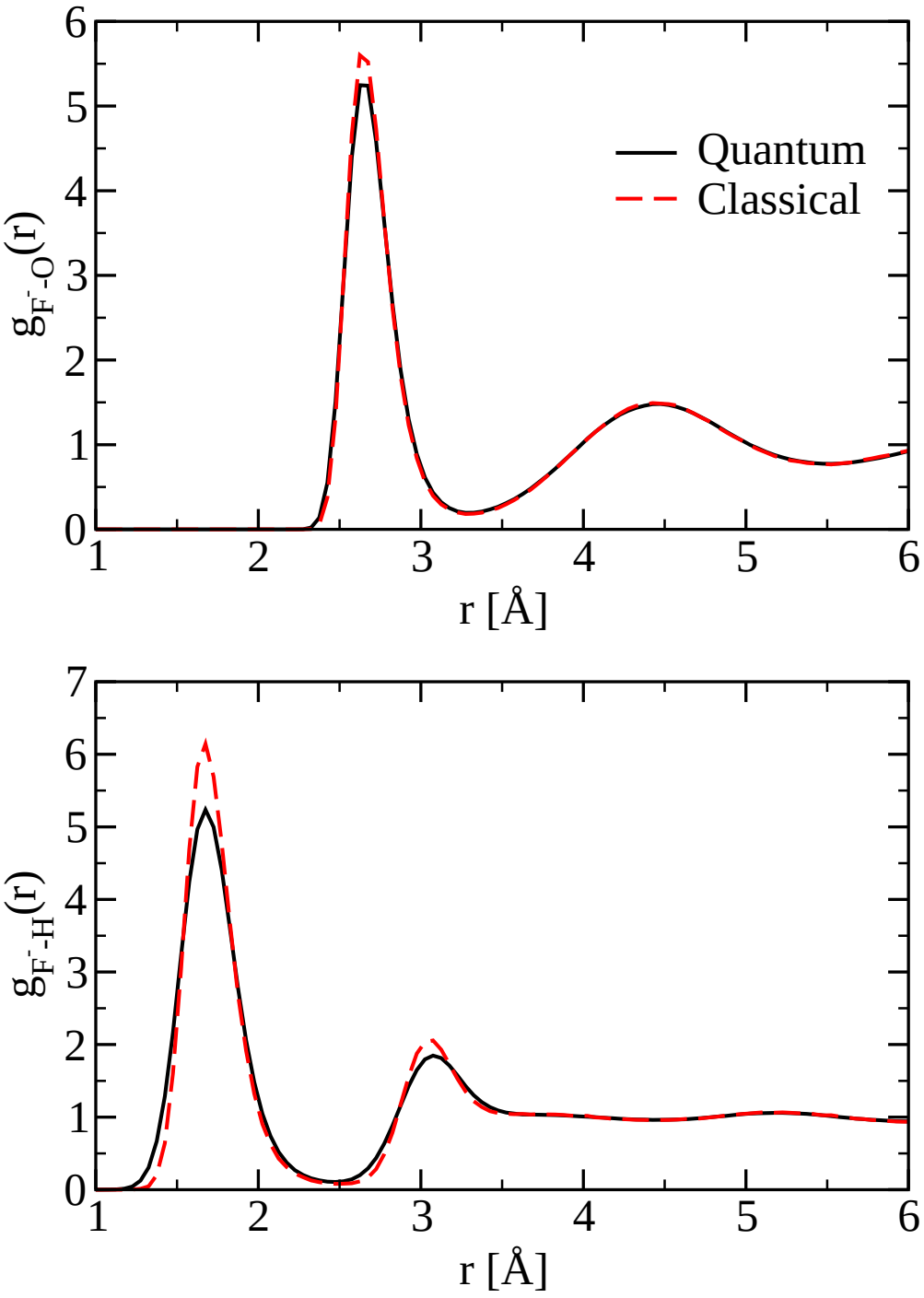

Figure 4.3: Ion-oxygen RDFs (top panel) and ion-hydrogen RDFs (bottom panel) for F^- from PIMD simulations (solid black lines) and classical MD simulations (dashed red lines) at 298 K.

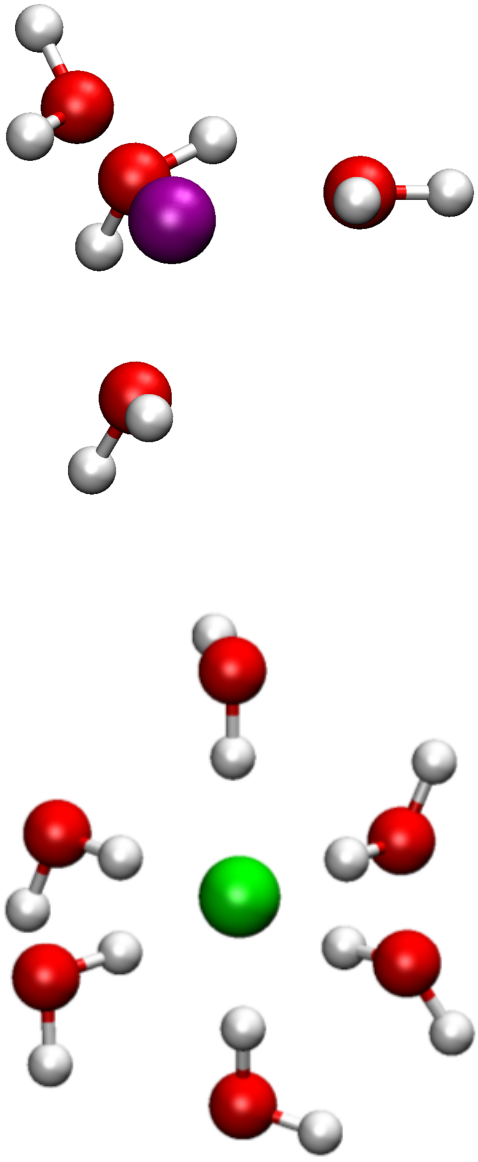

Figure 4.4: Snapshots of the first hydration shells of the Li^+ (upper panel) and F^- (lower panel) ions are shown here, as obtained from classical MD simulations at 298 K.

4.3 Calculation of Mean Residence Time and Mechanisms

4.3.1 Rate Theory Calculations

One method to calculate the rate constant k_{ex} is to treat the water exchange as a first-order rate process, or equivalently, to focus on the "reaction" in which a water molecule leaves the first hydration shell [6, 206]. Choosing the reaction coordinate to be r, the distance between the ion and the centre-of-mass of a water molecule, we can use rate theory to find k_{ex}. The most computationally tractable form for the rate constant is the Bennett-Chandler expression [256, 257],

$$k_{\mathrm{ex}} = \lim_{t\to\infty} k_{\mathrm{ex}}^{\mathrm{TST}} \kappa(t). \tag{4.8}$$

In this equation, $k_{\mathrm{ex}}^{\mathrm{TST}}$ is the transition state theory rate constant. This can be calculated using the potential of mean force, $W(r)$, the free energy as a function of the reaction coordinate,

$$k_{\mathrm{ex}}^{\mathrm{TST}} = \left(\frac{1}{2\pi\mu\beta}\right)^{1/2} \frac{\left(r^{\ddagger}\right)^2 e^{-\beta W(r^{\ddagger})}}{\int_0^{r^{\ddagger}} r^2 e^{-\beta W(r)}\,\mathrm{d}r}, \tag{4.9}$$

with μ the reduced mass of the ion-water pair and $r^{\ddagger}$ the value of r at the transition state; that is, the position of the maximum of $W(r)$ separating reactant and product states.

By itself, $k_{\mathrm{ex}}^{\mathrm{TST}}$ provides an approximation to the full rate constant k_{ex}. Within transition state theory, the assumption is made that if an ion-water pair is at the transition state, and the separation of the pair is increasing, then the reaction occurs.

In reality, this is not always the case: it is quite possible that some time later, this pair will recross the transition state and end up back in the reactant region. The transmission coefficient $\kappa(t)$ in Eqn. (4.8) corrects for this possibility, giving $k_{\mathrm{ex}} \leq k_{\mathrm{ex}}^{\mathrm{TST}}$.

Both $W(r)$ and $\kappa(t)$ can be calculated by simulation. $W(r)$ is a static property of the system, and is related to the ion-water radial distribution function $g_{\mathrm{I\text{–}H_2O}}(r)$ by,

$$W(r) = -\beta^{-1} \ln g_{\mathrm{I\text{–}H_2O}}(r). \tag{4.10}$$

The functions $g_{\mathrm{I\text{–}H_2O}}(r)$ were calculated from the same simulations used to find $g_{\mathrm{IO}}(r)$ and $g_{\mathrm{IH}}(r)$, described in Section 4.2.1. There is, however, one key difference. In RPMD rate theory, the most convenient reaction coordinate is the centroid, $\bar{r}$ of the ion-water distance r [104]. This was found to give much better statistics when calculating the rate constant than when the bead coordinates were used, because a single bead crossing the transition-state dividing surface was much more likely than the centroid to recross this surface. Using the centroid means that $\sim$100 times fewer trajectories had to be run to find the full rate constant. This means, however, that the PMF in Eqn. (4.9) must be replaced by the centroid PMF, $W(\bar{r})$ [258–260]. In the path-integral case, we thus calculated the PMF as $W(\bar{r}) = -\beta^{-1} \ln g_{\mathrm{I\text{–}H_2O}}(\bar{r})$ [260].

For the Li^+ ion, $g_{\mathrm{I\text{–}H_2O}}(r)$ is so small around $r^{\ddagger}$ that $W(r)$ is very noisy in this region. While it is possible to improve the sampling by using longer simulations, it is more cost-effective to use a thermodynamic integration to calculate the PMF here [206, 261]. For the classical PMF, we constrained the distance between the Li^+

ion and the centre of mass of a water molecule at distances between 2.2 Å and 3.8 Å (with 0.025 Å between successive values), and for the quantum PMF we constrained the centroid distance $\bar{r}$ between the same values. For each distance, the mean force $\langle F(r) \rangle$ on the constraint was recorded, and integrated to give $W(r)$ as,

$$W(r) - W(r_0) = -\int_{r_0}^{r} \langle F(r) \rangle \, \mathrm{d}r. \tag{4.11}$$

The constraints were applied using a method similar to RATTLE [262]; since only one Lagrange multiplier was used, it was calculated analytically.

The transmission coefficient is a dynamical property of the system, and was calculated using either classical MD in the NVE ensemble, or RPMD. The expression for $\kappa(t)$ within RPMD (which can be reduced to the classical expression by setting $n = 1$) is,

$$\kappa(t) = \frac{\left\langle \dot{\bar{r}}(0) \delta \left[\bar{r}(0) - r^{\ddagger} \right] \theta \left[\bar{r}(t) - r^{\ddagger} \right] \right\rangle_n}{\left\langle \dot{\bar{r}}(0) \delta \left[\bar{r}(0) - r^{\ddagger} \right] \theta \left[\dot{\bar{r}}(0) \right] \right\rangle_n}, \tag{4.12}$$

with $\bar{r}(t)$ the centroid of the reaction coordinate, $\dot{\bar{r}}(0)$ its velocity at time 0, $\delta[x]$ the Dirac delta function, and $\theta[x]$ the Heaviside step function.

The starting configurations for the calculations of the transmission coefficients must be drawn from a system in which the reaction coordinate is constrained at its transition-state value and equilibrated in the canonical ensemble. These configurations were generated by running simulations in the NVT ensemble, with the constraints applied as in the calculation of the PMF for Li^+. In the classical case, r was fixed at $r^{\ddagger}$, and in the path integral case the centroid $\bar{r}$ was fixed at $r^{\ddagger}$. 15 runs of 8 ns were carried out, with configurations stored every 4 ps. For every such run, each stored configuration was used to start a microcanonical simulation (of

which there were 2000 per run), along which $\kappa(t)$ was calculated using Eqn. (4.12). Averaging over all 15 runs gave the average transmission coefficient along with a standard error, from which the full rate constant k_{ex} could be found.

This technique has been used to find the MRTs of a number of ions, including Li^+ [206, 210, 213], Na^+ [6, 8], Fe^{2+} [8], Be^{2+} and Mg^{2+} [215], and the halide ions [214]. Because the method is designed for rare events (i.e., ones in which there is a potentially large reaction barrier), it is able to handle exchanges with rate constants that are too small to be accessed by other methods. An alternative rare-event method is transition path sampling (TPS) [263, 264], applied by Kerisit and Rosso to water exchange [8], which does not require a reaction coordinate to be defined in advance.

4.3.2 Direct Observation of Exchanges

The reported MRTs of water in the first hydration shells of monatomic ions tend to be on the order of 10-100 ps [4,7,206,234], which means that it should be possible to observe water exchange around these ions in a simulation. In doing so, we can not only calculate τ_{ex} for comparison with our rate theory results, but we can also go further and look at the water exchange mechanism. To observe the water exchange dynamics we use classical MD simulations in the microcanonical ensemble, and TRPMD simulations.

Impey, Madden and McDonald [4] were the first[2] to calculate τ_{ex} using a residence

[2]However, a related time correlation function, in which no allowance is made for short excursions out of the first solvation shell, pre-dated this residence correlation function [265].

correlation function $C_{\text{res}}(t)$, which describes the timescale on which members of the first hydration shell leave. A similar time correlation function, introduced by Luzar and Chander [266,267], has been used to calculate mean residence times as the decay time of a hydrogen-bond existence correlation function [207, 216].

In the TRPMD simulations, $C_{\text{res}}(t)$ is given by,

$$C_{\text{res}}(t) = \frac{\left\langle \sum_{i=1}^{N_w} \bar{S}_i(0;t^*)\bar{S}_i(t;t^*) \right\rangle_n}{\left\langle \sum_{i=1}^{N_w} \bar{S}_i(0;t^*) \right\rangle_n}, \tag{4.13}$$

where N_w is the number of water molecules in the system, and the residence function $\bar{S}_i(t;t^*)$ is 1 if the centroid of the i^{th} water molecule has not left the shell for a time period greater than t^* between time 0 and time t, and is zero otherwise. t^* is chosen to be 2 ps (approximately the time taken for a water molecule to diffuse over one molecular radius [4]). In classical MD simulations, for which $n = 1$, the centroid of the water molecule is the water molecule itself.

We can calculate the mean residence time by fitting the residence correlation function to an exponential decay at long times, such that $C_{\text{res}}(t) \simeq Ae^{-t/\tau_{\text{ex}}}$. This technique has been used to calculate the MRT for the alkali metals and halides [4, 7, 8, 203, 207, 216]. As compared to the method of the previous section, it can be used without applying any constraints or biases to the system, and so these simulations can give access to details of the exchange mechanism. However, it has been found that the computed MRT is sensitive to the value of the tolerance time t^*, leading to the proposal of a new method [212] based on the stable states picture of chemical reactions [268]. One other alternative method, which can be useful if it is difficult to fit $C_{\text{res}}(t)$ to an exponential, is simply to count the number of exchange

events per units time [24, 208]. Preliminary tests using our own simulation results showed near-perfect agreement with the MRT found by exponential fitting.

As long as we are able to observe a sufficient number of water exchanges in our microcanonical simulations, we can use our results to calculate some properties of the water while it leaves the first solvation shell, and of its replacement while it enters. Similar analyses were carried out by Rey and Hynes [6], with the sodium-water distance recorded for exchange events, and by Spångberg *et al.*, who characterized these events individually, for Li^+, using the scheme of Langford and Gray [231]. We will begin by looking at the average trajectories, from which the exchange mechanism can be inferred.

An exchange event was recorded every time a water molecule which had been in the first hydration shell of an ion for at least 5 ps (once again, the molecule was only allowed to have left for 2 ps at most) left the shell, and spent 95% of the next 5 ps outside (this meant that the molecule was allowed to re-enter the shell only very briefly). This molecule was then described as the "leaving" molecule. To find the molecule that replaced it (the "entering" molecule), we performed the same analysis in reverse: a water molecule entered the shell when it had been outside for 95% of the previous 5 ps, and was inside for the next 5 ps (once again, allowing for transient escapes). By matching up leaving and entering water molecules, the replacement for a leaving molecule was found.

We then calculated the microcanonical average trajectory for the leaving and entering molecules. In the microcanonical ensemble, time-reversal symmetry means that the average trajectory for the leaving molecule will be the same as the time-

reversed average trajectory for the entering molecule, so that we can improve our statistics by averaging over both of these, and vice versa for the entering molecule. These average trajectories were then used to find the reaction mechanism.

4.4 Results

4.4.1 Mean Residence Times

Fig. 4.5 shows the potentials of mean force for water exchange around the Li^+ and F^- ions. The height of the barrier to water exchange is, in classical simulations, 6.54 k_BT for Li^+ and 3.43 k_BT for F^-, and in path integral simulations, 6.28 k_BT for Li^+ and 3.35 k_BT for F^-. Habershon [216] reported a decrease in barrier height of 0.2 k_BT for F^- due to quantum effects, which is more than twice as large as the decrease we have seen here. As we will discuss in Sec. 4.5, this difference can be accounted for by the presence of competing quantum effects in our simulations.

From these PMFs, the k_{ex}^{TST} were calculated using Eqn. (4.9), and are given in the first column of Table 4.3. For Li^+, the transition-state theory rate constant for water exchange increases by 21% upon quantization, and for F^- the increase is 9%. These values echo our observations for $g_{IO}(r)$ in Section 4.2.2 for the two ions, in which the quantum effects were small for both ions, but more pronounced for Li^+.

In Fig. 4.6 we compare the transmission coefficients for these two reactions, with the plateau values $\kappa = \lim_{t\to\infty} \kappa(t)$ given in the second column of Table 4.3. Within the statistical uncertainty of these results, there is no effect on κ due to quantization of the nuclei. This means that as far as the rate is concerned, transition state theory can essentially account for the entirety of the effect.

The transmission coefficients for these reactions are quite small (between 0.1 and 0.2), which indicates that there is a large amount of recrossing from product to reactant. This is in agreement with several other studies of water exchange, in which

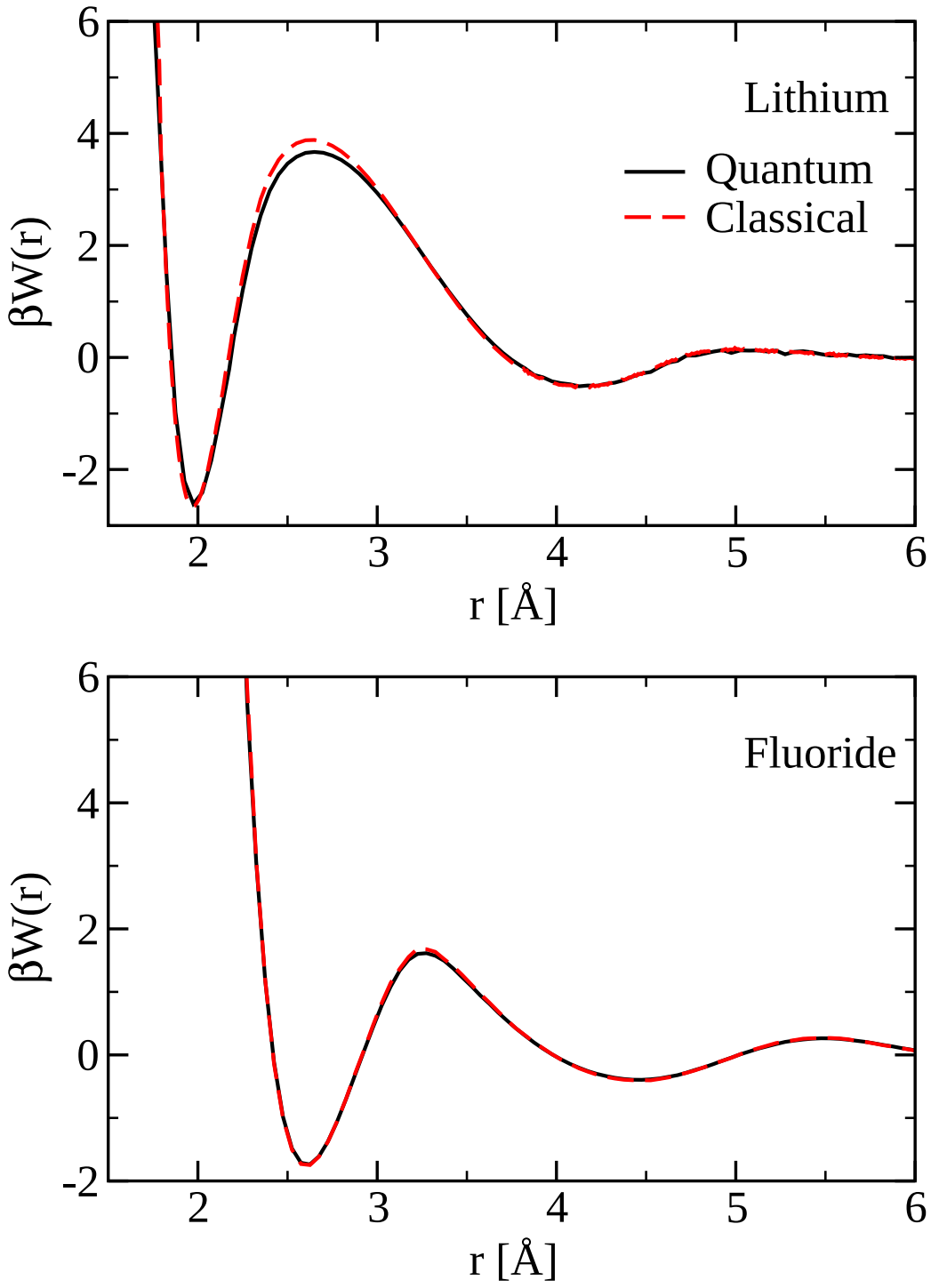

Figure 4.5: PMFs for water escaping the first solvation shell of Li^+ and F^- ions from PIMD simulations (solid black lines) and classical MD simulations (dashed red lines) at 298 K.

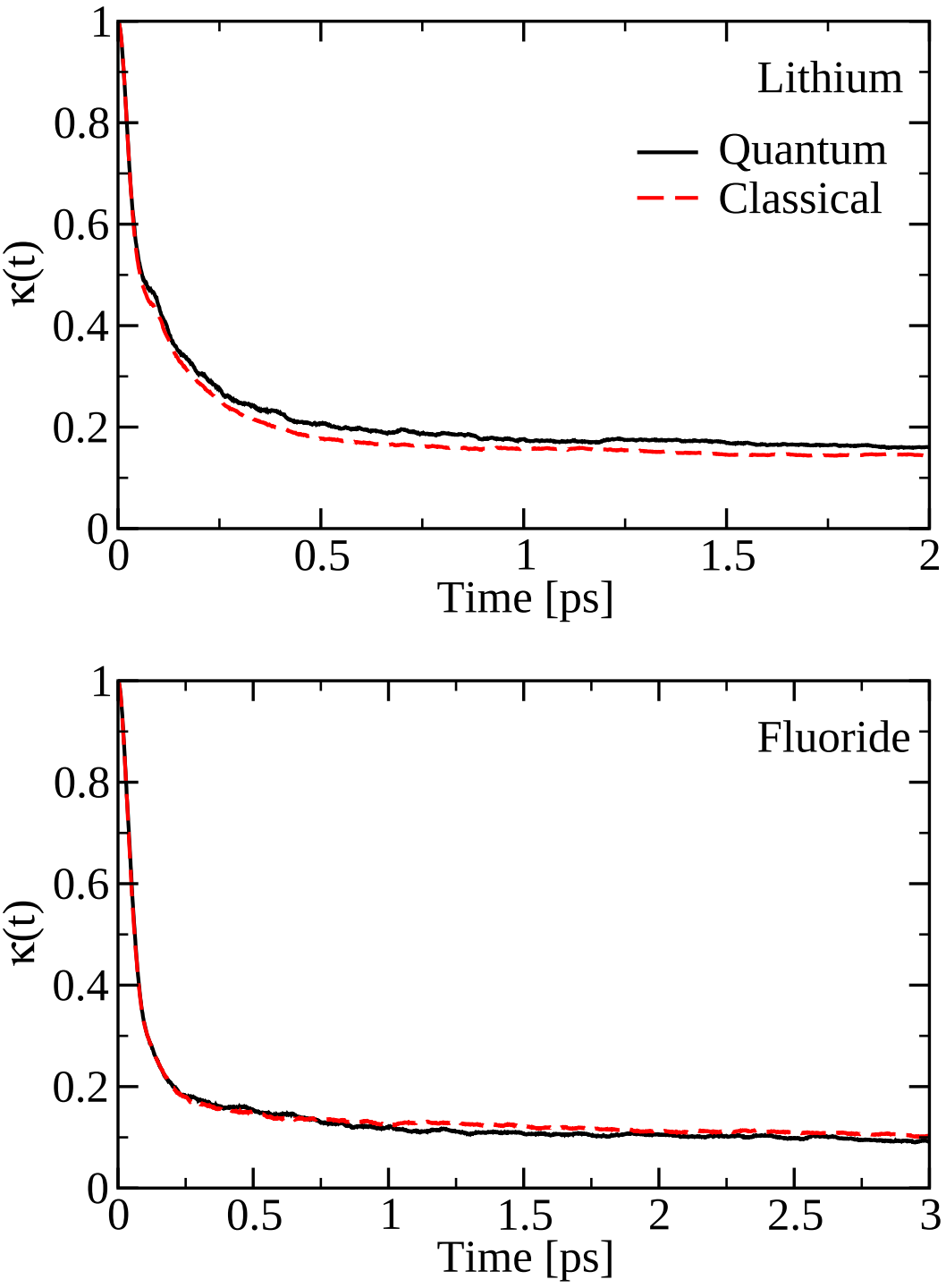

Figure 4.6: Transmission coefficients for water exchange around Li^+ and F^- ions from RPMD simulations (solid black lines) and classical MD simulations (dashed red lines) at 298 K.

values of κ between 0.04 and 0.22 have been found for several ions at atmospheric pressure [6, 8, 206, 210, 213–215]. The ion-water separation r by itself thus does not describe the water exchange very well, and is not a good reaction coordinate. This is not entirely surprising: given the rearrangements that must occur for a water molecule to leave the first shell and be replaced by one from the second shell, a better description of the reaction is likely to be given by a variable that is a function of all of the coordinates of the water molecules involved in these rearrangements.

The third and fourth columns of Table 4.3 give the full rate constants and MRTs τ_{RF} from the rate theory calculations. These can be compared to the MRTs calculated by direct simulation. The residence correlation functions $C_{\mathrm{res}}(t)$ for the two ions as calculated by TRPMD and classical MD are shown in Fig. 4.7, and the resulting residence times τ_{DS} obtained by fitting the long-time decay of $C_{\mathrm{res}}(t)$ to an exponential are given in the final column of Table 4.3. The mean residence times calculated using the two methods compare quite well, so that the results of direct simulations corroborate those of the rate theory.

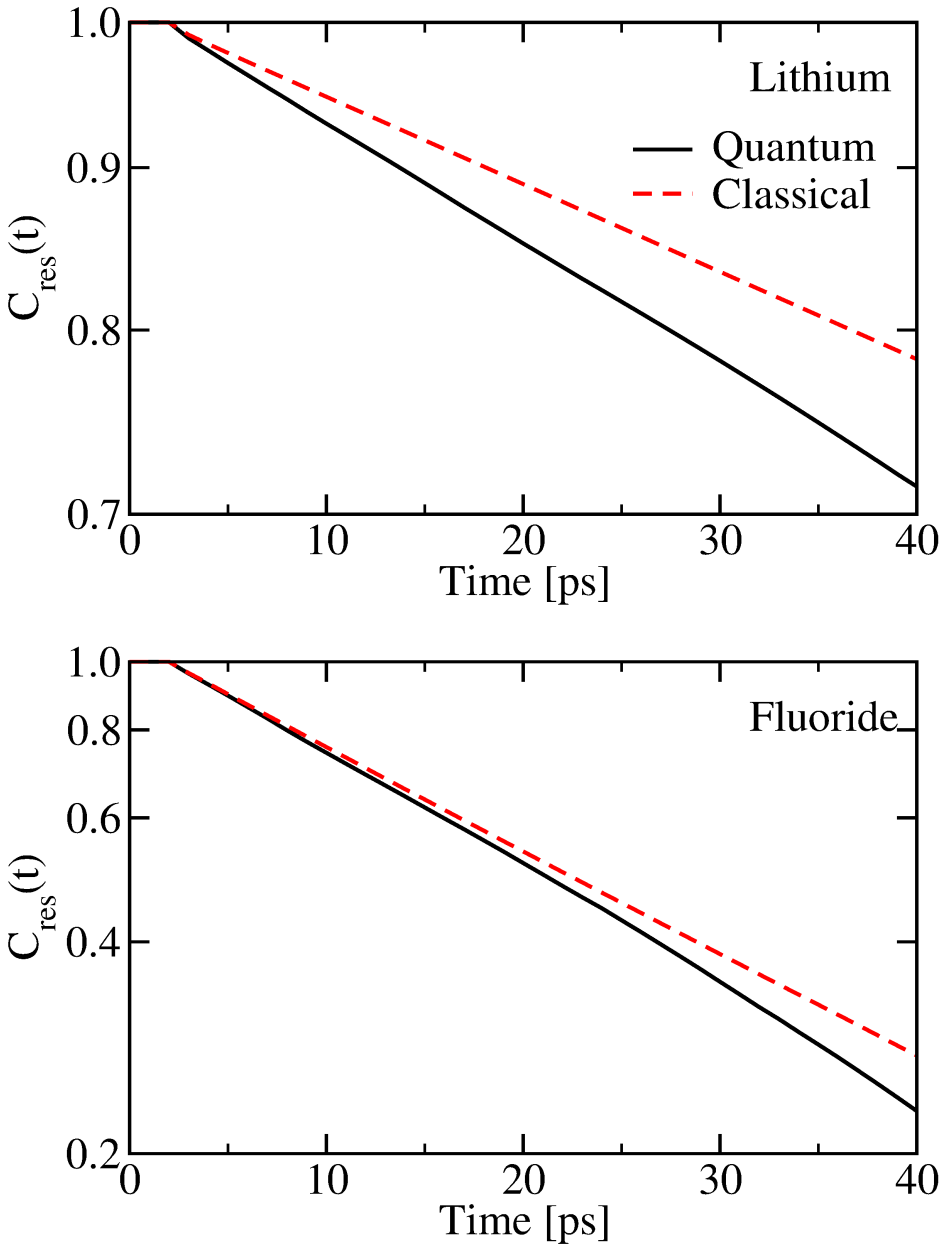

Figure 4.7: Residence correlation functions for water molecules in the first hydration shells of Li^+ and F^- ions from TRPMD simulations (solid black lines) and classical MD simulations (dashed red lines) at 298 K. Note that in both cases the scale of the vertical axis is logarithmic.

Table 4.3: Rate constants and mean residence times for water exchange around the Li^+ and F^- ions from classical and path integral simulations. k_{ex}^{TST} is the transition state theory rate constant for exchange, κ is the transmission coefficient and k_{ex} is the full rate constant. τ_{RF} and τ_{DS} are the mean residence times calculated using the reactive flux and the direct simulation methods, respectively. τ_{cl}/τ_{qm} is the ratio of classical to quantum mean residence times. Standard errors for the final digits are shown in parentheses.

	k_{ex}^{TST} [ns^{-1}]	κ	k_{ex} [ns^{-1}]	τ_{RF} [ps]	τ_{DS} [ps]
Li^+ Ion					
Classical	42	0.15(1)	6.2(4)	160(11)	160(9)
Quantum	51	0.16(1)	8.2(5)	121(8)	116(4)
			τ_{cl}/τ_{qm}	1.34	1.38
F^- Ion					
Classical	292	0.10(1)	29(3)	34(3)	29(1)
Quantum	319	0.10(1)	32(3)	31(3)	26(1)
			τ_{cl}/τ_{qm}	1.09	1.11

There are no experimental results with which we can directly compare our calculated MRTs, but an upper bound of 100 ps is suggested by QENS experiments [225]. For the F^- ion, τ_{ex} is certainly below this bound (τ_{ex} = 31.3 ps from rate theory and 26 ps from direct simulation), while for Li^+, we have obtained values that are slightly higher (τ_{ex} = 121 ps from rate theory and 116 ps from direct simulation); however, given the imprecision in the experimental result these values are reasonable. Along with the static properties of hydration, our models also describe the dynamical properties reasonably well, and we can proceed to use the results of our simulations to uncover more about the mechanism of water exchange and the origin of the quantum effects we have seen.

4.4.2 Exchange Mechanisms

The average ion-water distance for the molecule that leaves, and for its replacement, is shown in Fig. 4.8 for both ions. Using this Figure and the scheme of Langford and Gray [231], it is possible to classify the water exchange mechanism. For Li^+, the two water molecules cross inside the first solvation shell, but after the leaving molecule has begun escaping. This is an associative interchange, or I_a, mechanism, which is in agreement with other simulations of aqueous Li^+ [206, 210, 213].

Similarly, based on this Figure the exchange around F^- appears to go via a dissociative interchange, or I_d, mechanism – although the molecules cross very close to the first shell boundary, and there is little dissociative character. In fact, the situation around F^- is not so straightforward: it was found by Heuft and Meijer that this exchange has two mechanisms available to it, one associative and one dissociative

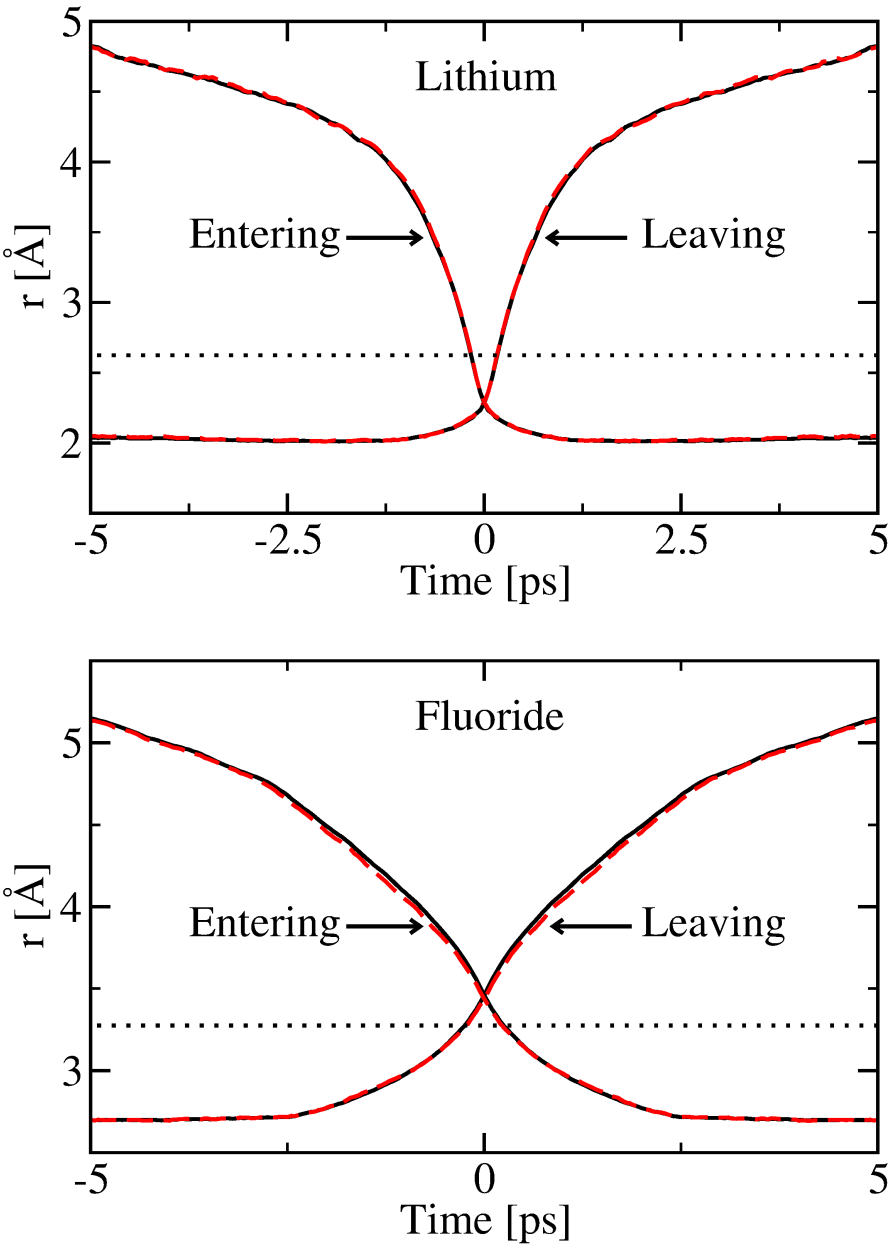

Figure 4.8: Microcanonical average trajectories for water molecules entering and leaving the first hydration shell of the Li^+ and F^- ions, averaged over all events, from TRPMD simulations (solid black lines) and classical MD simulations (dashed red lines). The dotted black line in each case shows the position of the first shell boundary.

[209]. Thus, we took each individual exchange observed in our simulations, and classified it as associative (if the leaving and replacing molecules crossed inside the first shell) or dissociative (if the leaving and replacing molecules crossed outside the first shell). The ratio of associative to dissociative exchanges was about 1:1, meaning that there are indeed two mechanisms in operation.

We then took the ion-water distances and averaged separately over the two mechanisms, as shown in Fig. 4.9. They can be classified as I_a and I_d, and are distinct from the average behaviour shown in Fig. 4.8.

To ensure that the I_a mechanism deduced for Li^+ was correct, we repeated this process for the cation. Fewer than 3% of the exchanges were classified as dissociative, so that water exchange around Li^+ proceeds via a single, associative pathway.

4.5 Competing Quantum Effects

Although the increase in water exchange rate due to quantum fluctuations is fairly small for both ions, it is larger for Li^+ than for F^-. We can attribute this to three causes.

Firstly, the binding of a water molecule to Li^+ is stronger than that for F^-. In aqueous halide solutions, a correlation was found between ion-water binding strength (which decreases down the group) and the quantum effect on τ_{ex} [216]. Because the cation and the anion have different modes of interaction with the surrounding water molecules (Li^+ interacts directly with the oxygens, and F^- with the hydrogens), the same explanation does not necessarily apply. We thus used classical MD and

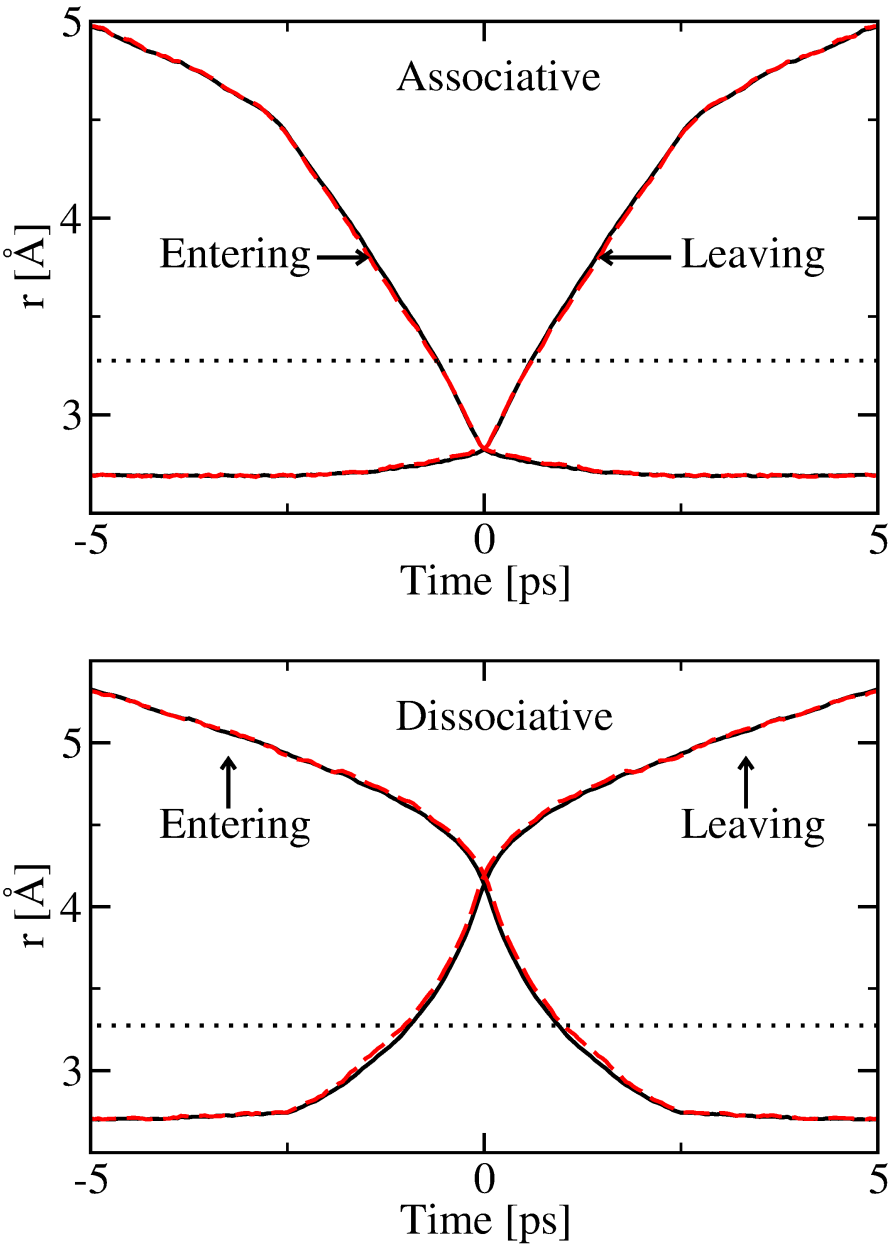

Figure 4.9: Microcanonical average trajectories for water molecules entering and leaving the first hydration shell of the F^- ions, averaged separately over associative and dissociative events, from TRPMD simulations (solid black lines) and classical MD simulations (dashed red lines). The dotted black line in each case shows the position of the first shell boundary.

PIMD to calculate the PMF for water exchange around water, which both donates hydrogen bonds to, and accepts them from, the surrounding molecules, meaning that it can be compared with both Li^+ and F^-.

The PMFs are shown in Fig. 4.10; the barrier height was 1.4 k_BT from classical simulations, smaller than the 3.4 k_BT found for F^-, and the k_{ex}^{TST} increased by 5 % upon the inclusion of quantum effects, also smaller than the 9 % for F^-. This backs up the argument that however the ion binds to its first hydration shell, more strongly bound ions give rise to a larger quantum effect on the MRT, and so partly explains the difference between Li^+ and F^-.

Secondly, the Li^+ ion is lighter than F^-; the ratio of the reduced masses of ion-water pairs is $\mu_{Li^+\cdots H_2O}/\mu_{F^-\cdots H_2O} \simeq 0.54$. To get an idea of the effect of the difference in masses, we consider a "heavy" lithium ion, with the mass of the fluoride but all other parameters identical. The PMFs from classical and path integral MD for water exchange around this ion are shown in Fig. 4.11. From these we found that k_{ex}^{TST} increases by 11% on quantization. This is smaller than the increase for regular Li^+, and is in fact quite close to the increase for F^-, suggesting that the difference in masses does indeed contribute significantly to the difference in quantum effects.

The third cause is the presence of competing quantum effects in the solvation of the fluoride ion, which are absent both in the solvation of lithium, and in the simulations of Ref. [216] using the rigid SPC/E water model. These competing effects are due to ZPE in the anharmonic O–H stretching coordinate (which tends to strengthen the O–H$\cdots F^-$ hydrogen bond) and in orthogonal coordinates (tending to weaken this hydrogen bond).

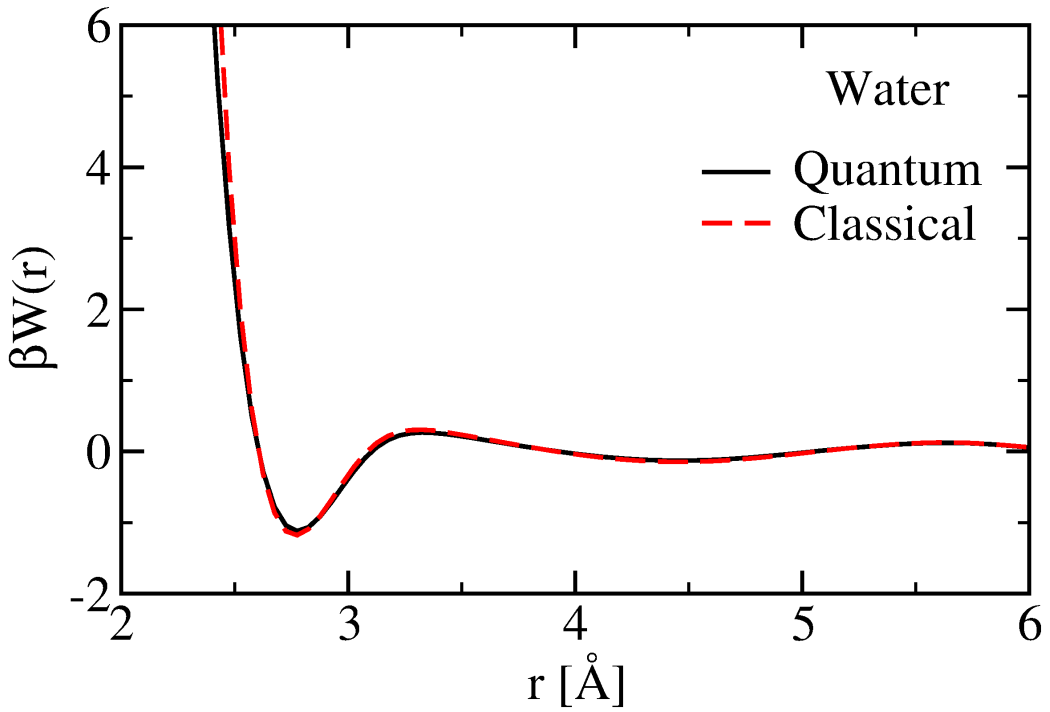

Figure 4.10: PMFs for water escaping the first solvation shell of water from PIMD simulations (solid black lines) and classical MD simulations (dashed red lines) at 298 K.

The quantum kinetic energy tensor $\langle T_{\alpha\beta} \rangle$ provides an ideal method for resolving the contribution of these individual effects to the total. As described in Section 2.4, we used the centroid virial estimator along with the mean-square displacement algorithm to calculate the kinetic energy tensor for every H atom in the molecular frame. Then, the average tensor and its eigenvalues were calculated for each type of H atom, which were classified according to their position relative to the ion.

In Table 4.4, the three eigenvalues $\langle T_i \rangle$ of the kinetic energy tensor, along with their sum $\langle T \rangle$, are shown for the two ionic solutions. Any H atoms not in the first

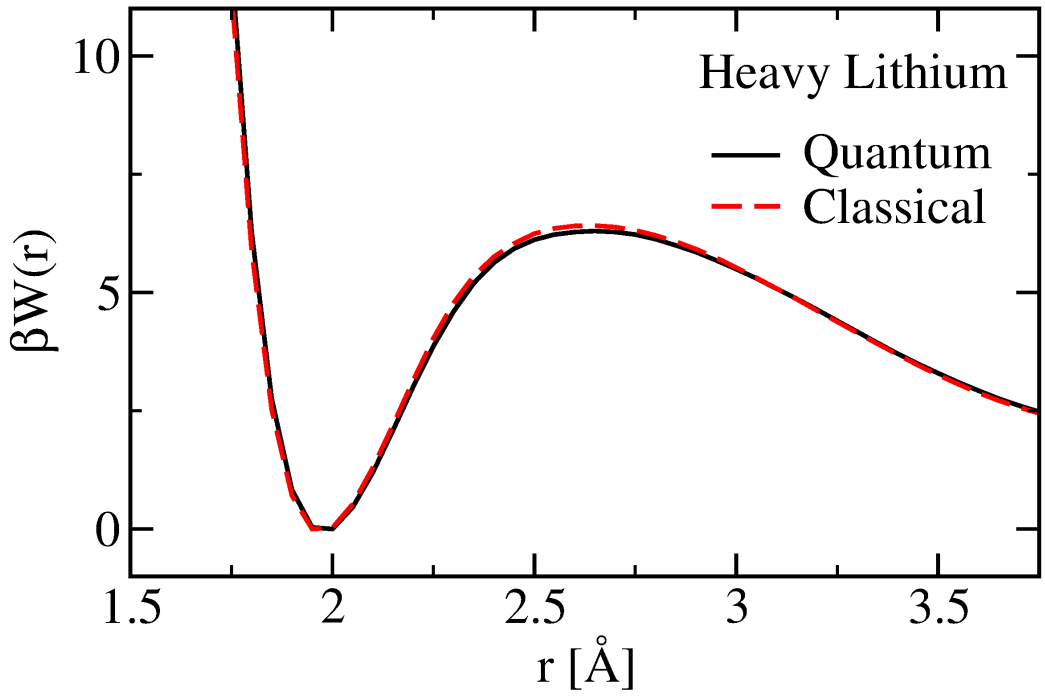

Figure 4.11: PMFs for water escaping the first solvation shell of a "heavy" lithium ion with the mass of F^-, from PIMD simulations (solid black lines) and classical MD simulations (dashed red lines) at 298 K.

hydration shell are described as being in the bulk.

Looking first at F^-, the total kinetic energy $\langle T \rangle$ (and its eigenvalues) are extremely similar in bulk water and in O–H bonds that are in the first shell but pointing away from the ion: only the O–H bonds directly participating in hydrogen bonds with fluoride have a significantly different kinetic energy. $\langle T_1 \rangle$ is smaller than its bulk value, meaning that the hydrogen atom is less confined in the O–H direction; this bond stretches more to take part in stronger hydrogen bonding. $\langle T_2 \rangle$ and $\langle T_3 \rangle$, however, are greater than in the bulk. This means that the hydrogen atom is more

Table 4.4: The eigenvalues of the kinetic energy tensor are shown for hydrogen atoms in various environments in PIMD solutions of the Li^+ and F^- ions at 298 K. As shown in Fig. 2.2, the T_1 direction is parallel to the O–H bond, the T_2 direction is perpendicular to the O–H bond in the plane of the water molecule, and T_3 is perpendicular to both. $\langle T \rangle$ is the sum of the three eigenvalues in each case.

[meV]	$\langle T_1 \rangle$	$\langle T_2 \rangle$	$\langle T_3 \rangle$	$\langle T \rangle$
Li^+ Ion				
First shell water	98.0	34.3	21.8	154.1
Bulk water	98.8	33.7	21.6	154.1
F^- Ion				
O–H$\cdots F^-$ hydrogen bonding	91.6	38.5	28.2	158.3
Other first shell hydrogen	99.0	33.8	21.6	154.4
Bulk water	98.9	33.7	21.5	154.1

confined in these directions, which is also due to the stronger O–H$\cdots$F$^-$ hydrogen bond as compared to O–H$\cdots$OH$_2$: it is more difficult for the O–H bond to librate away from the fluoride. These results are illustrated in Fig. 4.12.

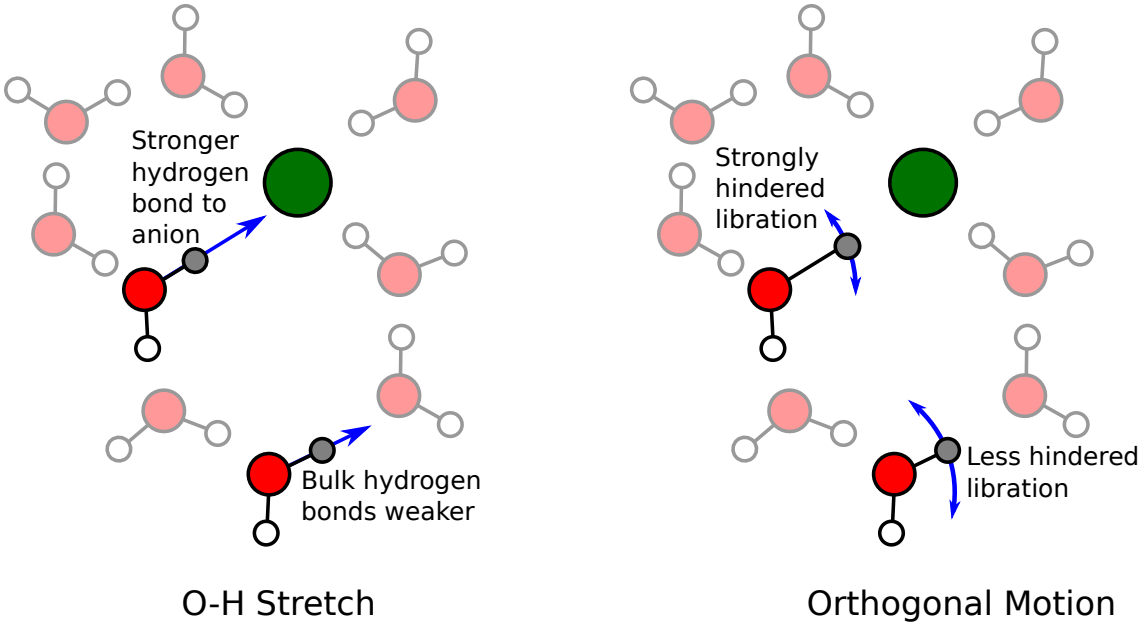

Figure 4.12: Competing quantum effects in fluoride hydration. Left panel: a hydrogen atom participating in a hydrogen bond with the anion is less confined in the O–H bond direction than a hydrogen atom in the bulk, since the O–H$\cdots$F$^-$ hydrogen bond is stronger than the O–H$\cdots$OH$_2$ hydrogen bond, and in the former the O–H bond can stretch further. Right panel: the atom participating in a hydrogen bond to F$^-$ is more confined in directions perpendicular to the O–H bond, since the stronger interactions with the anion than with other water molecules mean that libration in these directions is more difficult.

Overall, $\langle T \rangle$ is larger for those hydrogen atoms participating in O–H$\cdots$F$^-$ hydrogen-bonds than for those in the bulk, by 4.2 meV (approximately $k_\mathrm{B}T/6$). This is in accordance with the small reduction in MRT, since the first solvation shell is destabilized only by a small amount relative to the bulk when quantum effects are included; in addition, this net effect is clearly due to a competition of individual effects.

Looking now at the components of the kinetic energy tensor for Li^+, we see that while there is a small change in the eigenvalues $\langle T_i \rangle$ (these are in the same direction as for F^-: $\langle T_1 \rangle$ is decreased and $\langle T_2 \rangle$ and $\langle T_3 \rangle$ are increased), these are much smaller changes than for F^-, and the total quantum kinetic energy $\langle T \rangle$ is entirely unchanged by quantum effects. Because the Li^+ ion interacts most closely with the oxygen atoms in its first hydration shell, the quantum kinetic energy does not affect the exchange rate, and so these competing quantum effects do not play any part in explaining the quantum effect for Li^+.

The competing quantum effects in water exchange around F^- thus help to explain why the increase in MRT is larger for the lithium ion than for the fluoride ion, but also the disparity between our results and those of Ref. [216], in which the water model used was rigid. For such a model, we would expect that the decrease in $\langle T_1 \rangle$ would not be observed, while the other two components would still increase, meaning that $\langle T \rangle$ would increase more and the quantum-mechanical increase of the exchange rate would be larger.

We have accounted here for the three main differences between the Li^+ and F^- ions: their short-range ion-water interactions, their different masses and their opposite charges (which determine whether or not the water-ion interaction goes via

the oxygen or the hydrogen atoms), and we see that all of these contribute to the larger quantum effect observed for Li^+ than for F^-.

4.6 Outlook

The quantum effect on a number of static and dynamical properties of solutions of Li^+ and F^- (in particular, the rate of water exchange between the first solvation shell and the bulk) have been shown in this Chapter to be very small, and the effect on the water exchange mechanism is essentially zero. Because quantum effects in these solutions decrease with weaker ion-water binding, we expect that the remainder of the alkali metal cations (which bind water less strongly than Li^+) and the halide ions (which bind water less strongly than F^-) would show even weaker quantum effects.

For monovalent ions, a classical treatment gives a qualitatively excellent and a quantitatively quite good description of the water exchange dynamics: this means that previous work, in which water exchange was treated by classical simulations, is justified.

This leads us to ask: for higher-valent ions, how will these conclusions differ? The mean residence times for these ions are generally orders of magnitude longer than for monovalent ions. For example, for Ru^{2+} the MRT is 56 seconds, and for Ir^{3+} it is 288 years [234]. This means that the ion-water binding will be stronger, and that ZPE effects are expected to be larger. While it would be interesting to look into the effect of quantization on the rate of water exchange around such ions,

the very fact of their increased valency makes the simulations more complex; the more highly charged ions will distort the electron clouds of the surrounding water molecules, so that their polarizability cannot be ignored [215]. Often, such highly charged ions must be treated using *ab initio* simulation [24, 269]. However, this would represent a chance to observe potentially quite large quantum effects at room temperature, and so could be worth exploring in more detail.

Chapter 5

Nonlinear Light Scattering in Ionic Solutions[1]

5.1 Introduction

5.1.1 Second Harmonic Generation Scattering

In this Chapter, we will be combining two topics we have previously studied, as we consider the application of nonlinear optics to ionic solutions. Unlike the SFG spectroscopy experiments on which we focused in Chapter 3, we will look at non-resonant second harmonic scattering (SHS). In addition, while we were interested in fairly short-ranged effects of ionic charge in Chapter 4, we will now be investigating much longer-ranged correlations.

This work was also carried out in conjunction with experiments, which we will describe in Sec. 5.1.2. In the remainder of the current Section, we will give an introduction to SHS.

As described in Sec. 3.1.2, a high-intensity laser with frequency ω will induce not

[1]The work described in this Chapter is based on work that appears in Ref. [270]. Experiments were carried out by members of the Roke group.

only a polarization oscillating at ω, but also a second harmonic oscillating at 2ω.[2] The induced polarization will lead to radiation of light at frequency 2ω [271]. This is a second-order scattering process, and there are two distinct ways in which it can occur [272]:

- Incoherent scattering, in which molecules scatter independently [272,273]. By analogy with the second-order optical processes described in Chapter 3, this requires only that the molecules themselves have no centre of symmetry, and the total intensity of scattered light is proportional to the number of molecules [272,274].

- Coherent scattering, in which there is interference between light scattered by different molecules. For this to be measured, molecules must be orientationally ordered [274]; if they are randomly oriented then the average intensity of coherently scattered light is zero, and only incoherent scattering is observed.

This kind of scattering is usually described as hyper-Rayleigh scattering (HRS) or second harmonic scattering (SHS). Although the two are often used interchangeably [273], the distinction between them is that HRS is purely incoherent scattering, while SHS is more general, and can have a coherent component to the signal [272,273]. HRS was first reported in 1965 by Terhune *et al.* [275], who applied it to a number of liquids and to fused quartz. The setup they used is the same as is used in the experiments described in this Chapter, and is shown in Fig. 5.1, with the scattered

[2]there will also be higher-order harmonics, but the second is measured in the experiments described.

light detected at an angle of 90° to the incoming light. Both beams may be polarized either parallel (denoted P) or perpendicular (denoted S) to the scattering plane, and the polarization combinations used are denoted $X_{OUT}Y_{IN}Y_{IN}$,[3] where X (= P or S)

[3]The two Y_{IN} appearing in this notation reflect the fact that one outgoing photon requires two

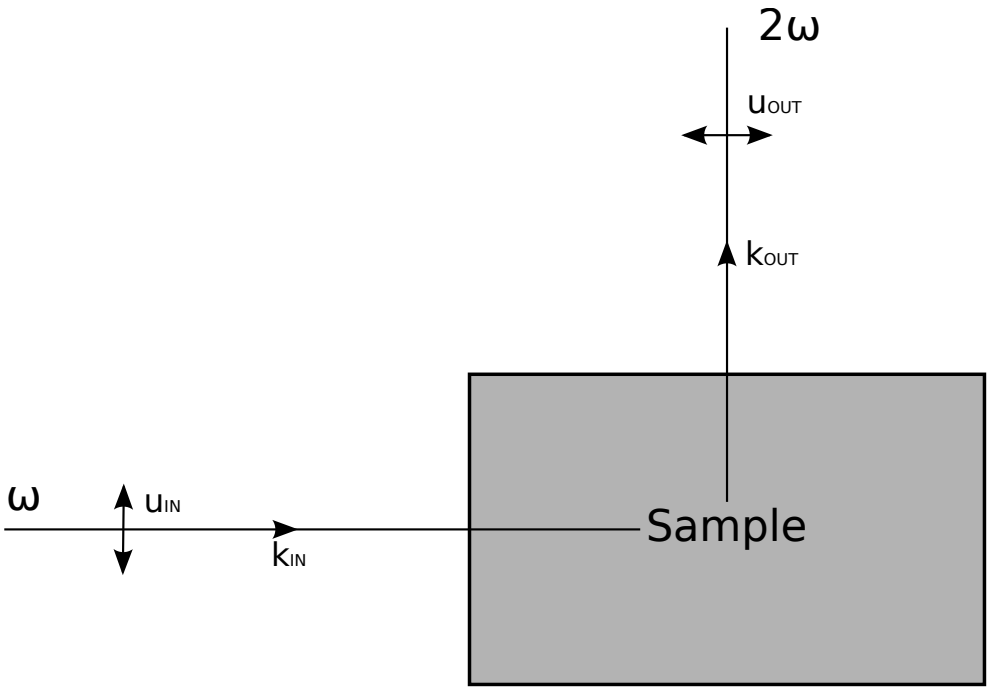

Figure 5.1: Setup of second harmonic generation scattering experiment: a beam of light with frequency ω is incident on a sample, and light scattered at 90° with frequency 2ω is detected. $\boldsymbol{u}_{IN}$ is the polarization vector of the incoming light, and $\boldsymbol{u}_{OUT}$ is that of the outgoing light. The polarization combination shown is denoted $P_{OUT}P_{IN}P_{IN}$, as described in the main text. $\boldsymbol{k}_{IN}$ is the wavevector of the incoming light and $\boldsymbol{k}_{OUT}$ is that of the outgoing light.

is the polarization of the outgoing light and Y (= P or S) the polarization of the incoming light. This notation is as used in Ref. [270].

The coherent and incoherent contributions to the signal can be resolved by varying the polarization combination. For example, if molecules are ordered by a radially directed field then a coherent signal is only seen for $P_{OUT}P_{IN}P_{IN}$ or $P_{OUT}S_{IN}S_{IN}$ polarizations [276]. Using the theory developed in Section 5.2.2 we will be able to account for this polarization dependence.

SHS experiments on dipolar liquids found a narrow peak characteristic of slowly relaxing orientational correlations, leading to the suggestion [277,278] that such liquids contain long-lived domains of ferroelectrically ordered molecules. The ordering of water molecules at the surface of hydrophobic droplets has also been studied with second-harmonic scattering [272, 279, 280], allowing the interfacial electronic structure to be probed.

The theory of second-order scattering has been understood for several decades: Bersohn *et al.* [274] give perhaps the simplest expression for the scattered intensity in terms of an equilibrium average of molecular hyperpolarizabilities over the orientations of the molecules. Maker [281] also accounted for the spectral line width of scattered light using the van Hove spatial and temporal correlation function. Both of these papers have served as starting points for theoretical work on the subject. In Section 5.2, we will describe the theory of second-harmonic scattering from a gas of non-interacting dipoles oriented by the Coulomb fields of ions [282]. Although this is a crude description of the solvent molecules, it does allow us to find an expression

incoming photons.

for the scattering intensity as a function of ion concentration.

A few simulations have been carried out with the goal of explaining HRS experiments [283–286]. Janssen *et al.* used MD simulations to calculate the intensity of light scattered by liquid nitrobenzene at different polarization combinations, with the calculated depolarization ratios (i.e., ratios of intensities for different polarization combinations) matching very well with experiment [283]. In order to calculate the scattering intensities, snapshots from the simulation were used along with hyperpolarizability tensors taken from *ab initio* calculations.

Pounds *et al.* used classical MD simulations to calculate the dipole density time correlation function of acetonitrile and thus address the question of its ferroelectricity [284]. The relaxation of ferroelectric ordering would lead to long-lived dipole density correlations, and these were not observed.

Some very recent work has been carried out to calculate hyperpolarizability tensors using atomistic simulations [285] and to compute the resonant HRS spectrum [286] for benzene derivatives, but there is still a dearth of simulations on HRS and SHS in the literature – and most importantly of all, none of the simulation-based studies that have been carried out concerned aqueous solutions. We proceed now to describe second-harmonic scattering experiments on these solutions, in which simulations will be extremely useful in rationalizing the results.

5.1.2 Experimental Details

When SHG scattering is carried out on aqueous ionic solutions, the centrosymmetry of the ions means that the signal comes entirely from the solvent molecules. By varying the ionic strength of the salt and the polarization combinations used, the degree of ordering induced by the ions can be found. To conform with the remainder of the Chapter we define the ionic strength,

$$\rho_{\mathrm{I}} = \sum_i \rho_i Z_i^2, \tag{5.1}$$

where ρ_i is the number density of ionic species i and Z_i is its charge in units of the electron charge.

Fig. 5.2 shows the intensity of scattered light from an aqueous solution of NaCl, normalized by the intensity scattered from pure water. All four possible polarization combinations are used, and the ionic strength is varied from 1 μM to 0.1 M for each combination. For the $\mathrm{P_{OUT}P_{IN}P_{IN}}$ and $\mathrm{P_{OUT}S_{IN}S_{IN}}$ polarizations, the intensity firstly increases with ionic strength but eventually saturates, reaching a plateau value (representing an increase of about 30% for the $\mathrm{P_{OUT}P_{IN}P_{IN}}$ combination and about 25% for the $\mathrm{P_{OUT}S_{IN}S_{IN}}$, although within the error bars the difference between the two is not statistically significant) by about 1 mM. In contrast, for the $\mathrm{S_{OUT}S_{IN}S_{IN}}$ and $\mathrm{S_{OUT}P_{IN}P_{IN}}$ polarizations, there is no change in the scattered intensity when the concentration of NaCl is increased. Shelton [282] has found a similar dependence of the SHGS signal on ion concentration, using KCl and the $\mathrm{P_{OUT}S_{IN}S_{IN}}$ polarization combination.

The interpretation of these results is as follows: the increase of the intensity

above its value in bulk water means that the orientational ordering of the solvent molecules increases, while the polarization dependence indicates that this ordering is radial [276], such as that due to the centrally directed electric fields of ions.

The increase in intensity at low ionic strengths is unsurprising: when the ions

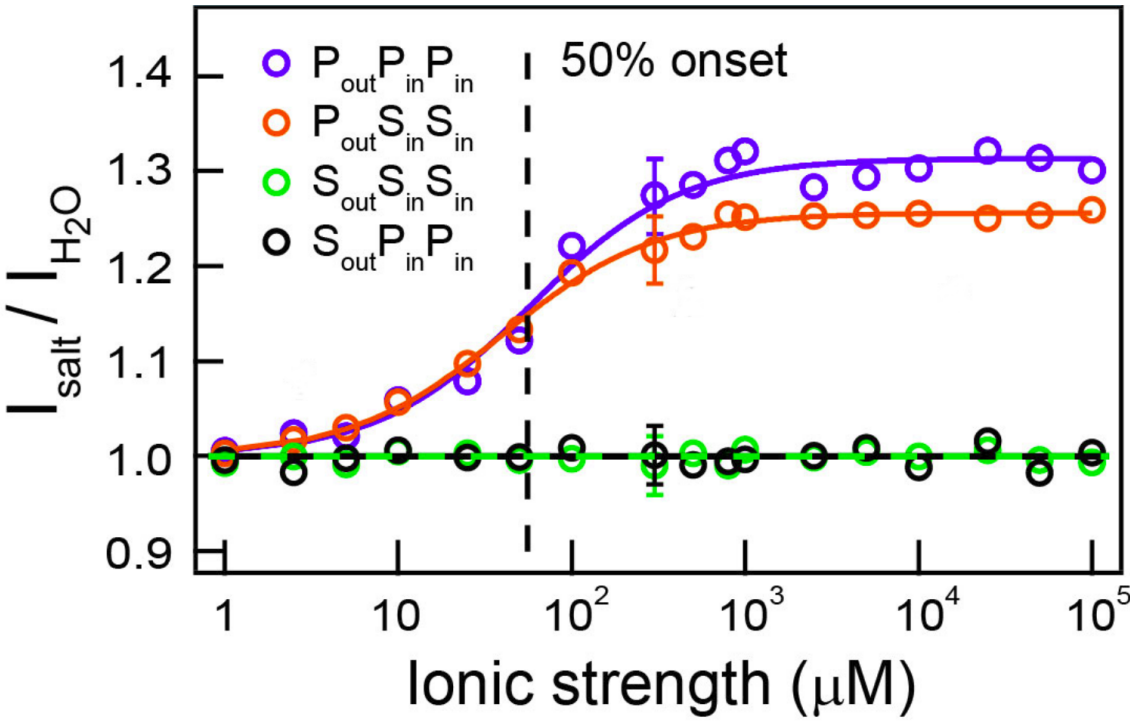

Figure 5.2: Second harmonic generation scattered intensities from NaCl solutions of varying ionic strengths, normalized by the intensity scattered from pure water. Four different polarization combinations are used ($P_{OUT}P_{IN}P_{IN}$, $P_{OUT}S_{IN}S_{IN}$, $S_{OUT}S_{IN}S_{IN}$ and $S_{OUT}P_{IN}P_{IN}$). The dashed vertical line shows the concentration at which the intensity is half its maximum value. Solid lines are fits to the Langmuir equation of Eqn. (5.2). The experimental setup is described in detail in Ref. [270]. This figure was produced by Yixing Chen from the Roke group [270].

are separated by fairly large distances and thus independently order the solvent, the degree of ordering should increase linearly with the number of ions; for higher ionic strength the ions are closer together, and are spatially correlated. A qualitative explanation for the plateau in intensity is that an ion's charge will be screened by the oppositely charged ions surrounding it, which will diminish the ability of each ion to order solvent molecules. This effect competes with the increase in the number of ions (which are the origins of the ordering). In Fig. 5.2 the data is fitted to the Langmuir equation,

$$\Delta I = \frac{A\rho_{\mathrm{I}}}{1 + A\rho_{\mathrm{I}}}, \tag{5.2}$$

where A is a constant. This functional form has the correct behaviour in the two limits (i.e., a linear increase for small ionic strengths and a plateau at large ones), and is also shown by Ref. [282] and in Section 5.2.4 to be the appropriate dependence for a mean-field theory of SHG scattering from ionic solutions.

This experiment was repeated with a wide range of different salts, as well as with H_2O replaced by D_2O. The left-hand panel of Fig. 5.3 shows the results for solutions of 20 different salts and of CCl_4 for the $P_{OUT}P_{IN}P_{IN}$ polarization. There are two important results in this panel: firstly, when CCl_4 is used as the solute, the intensity is unchanged from its bulk value, providing more evidence that the effect is due entirely to ordering by ions. The second result is very striking – not only is the same qualitative behaviour observed for these salts, but the parameters of the fitted Langmuir equation are also the same: the intensity's quantitative variation with ionic strength is unchanged.

The wide variety of salts used means that ions of different radii, electronic and

physical structures have been sampled, and the effect observed by the experiments is ion-nonspecific. This, in turn, suggests that the effect is long-ranged; near to an ion, the structure of water will depend on the ion's identity, so the observed intensity must be dominated by scattering from water molecules far away from the ions, whose local structure is less dependent on the identities of the ions that are ordering them.

The right-hand panel in Fig. 5.3 shows the result of replacing H_2O with D_2O, for the $P_{OUT}P_{IN}P_{IN}$ and $S_{OUT}S_{IN}S_{IN}$ polarization combinations. The intensities in this panel are normalized by those for scattering from the pure solvent. Qualitatively, the behaviour for D_2O is the same as for H_2O, but the two are quantitatively quite different. At the plateau, the intensity for scattering from D_2O has increased by only 9% from the value in bulk water, and the ionic strength at which half the maximum is achieved is about 5.6 times higher for D_2O.

As we shall see in Section 5.2.4, the similarity between the electronic properties of these two molecules [270] means that the intensity increases for both solvents would also be extremely similar within a mean-field theory; the difference in these properties cannot explain the results in Fig. 5.3. It is quite plausible that this is a nuclear quantum effect: hydrogen bonds in D_2O are stronger than those in H_2O [249], making it more difficult for an ion to perturb the structure of heavy water and reorient its molecules.

Although path-integral simulations are required to explain the difference between the signals from H_2O and D_2O, we defer these simulations to further work and focus in the remainder of this Chapter on qualitatively explaining the results for H_2O

using a combination of theory and classical simulations. We begin by deriving a mean-field theory of SHG scattering in solutions.

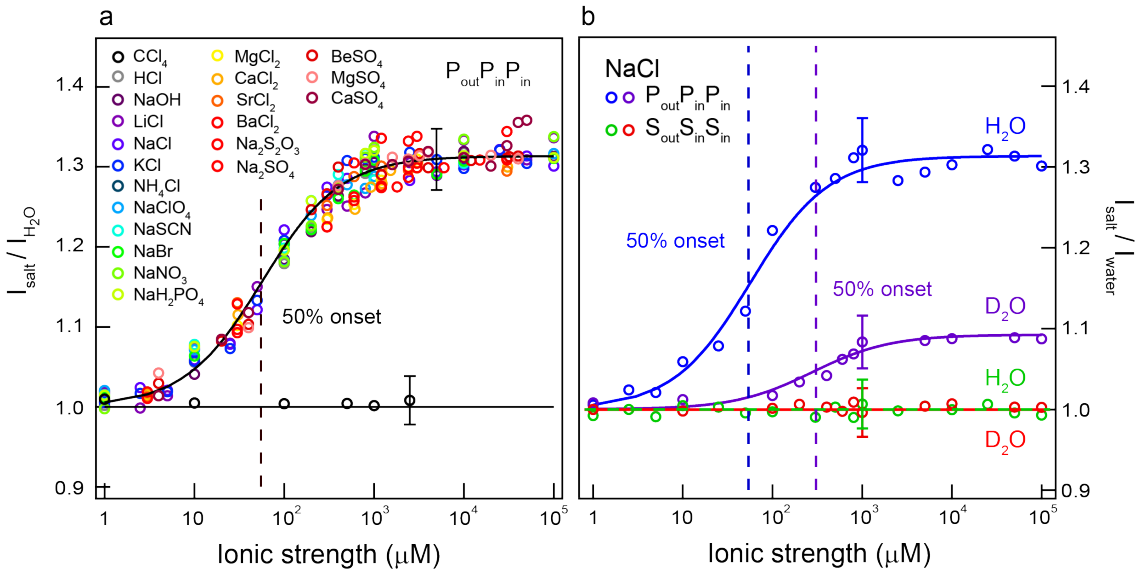

Figure 5.3: Left-hand panel: second harmonic generation scattered intensities from 20 ionic salts and from a solution of CCl_4 at varying ionic strength, normalized by the intensity scattered by pure water. The $P_{OUT}P_{IN}P_{IN}$ polarization combination was used to collect these results. Right-hand panel: second harmonic generation scattered intensities from NaCl dissolved in light and heavy water at varying concentrations, normalized by the intensity scattered from pure solvent. The $P_{OUT}P_{IN}P_{IN}$ and $S_{OUT}S_{IN}S_{IN}$ polarization combinations were used to collect these results. The dashed vertical lines show the concentrations at which the respective intensities are half their maximum values. The solid lines are fits to the Langmuir equation. For all experiments, the setup is as described in detail in Ref. [270]. This figure was produced by Yixing Chen from the Roke group [270].

5.2 Theoretical Description of Scattering

5.2.1 General Theory

In order to rationalize the results of these experiments we begin by developing a basic model for SHS in ionic solutions. Firstly, we will describe the theory of second-order scattering of light, closely following Bersohn *et al.* [274]. By analogy with Section 3.1.2, consider a molecule on which an oscillating electric field $\boldsymbol{E}(\omega)$ is incident. This will induce an oscillating dipole moment. Keeping terms up to second-order in the applied field, the component of the induced dipole moment in the i^{th} molecule-fixed direction is [274, 287],

$$\mu_i(\omega') \simeq \sum_j \alpha_{ij} E_j(\omega) + \sum_{j,k} \beta_{ijk} E_j(\omega) E_k(\omega), \tag{5.3}$$

where $\boldsymbol{\alpha}$ is the polarizability tensor of the molecule and $\boldsymbol{\beta}$ its first hyperpolarizability tensor. $E_j(\omega) = \boldsymbol{E}(\omega) \cdot \boldsymbol{e}_j$, where $\boldsymbol{e}_j$ is the unit vector in the j^{th} direction.

For an oscillating incident field,

$$\boldsymbol{E}(\omega) = E(\omega) \cos(\omega t)\, \boldsymbol{u}_{\text{IN}}, \tag{5.4}$$

with $\boldsymbol{u}_{\text{IN}}$ a unit vector specifying the polarization of the incoming light. The first term on the right-hand side of Eqn. (5.3) then oscillates at frequency ω, and the second term has a component oscillating at zero frequency and one at frequency 2ω. Thus, for the component of the induced dipole moment oscillating at frequency 2ω we can write,

$$\mu_i(2\omega) = \frac{1}{2} \sum_{j,k} \beta_{ijk} \left(\boldsymbol{e}_j \cdot \boldsymbol{u}_{\text{IN}}\right) \left(\boldsymbol{e}_k \cdot \boldsymbol{u}_{\text{IN}}\right) E(\omega)^2 \cos(2\omega t)\,. \tag{5.5}$$

If $\boldsymbol{u}_{\mathrm{OUT}}$ is the polarization at which light is detected, then the component of the induced dipole moment in this direction is,

$$\mu_{\mathrm{OUT}}(2\omega) = \frac{1}{2}\sum_{i,j,k}\beta_{ijk}\left(\boldsymbol{e}_i\cdot\boldsymbol{u}_{\mathrm{OUT}}\right)\left(\boldsymbol{e}_j\cdot\boldsymbol{u}_{\mathrm{IN}}\right)\left(\boldsymbol{e}_k\cdot\boldsymbol{u}_{\mathrm{IN}}\right)E(\omega)^2\cos\left(2\omega t\right). \tag{5.6}$$

According to classical electrodynamics, an oscillating dipole $\boldsymbol{\mu}$ produces an oscillating electric field (i.e., the scattered light) $\boldsymbol{E} = \frac{k}{R}\left(\boldsymbol{\mu}\times\hat{\boldsymbol{R}}\right)\times\hat{\boldsymbol{R}}$ at a displacement $\boldsymbol{R}$ from the molecule, where k is a constant [271]. For the component of the electric field in the direction of $\boldsymbol{u}_{\mathrm{OUT}}$, using the fact that the polarization of an electromagnetic wave is orthogonal to the direction of propagation so that $\boldsymbol{u}_{\mathrm{OUT}}\cdot\hat{\boldsymbol{R}} = 0$ we have,

$$E_{\mathrm{OUT}} = \boldsymbol{E}\cdot\boldsymbol{u}_{\mathrm{OUT}} = -\frac{k}{R}\mu_{\mathrm{OUT}}(2\omega). \tag{5.7}$$

The intensity of this field (and thus the intensity of light scattered by a single molecule) is obtained by taking the square of the electric field, averaging over one time period of the scattered wave and multiplying by a constant [274]. Since the timescale of molecular rotation is much longer than this period, we can assume that the orientation of the molecule is fixed during this time, and this averaging is equivalent to a time integral of the cosine function in Eqn. (5.6). This gives the expression,

$$I(2\omega) = \left(\kappa'\right)^2\beta_{\mathrm{OII}}\beta_{\mathrm{OII}}, \tag{5.8}$$

where,

$$\beta_{\mathrm{OII}} = \sum_{i,j,k}\beta_{ijk}\left(\boldsymbol{u}_{\mathrm{OUT}}\cdot\boldsymbol{e}_i\right)\left(\boldsymbol{u}_{\mathrm{IN}}\cdot\boldsymbol{e}_j\right)\left(\boldsymbol{u}_{\mathrm{IN}}\cdot\boldsymbol{e}_k\right), \tag{5.9}$$

is the OII$^{\mathrm{th}}$ component of the molecular hyperpolarizability in a reference frame defined by the experimental apparatus. κ' is a constant that depends on the exper-

imental setup and will be unimportant in our final results as we will only consider the ratio of two intensities.[4]

In a system of many molecules, the total intensity of scattered light is not simply the sum of the intensities scattered by each molecule: there will be interference between light scattered by different molecules. The total scattering intensity is written as the square modulus of a scattering amplitude. This amplitude is the sum of amplitudes for scattering from each molecule (which are proportional to the oscillating field components E_{OUT} for the molecule), each weighted by a phase factor. Since the electric field produced by the m^{th} molecule is proportional to its hyperpolarizability component β^m_{OII}, we can write the amplitude for scattering from this molecule as $\kappa'\beta^m_{\mathrm{OII}}$. The total amplitude is then [274],

$$E_{\mathrm{tot}} = \kappa' \sum_m \beta^m_{\mathrm{OII}} e^{i\boldsymbol{K}\cdot\boldsymbol{r}_m}, \tag{5.10}$$

where $\boldsymbol{K} = \boldsymbol{K}_{\mathrm{OUT}} - 2\boldsymbol{K}_{\mathrm{IN}}$ and $\boldsymbol{r}_m$ is the position of molecule m. The intensity of scattered light for a given arrangement of molecules is then proportional to the square modulus of this amplitude. Since we have considered so far only one such arrangement, we must average over all possible positions and orientations of the molecules to give the total intensity of light scattered as,

$$I(2\omega, \boldsymbol{K}) = \kappa \sum_{m,n} \left\langle \beta^m_{\mathrm{OII}} \beta^n_{\mathrm{OII}} e^{i\boldsymbol{K}\cdot(\boldsymbol{r}_m - \boldsymbol{r}_n)} \right\rangle. \tag{5.11}$$

[4]The prefactor κ' depends on R, the distance between the molecule and the detector. However, we assume here that R is the same for all molecules, which will be a good approximation so long as the distance between any two molecules in our experimental sample is much smaller than the distance between the sample and the detector.

This expression can be split into two terms: the intensity of incoherent scattering (made up of the terms in Eqn. (5.11) for which $n = m$), and the intensity of coherent scattering (the terms for which $n \neq m$),

$$I(2\omega, \boldsymbol{K}) = I_{\text{inc}}(2\omega, \boldsymbol{K}) + I_{\text{coh}}(2\omega, \boldsymbol{K}), \tag{5.12a}$$

$$I_{\text{inc}}(2\omega, \boldsymbol{K}) = \kappa \sum_m \left\langle (\beta_{\text{OII}}^m)^2 \right\rangle, \tag{5.12b}$$

$$I_{\text{coh}}(2\omega, \boldsymbol{K}) = \kappa \sum_{m,n' \neq m} \left\langle \beta_{\text{OII}}^m \beta_{\text{OII}}^n e^{i\boldsymbol{K}\cdot(\boldsymbol{r}_m - \boldsymbol{r}_n)} \right\rangle. \tag{5.12c}$$

Eqn. (5.12b) is the intensity of light scattered when a molecule absorbs two photons of frequency ω and spontaneously emits a photon of frequency 2ω at some later time [273]. Each molecule does so independently, and the total scattering intensity is the sum of intensities scattered by each molecule,

$$\begin{aligned} I_{\text{inc}}(2\omega, \boldsymbol{K}) &= \kappa N \left\langle \beta_{\text{OII}}^2 \right\rangle \\ &= \kappa \rho_{\text{S}} V \left\langle \beta_{\text{OII}}^2 \right\rangle, \end{aligned} \tag{5.13}$$

where $\langle \beta_{\text{OII}}^2 \rangle$ is an average over all molecules, ρ_{S} is the solvent number density and V the volume of the solution.

The incoherent contribution to the scattered light will always be present in the experimentally measured intensity. The contribution described by Eqn. (5.12c), due to coherently scattered light, is responsible for the variation of the signal with ion concentration. It is due to the interference of light scattered by different molecules, and is nonzero if molecules are orientationally correlated [272, 274]; otherwise, the average over mutual orientations in Eqn. (5.12c) can be written as a product of two averages, both of which will be zero. Thus, the increase of the scattered signal in

Figs. 5.2 and 5.3 is due to an increase in orientational ordering. In order to explain this ordering, we will derive a simple model for $I_{\mathrm{coh}}(2\omega, \boldsymbol{K})$ in an ionic solution.

5.2.2 Ionic Solutions

A basic theory for SHS from ionic solutions was presented by Shelton [282]. Using this reference as a starting point, we derive a mean-field theory for the scattering and appraise its ability to account for the experimental observations. The derivation in this Section is more in-depth than that of Ref. [282], and the final expression we obtain is somewhat more general.

We begin by considering the water molecules in an ionic solution to be dipoles that interact with the solute but not with each other. The orientational ordering of water molecules is then caused entirely by the local electric field due to the ions. Perhaps the best way to visualize such a model is to build it up in two steps, as illustrated in Fig. 5.4:

1. Firstly, take the ions to be point charges in a dielectric continuum, as was discussed in Sec. 4.1.1. We will consider the appropriate spatial distribution of these ions in Sec. 5.2.4.

2. This system is then filled with a uniform gas of independent dipoles (the water molecules), which align themselves with the local electric field.

The average in Eqn. (5.12c) is a thermodynamic average over the positions of the solvent molecules, their orientations and the spatial distribution of the ions. Since the water molecules are uniformly distributed in space we need not consider the

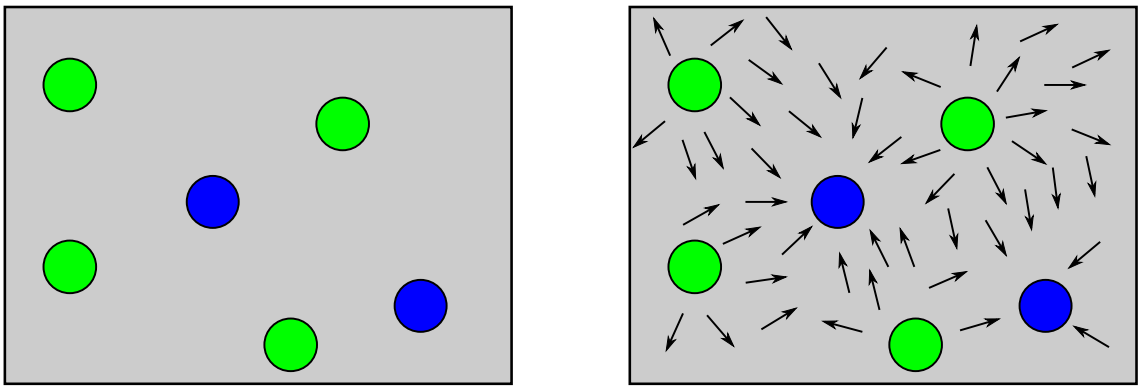

1. Ions in dielectric continuum

2. Independent dipoles added

Figure 5.4: Illustration of the mean-field theory for SHS. Firstly, ions are embedded in a dielectric continuum (although they are point charges in the theory, they are shown here with finite volumes for clarity), and then a uniform gas of independent dipoles (representing the water molecules) is added to the system. These dipoles are oriented by the local electric field.

average over their positions. Thus we can write,

$$I_{\mathrm{coh}}(2\omega, \boldsymbol{K}) = \kappa \left\langle \sum_{m,n\neq m} \langle \beta_{\mathrm{OII}}^{m} \beta_{\mathrm{OII}}^{n} \rangle_{\mathrm{or}} \, e^{i\boldsymbol{K}\cdot(\boldsymbol{r}_m - \boldsymbol{r}_n)} \right\rangle_{\mathrm{ion}} , \tag{5.14}$$

where $\langle \cdots \rangle_{\mathrm{or}}$ is an average over molecular orientations and $\langle \cdots \rangle_{\mathrm{ion}}$ is an average over ion positions.

Since the molecules do not interact with each other, the average over mutual orientations can be written as a product of averages, $\langle \beta_{\mathrm{OII}}^{m} \beta_{\mathrm{OII}}^{n} \rangle_{\mathrm{or}} = \langle \beta_{\mathrm{OII}}^{m} \rangle_{\mathrm{or}} \langle \beta_{\mathrm{OII}}^{n} \rangle_{\mathrm{or}}$, where the first average is over the orientations of molecule m, and the second over orientations of molecule n. The energy of a dipole in an electric field $\boldsymbol{E}$ is $-\boldsymbol{\mu}_0 \cdot \boldsymbol{E}$, where $\boldsymbol{\mu}_0$ is the dipole moment. This means that $\langle \beta_{\mathrm{OII}}^{m} \rangle_{\mathrm{or}}$ can be rewritten as $\left\langle \beta_{\mathrm{OII}}^{m} e^{+\boldsymbol{\mu}_0 \cdot \boldsymbol{E}(\boldsymbol{r}_m)/k_{\mathrm{B}}T} \right\rangle_0$, where $\langle \cdots \rangle_0$ is an unweighted average over all orientations of

molecule m and $\boldsymbol{E}(\boldsymbol{r}_m)$ is the electric field at the position of molecule m. If θ_m is the angle between the dipole moment of molecule m and the electric field at $\boldsymbol{r}_m$ then we can further write,

$$I_{\rm coh}(2\omega,\boldsymbol{K}) = \kappa\left\langle \sum_{m,n\neq m} \left\langle \beta_{\rm OII}^{m} e^{+\mu_0 E(\boldsymbol{r}_m)\cos\theta_m/k_{\rm B}T}\right\rangle_0 \left\langle \beta_{\rm OII}^{n} e^{+\mu_0 E(\boldsymbol{r}_n)\cos\theta_n/k_{\rm B}T}\right\rangle_0 e^{i\boldsymbol{K}\cdot(\boldsymbol{r}_m-\boldsymbol{r}_n)}\right\rangle_{\rm ion}. \tag{5.15}$$

The orientational averages in these equations are tractable once the Boltzmann factors are expanded to linear order in $1/T$. The method for doing so is described in Appendix B, and the result is,

$$I_{\rm coh}(2\omega,\boldsymbol{K}) \simeq \kappa\left\langle \sum_{m,n\neq m} \left[\frac{\mu_0\beta_{\parallel,\perp}\boldsymbol{E}(\boldsymbol{r}_m)\cdot\boldsymbol{u}_{\rm OUT}}{3k_{\rm B}T}\right]\left[\frac{\mu_0\beta_{\parallel,\perp}\boldsymbol{E}(\boldsymbol{r}_n)\cdot\boldsymbol{u}_{\rm OUT}}{3k_{\rm B}T}\right] e^{i\boldsymbol{K}\cdot(\boldsymbol{r}_m-\boldsymbol{r}_n)}\right\rangle_{\rm ion}, \tag{5.16}$$

where $\beta_\parallel$ and $\beta_\perp$ are defined in Eqns. (B.10) of Appendix B; the former is appropriate when $\boldsymbol{u}_{\rm OUT}$ is parallel to $\boldsymbol{u}_{\rm IN}$ (that is, for the $\rm S_{OUT}S_{IN}S_{IN}$ polarization combination), and the latter when they are perpendicular (for all other combinations).

In the double sum of Eqn. (5.16) there are $N_{\rm S}^2 - N_{\rm S}$ terms, where $N_{\rm S}$ is the number of solvent molecules. In the thermodynamic limit ($N_{\rm S}\to\infty$), we would expect the error due to reintroducing the $n = m$ term into the second sum to be negligible. If $E_{\rm O}(\boldsymbol{r}) = \boldsymbol{E}(\boldsymbol{r})\cdot\boldsymbol{u}_{\rm OUT}$ is the component of the electric field in the direction of the outgoing polarization then we have,

$$I_{\rm coh}(2\omega,\boldsymbol{K}) = \kappa\left(\frac{\mu_0\beta_{\parallel,\perp}}{3k_{\rm B}T}\right)^2\left\langle \sum_{m,n} E_{\rm O}(\boldsymbol{r}_m)E_{\rm O}(\boldsymbol{r}_n)e^{i\boldsymbol{K}\cdot(\boldsymbol{r}_m-\boldsymbol{r}_n)}\right\rangle_{\rm ion}. \tag{5.17}$$

The electric field component $E_{\rm O}(\boldsymbol{r}_m)$ at $\boldsymbol{r}_m$ is a linear superposition of fields due

to all of the ions in the solution. We can thus write it as a sum over all ions,

$$E_{\mathrm{O}}(\boldsymbol{r}_m) = \sum_{\mu} e^{\mu}_{\mathrm{O}}(\boldsymbol{r}_m - \boldsymbol{r}_\mu), \tag{5.18}$$

with $e^{\mu}_{\mathrm{O}}(\boldsymbol{r}_m - \boldsymbol{r}_\mu)$ the component of the Coulomb field in the direction of $\boldsymbol{u}_{\mathrm{OUT}}$ at position $\boldsymbol{r}_m$ due to an ion at $\boldsymbol{r}_\mu$; from here onwards Latin indices will refer to water molecules and Greek indices to ions. Using Eqn. (5.18) we can rewrite the intensity of coherently scattered light as,

$$I_{\mathrm{coh}}(2\omega, \boldsymbol{K}) = \kappa \left(\frac{\mu_0 \beta_{\parallel,\perp}}{3 k_{\mathrm{B}} T}\right)^2 \left\langle \sum_{\mu,\nu} e^{i\boldsymbol{K}\cdot(\boldsymbol{r}_\mu - \boldsymbol{r}_\nu)} \times \right.$$
$$\left. \sum_m e^{\mu}_{\mathrm{O}}(\boldsymbol{r}_m - \boldsymbol{r}_\mu) e^{i\boldsymbol{K}\cdot(\boldsymbol{r}_m - \boldsymbol{r}_\mu)} \sum_n e^{\nu}_{\mathrm{O}}(\boldsymbol{r}_n - \boldsymbol{r}_\nu) e^{-i\boldsymbol{K}\cdot(\boldsymbol{r}_n - \boldsymbol{r}_\nu)} \right\rangle_{\mathrm{ion}}. \tag{5.19}$$

The term in angular brackets consists of three factors. The first of these depends only on the relative positions of pairs of ions, while the second and third terms involve the positions of water molecules relative to a particular ion. These latter two terms have a very similar form, and we can define a scattering form factor,

$$\begin{aligned} F_\mu(\boldsymbol{K}) &= \sum_m e^{\mu}_{\mathrm{O}}(\boldsymbol{r}_m - \boldsymbol{r}_\mu) e^{i\boldsymbol{K}\cdot(\boldsymbol{r}_m - \boldsymbol{r}_\mu)}, \\ &\equiv \sum_m e^{\mu}_{\mathrm{O}}(\boldsymbol{r}_m) e^{i\boldsymbol{K}\cdot\boldsymbol{r}_m}, \end{aligned} \tag{5.20}$$

where the second line is a consequence of the uniform spatial distribution of the water molecules: we can change variables from their absolute positions in the solution to their positions relative to the μ^{th} ion. We can then write,

$$I_{\mathrm{coh}}(2\omega, \boldsymbol{K}) = \kappa \left(\frac{\mu_0 \beta_{\parallel,\perp}}{3 k_{\mathrm{B}} T}\right)^2 \left\langle \sum_{\mu,\nu} e^{i\boldsymbol{K}\cdot(\boldsymbol{r}_\mu - \boldsymbol{r}_\nu)} F_\mu(\boldsymbol{K}) F_\nu(\boldsymbol{K}) \right\rangle_{\mathrm{ion}}. \tag{5.21}$$

In order to evaluate $F_\mu(\boldsymbol{K})$ we introduce the solvent density $\rho_{\mathrm{S}}(\boldsymbol{r}) = \sum_m \delta(\boldsymbol{r} - \boldsymbol{r}_m)$ as a sum of delta functions, allowing us to replace the sum by an integral over the

volume V of the solution [288],

$$F_\mu(\boldsymbol{K}) = \int_V \rho_\mathrm{S}(\boldsymbol{r}) e^\mu_\mathrm{O}(\boldsymbol{r}) e^{i\boldsymbol{K}\cdot\boldsymbol{r}}\,\mathrm{d}^3\boldsymbol{r}. \tag{5.22}$$

Assuming that the solvent density is constant and equal to ρ_S we obtain,

$$F_\mu(\boldsymbol{K}) = \rho_\mathrm{S} \int_V e^\mu_\mathrm{O}(\boldsymbol{r}) e^{i\boldsymbol{K}\cdot\boldsymbol{r}}\,\mathrm{d}^3\boldsymbol{r}. \tag{5.23}$$

Inserting the expression,

$$e^\mu_\mathrm{O}(\boldsymbol{r}) = \frac{f(0)Q_\mu}{4\pi\varepsilon}\frac{\boldsymbol{r}\cdot\boldsymbol{u}_\mathrm{OUT}}{r^3}, \tag{5.24}$$

for the component of a Coulomb field in the direction of $\boldsymbol{u}_\mathrm{OUT}$ we find,

$$F_\mu(\boldsymbol{K}) = \frac{f(0)Q_\mu\rho_\mathrm{S}}{4\pi\epsilon}\int_V \frac{\boldsymbol{r}\cdot\boldsymbol{u}_\mathrm{OUT}}{r^3} e^{i\boldsymbol{K}\cdot\boldsymbol{r}}\,\mathrm{d}^3\boldsymbol{r}. \tag{5.25}$$

Q_μ is the charge of ion μ, ϵ is the permittivity of the solution and $f(0)$ is the Onsager local field factor [289], which accounts for the increased field at the position of a molecule due to the polarization of the surrounding solvent by this molecule.

Assuming that the solution is contained in a spherical volume, we can use polar coordinates to carry out the integral in Eqn. (5.25). However, since it contains two scalar products the integrand is in general a complicated function of the polar angles. We can simplify this expression by making use of $\boldsymbol{\nabla}_K$, the gradient operator with respect to the vector $\boldsymbol{K}$,

$$\begin{aligned} F_\mu(\boldsymbol{K}) &= \frac{f(0)Q_\mu\rho_\mathrm{S}}{4\pi\epsilon}\boldsymbol{u}_\mathrm{OUT}\cdot\int_V \frac{\boldsymbol{r}e^{i\boldsymbol{K}\cdot\boldsymbol{r}}}{r^3}\,\mathrm{d}^3\boldsymbol{r}, \\ &= \frac{f(0)Q_\mu\rho_\mathrm{S}}{4\pi\epsilon i}\boldsymbol{u}_\mathrm{OUT}\cdot\boldsymbol{\nabla}_K\int_V \frac{e^{i\boldsymbol{K}\cdot\boldsymbol{r}}}{r^3}\,\mathrm{d}^3\boldsymbol{r}. \end{aligned} \tag{5.26}$$

There is now only a single scalar product in the integrand, and we can define the polar axis to be parallel to $\boldsymbol{e}_K$ (the unit vector in the direction of $\boldsymbol{K}$), which will

give $\boldsymbol{K}\cdot\boldsymbol{r} = Kr\cos\theta$. If the solution volume has radius R then integration over the polar angles gives,

$$\begin{aligned} F_\mu(\boldsymbol{K}) &= \frac{f(0)Q_\mu\rho_{\mathrm{S}}}{\epsilon i}\boldsymbol{u}_{\mathrm{OUT}}\cdot\boldsymbol{\nabla}_K\int_0^R\frac{\sin(Kr)}{Kr^2}\,\mathrm{d}r, \\ &= \frac{f(0)Q_\mu\rho_{\mathrm{S}}}{\epsilon i}\left(\boldsymbol{u}_{\mathrm{OUT}}\cdot\boldsymbol{e}_K\right)\left[\frac{\sin(KR)-KR}{K^2R}\right]. \end{aligned} \tag{5.27}$$

In general, we will require the thermodynamic ($R\to\infty$) limit,

$$F_\mu(\boldsymbol{K}) = -\frac{f(0)Q_\mu\rho_{\mathrm{S}}}{\epsilon iK}\left(\boldsymbol{u}_{\mathrm{OUT}}\cdot\boldsymbol{e}_K\right). \tag{5.28}$$

Inserting this into Eqn. (5.21) gives,

$$I_{\mathrm{coh}}(2\omega,\boldsymbol{K}) = \kappa\left(\frac{\mu_0\beta_{\parallel,\perp}}{3k_{\mathrm{B}}T}\right)^2\left(\frac{f(0)e\rho_{\mathrm{S}}}{\epsilon K}\right)^2\left(\boldsymbol{u}_{\mathrm{OUT}}\cdot\boldsymbol{e}_K\right)^2\left\langle\sum_{\mu,\nu}e^{i\boldsymbol{K}\cdot(\boldsymbol{r}_\mu-\boldsymbol{r}_\nu)}Z_\mu Z_\nu\right\rangle_{\mathrm{ion}}, \tag{5.29}$$

with $Z_\mu = Q_\mu/e$, where e is the electron charge.

The product in angular brackets is related to the charge-charge structure factor $S(\boldsymbol{K},\rho)$ for the solution [131] by,

$$S(\boldsymbol{K},\rho) = \frac{1}{\rho V}\left\langle\sum_{\mu,\nu}e^{i\boldsymbol{K}\cdot(\boldsymbol{r}_\mu-\boldsymbol{r}_\nu)}Z_\mu Z_\nu\right\rangle_{\mathrm{ion}}, \tag{5.30}$$

with ρ the total number density of ions. For the purposes of this work, the most useful expression for $S(\boldsymbol{K},\rho)$ is [131],

$$\begin{aligned} S(\boldsymbol{K},\rho) = &\left(Z_+^2+Z_-^2\right)+ \\ &\frac{4\pi\rho}{K}\int_0^\infty r\sin(Kr)\left[Z_+^2h_{++}(r)+Z_-^2h_{--}(r)+2Z_+Z_-h_{+-}(r)\right]\,\mathrm{d}r, \end{aligned} \tag{5.31}$$

where $h_{\mu\nu}(r) = g_{\mu\nu}(r)-1$. For a 1:1 electrolyte this expression becomes,

$$S(\boldsymbol{K},\rho) = 2+\frac{4\pi\rho}{K}\int_0^\infty r\sin(Kr)\left[g_{++}(r)+g_{--}(r)-2g_{+-}(r)\right]\,\mathrm{d}r. \tag{5.32}$$

The intensity of coherently scattered light may now be written,

$$I_{\mathrm{coh}}(2\omega, \boldsymbol{K}) = \kappa \left(\frac{\mu_0 \beta_{\parallel,\perp}}{3k_{\mathrm{B}}T}\right)^2 \left(\frac{f(0)Q\rho_{\mathrm{S}}}{\epsilon K}\right)^2 (\boldsymbol{u}_{\mathrm{OUT}} \cdot \boldsymbol{e}_K)^2 \, V \rho S(\boldsymbol{K}, \rho). \tag{5.33}$$

We turn now to the intensity of incoherently scattered light,

$$I_{\mathrm{inc}}(2\omega, \boldsymbol{K}) = \kappa \sum_m \left\langle (\beta_{\mathrm{OII}}^m)^2 \right\rangle_{\mathrm{or}}. \tag{5.34}$$

Writing this as an unweighted average over orientations gives,

$$I_{\mathrm{inc}}(2\omega, \boldsymbol{K}) = \kappa \sum_m \left\langle (\beta_{\mathrm{OII}}^m)^2 \, e^{+\boldsymbol{\mu}_0 \cdot \boldsymbol{E}(\boldsymbol{r}_m)/k_{\mathrm{B}}T} \right\rangle_0. \tag{5.35}$$

Expanding the Boltzmann factor as a Taylor series in $1/T$, and noting that the first-order term vanishes (this is an average of a product of seven scalar products, which as discussed in Appendix B is zero) we have,

$$I_{\mathrm{inc}} \simeq \kappa \sum_m \left\langle (\beta_{\mathrm{OII}}^m)^2 \right\rangle = \kappa \rho_{\mathrm{S}} V \left\langle \beta_{\mathrm{OII}}^2 \right\rangle, \tag{5.36}$$

which is exactly the same as in Eqn. (5.12b). The intensity of incoherently scattered light is approximately equal to the background intensity $I_{\mathrm{B}}(\boldsymbol{K})$ due to pure solvent.

We can now write down an expression for the ratio of scattering intensity $I_{\mathrm{S}}(\boldsymbol{K}, \rho)$ from a solution with ion number density ρ to the background intensity $I_{\mathrm{B}}(\boldsymbol{K})$ by inserting Eqns. (5.33) and (5.36) into Eqn. (5.12) and dividing by $I_{\mathrm{inc}}(2\omega, \boldsymbol{K})$ to give,

$$\Delta I = \frac{I_{\mathrm{S}}(\boldsymbol{K}, \rho)}{I_{\mathrm{B}}(\boldsymbol{K})} = 1 + A\rho S(\boldsymbol{K}, \rho), \tag{5.37}$$

where A is a constant that depends only on the experimental setup and properties of the solvent molecules,

$$A = \left(\frac{\mu_0}{3k_{\mathrm{B}}T}\right)^2 \left(\frac{f(0)e}{\epsilon K}\right)^2 (\boldsymbol{u}_{\mathrm{OUT}} \cdot \boldsymbol{e}_K)^2 \, \frac{\beta_{\parallel,\perp}}{\langle \beta_{\mathrm{OII}}^2 \rangle} \rho_{\mathrm{S}}. \tag{5.38}$$

We see from this expression that the theory can account for the polarization dependence of the SHS signal through the factor $(\boldsymbol{u}_{\mathrm{OUT}} \cdot \boldsymbol{e}_K)^2$. The term $\boldsymbol{u}_{\mathrm{OUT}} \cdot \boldsymbol{r}$ in Eqn. (5.25) is the origin of this factor, so that the polarization dependence is a consequence of the fact that the electric field due to an ion is radially directed (that is, proportional to the vector $\boldsymbol{r}$).

As in Fig. 5.1, the scattering wavevector $\boldsymbol{K}$ is in the scattering plane and $\boldsymbol{u}_{\mathrm{OUT}}$ is either in the plane ($\mathrm{P}_{\mathrm{OUT}}$) or orthogonal to it ($\mathrm{S}_{\mathrm{OUT}}$). Only in the former case will the intensity of coherently scattered light be nonzero, so that the only polarization combinations in which we can observe coherent scattering are $\mathrm{P}_{\mathrm{OUT}}\mathrm{P}_{\mathrm{IN}}\mathrm{P}_{\mathrm{IN}}$ and $\mathrm{P}_{\mathrm{OUT}}\mathrm{S}_{\mathrm{IN}}\mathrm{S}_{\mathrm{IN}}$. This is an encouraging sign that the theory is on the right track.

5.2.3 Ion-Nonspecificity

Before applying this theory to solutions of arbitrary concentrations, we will first consider the infinitely dilute limit of a single ion, which will allow us to explain the independence of experimental results on the identity of the dissolved salt. When considering a single ion, $S(\boldsymbol{K}, \rho) = 1$ and ρ is a constant.

Rather than looking at an infinite volume, let us take a sphere of radius R surrounding the ion, and assume that all solvent molecules are within this sphere; this situation is illustrated in Fig. 5.5. In this case, Eqn. (5.27) should be used rather than Eqn. (5.28) for the scattering form factor $F_\mu(\boldsymbol{K})$, and we obtain for the intensity of coherently scattered light,

$$I_{\mathrm{coh}}(2\omega, \boldsymbol{K}) = B\frac{[\sin(KR) - KR]^2}{K^4R^2}, \tag{5.39}$$

where B is a constant. For $RK \ll 1$ this can be approximated as,

$$I_{\mathrm{coh}}(2\omega, \boldsymbol{K}) \simeq BK^2R^4. \tag{5.40}$$

Given that $K = 2.3 \times 10^7$ m in the experiments we are considering, this approximation is reasonable for spheres of radii up to around 40 nm. The greater contribution to $I_{\mathrm{coh}}(2\omega, \boldsymbol{K})$ will come from the volume further away from the ion, where the solvent structure is essentially independent of the ion's identity. This independence is passed on to the intensity of the coherently scattered light, accounting for the ion-nonspecificity.

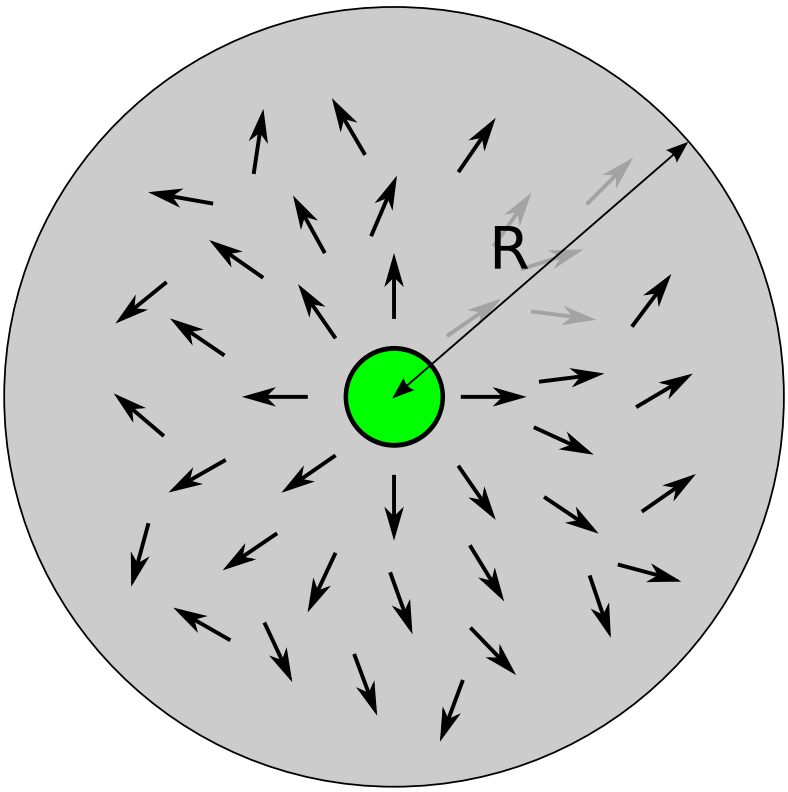

Figure 5.5: In the mean-field model for SHS, we consider the light scattered coherently by a sphere of radius R surrounding an ion and containing solvent molecules. The electric field of the ion (green circle) will orientationally order the dipoles of these molecules (black arrows), and the net dipole density will coherently scatter light.

5.2.4 The Structure Factor

As in Eqn. (5.32), $S(\boldsymbol{K}, \rho)$ tends to a constant at low number density ρ, so that ΔI will begin by increasing linearly with ρ. For ΔI to plateau at high density, we require that $S(\boldsymbol{K}, \rho) \propto 1/\rho$ for large ρ. With this in mind, we turn now to look at the spatial distribution of ions.

Perhaps the simplest theory to describe ion-ion correlations is that of Debye and Hückel (D-H) [290, 291], in which each ion is surrounded by a diffuse cloud of the opposite charge, screening its electric field. This leads to an exponential damping of the Coulomb potential,[5]

$$V(r) = \frac{Ze}{4\pi\epsilon}\frac{e^{-\kappa_{\mathrm{D}} r}}{r}, \tag{5.41}$$

where,

$$\kappa_{\mathrm{D}} = \left(\frac{2\rho_{\mathrm{I}} e^2}{\epsilon k_{\mathrm{B}} T}\right)^{1/2}. \tag{5.42}$$

κ_{D}^{-1} is called the Debye length, and gives the extent of the surrounding ionic atmosphere. The energy of a body with charge $Q = Ze$ at a distance r from the central ion is given by $ZeV(r)$, and since this is a mean-field theory in which the electric potential does not fluctuate [292], this energy is equal to the potential of mean force and we can immediately write down the radial distribution functions

[5] Eqn. (5.41) is appropriate for the electric field at the position of an ion. For the electric field experienced by a water molecule it must be multiplied by the local field factor $f(0)$.

$g_{++}(r)$, $g_{--}(r)$ and $g_{+-}(r)$,

$$g_{++}(r) = \exp\left(-\frac{Z_+^2 e^2}{4\pi\epsilon k_\mathrm{B}T}\frac{e^{-\kappa_\mathrm{D}r}}{r}\right), \tag{5.43a}$$

$$g_{--}(r) = \exp\left(-\frac{Z_-^2 e^2}{4\pi\epsilon k_\mathrm{B}T}\frac{e^{-\kappa_\mathrm{D}r}}{r}\right), \tag{5.43b}$$

$$g_{+-}(r) = \exp\left(-\frac{Z_+ Z_- e^2}{4\pi\epsilon k_\mathrm{B}T}\frac{e^{-\kappa_\mathrm{D}r}}{r}\right). \tag{5.43c}$$

As a concrete example, we will consider 1:1 electrolytes for the remainder of this Section, in which case the ionic strength ρ_I becomes the total ion number density ρ. A generally applicable theory is obtained by replacing ρ with ρ_I in the following results. The RDFs for a 1:1 electrolyte are,

$$g_{++}(r) = g_{--}(r) = \exp\left(-\frac{e^2}{4\pi\epsilon k_\mathrm{B}T}\frac{e^{-\kappa_\mathrm{D}r}}{r}\right), \tag{5.44a}$$

$$g_{+-}(r) = \exp\left(+\frac{e^2}{4\pi\epsilon k_\mathrm{B}T}\frac{e^{-\kappa_\mathrm{D}r}}{r}\right). \tag{5.44b}$$

These results hold for a theory in which the ions are point charges. In a more sophisticated treatment [291], the electrostatic potential of Eqn. (5.41) is multiplied by a prefactor $\frac{\exp(\kappa_\mathrm{D}a)}{1+\kappa_\mathrm{D}a}$, for ions of mean radius a. However, this factor changes by only 2% over the concentration range of interest, and does not make an appreciable difference to our results over this range, so we will omit it in our theory.

Given these radial distribution functions, we can calculate the structure factor for this system using Eqn. (5.32). This requires that the RDFs be expanded to first

order in $1/T$, and gives,

$$\begin{aligned} S(\boldsymbol{K},\rho) &= 2 + \frac{8\pi\rho}{K}\int_0^\infty r\sin(Kr)\left[g_{++}(r) - g_{+-}(r)\right]\,\mathrm{d}r, \\ &\simeq 2 - \frac{8\pi\rho}{K}\int_0^\infty r\sin(Kr)\left[\frac{e^2}{2\pi\epsilon k_\mathrm{B}T}\frac{e^{-\kappa_D r}}{r}\right]\,\mathrm{d}r, \\ &= 2 - \frac{4e^2}{\epsilon k_\mathrm{B}T}\frac{\rho}{K^2+\kappa_D^2}, \\ &= \frac{2K^2}{K^2+\kappa_\mathrm{D}^2}, \\ &= \frac{2}{1+\rho/\rho_\mathrm{D}}, \end{aligned} \tag{5.45}$$

with $\rho_\mathrm{D} = \frac{K^2\epsilon k_\mathrm{B}T}{2e^2}$ [282]. Under the conditions used in the experiments of this Chapter, $\rho_\mathrm{D} = 48.7\ \mu$M.

As discussed at the beginning of this Section, $S(\boldsymbol{K},\rho)$ should be proportional to $1/\rho$ at large ρ in order for the intensity to plateau at high concentrations. We see from Eqn. (5.45) that this is the case, and so this theory is capable of accounting qualitatively for the experimental observations. To make a quantitative comparison, we insert this structure factor into Eqn. (5.37) and find,

$$\Delta I = 1 + \frac{C\rho/\rho_\mathrm{D}}{1+\rho/\rho_\mathrm{D}}, \tag{5.46}$$

with the constant C defined,

$$C = \left(\frac{\mu_0}{3}\right)^2 \frac{f(0)^2}{\epsilon k_\mathrm{B}T}\left(\boldsymbol{u}_\mathrm{OUT}\cdot\boldsymbol{e}_K\right)^2 \frac{\beta_{\parallel,\perp}}{\langle\beta_\mathrm{OII}^2\rangle}\rho_\mathrm{S}. \tag{5.47}$$

This theory predicts a Langmuir equation-like dependence of the intensity increase on ion concentration. ρ_D is the concentration (or more generally, ionic strength) at which the intensity reaches half its maximum. Fig. 5.6 compares the predictions of D-H theory with the experimental results of Section 5.1.2 using

$\mu_0 = 2.95$ D [293], $f(0) = 3.15$ [282], $\varepsilon/\varepsilon_0 = 78.45$ [294] and $\beta_\perp / \langle\beta_{\mathrm{XZZ}}\rangle = 2.7986$ [270, 295]. We see that although the theoretical treatment does lead to a plateau, it predicts an intensity at this plateau (an 175% increase over pure solvent) that is much larger than that measured (a 30% increase).

It was observed in Ref. [282] that this theory over-predicts the intensity at high concentrations, and several possible reasons were given for this discrepancy. In particular, a decrease of $f(0)$ from its accepted value of 3.15 was found to give better agreement between theory and experiments.[6] However, we carried out preliminary computations that suggest that $f(0)$ should not be decreased.

Atomistic simulations by members of the Ceriotti group [296] show that allowing instantaneous fluctuations in the molecular hyperpolarizability gives much better agreement with experimental SHS results than those that are obtained when the hyperpolarizability is static. This implies that the assumption of a static hyperpolarizability inherent in the theory we have derived is also partly to blame for the discrepancy between theoretical and experimental results.

Another likely source of disagreement between theory and experiment is the approximation of independent dipoles; rather than being orientationally ordered only by the ions, water molecules are also correlated with each other in a complex hydrogen-bonding network. Under the influence only of the ions, nearby water molecules would tend to align their dipoles with each other, whereas the inclusion

[6]The ionic strength at which the intensity increase reaches half its maximum value is quite similar for the theoretical and the experimental results (48.7 μM from theory and 55 μM from experiment), so that such a rescaling would make the two results agree quite well.

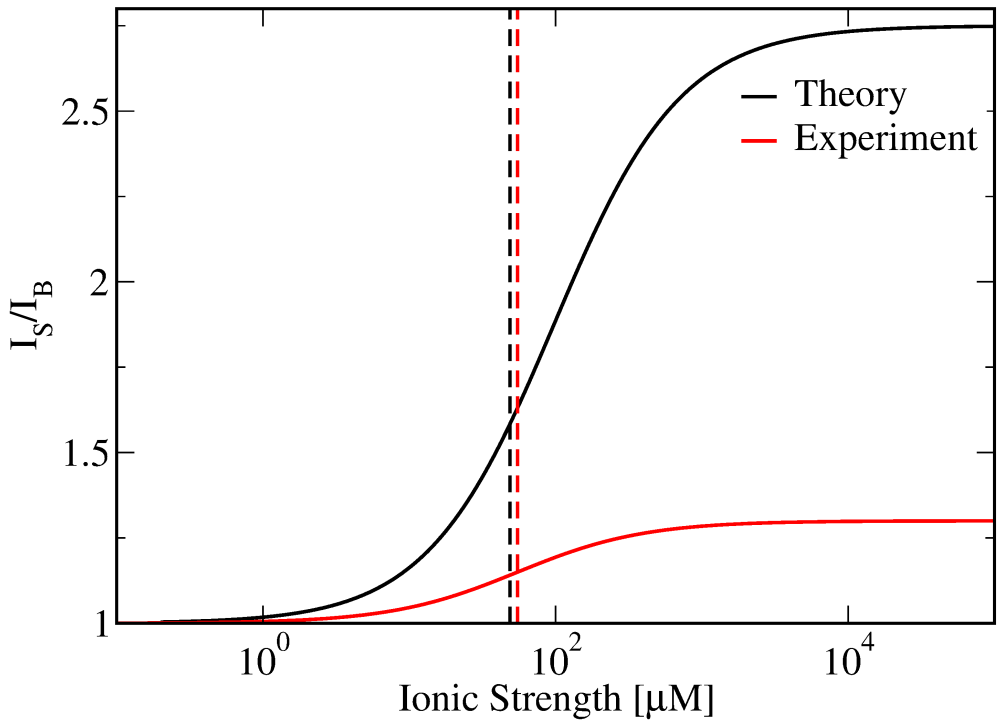

Figure 5.6: The SHS intensity from an ionic solution as a function of concentration, in the $P_{OUT}S_{IN}S_{IN}$ polarization combination, as predicted by D-H theory (black line) and as found in experiment (the red line is the fitted Langmuir equation, as shown in Fig. 5.2). The dashed vertical lines show the concentration at which the density increase reaches half its maximum. The intensity is normalized in both cases by the intensity of scattering by pure solvent.

of intermolecular interactions would tend to disrupt this alignment, decreasing the ordering due to the ion and thus decreasing the intensity ΔI.

We are also ignoring the quantum-mechanical nature of the nuclei involved. Since

the differences in the relevant electronic properties of H_2O and D_2O are very small, the theory would predict an extremely small difference between intensities for the two. Both the intermolecular correlations and nuclear quantization would need to be taken into account to fully understand the fairly large isotope effect seen.

In the next section we will run classical atomistic simulations. This will allow us to account for the orientational correlations between water molecules, as well as to ascertain how well the D-H theory captures ion-ion and ion-water correlations.

5.3 Long-Ranged Correlations

5.3.1 Simulation Details

While there has been some discussion in the literature about the range over which an ion affects the structure of water [297], the need for large system sizes has made longer-ranged effects difficult to detect by simulation. Since we are looking at correlations over long distances, we will need to use much larger simulation boxes than we have done thus far.

For this reason, the remainder of this Chapter comprises a preliminary, classical study of the long-ranged correlations in liquid water. While this will not allow us to explain the isotope effect described in Section 5.1.2, and will probably preclude quantitative agreement with experiments (since the isotope effect points to a quantum-mechanical contribution), it will allow us to describe the situation qualitatively, without the added computational effort of path integral simulations.

For the remainder of this Chapter we will consider a solution of NaCl. For this 1:1

electrolyte, the ionic strength is equal to the concentration, or equivalently $\rho_I = \rho$. The question of ion concentration must also be addressed: for a fixed simulation box size, a smaller concentration requires fewer ions, and for a fixed number of ions a larger box size is required. Both of these considerations impose a lower bound on the concentrations we can simulate. In this work, we are restricted to concentrations within the plateau region of Fig. 5.2. In order to understand the correlations as well as possible, we will thus choose a fairly high concentration to maximize the statistics gathered.

Starting with boxes containing 27000 water molecules at the experimental density of the pure liquid, we replaced 80 of these molecules with a Na^+ ion and 80 with a Cl^- ion, giving a $\sim$0.32 M NaCl concentration in a cubic box of length $\sim$93 Å. Although we have used the q-TIP4P/F model thus far, no force field exists for its interactions with either of these two ions. We will thus use the simpler, rigid SPC/E model [16] to describe water-water interactions. Since we are not concerned in this Chapter with simulating nuclear quantum effects, and because this model has the advantages that many good-quality ion-water interactions exist [252], and that being rigid we can use longer timesteps in our simulations, we will use it to get a qualitative idea of the long-range correlations in the aqueous solution. For the ion-water interactions we will use the Lennard-Jones parameters of Reif and Hühnenberger [298].

In total, 20 such boxes were used; after equilibration these were evolved for 1 ns in the NVT ensemble at 300 K. These simulations were carried out using the LAMMPS software package [299], which uses a Nosé-Hoover thermostat [300, 301]

to control the temperature and the RATTLE algorithm [262] to enforce O–H bond constraints.

From these simulations, there are a number of functions that we can calculate to look at the long-range correlations in the solution. The most obvious of these are the various radial distribution functions. The inter-ion correlations are described by $g_{\mathrm{Na^+\text{–}Cl^-}}(r)$, $g_{\mathrm{Na^+\text{–}Na^+}}(r)$ and $g_{\mathrm{Cl^-\text{–}Cl^-}}(r)$. All of these are calculable in D-H theory, as in Eqns. (5.44), so that a comparison will show how well this theory accounts for the spatial distribution of the ions. We will also calculate $g_{\mathrm{Na^+\text{–}O}}(r)$ and $g_{\mathrm{Cl^-\text{–}O}}(r)$ to look at the ion-water spatial correlation.

The orientational ordering of water molecules is responsible for the augmentation of the SHS signal over that for pure water, and so we will focus on orientational correlations. The first correlation function to be calculated describes the ordering of molecules by an ion. $\langle \cos\theta \rangle (r)$ is the average projection of a molecular dipole moment on the ion-water vector, where r is the ion-oxygen distance; this is illustrated in Fig. 5.7.

$\langle \cos\theta \rangle (r)$ is calculated separately for Na^+ and for Cl^- ions. For each type of ion, $\cos\theta$ and r are recorded for every ion-water pair whose separation is less than a cutoff distance; the $\cos\theta$ are binned as a function of r and used to find the average. We will use a cutoff of 20 Å, which should give a reasonable idea of the longer-range correlations.

For an ion whose mean electric field at distance r is $E(r)$, an approximate

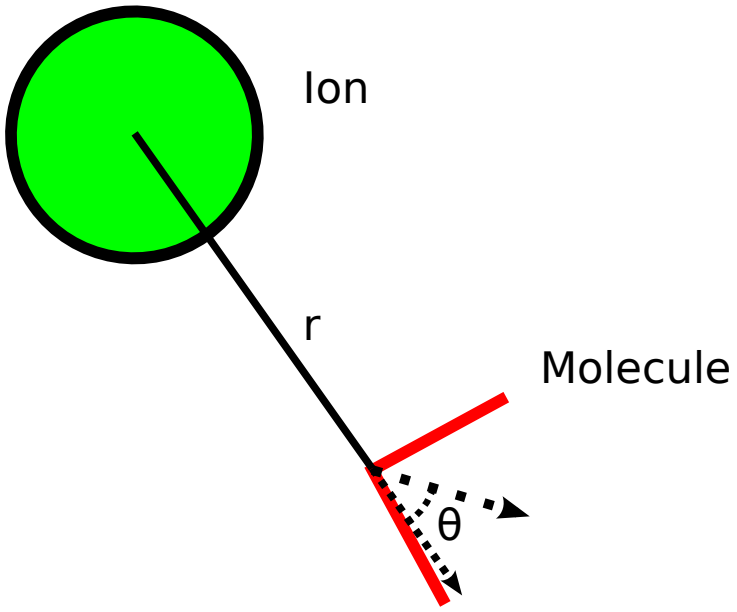

Figure 5.7: Illustration of the orientational correlation function $\langle \cos\theta \rangle (r)$: r is the separation between an ion and a water molecule, and $\cos\theta$ is the projection of the molecular dipole moment on the vector pointing from the ion to the molecule.

statistical-mechanical expression for $\langle \cos\theta \rangle (r)$ is given in Appendix C as,

$$\langle \cos\theta \rangle (r) \simeq \frac{\mu_0 E(r)}{3k_{\mathrm{B}}T}, \tag{5.48}$$

where μ_0 is the permanent dipole moment of the molecule. This will allow us to compare the ordering of water molecules by an ion to the results of D-H theory. The most important orientational correlations for describing the experimental results are those between pairs of water molecules: in the experiments we are considering, the ions are invisible. We calculated $\langle \cos\psi \rangle (r)$, the average projection of two molecular dipole moments as a function of r, the distance between them. This is illustrated in Fig. 5.8. In Sec. 5.3.4 we derive an expression for $\langle \cos\psi \rangle (r)$ within D-H theory, for comparison with the function found from simulations.

$\langle \cos\psi \rangle (r)$ is calculated in a similar way to $\langle \cos\theta \rangle (r)$: for every pair of water molecules whose separation is less than a cutoff value, the separation and projection are recorded, $\cos\psi$ is binned as a function of r and used to find the average.

By comparing $\langle \cos\psi \rangle (r)$ as calculated in a $\sim$0.32 M solution with that calculated for pure water, we can find the effect of ions on the orientational correlation of the two water molecules. To achieve this, we repeated our simulations with boxes containing 27000 molecules and no ions, and calculated $\langle \cos\psi \rangle (r)$ for pure water.

5.3.2 Ion-Ion Correlations

Fig 5.9 shows the radial distribution functions $g_{++}(r)$ and $g_{--}(r)$ from our simulations, as well as those predicted by D-H theory. The relative unlikelihood of observing a pair of ions with the same charge in close proximity is illustrated by the

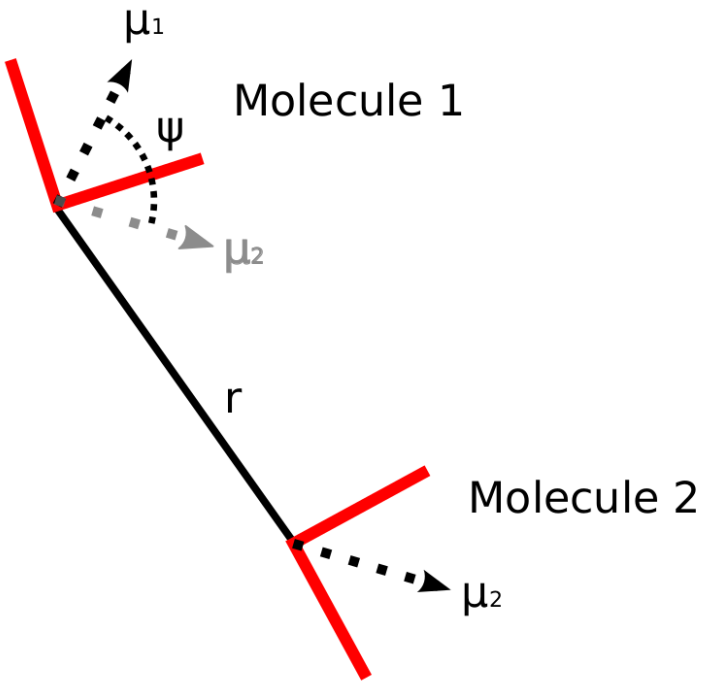

Figure 5.8: Illustration of the orientational correlation function $\langle \cos\psi \rangle (r)$: r is the distance between two water molecules, $\boldsymbol{\mu}_1$ and $\boldsymbol{\mu}_2$ are their dipole moment vectors (shown as black dotted lines) and $\cos\psi = \hat{\boldsymbol{\mu}}_1 \cdot \hat{\boldsymbol{\mu}}_2$. The dipole moment of molecule 2 has been shown in grey at the position of molecule 1 to better illustrate the angle ψ.

fact that these functions are smaller than unity over the entire range studied.

Unsurprisingly, the structure of pairs of like-charged ions is qualitatively different in the theory to that in the simulations. D-H theory misses out on the short-range structure in the RDFs, since it includes only the direct Coulomb repulsion between two like-charged ions. In reality, there will also be attractive dispersion forces and short-ranged Pauli repulsion, as well as indirect interactions mediated by the solvent.

However, the theoretical predictions are quantitatively quite good: although the structure is missed, in each case the theoretical curve follows the simulation results reasonably closely, except at very short distances. Because we are modelling the ions as point particles in D-H theory, they can approach each other infinitesimally closely, whereas in reality ions cannot approach within a hard-sphere radius. While it is possible to correct for this discrepancy by cutting off the RDFs at small r, the choice of cutoff is arbitrary, and for the sake of generality we have not done so.

The radial distribution functions $g_{\mathrm{Na^+\text{–}Cl^-}}(r)$ as given by simulation and theory are shown in Fig. 5.10. In the simulated RDF, there are two well-defined peaks which represent pairs of ions in direct contact and solvent-separated ion pairs (in which one water molecule lies between the ions) [302]. As in Sec. 4.3 we can use this RDF to calculate a potential of mean force, and then apply transition-state theory to give an upper bound to the rate of interconversion of these species, whose reciprocal gives the minimum lifetime for contact ion pairs as 24 ps, suggesting that these pairs are quite long-lived. However, the coordination number of Cl^- ions in direct contact with Na^+ is only 0.1, so that even at a concentration of 0.32 M only a small fraction of ions are paired and we need not modify the theory to account for

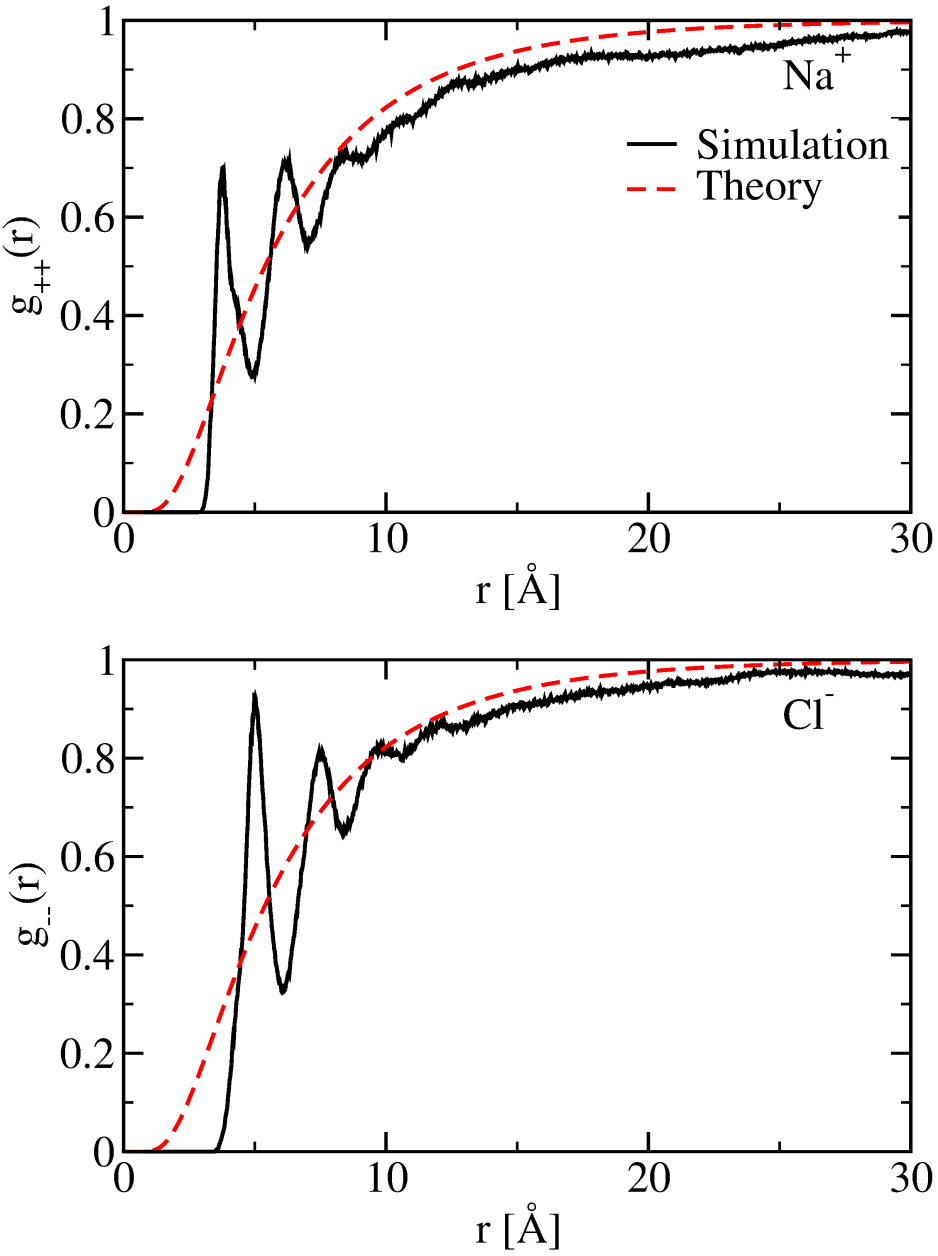

Figure 5.9: Radial distribution functions for Na^+–Na^+ (upper panel) and Cl^-–Cl^- (lower panel) ion pairs, calculated using classical MD simulations (solid black lines) and using the D-H theory result of Eqn. (5.44a) (dashed red lines). In all calculations, the temperature is 300 K.

these pairs.

In this case, the theoretical predictions are in poorer agreement with simulations: the short-range divergence of $g_{+-}(r)$ in the theory means that there are no ion-pair peaks - the function reaches its maximum at $r = 0$. In order to obtain physically meaningful results, one would need to apply a cutoff to the function at some hard-sphere radius, and there is no such cutoff at which the two RDFs would agree particularly well.

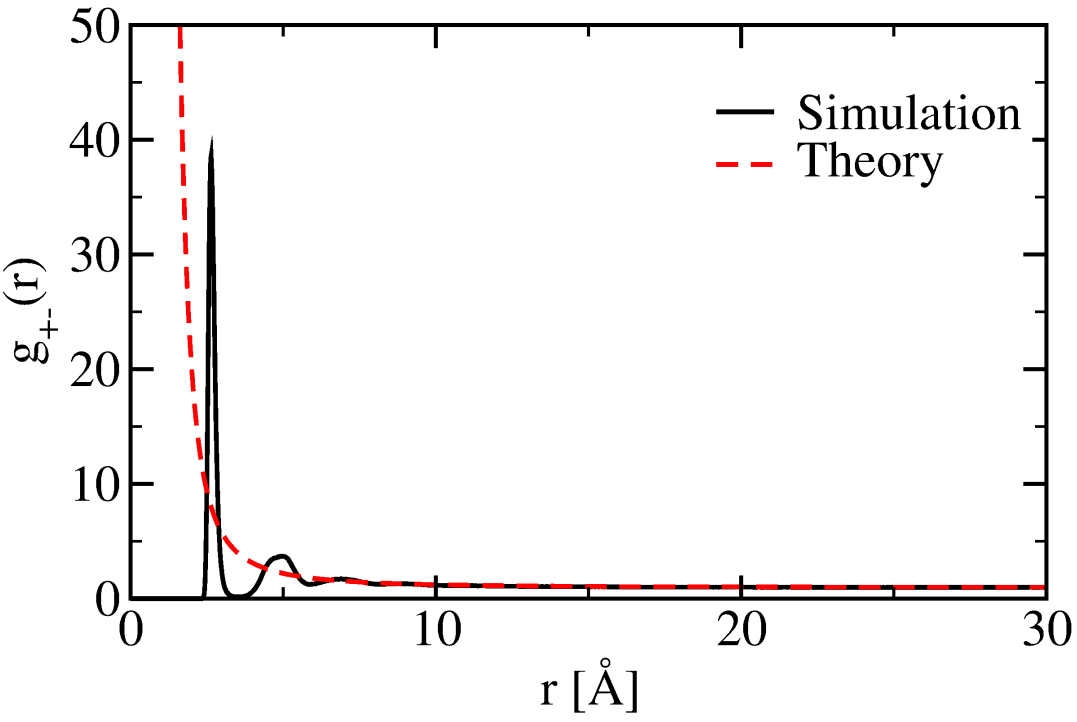

Figure 5.10: Radial distribution functions for Na^+–Cl^- ion pairs, calculated using classical MD simulations (solid black line) and using the D-H theory result of Eqn. (5.44b) (dashed red line). In both calculations, the temperature is 300 K.

In principle, we could use the calculated RDFs with Eqn. (5.32) to calculate a structure factor $S(\boldsymbol{K}, \rho)$, which we could compare with that of D-H theory. Fig. 5.11 shows the integrand of this equation,

$$s(r) = \frac{4\pi\rho}{K} r \sin(Kr) \left[g_{++}(r) + g_{--}(r) - 2g_{+-}(r) \right], \tag{5.49}$$

from our simulations, as well as the integrand of Eqn. (5.45) for comparison. We note that although our simulated integrand does not decay closely enough to zero over the distance range studied for the integral to converge, it is matched quite well by the integrand from D-H theory at large r, so that this can be used for the long-distance tail.

However, Eqn. (5.32) is a sum of two terms, both of which are very similar in magnitude but opposite in sign. In D-H theory, $S(\boldsymbol{K}, \rho = 0.32 \text{ M}) \simeq 5 \times 10^{-4}$, representing a very small relative difference between the two terms, both of which have a magnitude on the order of 1. The uncertainty in our simulation results is larger than this, and leaves us unable to find a structure factor with any confidence.

The good agreement shown in Fig. 5.11 between the decay of the two integrands to zero at long distances suggests that despite the short-range discrepancies, the long-range correlations between pairs of ions are as predicted by theory.

5.3.3 Ion-Water Correlations

The spatial correlations of water molecules by ions are shown in the ion-oxygen RDFs of Fig. 5.12. While we cannot compare these functions with D-H theory, which treats the solvent as a dielectric continuum, they will be referred to further

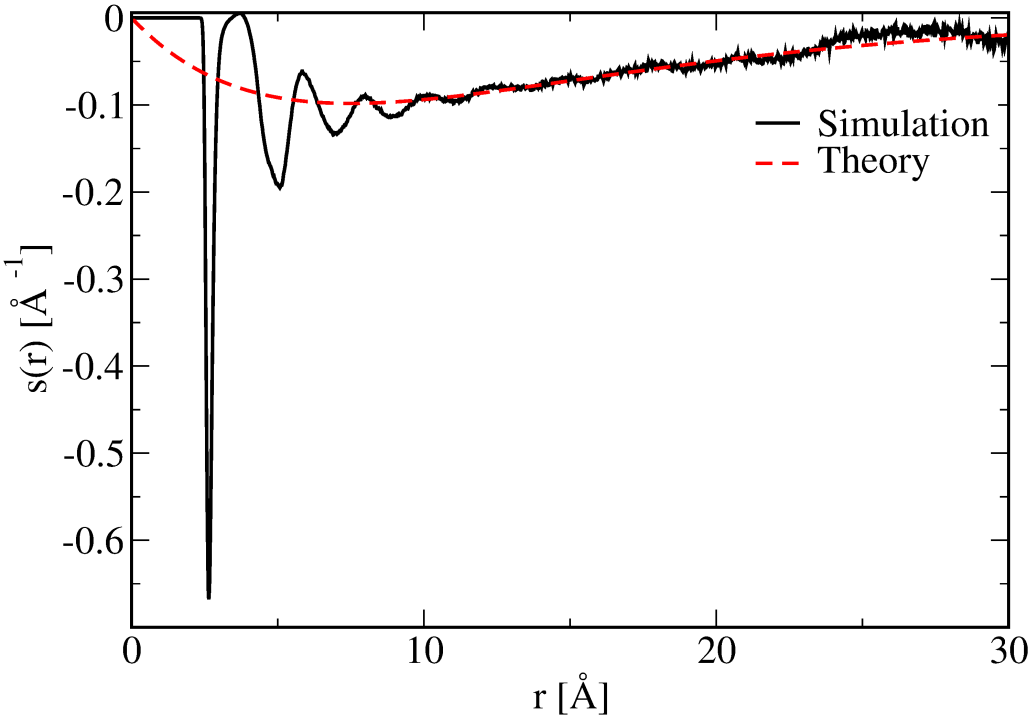

Figure 5.11: The integrand $s(r)$ that appears in Eqn. (5.32) for the structure factor, using the results of our classical MD simulations at 300 K (solid black lines) and D-H theory (dashed red lines).

on in this Chapter, and show the structure of the hydration shells surrounding these ions. For each ion we can define a hard-sphere radius as the position of the first hydration shell, which is at around 2.4 Å for Na^+ and 3.1 Å for Cl^-, giving an average hard-sphere radius of about 2.75 Å.

The orientational correlation of water molecules by the ions, as shown by $\langle \cos\theta \rangle (r)$, will also provide a test of the D-H theory's ability to describe the systems at which

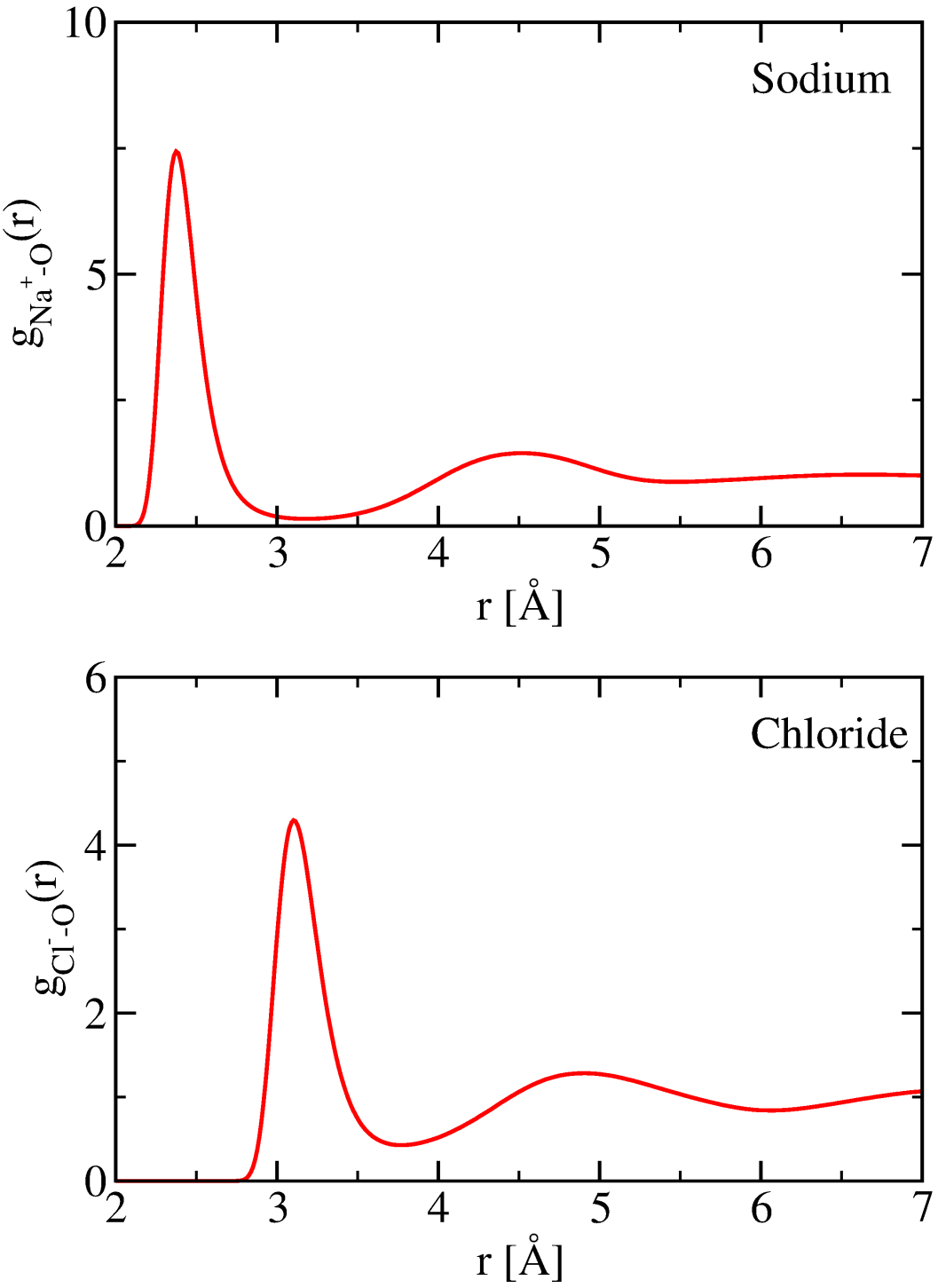

Figure 5.12: Ion-oxygen RDFs for Na^+ (top panel) and Cl^- (bottom panel) from classical MD simulations at 300 K using the SPC/E model of water.

we have looked. This correlation function is shown in Fig. 5.13, with that predicted by D-H theory using the dipole moment and permittivity of SPC/E water. Although there is disagreement at short ranges due to the fact that the theory does not account for the coordination shells of water molecules and of other ions surrounding a central ion, at larger distances the agreement is quite good.

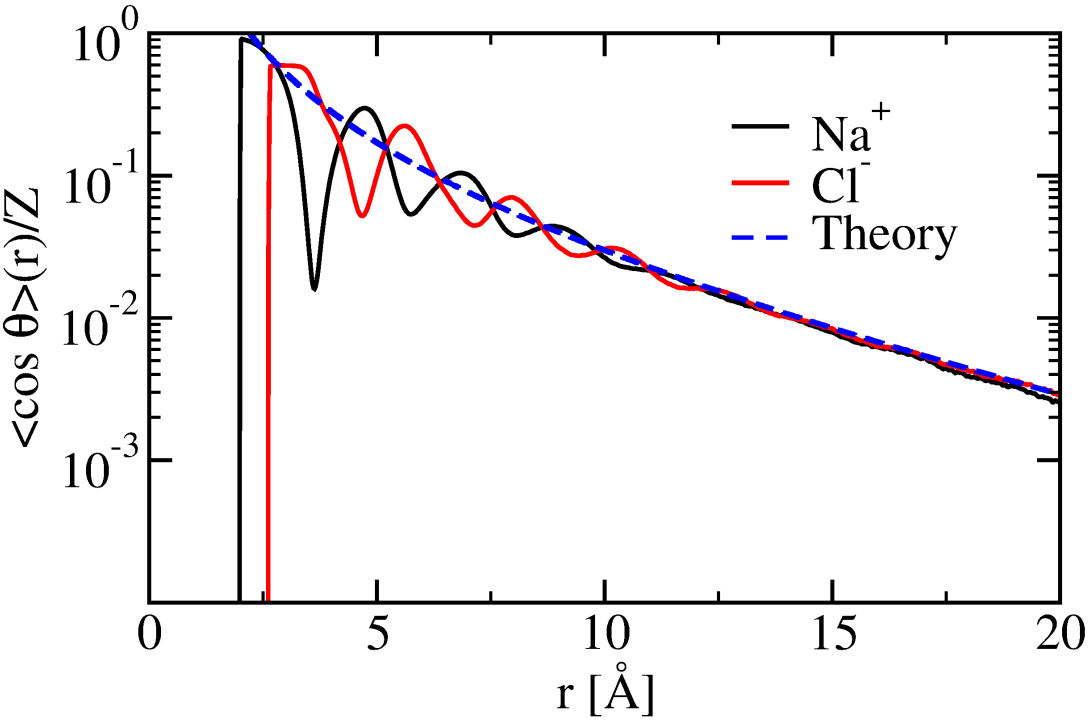

Figure 5.13: The average projection per unit charge of the dipole moment of a water molecule onto the ion-water vector in a ~ 0.32 M solution of NaCl. The solid lines show $\langle \cos\theta \rangle (r)$ for Na^+ (black line) and $-\langle \cos\theta \rangle (r)$ for Cl^- (red line), as calculated using classical MD simulations at 300 K. The blue dashed line shows the prediction of D-H theory, as in Eqn. (5.48).

The implication of these results, along with those of Sec. 5.3.2, is that D-H theory describes these solutions reasonably well in terms of long-distance correlations. Despite the qualitative success of the theory of Sec. 5.2.2 on which it is based, it cannot quantitatively account for the experimental results. A key omission of this theory is the neglect of interactions between water molecules. We look now at how well the theory can account for the orientational correlations between these molecules.

5.3.4 Water-Water Correlations

While Sections 5.3.2 and 5.3.3 show us that D-H theory can predict the mean ion-ion and ion-water interactions reasonably well at longer ranges, it is the correlations between water molecules that determine the intensity of SH scattered light. $\langle \cos\psi \rangle (r)$ is the simplest function embodying these correlations; we will now show that it is possible to derive a theoretical expression for this function, making its calculation doubly attractive.

In Appendix C.2, we show that an approximate expression for $\langle \cos\psi \rangle (r)$ is given by,

$$\langle \cos\psi \rangle (r) \simeq \left(\frac{\mu_0}{k_{\mathrm{B}} T} \right)^2 \langle \boldsymbol{E}(0) \cdot \boldsymbol{E}(r) \rangle_{\mathrm{ion}} , \tag{5.50}$$

where $\boldsymbol{E}(0)$ is the electric field at some arbitrarily chosen origin and $\boldsymbol{E}(r)$ is the field at a point which is a distance r from the origin.

The field at a point r is the superposition of Coulomb fields due to all ions in

the solution. This allows us to write,

$$\begin{aligned}\langle\cos\psi\rangle(r) &= -\left(\frac{\mu_0 f(0)}{12\pi\epsilon k_\mathrm{B}T}\right)^2 \left\langle \sum_\mu \sum_\nu Q_\mu Q_\nu \frac{\boldsymbol{r}_\mu \cdot (\boldsymbol{r}-\boldsymbol{r}_\nu)}{r_\mu^3 \left|\boldsymbol{r}-\boldsymbol{r}_\nu\right|^3} \right\rangle_\mathrm{ion} \\ &= -\left(\frac{\mu_0 f(0)}{12\pi\epsilon k_\mathrm{B}T}\right)^2 \left\langle \sum_\mu \sum_\nu Q_\mu Q_\nu \boldsymbol{\varepsilon}(\boldsymbol{r}_\mu)\cdot\boldsymbol{\varepsilon}(\boldsymbol{r}-\boldsymbol{r}_\nu) \right\rangle_\mathrm{ion}, \end{aligned} \tag{5.51}$$

where $\boldsymbol{\varepsilon}(\boldsymbol{r}) = \boldsymbol{r}/r^3$. We then split both sums up into individual sums over positive and negative ions. Assuming a 1:1 electrolyte,

$$\begin{aligned}\langle\cos\psi\rangle(r) = -\left(\frac{\mu_0 Q f(0)}{12\pi\epsilon k_\mathrm{B}T}\right)^2 \Bigg\{ &\left\langle \sum_{\mu\in+}\sum_{\nu\in+} \boldsymbol{\varepsilon}(\boldsymbol{r}_\mu)\cdot\boldsymbol{\varepsilon}(\boldsymbol{r}_\nu) \right\rangle_\mathrm{ion} + \\ &\left\langle \sum_{\mu\in-}\sum_{\nu\in-} \boldsymbol{\varepsilon}(\boldsymbol{r}_\mu)\cdot\boldsymbol{\varepsilon}(\boldsymbol{r}_\nu) \right\rangle_\mathrm{ion} - \\ &\left\langle \sum_{\mu\in+}\sum_{\nu\in-} \boldsymbol{\varepsilon}(\boldsymbol{r}_\mu)\cdot\boldsymbol{\varepsilon}(\boldsymbol{r}_\nu) \right\rangle_\mathrm{ion} - \left\langle \sum_{\mu\in-}\sum_{\nu\in+} \boldsymbol{\varepsilon}(\boldsymbol{r}_\mu)\cdot\boldsymbol{\varepsilon}(\boldsymbol{r}_\nu) \right\rangle_\mathrm{ion} \Bigg\}, \end{aligned} \tag{5.52}$$

where, for example, $\mu \in +$ indicates that the sum runs over all ions that are positively charged.

Because of the correlations between ions, terms in Eqn. (5.52) with $\mu = \nu$ must be treated differently to those with $\mu \neq \nu$, so that the sum is further split up as,

$$\left\langle \sum_{\mu\in+} \boldsymbol{\varepsilon}(\boldsymbol{r}_\mu)\cdot\boldsymbol{\varepsilon}(\boldsymbol{r}-\boldsymbol{r}_\mu) \right\rangle_\mathrm{ion} + \left\langle \sum_{\mu\in+}\sum_{\nu\neq\mu\in+} \boldsymbol{\varepsilon}(\boldsymbol{r}_\mu)\cdot\boldsymbol{\varepsilon}(\boldsymbol{r}-\boldsymbol{r}_\nu) \right\rangle_\mathrm{ion}. \tag{5.53}$$

Once again, we can replace the sums with integrals. Unlike the water molecules of Sec. 5.2.2 the ions are not uniformly distributed, which we must account for by using $\rho(\boldsymbol{r}_\mu - \boldsymbol{r}_\nu) = \rho g_{++}(\boldsymbol{r}_\mu - \boldsymbol{r}_\nu)$ for the local density of ions, where ρ is their mean density. This first average thus becomes,

$$\rho \int \mathrm{d}^3\boldsymbol{r}_1\, \boldsymbol{\varepsilon}(\boldsymbol{r}_1)\cdot\boldsymbol{\varepsilon}(\boldsymbol{r}-\boldsymbol{r}_1) + \rho^2 \int \mathrm{d}^3\boldsymbol{r}_1 \int \mathrm{d}^3\boldsymbol{r}_2\, \boldsymbol{\varepsilon}(\boldsymbol{r}_1)\cdot\boldsymbol{\varepsilon}(\boldsymbol{r}-\boldsymbol{r}_2) g_{++}(\boldsymbol{r}_1-\boldsymbol{r}_2). \tag{5.54}$$

The second average in Eqn. (5.52) must be treated in an analogous way, and the final two averages are similar but without a $\mu = \nu$ term. This allows us to write,

$$\langle \cos\psi \rangle (r) = -\rho \left(\frac{\mu_0 Q f(0)}{12\pi\epsilon k_\mathrm{B} T} \right)^2 \int \mathrm{d}^3\boldsymbol{r}_1 \int \mathrm{d}^3\boldsymbol{r}_2 \, \boldsymbol{\varepsilon}(\boldsymbol{r}_1) \cdot \boldsymbol{\varepsilon}(\boldsymbol{r} - \boldsymbol{r}_2) \left\{ 2\delta(\boldsymbol{r}_1 - \boldsymbol{r}_2) + \right.$$
$$\left. \rho \left[g_{++}(\boldsymbol{r}_1 - \boldsymbol{r}_2) + g_{--}(\boldsymbol{r}_1 - \boldsymbol{r}_2) - 2g_{+-}(\boldsymbol{r}_1 - \boldsymbol{r}_2) \right] \right\}. \quad (5.55)$$

Calling the term in braces $S(\boldsymbol{r}_1 - \boldsymbol{r}_2)$ we note from Eqn. (5.32) that it is related to the structure factor $S(\boldsymbol{K})$ by the Fourier transform $S(\boldsymbol{K}) = \int S(\boldsymbol{r}) e^{-i\boldsymbol{K}\cdot\boldsymbol{r}} \, \mathrm{d}^3\boldsymbol{r}$. Thus,

$$\langle \cos\psi \rangle (r) = -\rho \left(\frac{\mu_0 Q f(0)}{12\pi\epsilon k_\mathrm{B} T} \right)^2 \int \mathrm{d}^3\boldsymbol{r}_1 \int \mathrm{d}^3\boldsymbol{r}_2 \, \boldsymbol{\varepsilon}(\boldsymbol{r}_1) \cdot \boldsymbol{\varepsilon}(\boldsymbol{r} - \boldsymbol{r}_2) S(\boldsymbol{r}_1 - \boldsymbol{r}_2). \quad (5.56)$$

In order to make this double integral more tractable, we use the Fourier convolution theorem [303] to write,

$$\langle \cos\psi \rangle (r) = -\rho \left(\frac{\mu_0 Q f(0)}{12\pi\epsilon k_\mathrm{B} T} \right)^2 \frac{1}{(2\pi)^3} \int \boldsymbol{\varepsilon}(\boldsymbol{K}) \cdot \boldsymbol{\varepsilon}(\boldsymbol{K}) S(\boldsymbol{K}) e^{i\boldsymbol{K}\cdot\boldsymbol{r}} \, \mathrm{d}^3\boldsymbol{K}, \quad (5.57)$$

where $\boldsymbol{\varepsilon}(\boldsymbol{K}) = \int \boldsymbol{\varepsilon}(\boldsymbol{r}) e^{-i\boldsymbol{K}\cdot\boldsymbol{r}} \, \mathrm{d}^3\boldsymbol{r}$ is the Fourier transform of $\boldsymbol{\varepsilon}(\boldsymbol{r})$. In Appendix C.3 we show that $\boldsymbol{\varepsilon}(\boldsymbol{K}) = -4\pi i \boldsymbol{e}_K / K$, with $\boldsymbol{e}_K$ the unit vector in the direction of $\boldsymbol{K}$, so that the correlation function can be written in terms of the structure factor,

$$\langle \cos\psi \rangle (r) = \rho \left(\frac{\mu_0 Q f(0)}{3\epsilon k_\mathrm{B} T} \right)^2 \frac{1}{(2\pi)^3} \int \frac{S(\boldsymbol{K})}{K^2} e^{i\boldsymbol{K}\cdot\boldsymbol{r}} \, \mathrm{d}^3\boldsymbol{K}. \quad (5.58)$$

If $S(\boldsymbol{K})$ depends only on the magnitude of $\boldsymbol{K}$ then this can be simplified to,

$$\langle \cos\psi \rangle (r) = \frac{\rho}{2} \left(\frac{\mu_0 Q f(0)}{3\pi\epsilon k_\mathrm{B} T} \right)^2 \int_0^\infty \frac{S(K)}{Kr} \sin(Kr) \, \mathrm{d}K. \quad (5.59)$$

Inserting the structure factor of Eqn. (5.45) we find the D-H prediction for our correlation function,

$$\langle \cos\psi \rangle (r) = \frac{\rho}{2\pi} \left(\frac{\mu_0 Q f(0)}{3\epsilon k_\mathrm{B} T} \right)^2 \frac{e^{-\kappa_\mathrm{D} r}}{r}. \quad (5.60)$$

At small concentrations $\langle \cos\psi \rangle (r)$ increases with ρ, as the addition of more ions means more ordering of molecular dipoles. However, at large concentrations the $e^{-\kappa_{\mathrm{D}} r}$ term will dominate, meaning that $\langle \cos\psi \rangle (r)$ will decrease with increasing ρ. The size of the oppositely charged atmosphere surrounding an ion (illustrated by its radius κ_{D}^{-1}) will decrease with increasing ion concentration, reflecting a greater degree of screening, and the electric field will change more rapidly with distance, giving faster decorrelation.

Eqn. (5.60) has the disadvantage that it diverges as r tends to zero. The reason for this is that we have considered a solution in which the entire volume is filled with water molecules. $\langle \cos\psi \rangle (0) \simeq \left(\frac{\mu_0}{3k_{\mathrm{B}}T} \right)^2 \langle \boldsymbol{E}(0) \cdot \boldsymbol{E}(0) \rangle$ is thus an average over all space of the mean squared electric field, and this includes points which are infinitesimally close to an ion, where the field is infinite.

This is clearly unphysical: $\langle \cos\psi \rangle (0)$ is the average dot product of the dipole moments of two water molecules occupying the same position; this is perfectly permissible because the molecules are non-interacting within the theory. Physically we would expect this value to be less than unity (a value of 1 would indicate that two dipoles at the same position always point in the same direction, with no fluctuations).

We can improve upon the derivation in this Section by excluding from the integral in Eqn. (5.56) any volume where the water molecules are within a distance a of the ion. This is equivalent to adding a hard-sphere repulsive interaction between the ions and water molecules, and will mean that water molecules are not found at positions with infinite electric fields, giving a finite value for $\langle \cos\psi \rangle (0)$. To exclude

this volume we make the replacement,

$$\boldsymbol{\varepsilon}(\boldsymbol{r}) \rightarrow \boldsymbol{\varepsilon}(\boldsymbol{r})\Theta\left[r-a\right], \tag{5.61}$$

where $\Theta\left[r-a\right]$ is the Heaviside step function, which will be zero when the distance r is less than a, and one otherwise. Recalculating the Fourier transform of $\boldsymbol{\varepsilon}(\boldsymbol{r})$ using the method of Appendix C.3 we find,

$$\boldsymbol{\varepsilon}(\boldsymbol{K}) = -\frac{4\pi i \sin\left(Ka\right)}{K^2 a}\boldsymbol{e}_K. \tag{5.62}$$

Inserting this expression into Eqn. (5.57) and using the D-H structure factor,[7]

$$\left\langle \cos\psi \right\rangle_{\mathrm{HS}}(r) = \rho\left(\frac{\mu_0 Q f(0)}{3\pi\epsilon k_{\mathrm{B}}T}\right)^2 \int_0^\infty \frac{\sin^2\left(Ka\right)\sin\left(Kr\right)}{Ka^2 r\left(K^2+\kappa_{\mathrm{D}}^2\right)}\,\mathrm{d}K. \tag{5.63}$$

As described in Appendix C.4, this integral can be evaluated using the residue theorem to give,

$$\left\langle \cos\psi \right\rangle_{\mathrm{HS}}(r) = \rho\left(\frac{\mu_0 Q f(0)}{3a\varepsilon\kappa_{\mathrm{D}}k_{\mathrm{B}}T}\right)^2 \frac{1}{8\pi r}\times \\ \left(1-2e^{-\kappa_{\mathrm{D}}r}+e^{-\kappa_{\mathrm{D}}(2a+r)}-\mathrm{sgn}\left[2a-r\right]\left\{e^{-\kappa_{\mathrm{D}}|2a-r|}-1\right\}\right), \tag{5.64}$$

where $\mathrm{sgn}\left[x\right]$ is 1 if $x>0$ and -1 if $x<0$. The $r\rightarrow 0$ limit of $\left\langle \cos\psi \right\rangle_{\mathrm{HS}}(r)$ is,

$$\left\langle \cos\psi \right\rangle_{\mathrm{HS}}(r\rightarrow 0) = \rho\left(\frac{Qf(0)}{2a\varepsilon}\right)^2 \frac{1}{\pi\kappa_{\mathrm{D}}}\left[1-e^{-2\kappa_{\mathrm{D}}a}\right], \tag{5.65}$$

[7]Since we are now no longer averaging over the entire system volume, more properly we should multiply Eqn. (5.63) by a correction factor to account for the excluded volume due to the ions. However, for the ion concentration and radius we are considering, this correction increases $\left\langle \cos\psi \right\rangle_{\mathrm{HS}}(r)$ by slightly less than 1%, and so has been omitted for simplicity.

and at long distances,

$$\langle \cos\psi \rangle_{\mathrm{HS}}(r) = \frac{\sinh^2(\kappa_{\mathrm{D}} a)}{(\kappa_{\mathrm{D}} a)^2} \langle \cos\psi \rangle (r) \tag{5.66}$$

$$\geq \langle \cos\psi \rangle (r), \tag{5.67}$$

where the radius a that we will use is such that $\frac{\sinh^2(\kappa_{\mathrm{D}} a)}{(\kappa_{\mathrm{D}} a)^2} \simeq 1 + \frac{(\kappa_{\mathrm{D}} a)^2}{3}$.

Fig. 5.14 compares the orientational correlation functions $\langle \cos\psi \rangle (r)$ of Eqn. (5.60) and $\langle \cos\psi \rangle_{\mathrm{HS}}(r)$ of Eqn. (5.64) using a hard-sphere radius of $a = 2.75$ Å, which is the average of the ion-oxygen radii of $g_{\mathrm{Na^+\text{–}O}}(r)$ and $g_{\mathrm{Cl^-\text{–}O}}(r)$. Eqn. (5.64) predicts that $\langle \cos\psi \rangle (0) \simeq 0.02$, indicating a very small degree of correlation between water molecules at the same point in space, or equivalently a very weak local electric field. We will compare both of these functions to the results of our simulations in order to appraise the quality of each.

Firstly, we compare in Fig. 5.15 the correlation function $\langle \cos\psi \rangle (r)$ for simulations of ~ 0.32 M NaCl solution and of pure water. As seen in the top panel of this Figure, the two results appear to be very similar when compared over the entire length range. However, the bottom panel shows the long-distance tails of both of these functions, where we see that correlations at these distances are much larger for the solution: after 10 Å, $\langle \cos\psi \rangle (r)$ for pure water is oscillating around zero, whereas for aqueous NaCl this function has not yet decayed to zero. We thus see that the ions have induced long-distance correlations that are not present in the pure solvent, and which are the origin of the SHS signal.

Next, we wish to compare our simulation results to the theoretical results discussed in this Section. Fig. 5.16 shows $\langle \cos\psi \rangle (r)$ from simulations of NaCl solutions

and from the D-H theoretical results, both with point charges and with hard spheres. At short ranges (below about 10 Å), both theories agree quite poorly with the simulated results, which show several peaks and also take negative values between these peaks. The theoretical results not only fail to capture the peaks, but are positive for all values of r.

The upper panel of Fig. 5.16 appears to be most important in determining why D-H theory fails to quantitatively account for the results of the SHS experiments;

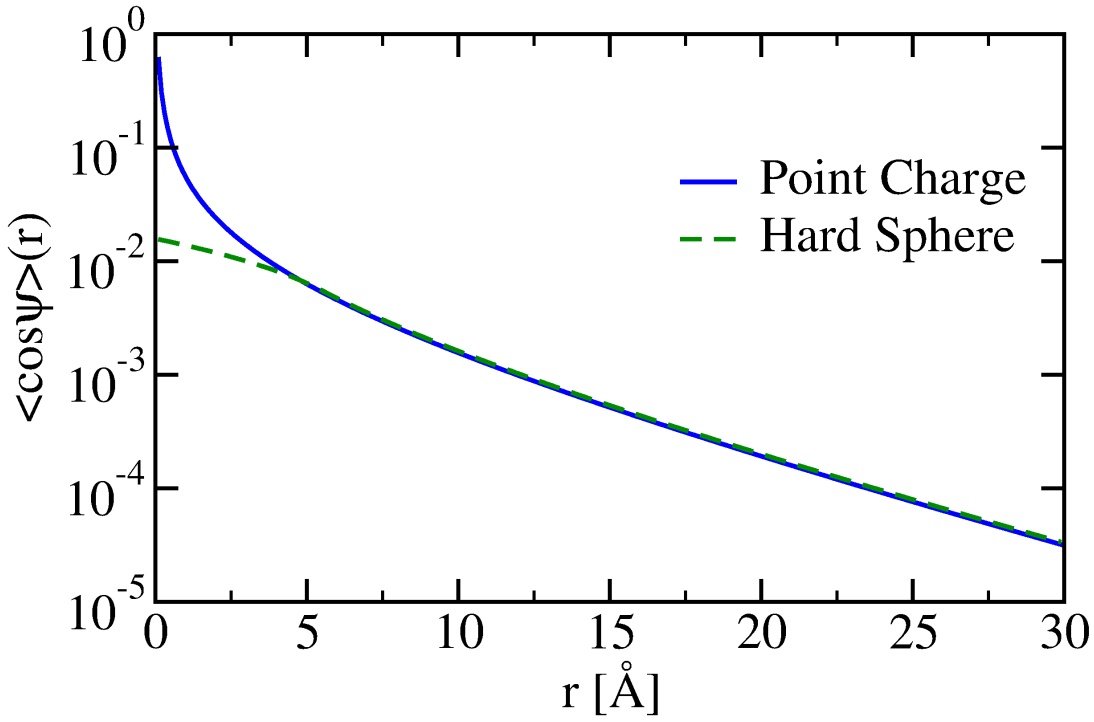

Figure 5.14: Orientational correlation function $\langle \cos\psi \rangle (r)$ as predicted by the point-charge theory of Eqn. (5.60) (solid blue line) and the hard-sphere theory of Eqn. (5.64). The physical parameters used were those appropriate to a ~ 0.32 M solution of NaCl in SPC/E water at 300 K.

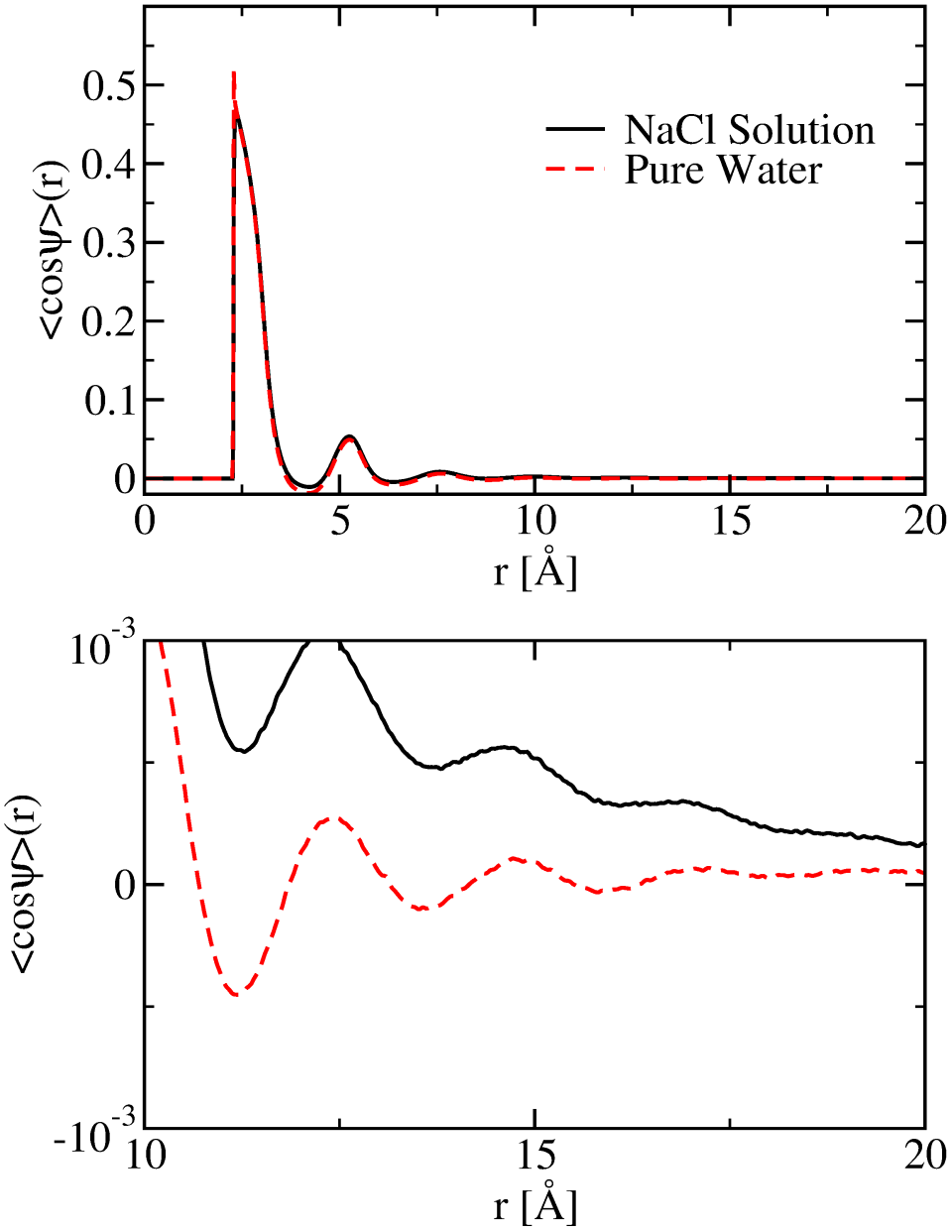

Figure 5.15: Orientational correlation function $\langle \cos \psi \rangle (r)$ for a $\sim$ 0.32 M NaCl solution (solid black curve) and for pure water (dashed red curve) as obtained from MD simulations at 300 K. In the bottom panel, the axes are zoomed in to show the long-ranged correlations between water molecules.

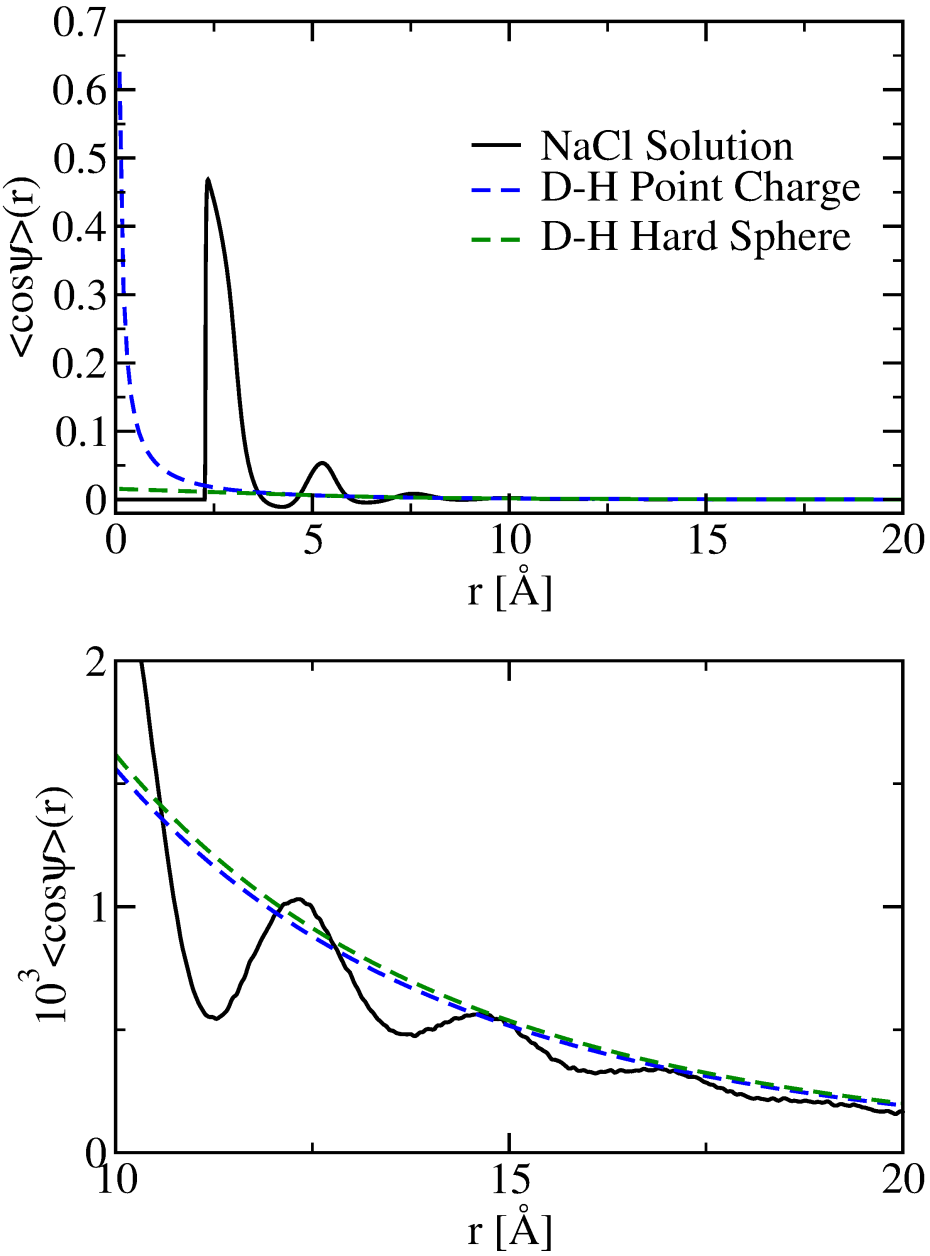

Figure 5.16: Orientational correlation function $\langle \cos\psi \rangle (r)$ for a $\sim$ 0.32 M NaCl solution (solid black curve) as obtained from MD simulations at 300 K, compared with the predictions of D-H theory using point charges (dashed blue curve) and hard spheres (dashed green curve) to represent the ions. In the bottom panel, the axes are zoomed in to show the long-ranged correlations between water molecules.

the long-distance decay of the correlation function is reasonably well captured (and the long-distance correlations in the D-H theory give rise to a signal), and it is the behaviour at short distances that compares unfavourably between the two (since within D-H theory the local electric field at the position of a water molecule does not include the field due to the other water molecules). This supports our suggestion that D-H theory fails to predict the correct plateau intensity because it ignores the short-range correlations between water molecules: the complex H-bonding network must be taken into account to truly explain the experimentally observed SHS intensity.

5.4 Conclusions and Future Work

We have looked in this Chapter at second harmonic generation scattering by an ionic solution: the intensity of scattered light was found to increase linearly with ion concentration at low concentrations, and to level off at high concentrations, with the intensity being independent of the identities of ions. Using the D-H theory we were able to account qualitatively for these observations; the linear increase is due to the fact that ions separated by large distances will orient molecules independently, and the plateau is caused by the increased screening of each ion's charge as the number of ions surrounding it increases. The ion-nonspecificity is a consequence of the fact that the contribution of molecules to the intensity increases with their distance from an ion.

However, D-H theory fails to give the correct signal intensity at the plateau. By calculating a number of correlation functions, we found that this theory is quite

successful at predicting long-range correlations, and that it is the short-ranged behaviour for which its predictions are unsuccessful. The assumption that water molecules do not interact with each other is clearly invalid, since water molecules form hydrogen-bonding networks and the orientation of a water molecule will be determined by both the ions and the local structure of the network.

This leaves several avenues open for further work. Among these, perhaps the three most important are:

- The calculation of the SHS intensity from the results of the simulations would give an idea of how close these simulations are to the situation observed in experiments. Work is currently underway by members of the Ceriotti group to implement these calculations.

- The significant isotope effect observed when H_2O is replaced by D_2O as the solvent is a sign that nuclear quantum effects must be taken into account. By re-running the simulations of this chapter with PIMD, we will be able to find the extent to which quantum mechanics is responsible for these results. For example, the change in SHS intensity on quantization will be particularly interesting, as will the orientational correlation function $\langle \cos \psi \rangle (r)$.

- An improved theory for SHS from ionic solutions would take into account the interactions between water molecules. The theory derived in Sec. 5.2.2 is only a mean-field approximation, and an improvement on this would very likely be much more complicated, but well worth exploring.

Chapter 6

Nuclear Quantum Effects in Water Jumps[1]

6.1 Introduction

6.1.1 Water Reorientation Dynamics

In this Chapter we return to the dynamics of water molecules, considering the mechanism by which they reorient. Such motion is key in the transport of protons in liquid water [304, 305] (in which the rate-limiting step is the breaking of hydrogen bonds), and in protein folding and binding [306, 307]. We will look at molecular rotations, as opposed to the translations with which we were concerned in Chapter 4, but in fact the two are not independent. As we shall see, the exchange of hydrogen-bond acceptors in liquid water, which facilitates their diffusion, occurs via angular jumps of the donor [98, 308]. In addition, within hydrodynamic theory the translational and rotational diffusion constants are both inversely proportional to the viscosity of the medium [309], providing a relation between the two types of

[1] The work described in this chapter was carried out in collaboration with members of the Laage and Hynes groups.

motion.

Water reorientation can be described by the orientational correlation function [310, 311],

$$C_l(t) = \langle P_l \left[\boldsymbol{e}_{\mathrm{OH}}(t) \cdot \boldsymbol{e}_{\mathrm{OH}}(0) \right] \rangle \,, \tag{6.1}$$

where $P_l\,[x]$ is the l^{th} order Legendre polynomial and $\boldsymbol{e}_{\mathrm{OH}}(t)$ is a unit vector in the direction of an O–H bond at time t. By fitting the long-time decay of these functions to the exponential form $C_l(t) \simeq Ae^{-t/\tau_l}$ one can extract the l^{th}-order relaxation time τ_l.

The second-order relaxation time τ_2 can be measured by fluorescence depolarization experiments [312, 313]. In such an experiment, femtosecond laser pulses are incident upon a sample, with a pump beam exciting vibrational modes; a second beam (the probe), polarized at 45° to the original, is used to produce an absorption spectrum.

The component of the probe polarized parallel to the pump gives the parallel absorption $\Delta\alpha_{\parallel}(t)$, with t the time delay between pump and probe, and the perpendicularly polarized component gives the perpendicular absorption $\Delta\alpha_{\perp}(t)$. These two components can be combined to give the anisotropy,

$$R(t) = \frac{\Delta\alpha_{\parallel}(t) - \Delta\alpha_{\perp}(t)}{\Delta\alpha_{\parallel}(t) + 2\Delta\alpha_{\perp}(t)}. \tag{6.2}$$

$R(t)$ measures the extent to which the vibrationally excited bonds have rotated; that is, the closer a bond is to its initial orientation, the greater the signal will be in the direction of the pump pulse, while being less in perpendicular directions, and the larger the numerator in Eqn. (6.2). The denominator is not affected by polarization,

and simply provides a normalization. The anisotropy is related to the second-order orientational correlation function by $R(t) \simeq \frac{2}{5}C_2(t)$ [312, 314], so that its long-time exponential decay gives τ_2.

Other methods for measuring second-order relaxation times include QENS, in which relaxation times are found by fitting to neutron scattering cross-sections [315], and NMR, in which the spin-lattice relaxation time is proportional to the correlation time of the function $\langle P_2 \left[\boldsymbol{e}_{\mathrm{HH}}(t) \cdot \boldsymbol{e}_{\mathrm{HH}}(0) \right] \rangle$, with $\boldsymbol{e}_{\mathrm{HH}}(t)$ the unit vector between the two H atoms of a water molecule at time t.

The first-order relaxation time τ_1 can be approximated using dielectric relaxation [316–318]. In THz spectroscopy, the reflection of light from a system is used to calculate a complex dielectric function $\hat{\varepsilon}(\omega)$ of the frequency of light ω. $\hat{\varepsilon}(\omega)$ is fitted to the form,

$$\hat{\varepsilon}(\omega) = \varepsilon_\infty + \frac{\varepsilon_s - \varepsilon_I}{1 + \mathrm{i}\omega\tau_{\mathrm{D}}} + \frac{\varepsilon_I - \varepsilon_\infty}{1 + \mathrm{i}\omega\tau'}, \tag{6.3}$$

where ε_s is the static dielectric constant, ε_∞ the infinite-frequency dielectric constant, and if the two Lorentzians are suitably separated ε_I is the intermediate dielectric constant between these regions [316]. The longer relaxation time $\tau_{\mathrm{D}} \gg \tau'$ can thus be extracted. This so-called Debye relaxation time characterizes the long-time decay of the time correlation function $\langle P_1 \left[\boldsymbol{M}(t) \cdot \boldsymbol{M}(0) \right] \rangle \simeq A e^{-t/\tau_{\mathrm{D}}}$, where $\boldsymbol{M}(t)$ is the total dipole moment of the system at time t [71].

Because $\boldsymbol{M}(t)$ is a property of the entire system, rather than of a single molecule, this is not in the form of Eqn. (6.1), and $\tau_{\mathrm{D}} \neq \tau_1$. However, an approximate relation

between the two is given by continuum electrostatics [316],

$$\tau_1 \simeq \frac{2\varepsilon_0 + \varepsilon_\infty}{3\varepsilon_0}\tau_{\mathrm{D}}. \tag{6.4}$$

At the present time, only τ_2 can be accurately measured experimentally. This is unfortunate because, as we will describe shortly, the ratios between different relaxation times would give some insight into the mechanism of reorientation. However, in an atomistic simulation any τ_l can be calculated. The relaxation times τ_1 and τ_2 have been extensively computed using classical simulations of various water models, for pure water [3,4,98,308,319–322], ionic solutions [323–325], and biochemical systems [326–329]. Quantum-mechanical simulations have also been used [28,31,32,52]: the disruption of the hydrogen-bond network by quantum fluctuations has been shown to lead to a decrease in the τ_l times.

6.1.2 Water Jumps

For many decades, the prevailing model for water reorientation was that of Debye [330], in which molecules undergo an angular Brownian motion comprising infinitesimally small, uncorrelated rotations. As shown in Appendix D, this picture allows the relaxation times τ_l to be written in terms of a rotational diffusion constant D_{R},

$$\tau_l = \frac{1}{D_{\mathrm{R}} l(l+1)}. \tag{6.5}$$

Despite having been used in analyzing the results of experiments [315,331,332], there are several pieces of evidence that the mechanism of water reorientation is not simply diffusive. In particular:

- Using Eqn. (6.5) gives the ratio between two relaxation times as $\tau_l/\tau_m = \frac{m(m+1)}{l(l+1)}$. For example, τ_1/τ_2 would be equal to 3. Although experiments do not give access to this ratio, it can be calculated by atomistic simulation, in which values between 2.0 and 2.9 are found [3, 98, 319–322, 333]. In fact, as early as 1971 Rahman and Stillinger attributed a ratio of $\tau_1/\tau_2 \simeq 2.7$ to the reorientation of water by stochastic jumps of finite size, as opposed to the infinitesimal jumps in the Debye model [3].

- Using a rotational diffusion constant calculated from the results of simulations, it is possible to use Eqn. (6.5) to obtain a value of τ_2 that can be compared with experiments. However, such comparisons have been unsatisfactory; the diffusion constant of Ref. [333] leads to a value of τ_2 that is an order of magnitude smaller than the experimental value [98].

An alternative water reorientation mechanism was suggested recently by Laage and Hynes [98, 308]: rather than continuous motion, molecules change between hydrogen bond acceptors by sudden "jumps".[2] Indeed, by taking a simulated box of water molecules and considering the projection of an O–H bond onto a space-fixed axis, one can see that it does indeed undergo sudden, sharp jumps [98, 334]. This result is reproduced in Fig. 6.1 for the q-TIP4P/F water model.

In detail, the water jump mechanism proceeds as follows [308]: firstly, fluctu-

[2] A similar mechanism involving large angular jumps was suggested by O'Reilly in 1974 [334], in which these jumps were due to hard-sphere collisions between molecules. As described further on in this Chapter, however, the mechanism of Laage and Hynes has garnered significant evidence from experiments and simulations.

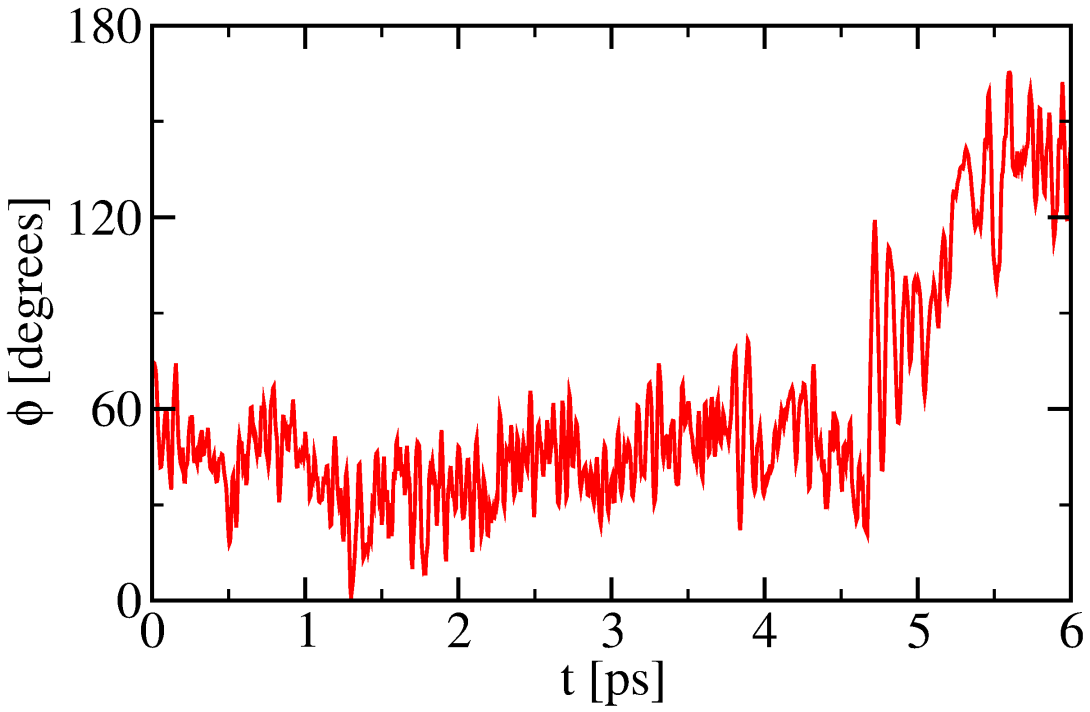

Figure 6.1: Time-evolution of ϕ, the angle between the centroid of an O–H bond vector and an arbitrary axis, during a TRPMD simulation. A large-angle jump occurs at around 4.7 ps. Such jumps have been pointed out in Refs. [98, 334, 335].

ations in the environment surrounding a molecule cause one of its hydrogen bond donors to move away, while a molecule from its second shell moves towards it. When these two molecules are equidistant from the central molecule, the hydrogen bonding O–H quickly reorients to make the incoming molecule the hydrogen bond acceptor. Following this, the outgoing molecule continues on to the second hydration shell and the incoming molecule enters the first shell.

Within this model, expressions can be derived for the relaxation times. The

reorientation of hydrogen-bonding O–H bonds is due to two processes:

1. The first of these is the jumping of O–H bonds between hydrogen bond acceptors. The relaxation times τ_l for molecules reorienting via large-angle jumps are based on Ivanov's expression for a molecule reorienting by large-amplitude jumps [336],

$$\tau_l^{\text{jump}} = \tau_0 \left[1 - \frac{1}{2l+1} \frac{\sin\left([2l+1] \frac{\Delta\theta}{2} \right)}{\sin\left(\frac{\Delta\theta}{2} \right)} \right]^{-1}, \tag{6.6}$$

   with τ_0 the average time between jumps and $\Delta\theta$ their angular amplitude. τ_l^{jump} describes the exponential decay of $\langle P_l \left[\tilde{\boldsymbol{e}}_{\text{OH}}(t) \cdot \tilde{\boldsymbol{e}}_{\text{OH}}(0) \right] \rangle$, with $\tilde{\boldsymbol{e}}_{\text{OH}}(t)$ the unit O–H vector in a time-dependent coordinate system defined by the local O$\cdots$O vectors.

2. In between jumps, the O–H bonds retain their own orientations with respect to this local coordinate system. The O$\cdots$O vectors defining the local system do not, however, retain their orientation with respect to a system defined by the laboratory, so that the O–H bond will reorient even when not jumping. This reorientation is characterized by relaxation times τ_l^{frame}, which describe the exponential decay of $\langle P_l \left[\boldsymbol{e}_{\text{OO}}(t) \cdot \boldsymbol{e}_{\text{OO}}(0) \right] \rangle$, with $\boldsymbol{e}_{\text{OO}}(t)$ the unit O$\cdots$O vector at time t.

   This frame reorientation is described quite well by the Debye diffusive model up to $l = 3$ [98,308], and has a longer timescale than the water jumps: $\tau_l^{\text{jump}} \ll \tau_l^{\text{frame}}$.

Both of these reorientation processes are combined in an "extended jump model" (EJM). Since the two processes occur independently, the time correlation function

$C_l(t)$ is the product of two functions, one due to hydrogen bond jumps with relaxation time τ_l^{jump} and one due to frame reorientation with relaxation time τ_l^{frame}. The product function thus has a decay time whose reciprocal, $1/\tau_l$, is equal to $1/\tau_l^{\text{jump}} + 1/\tau_l^{\text{frame}}$. Explicitly this is,

$$\frac{1}{\tau_l} = \frac{1}{\tau_0}\left[1 - \frac{1}{2l+1}\frac{\sin\left([2l+1]\frac{\Delta\theta}{2}\right)}{\sin\left(\frac{\Delta\theta}{2}\right)}\right] + D_{\text{R}}l(l+1), \tag{6.7}$$

with D_{R} the rotational diffusion constant for the O$\cdots$O vectors.

Since the only relaxation time that can be measured directly in an experiment is τ_2, this alone cannot give any evidence for or against the angular jump mechanism. The interpretation of QENS results, however, provides some backing for this model of water reorientation: when the Debye model is used to obtain τ_1 and τ_2 from the results of QENS experiments [315], the values obtained are about twice as large as those found by other methods [337]. If the EJM is used to fit the QENS spectra instead, then the agreement with the τ_l from other sources is much better [337].

Even more direct evidence for the operation of the EJM is given by 2D-IR spectroscopy [338]: by developing a frequency-dependent version of the extended jump model, it was shown that the frequency-dependence of the 2-dimensional anisotropy obtained from these spectra could only be explained by the occurrence of angular jumps. The EJM has also been used successfully to describe the 2D-IR spectra of water in the first hydration shell of the BF_4^- [228] and ClO_4^- [230] ions.

These jumps are by now well-established in the results of both simulations and experiments. In this Chapter, we will be concerned with the effect of quantum fluctuations on the dynamics of the angular jump mechanism, as embodied in the

effects on the parameters τ_0, $\Delta\theta$ and D_R. We will begin by describing a further extension to the extended jump model that takes into account the distribution of jump angles, allowing us to find these three parameters by fitting calculated τ_l times to the model.

6.2 Including the Distribution of Jump Angles

As described in Sec. 6.1.1, the relaxation times τ_l are readily available from the results of atomistic simulations. A reasonable way to gauge the effects of quantum mechanics on the water jump reaction is therefore to calculate a few of these times. By fitting them to the extended jump model, we can obtain the three model parameters: the jump time τ_0, jump angle $\Delta\theta$ and the rotational diffusion constant D_R for O$\cdots$O reorientation. This fitting will be especially useful when calculating the effect of quantum fluctuations, since it is much easier to calculate the τ_l values and find the three parameters by fitting than it is to calculate these parameters directly from the results of TRPMD simulations.

We began by running classical simulations on 20 boxes containing 216 q-TIP4P/F water molecules at the experimental density, each of which had been equilibrated at 298 K. These systems were evolved at constant energy for 500 ps, and the results used to calculate the first seven $C_l(t)$ time correlation functions, from which the first seven τ_l times could be calculated by fitting the functions to exponential decays. Fig. 6.2 shows the average correlation functions. We note that there are three regions in each case: for short times there is a non-exponential decay due to librations [98], at

intermediate times the function decays exponentially and at longer times the decay becomes too noisy to fit. It is to the intermediate region that we have fitted the exponential decay.

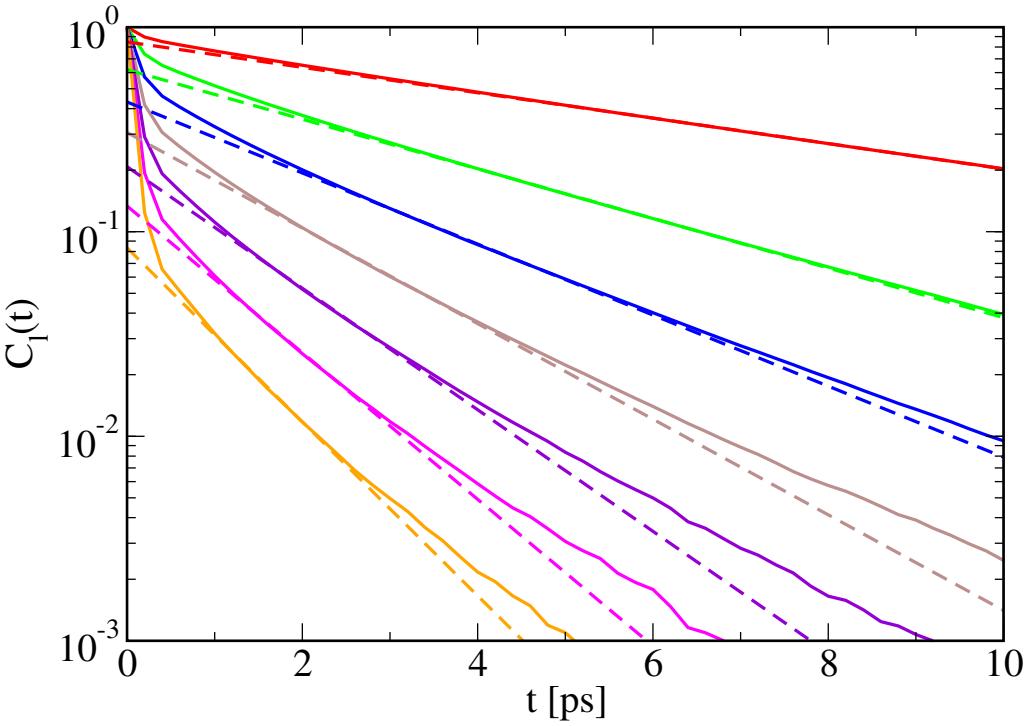

Figure 6.2: The first seven Legendre correlation functions $C_l(t)$ as defined in Eqn. (6.1), calculated using classical MD simulations in the NVE ensemble. The solid coloured lines show the functions calculated from simulation results, and the dashed coloured lines show the corresponding fits to an exponential decay, $C_l(t) \simeq Ae^{-t/\tau_l}$.

The resulting relaxation times, along with their best-fit to Eqn. (6.7), are shown

in Fig. 6.3.

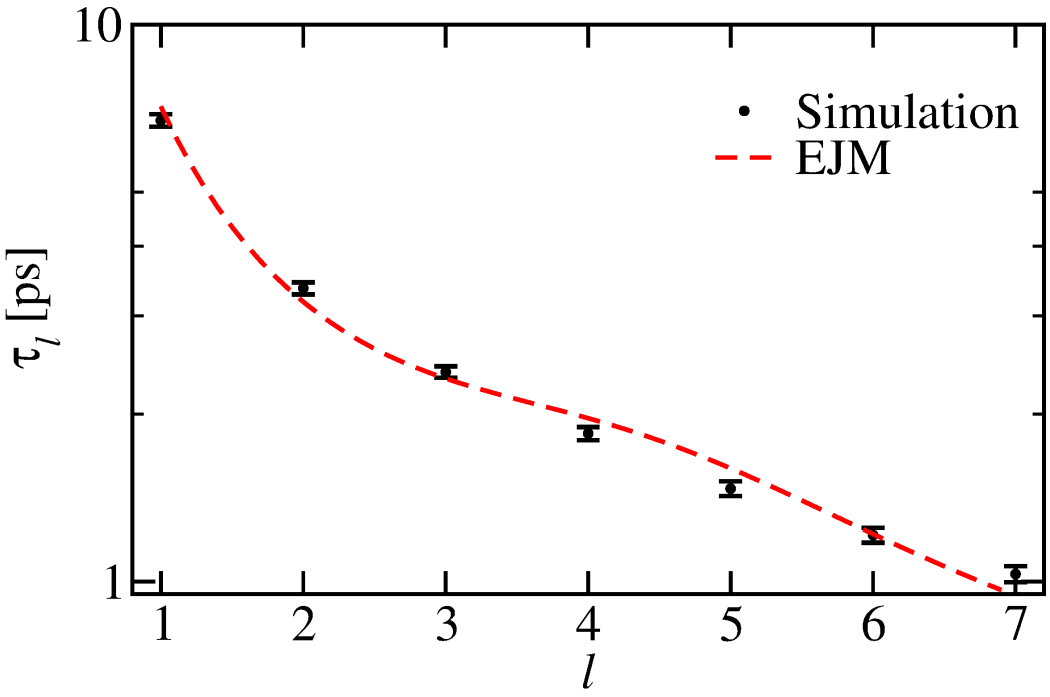

Figure 6.3: Fitting to the EJM of Eqn. (6.7). Black circles show τ_l simulation times as calculated using classical MD simulations in the NVE ensemble. The dashed red line gives the best fit of the EJM to these data.

The EJM fits these data quite well, and we can extract from this fit a jump time $\tau_0 = (4.8 \pm 0.2)$ ps, a rotational diffusion constant $D_{\mathrm{R}} = (14.9 \pm 0.4)$ ns^{-1} and an average jump angle $\Delta\theta = (79 \pm 2)^\circ$. However, to test that these results are meaningful they should be compared with values calculated directly from simulations.

To find the average jump angle $\Delta\theta$, we used the jump angle distribution $P(\theta)$, defined such that $P(\theta)\,\mathrm{d}\theta$ is the probability of a jump occurring with an angle

between θ and $\theta + \mathrm{d}\theta$. The average angle is given by,

$$\Delta\theta = \int_0^\pi \theta P(\theta)\,\mathrm{d}\theta. \tag{6.8}$$

This function was calculated for q-TIP4P/F as in Ref. [98] by members of the Laage group, based on the observation of individual jump events in MD simulations. Fig. 6.4 shows the angular jump distribution. In Sec. 6.3 this will be compared to the distribution obtained from TRPMD simulations, in order to ascertain the quantum effect on the mechanism.

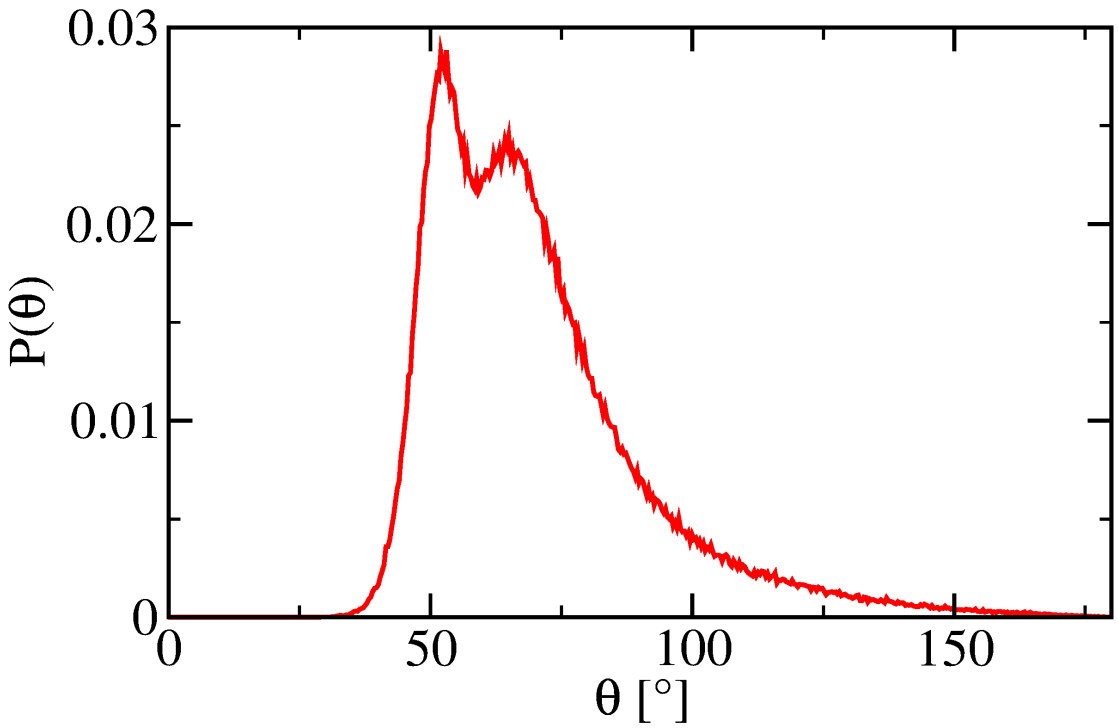

Figure 6.4: Distribution of jump angles calculated using classical MD simulations in the NVE ensemble. These data were provided by Silvio Pipolo.

τ_0 is calculated [98] using the stable-states picture of reaction rates [268]. For

each O–H bond hydrogen-bonded to another molecule, we can define a function $P_{\mathrm{P}}(t)$ such that $P_{\mathrm{P}}(0) = 0$, and this function continues equal to zero until the O–H bond is hydrogen-bonded to a different acceptor, after which $P_{\mathrm{P}}(t) = 1$. τ_0 is defined as the relaxation time of the time correlation function,

$$1 - \langle P_{\mathrm{P}}(t) \rangle \simeq A e^{-t/\tau_0}. \tag{6.9}$$

D_{R} is the rotational diffusion constant appropriate for O$\cdots$O frames, and so can be found by calculating the τ_l times for the O$\cdots$O vectors that remain hydrogen-bonded over the time of the calculation, and fitting them to the diffusive formula,

$$\tau_l^{\mathrm{frame}} = \frac{1}{D_{\mathrm{R}} l(l+1)}. \tag{6.10}$$

In order to find hydrogen-bonds in the results of our simulations, we use the probabilistic analysis of molecular motifs (PAMM) algorithm [339]. The definition of an H-bond is constructed by finding the probability distribution of certain structural parameters for O–H$\cdots$O groups using the results of a simulation, and identifying regions in this parameter space that correspond to hydrogen bonds. This is similar to (though more advanced than) the analysis of Sec. 3.2.2, in which the joint probability distribution of z and $\cos\theta$ was used to define a region corresponding to dangling O–H bonds. PAMM automates the process, meaning that the definition of hydrogen bonds does not need to be specified in advance.

Table 6.1 compares the fitted values with those calculated directly, and we note that the agreement is quite poor; all three of these parameters are over-predicted by fitting the computed relaxation times τ_l to Eqn. (6.7), indicating that although the calculated relaxation times fit quite well to the EJM, the parameters extracted

from this fit do not reflect the true physics of the problem. Because we wish to find the quantum-mechanical values of these parameters by the same method, we must ensure that fitting to the model gives the correct physical values.

Table 6.1: The EJM parameters τ_0, D_{R} and $\Delta\theta$ calculated by fitting computed τ_l values to Eqn. (6.7) are compared to the parameters calculated by direct MD simulation. The uncertainties in final digits are shown in brackets.

	τ_0 [ps]	D_{R} [ns^{-1}]	$\Delta\theta$ [°]
EJM	4.8(2)	14.9(4)	79(2)
MD	4.1(1)	12.8(3)	70

Looking again at Fig. 6.4, we see that the jump distribution $P(\theta)$ has quite a complicated form: it cannot be defined solely by the average $\Delta\theta$. It has been noted previously [98,340] that by taking into account the jump distribution, the agreement between the values of τ_1 and τ_2 predicted by the EJM and those values calculated from direct simulation is much better. Rather than fitting our calculated relaxation times to Eqn. (6.7) we will therefore adjust this equation to take into account the distribution. The method for doing so is described by Ivanov [336], and requires that Eqn. (6.7) be modified to give,

$$\frac{1}{\tau_l} = \frac{1}{\tau_0}\left[1 - \frac{1}{2l+1}\int_0^{\pi} P(\theta)\frac{\sin\left([2l+1]\,\frac{\theta}{2}\right)}{\sin\left(\frac{\theta}{2}\right)}\,\mathrm{d}\theta\right] + D_{\mathrm{R}}l(l+1). \tag{6.11}$$

We refer to the model of Eqn. (6.11) as the extended jump model with angular distribution (EJMD). One can recover the EJM from this expression by assum-

ing that jumps occur at only one angle $\Delta\theta$ and setting $P(\theta) = \delta(\theta - \Delta\theta)$. With Eqn. (6.11) we have only two fitting parameters, τ_0 and D_{R}, and must use as input the first seven relaxation times and the distribution $P(\theta)$.

In Table 6.2 we compare the newly fitted parameters with those calculated directly from our simulation results, and see that as in Refs. [212,340], the agreement is now much better; within the error bars, the results match. Fitting to the EJMD thus allows us to extract reasonable values for τ_0 and D_{R}.

Table 6.2: The EJMD parameters τ_0 and D_{R} calculated by fitting computed τ_l values to Eqn. (6.11) are compared to the parameters calculated by direct simulation. The uncertainties in final digits are shown in brackets.

	τ_0 [ps]	D_{R} [ns^{-1}]
EJMD	3.9(2)	13.1(4)
MD	4.1(1)	12.8(3)

Although Eqn. (6.11) gives values of τ_0 and D_{R} much closer to the correct ones than the values obtained from Eqn. (6.7), the fitting of the data to the former is only a little better, as is illustrated in Fig. 6.5. For small values of l, the two fitted lines look very similar, and it is only for larger values of l that there is a difference between the two, with the EJMD somewhat more closely fitting the data. Nevertheless, one could fit the data to either equation with a similar degree of success.

To ensure that this result is not specific to the q-TIP4P/F model, we repeated the analysis for the SPC/E model [16]. Table 6.3 compares the parameters obtained

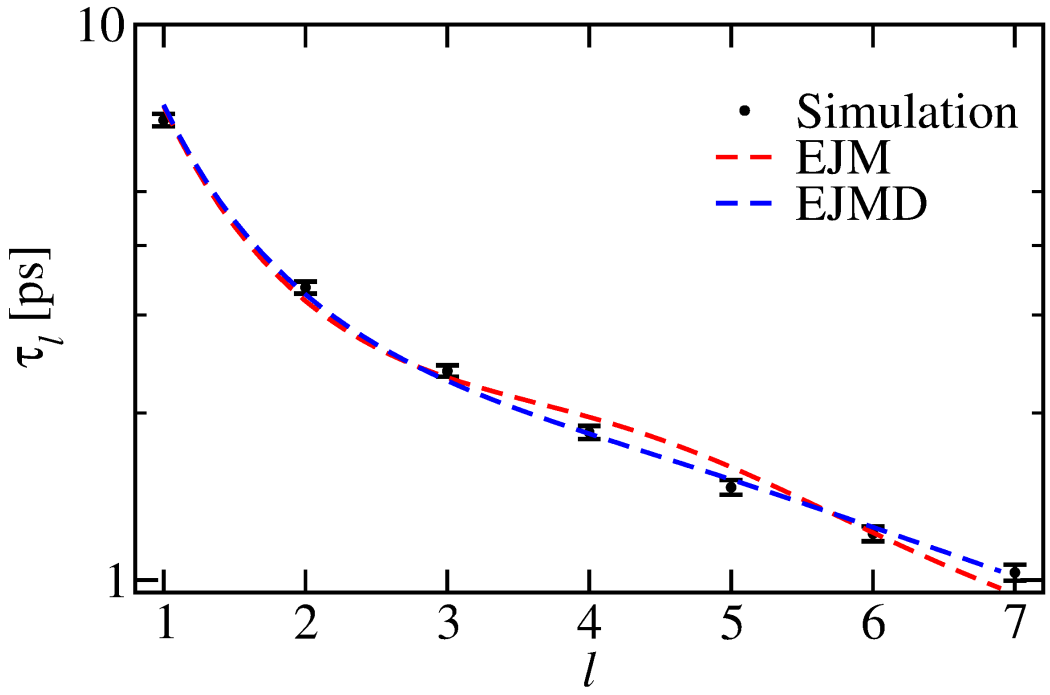

Figure 6.5: Fitting to the EJM of Eqn. (6.7) and to the EJMD of Eqn. (6.11). Black circles show τ_l times as calculated using classical MD simulations in the NVE ensemble. The dashed red line gives the best fit of these data to the EJM and the dashed blue line gives the best fit to the EJMD. The ordinate is logarithmic in order to highlight the difference between the two lines at large l.

by fitting to the EJM, and those by fitting to the EJMD, with the results calculated directly. Within the uncertainties, the rotational diffusion constant D_{R} predicted by both models is the same, and both agree with the value calculated directly by MD simulation; the jump time τ_0, however, is better predicted when the jump angle distribution is used.

Table 6.3: The results of fitting the first seven relaxation times τ_l, calculated using the SPC/E water model, to the EJM of Eqn. (6.7) and to the EJMD of Eqn. (6.11), compared to these same parameters calculated using classical molecular dynamics (MD) simulations. The uncertainties in final digits are shown in brackets.

	τ_0 [ps]	D_{R} [ns^{-1}]	$\Delta\theta$ [°]
EJM	3.9(2)	22.5(7)	82(3)
EJMD	3.3(1)	21.3(7)	–
MD	3.2(1)	22.4(3)	67

6.3 Nuclear Quantum Effects

6.3.1 Calculating Relaxation Times with TRPMD

We wish now to repeat our analysis for TRPMD simulations, which will allow us to calculate the quantum effect on τ_0 and D_{R}. In order to do so, we must derive the appropriate method for calculating τ_l relaxation times with RPMD.

The RPMD approximations to the first two Kubo-transformed Legendre polynomial correlation functions $\tilde{C}_1(t)$ and $\tilde{C}_2(t)$ are given in Ref. [28]. Here we find a general expression for any higher-order orientational correlation function.

The Kubo-transform of Eqn. (6.1) is,

$$\tilde{C}_l(t) = \frac{1}{\beta}\int_0^\beta \left\langle P_l\left[\hat{\boldsymbol{e}}_{\mathrm{OH}}\left(-i\lambda\hbar\right)\cdot\hat{\boldsymbol{e}}_{\mathrm{OH}}(t)\right]\right\rangle \,\mathrm{d}\lambda, \tag{6.12}$$

with $\hat{\boldsymbol{e}}_{\mathrm{OH}}(t)$ the vector operator describing the orientation of an O–H bond at time t and $\hat{\boldsymbol{e}}_{\mathrm{OH}}(-i\lambda\hbar) = e^{+\lambda\hat{H}}\hat{\boldsymbol{e}}_{\mathrm{OH}}e^{-\lambda\hat{H}}$.

We can rewrite Eqn. (6.12) as,

$$\tilde{C}_l(t) = \sum_{m=0}^{l} a_{l,m}\tilde{F}_m(t), \tag{6.13}$$

where,

$$\tilde{F}_m(t) = \frac{1}{\beta}\int_0^\beta \left\langle\left(\hat{\boldsymbol{e}}_{\mathrm{OH}}\left(-i\lambda\hbar\right)\cdot\hat{\boldsymbol{e}}_{\mathrm{OH}}(t)\right)^m\right\rangle \,\mathrm{d}\lambda, \tag{6.14}$$

and $a_{l,m}$ is the coefficient of x^m in the l^{th} Legendre polynomial $P_l\left[x\right]$.

We need now to calculate the approximation to the time correlation function $\tilde{F}_m(t)$ in the most straightforward form for RPMD calculations. For this, we note that,

$$\hat{\boldsymbol{e}}_{\mathrm{OH}}\left(-i\lambda\hbar\right)\cdot\hat{\boldsymbol{e}}_{\mathrm{OH}}(t) = \sum_{i=1}^{3}\hat{e}^i_{\mathrm{OH}}\left(-i\lambda\hbar\right)\hat{e}^i_{\mathrm{OH}}(t), \tag{6.15}$$

with $\hat{e}^i_{\mathrm{OH}}(t)$ the i^{th} Cartesian component of $\hat{\boldsymbol{e}}_{\mathrm{OH}}(t)$. Using the multinomial theorem we have,

$$\begin{aligned}\left(\hat{\boldsymbol{e}}_{\mathrm{OH}}\left(-i\lambda\hbar\right)\cdot\hat{\boldsymbol{e}}_{\mathrm{OH}}(t)\right)^m &= \sum_{j_1+j_2+j_3=m}\left(\frac{m!}{j_1!j_2!j_3!}\right)\prod_{i=1}^{3}\left[\hat{e}^i_{\mathrm{OH}}\left(-i\lambda\hbar\right)\hat{e}^i_{\mathrm{OH}}(t)\right]^{j_i}\\ &= \sum_{j_1+j_2+j_3=m}\left(\frac{m!}{j_1!j_2!j_3!}\right)\hat{\mathcal{E}}_{\boldsymbol{j}}\left(-i\lambda\hbar\right)\hat{\mathcal{E}}_{\boldsymbol{j}}(t). \qquad (6.16)\end{aligned}$$

All j_i in the sum are greater than zero, and the vector $\boldsymbol{j} = (j_1, j_2, j_3)$. The operator $\hat{\mathcal{E}}_{\boldsymbol{j}}(t)$ is defined as,

$$\hat{\mathcal{E}}_{\boldsymbol{j}}(t) = \left(\left[\hat{e}^1_{\mathrm{OH}}\right]^{j_1}\left[\hat{e}^2_{\mathrm{OH}}\right]^{j_2}\left[\hat{e}^3_{\mathrm{OH}}\right]^{j_3}\right)(t). \qquad (6.17)$$

We can then write Eqn. (6.14) in a form that is amenable to RPMD approximation,

$$\tilde{F}_m(t) = \sum_{j_1+j_2+j_3=m}\left(\frac{m!}{j_1!j_2!j_3!}\right)\frac{1}{\beta}\int_0^\beta\left\langle\hat{\mathcal{E}}_{\boldsymbol{j}}\left(-i\lambda\hbar\right)\hat{\mathcal{E}}_{\boldsymbol{j}}(t)\right\rangle\mathrm{d}\lambda. \qquad (6.18)$$

This equation has the same form as Eqn. (2.17), so that following the rule described at the end of Sec. 2.3 and in Ref. [50] gives the approximation to this time correlation function as,

$$\tilde{F}^{\mathrm{RPMD}}_m(t) = \sum_{j_1+j_2+j_3=m}\left(\frac{m!}{j_1!j_2!j_3!}\right)\left\langle\mathcal{E}_{n,\boldsymbol{j}}(0)\mathcal{E}_{n,\boldsymbol{j}}(t)\right\rangle_n, \qquad (6.19)$$

with $\mathcal{E}_{n,\boldsymbol{j}}(t)$ the average of $\mathcal{E}_{\boldsymbol{j}}(t)$ over all replicas,

$$\mathcal{E}_{n,\boldsymbol{j}}(t) = \frac{1}{n}\sum_{k=1}^{n}\left(\left[e^1_k\right]^{j_1}\left[e^2_k\right]^{j_2}\left[e^3_k\right]^{j_3}\right)(t), \qquad (6.20)$$

where e^i_k is the i^{th} Cartesian component of the k^{th} replica of the vector $\boldsymbol{e}_{\mathrm{OH}}$.

Eqn. (6.19) allows us to write the RPMD approximation to the time correlation function $\tilde{C}_l(t)$ as,

$$\tilde{C}^{\mathrm{RPMD}}_l(t) = \sum_{m=0}^{l}a_{l,m}\sum_{j_1+j_2+j_3=m}\left(\frac{m!}{j_1!j_2!j_3!}\right)\left\langle\mathcal{E}_{n,\boldsymbol{j}}(0)\mathcal{E}_{n,\boldsymbol{j}}(t)\right\rangle_n, \qquad (6.21)$$

and thus to calculate the quantum-mechanical τ_l from the long-time decay of this function. The time correlation function of Eqn. (6.21) must be averaged over all distinct chemical entities. For O–H bonds the number of entities is $2N_{\mathrm{w}}$, where N_{w} is the number of water molecules in the simulation. For a direct calculation of D_{R}, the entities are O$\cdots$O pairs that are hydrogen-bonded continuously for at least some minimum time t_{min}. Because each time a hydrogen bond is broken and a new one formed (or the previous one is re-formed) a new H-bond is counted, the number of entities is much greater, and requires more computer memory to store.[3] This makes fitting to the τ_l times preferable to a direct calculation of D_{R}.

6.3.2 Fitting Results

We then carried out TRPMD simulations on 20 systems each containing 216 water molecules at the experimental density, which had been equilibrated using PIMD simulations at 298 K. The first seven $C_l(t)$ time correlation functions are shown in Fig. 6.6, and were used to calculate the first seven τ_l times.

Before fitting these times to the EJMD the jump angle distribution $P(\theta)$ from TRPMD simulations was required. This was calculated by members of the Laage group, and is compared in Fig. 6.7 with its classical counterpart. These two functions are essentially identical, which strongly suggests that the mechanism of water jumps is unchanged by quantum mechanics. The only effect that quantum fluctuations

[3]Instead of storing the TRPMD time correlation function for each entity, one could alternatively run through the simulation once per H-bond and accumulate the average time correlation function in this way; however, this is costly in terms of computer time rather than memory.

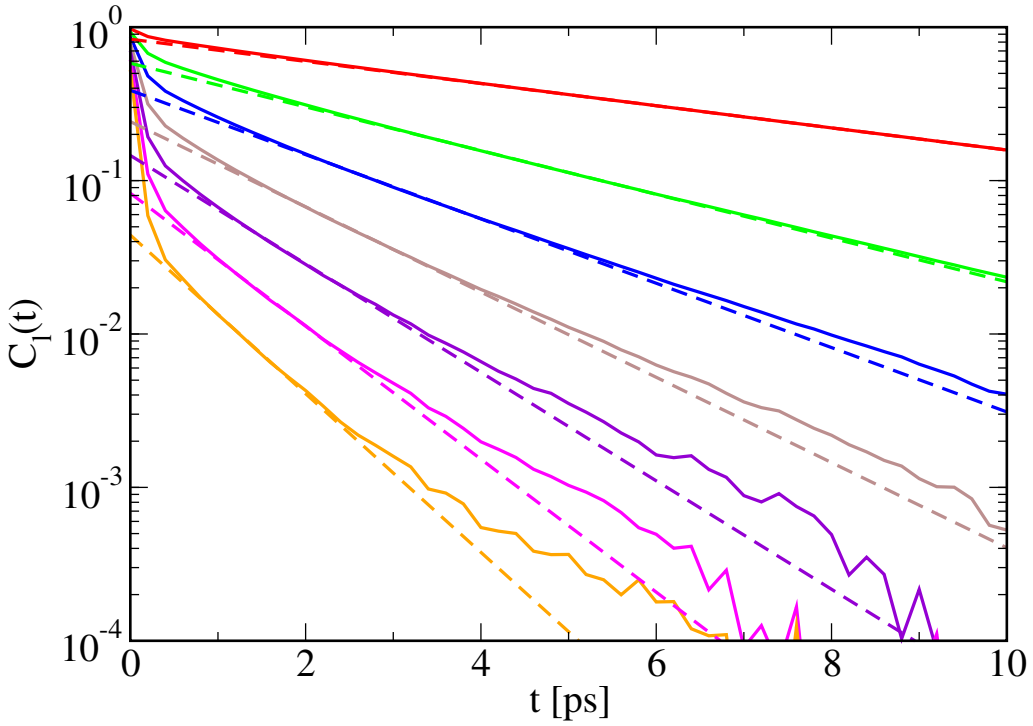

Figure 6.6: The first seven Legendre correlation functions $C_l(t)$, calculated using TRPMD simulations. The solid coloured lines show the functions calculated from simulation results, and the dashed coloured lines show the corresponding fits to an exponential decay, $C_l(t) \simeq Ae^{-t/\tau_l}$.

could have on the water jumps, then, is on the jump rate $k_0 = 1/\tau_0$ and the rotational diffusion constant D_{R}.

The first seven τ_l relaxation times from TRPMD simulations are shown in Fig. 6.8, along with the results of fitting to the EJMD. As in the classical case, the fitting is quite good.

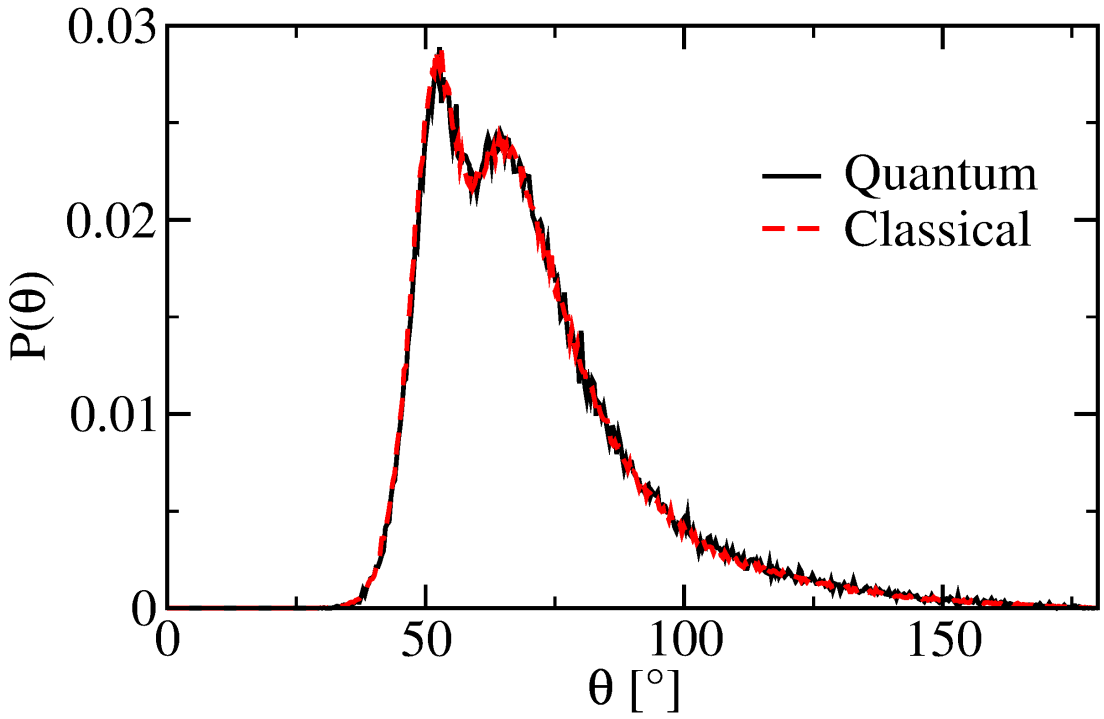

Figure 6.7: Comparison of the jump angle distribution calculated using TRPMD (solid black lines) and classical MD (dashed red lines) simulations. These data were provided by Silvio Pipolo.

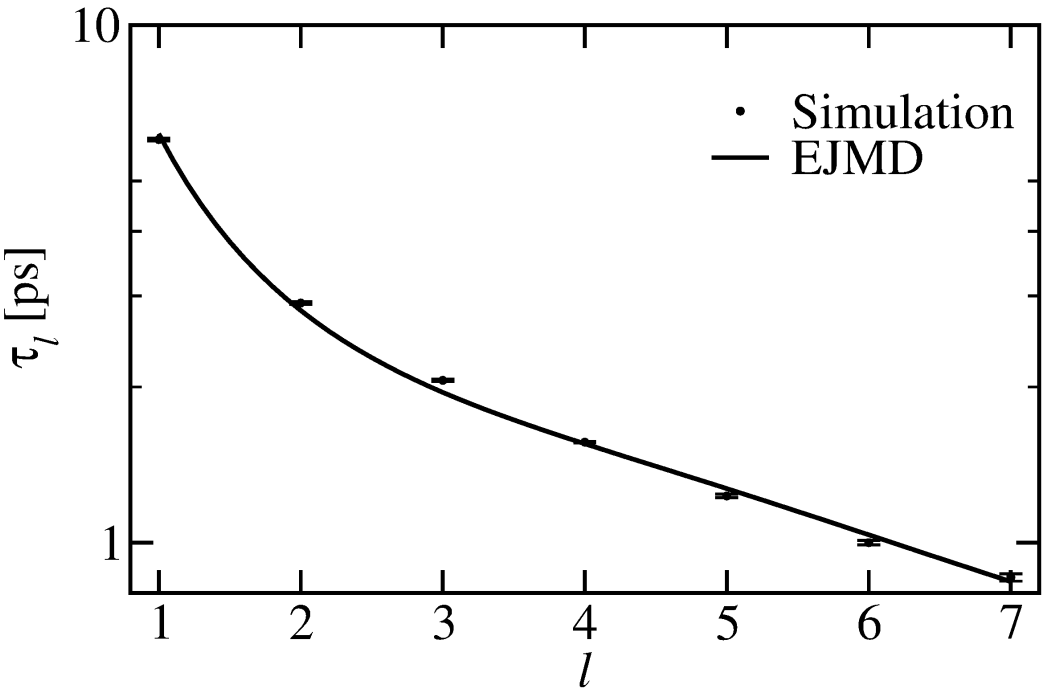

Figure 6.8: Fitting of τ_l times calculated using TRPMD simulations (black circles) to the EJMD of Eqn. (6.11). The solid black line gives the best fit of the EJMD to these data.

In Fig. 6.9 we plot the results of fitting the first seven τ_l times from classical and quantum simulations to the EJMD. As has been noted previously [28,31,32,52] the τ_l times decrease when quantum mechanical effects are accounted for. For all values of l the quantum effect (ratio of classical to quantum relaxation times) is fairly small, but it increases slightly with increasing l, from 14% at $l = 1$ to around 20% at large l. A similar increase in quantum effects on the correlation times $\bar{\tau}_l$ with increasing l was observed in Ref. [28].

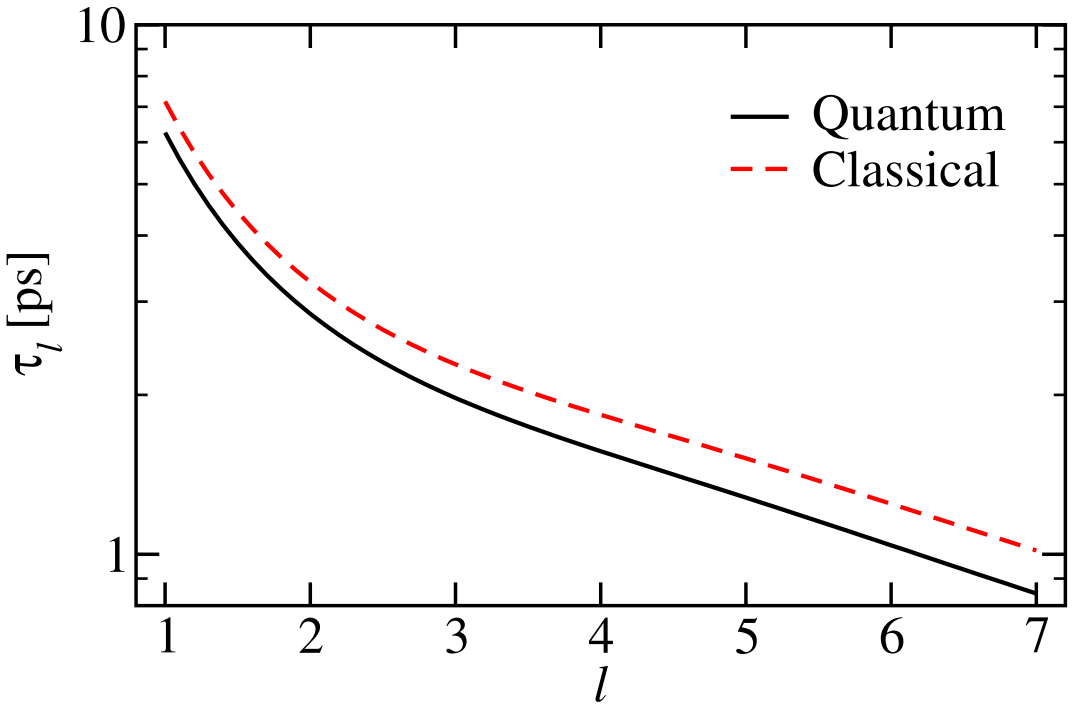

Figure 6.9: Results of fitting the first seven τ_l relaxation times as calculated from TRPMD (solid black lines) and classical MD (dashed red lines) simulations. The ordinate is logarithmic to better show the differing magnitudes of the quantum effects for different l.

We can use this increase in the quantum effect to predict the relative magnitudes of the quantum effects on τ_0 and on D_{R}; we can rewrite Eqn. (6.11) in the form,

$$\frac{1}{\tau_l} = \frac{g_l}{\tau_0} + D_{\mathrm{R}} l(l+1), \tag{6.22}$$

where,

$$g_l = 1 - \frac{1}{2l+1} \int_0^{\pi} P(\theta) \frac{\sin\left([2l+1]\,\frac{\theta}{2}\right)}{\sin\left(\frac{\theta}{2}\right)}\,\mathrm{d}\theta. \tag{6.23}$$

In the limit as $l \to \infty$, $g_l \to 1$. The quantum effect in τ_l can then be written,

$$\frac{\tau_l^{\mathrm{cl}}}{\tau_l^{\mathrm{qm}}} = \frac{g_l/{\tau_0}^{\mathrm{qm}} + {D_{\mathrm{R}}}^{\mathrm{qm}} l(l+1)}{g_l/{\tau_0}^{\mathrm{cl}} + {D_{\mathrm{R}}}^{\mathrm{cl}} l(l+1)}. \tag{6.24}$$

The superscript "cl" represents a classical quantity and "qm" a quantum one, and we have used the fact that g_l, like the distribution $P(\theta)$, is unchanged between classical and quantum-mechanical simulations. For large l, the terms involving jump rates in the numerator and the denominator will tend to constants and,

$$\lim_{l\to\infty} \frac{\tau_l^{\mathrm{cl}}}{\tau_l^{\mathrm{qm}}} = \frac{{D_{\mathrm{R}}}^{\mathrm{qm}}}{{D_{\mathrm{R}}}^{\mathrm{cl}}}. \tag{6.25}$$

This means that the quantum effect is dominated by the effect on the rotational diffusion constant. For small l both the τ_0 and D_{R} terms will contribute to the quantum effect, but the contribution of D_{R} will decrease with decreasing l. The quantum effect on the jump rate thus makes a larger contribution to the total effect at small l. The increase of quantum effect with l then suggests that the quantum effect on D_{R} will be larger than that on τ_0.

The parameters obtained from the fitted τ_l to the EJMD are compared in Table 6.4 with the classical values found in Sec. 6.2. The jump rate increases by $(13 \pm 3)\%$ when quantum effects are included, and the rotational diffusion constant increases

by $(20 \pm 4)\%$. These effects are both reasonably small, and both are quite close to the quantum effect of 15% observed for the (translational) self-diffusion coefficient of q-TIP4P/F water [32]. In fact, within the error bars the quantum effects on $k_0 = 1/\tau_0$ and on D_R overlap.

Table 6.4: The EJMD parameters τ_0 and D_R calculated by fitting computed τ_l values to Eqn. (6.11) for classical MD and TRPMD simulations. The uncertainties in final digits are shown in brackets.

	τ_0 [ps]	D_R [ns^{-1}]
MD	3.9(2)	13.1(4)
TRPMD	3.48(2)	15.8(1)

For both k_0 and D_R, the rate-determining step involves the reorganization of the hydrogen-bonding network; as found by Laage and Hynes [98], a water jump is activated by the slow rearrangement of the local environment such that the current hydrogen-bond acceptor and its replacement are equidistant from the donor molecule, and the sudden change from one acceptor to another is a fast step. The reorientation of an O$\cdots$O vector will also entail the alteration of its local environment. The effects we see, therefore, are a consequence of the quantum-mechanical weakening of H-bonds.

6.4 The Origin of the Quantum Effects

The temperature dependence of $k_0 = 1/\tau_0$ and D_{R} will help us to attribute the quantum effects on these properties to zero point energy or to tunnelling. These two rates could be expected to obey the Arrhenius relation,

$$\ln k = \ln A - \frac{E_{\mathrm{a}}}{k_{\mathrm{B}}T}, \tag{6.26}$$

so that a plot of their logarithms against $1/T$ will allow us to extract an activation energy E_{a} for each. Comparing the classical and the quantum-mechanical E_{a} will give an idea of how much ZPE contributes to each quantum effect, since zero-point energy in the reactant and in the transition state will affect the height of the barrier that must be surmounted to activate the reaction, as illustrated in Fig. 6.10. Furthermore, a positive deviation from the Arrhenius equation would signify that tunnelling was also in operation.

We repeated our classical MD and TRPMD simulations using systems equilibrated at various temperatures between 260 K and 350 K using the experimental density at each temperature, and fitted the results to the EJMD at each temperature. We recalculated the jump angle distribution for each temperature studied, and found the distribution to be essentially independent of temperature. Fig. 6.11 shows the Arrhenius plot for τ_0 and D_{R}. Although the fitting of these points to a straight line is not perfect, it is quite reasonable and shows no significant upward deviation. Although Arrhenius behaviour can be observed even when there is tunnelling [341], these results give no evidence that tunnelling is occurring, and are consistent with ZPE as the origin of the quantum effects that we have seen. Although small at

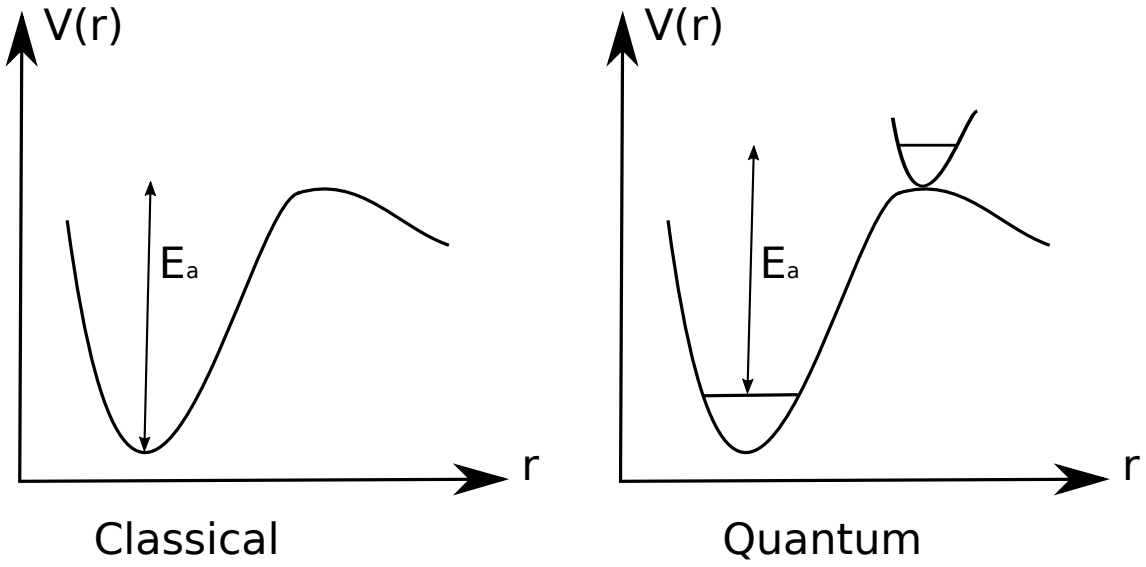

Figure 6.10: Schematic potential-energy profile for a chemical reaction. Left-hand panel: in the classical case the activation energy E_a is the difference between the transition state and the bottom of the reactant well. Right-hand panel: quantum-mechanically, both the reactant and the transition state will have a ZPE, and the difference between the ZPE in the transition state and that in the reactant well is added to the activation energy.

every temperature, the quantum effects increase with decreasing temperature, with essentially no effect at 350 K in either case and an increase of 34% for k_0 and 45% for D_R at 260 K.

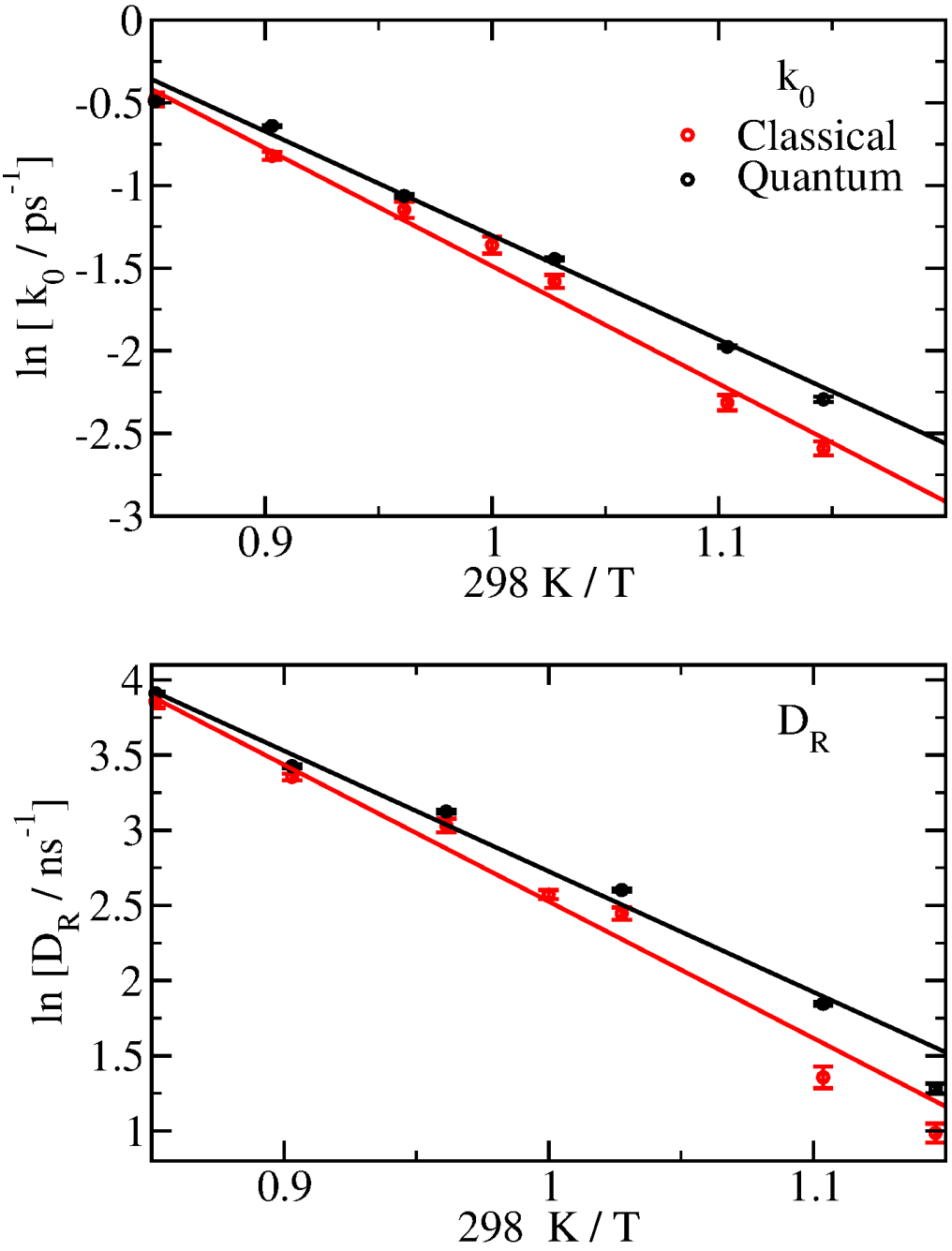

Figure 6.11: Arrhenius plot of the jump rate $k_0 = 1/\tau_0$ and rotational diffusion constant D_{R}, as obtained from classical MD and from TRPMD simulations.

For each of these parameters the classical and quantum-mechanical activation energies are shown in Table 6.5, along with an estimate of ΔZPE, the difference in zero point energies between the reactant and the transition state, in each case. In both cases ΔZPE is about 20% of the activation energy, and the ΔZPE associated with D_{R} appears slightly larger than that associated with k_0, though the difference is not statistically significant. This is in accord with the fact that while the quantum effect for D_{R} is larger than for k_0, the error bars associated with these two effects overlap.

Table 6.5: Activation energies for the jump rate k_0 and rotational diffusion constant D_{R} as calculated from the Arrhenius plot of Fig. 6.11. $E_{\mathrm{a}}^{\mathrm{cl}}$ is the activation energy from classical simulations and $E_{\mathrm{a}}^{\mathrm{qm}}$ is calculated from classical simulations. $\Delta\mathrm{ZPE} = E_{\mathrm{a}}^{\mathrm{cl}} - E_{\mathrm{a}}^{\mathrm{qm}}$. All energies are given in units of the thermal energy $k_{\mathrm{B}}T$ at 298 K.

	$E_{\mathrm{a}}^{\mathrm{cl}}$	$E_{\mathrm{a}}^{\mathrm{qm}}$	ΔZPE
k_0	7.1(4)	6.3(1)	0.8(4)
D_{R}	9.1(4)	8.0(1)	1.1(4)

6.5 Conclusions

In this Chapter, we have shown that the quantum effects on the rate of water jumps and on the rotational diffusion constant of O$\cdots$O vectors are comparatively small

(10-20%). The fact that the classical and quantum jump angle distributions are essentially identical means that there is no change in the mechanism of the jumps. These results are similar to those for the exchange of water molecules around ions in Chapter 4; once again, a classical treatment will give an excellent qualitative description of the physics of O–H bond reorientation, and a quantitatively reasonable one.

It is worth noting that other quantum effects might be in operation in the reorientation of O–H bonds. The rotation of the bond during a water jump is a high-frequency motion, and quantization of this motion may lead to a more significant effect [98]. However, this is the fast step in the water jump reaction, and the quantum effects in the rate-limiting step (that is, the environmental reorganization) are likely to make the dominant contribution to the quantum effect in τ_0, meaning that by fitting to the EJMD we cannot access the quantum effects in the bond rotation.

Chapter 7

Conclusion

7.1 Nuclear Quantum Effects in Water

In this Thesis, we have studied the structure and dynamics of aqueous systems, paying particular attention to those in which nuclear quantum effects may be important. We have seen examples of phenomena in which NQEs play a vital role, as well as examples of properties which would suffer very little from being calculated classically.

In Chapter 3 we considered the preference for H over D atoms in the dangling bond sites at the surface of liquid water. Sum-frequency generation spectroscopy experiments performed by members of the Chen group on isotopically substituted water gave a free-energy change of (-2.3 ± 0.7) meV for the replacement of H atoms in the bulk with D atoms at the surface. We were able to extract a free energy of fractionation from PIMD simulations that matched the experimental result within the error bars. The origin of the preference is the decrease in confinement of an H or a D atom on going from the bulk to the surface – an effect that is more pronounced for the lighter atom. We also resolved the free energy change into two contributions,

one from motion parallel to the O–H bond (which favours the bulk) and one from motion perpendicular to the bond (which favours the surface). The net effect is fairly small, with a 50:50 bulk ratio of H:D corresponding to a 52:48 ratio at the surface. However, it is experimentally observable and may contribute to the higher rate of evaporation of light over heavy water – which has geochemical applications such as the analysis of water samples [140–142]. Without explicitly accounting for nuclear quantum effects, it would simply not be possible to observe this preference in simulations.

Chapter 4 focused on the dynamics of water exchange between the first and second hydration shells of ions. While quantum fluctuations increase the rate of exchange around monatomic, monovalent ions, these increases are only modest, and are not accompanied by a change in the mechanism followed. A larger quantum effect on the rate of exchange around Li^+ was found than on that around F^-. Of the two ions, Li^+ has the lower mass, and binds water more strongly: these factors will lead to more ZPE in the coordinates responsible for exchange around the cation. In addition, there is a competing quantum effect in the exchange around F^- that is absent in the exchange around Li^+: for the H atom interacting directly with the anion, ZPE in the direction of the O–H bond will tend to slow down exchange, while ZPE in perpendicular directions will tend to speed it up. The rate itself can vary considerably depending on the potential model used for the ion-water interaction, and this variation can dwarf the quantum effect; it is thus entirely reasonable to model water exchange in these systems using classical molecular dynamics.

The long-range ordering of water molecules in ionic solutions was the subject of

Chapter 5. Second harmonic scattering experiments were performed by members of the Roke group on several ionic solutions of varying ionic strength ρ_{I}, and the intensity of scattered light was found to increase with ionic strength for small ρ_{I}, reaching a plateau at large ionic strength. The ρ_{I}-dependence of the intensity obeys a Langmuir-like equation, whose parameters are independent of the identity of the solute. Both of these findings are explained qualitatively by a mean-field approach based on Debye-Hückel theory: an increase in concentration means that more ions are present to order water molecules, but also that the screening of each ion's charge increases, diminishing its ability to order the molecules. The competition between these effects is responsible for the intensity plateau at high concentration. The ion-nonspecificity is a consequence of the fact that volume elements further from an ion contribute more to the scattering intensity than volume elements closer to it (the structure of water molecules further from the ion is much less dependent on the identity of the ion). We then used classical MD simulations to investigate the spatial and orientational correlations in concentrated ionic solutions, and to compare these to the predictions of Debye-Hückel theory. The long-range correlations are described quite well by this theory, accounting for its ability to qualitatively explain the effects observed. At shorter ranges the theory does not describe the correlations so well, which accounts to some extent for its quantitative failures.

Chapter 6 returned to the dynamics of water molecules, investigating the effect of quantum fluctuations on the reorientation of O–H bonds. Within the extended jump model [98, 308], this reorientation is described by three quantities: the rate of angular jumps in which a hydrogen-bond donor suddenly switches to a new acceptor,

the average angle of these jumps, and the rotational diffusion constant for intact hydrogen bonds. We found that if this model is modified to include the distribution of jump angles, then it is possible, by calculating several Legendre relaxation times for O–H bonds and fitting to the model, to obtain the correct jump rate and rotational diffusion constant. By fitting classical and quantum-mechanical relaxation times in this way, we were able to find the quantum effect on these two quantities. Both are increased slightly by quantum fluctuations, with the mechanism once again being unchanged. These effects were attributed to ZPE in the coordinates responsible for environmental reorganization, and their small magnitude suggests that a classical treatment would give a reasonable description of the water jump reaction.

In summary, although the results of isotopic substitution experiments can show nuclear quantum effects, even if quite subtle, that require path integral simulations to fully account for, we have found in the preceding work that aqueous systems can often be simulated accurately without the need to include NQEs, as the properties in which we have been interested change by only a small degree on quantization.

This conclusion may at first seem anticlimactic: after all, water is an archetypal system for studying nuclear quantum effects [25–33]. However, the fact that classical simulations can be sufficient to qualitatively, and even semi-quantitatively, understand water, in no way diminishes its mystery – it simply means that water can be quite well understood without the need to consider NQEs.

7.2 Further Work

A number of directions for further work have been suggested in previous chapters of this Thesis. Here we recap the two most significant of these:

- Although the nuclear quantum effects on water exchange around monovalent ions are quite small, the quantum-mechanical increase of the exchange rate has been found to be greater for ions that bind water molecules more strongly [216]. For higher-valent ions, whose mean residence times are many orders of magnitude larger, it might be possible to observe very significant nuclear quantum effects. These NQEs could then be responsible for the reactivity of biochemically and industrially useful ions.

- In Chapter 5 we ran classical simulations of concentrated ionic solutions to understand the long-ranged correlations that give rise to a second-harmonic scattering signal. In order to fully understand the experimental results, we need to take into account nuclear quantum effects, and also to use larger systems, allowing for a larger range of concentrations than the range that was available to us in this study. Furthermore, the calculation of the SHS intensity from these simulations would provide the best comparison to experiments. Work in all of these directions is currently ongoing.

Appendices

Appendix A

Derivation of the Ring Polymer Isomorphism

We begin with Eqn. (2.1), reprinted here for clarity:

$$\langle A \rangle = \frac{1}{Z} \mathrm{tr} \left[\hat{A} e^{-\beta \hat{H}} \right]. \tag{2.1}$$

Let us consider a one-dimensional system (the generalization to multiple dimensions is straightforward but notationally less simple). Taking A to be a configurational property of the system, it is a function only of the system's coordinate q, so that $\hat{A} \equiv A(\hat{q})$. We evaluate the trace using a complete set of position eigenstates,

$$\langle A \rangle = \frac{1}{Z} \int \mathrm{d}q_1 \, \langle q_1 | \hat{A} e^{-\beta \hat{H}} | q_1 \rangle. \tag{A.1}$$

Next, we write the Hamiltonian operator as a sum of kinetic and potential energy operators, $\hat{H} = \hat{T} + \hat{V}$. While $\hat{V} \equiv V(\hat{q})$ is a function of the coordinate, $\hat{T}$ is not and $e^{-\beta \hat{T} - \beta \hat{V}} | q_1 \rangle$ is difficult to evaluate. However, we can use the approximation,

$$\begin{aligned} e^{-\beta \hat{T} - \beta \hat{V}} &= \left(e^{-\beta_n \hat{T} - \beta_n \hat{V}} \right)^n \\ &\simeq \left(e^{-\beta_n \hat{V}/2} e^{-\beta_n \hat{T}} e^{-\beta_n \hat{V}/2} \right)^n, \end{aligned} \tag{A.2}$$

where $\beta_n = \beta/n$. The error in this expression is $\mathcal{O}\left(\beta_n^3\right)$, which will vanish as $n \to \infty$. If $\langle A \rangle_n$ is the approximation to Eqn. (2.1) using a finite n then,

$$\langle A \rangle_n = \frac{1}{Z} \int \mathrm{d}q_1 \, \langle q_1 | A(\hat{q}) e^{-\beta_n \hat{V}/2} e^{-\beta_n \hat{T}} e^{-\beta_n \hat{V}/2} \cdots e^{-\beta_n \hat{V}/2} e^{-\beta_n \hat{T}} e^{-\beta_n \hat{V}/2} | q_1 \rangle, \quad \text{(A.3)}$$

where the ellipsis stands for $n-2$ factors of $e^{-\beta_n \hat{V}/2} e^{-\beta_n \hat{T}} e^{-\beta_n \hat{V}/2}$. Between each pair of these factors in the integral, we insert a complete set of position eigenstates,

$$\langle A \rangle_n = \frac{1}{Z} \int \mathrm{d}q_1 \int \mathrm{d}q_2 \cdots \int \mathrm{d}q_n \times \\ \langle q_1 | A(\hat{q}) e^{-\beta_n \hat{V}/2} e^{-\beta_n \hat{T}} e^{-\beta_n \hat{V}/2} | q_2 \rangle \cdots \langle q_n | e^{-\beta_n \hat{V}/2} e^{-\beta_n \hat{T}} e^{-\beta_n \hat{V}/2} | q_1 \rangle. \quad \text{(A.4)}$$

Using the fact that $\hat{A}$ and $\hat{V}$ are functions of position,

$$\langle A \rangle_n = \frac{1}{Z} \int \mathrm{d}q_1 \int \mathrm{d}q_2 \cdots \int \mathrm{d}q_n \, A(q_1) e^{-\beta_n \sum_{k=1}^{n} V(q_k)} \langle q_1 | e^{-\beta_n \hat{T}} | q_2 \rangle \cdots \langle q_n | e^{-\beta_n \hat{T}} | q_1 \rangle. \quad \text{(A.5)}$$

The kinetic energy is not a function of position, but does depend on the momentum p. To evaluate the matrix element $\langle q_k | e^{-\beta_n \hat{T}} | q_{k+1} \rangle$, where cyclic boundary conditions are applied such that $k+1 = 1$ if $k = n$, we insert a complete set of momentum eigenstates,

$$\begin{aligned} \langle q_k | e^{-\beta_n \hat{T}} | q_{k+1} \rangle &= \int \mathrm{d}p \, \langle q_k | p \rangle \langle p | e^{-\beta_n \hat{T}} | q_{k+1} \rangle, \\ &= \int \mathrm{d}p \, \langle q_k | p \rangle e^{-\beta_n p^2/2m} \langle p | q_{k+1} \rangle, \\ &= \frac{1}{2\pi\hbar} \int \mathrm{d}p \, e^{-\beta_n p^2/2m + ip(q_k - q_{k+1})/\hbar}, \\ &= \frac{1}{2\pi\hbar} \left(\frac{2\pi m}{\beta_n} \right)^{1/2} e^{-\beta_n m \omega_n^2 (q_k - q_{k+1})^2/2}, \end{aligned} \quad \text{(A.6)}$$

with $\omega_n = 1/\beta_n\hbar$. Here we have used the identity $\langle p|q\rangle = \frac{1}{(2\pi\hbar)^{1/2}} e^{-ipq/\hbar}$. Inserting our result into Eqn. (A.5) gives,

$$\langle A\rangle_n = \frac{1}{(2\pi\hbar)^n\, Z}\left(\frac{2\pi m}{\beta_n}\right)^{1/2} \int \mathrm{d}q_1 \cdots \int \mathrm{d}q_n\, A(q_1) e^{-\beta_n \sum_{k=1}^{n}\left\{V(q_k)+\frac{1}{2}m\omega_n(q_k-q_{k+1})\right\}}. \tag{A.7}$$

This expression is similar to the configurational part of the integrals in Eqn. (2.2); our current integral lacks a kinetic energy term, the inclusion of which would allow us to perform molecule dynamics. We use the fact that,

$$\left(\frac{2\pi m}{\beta_n}\right)^{1/2} = \left(\frac{m}{m'}\right)^{1/2} \int \mathrm{d}p\, e^{-\beta_n p^2/2m'}, \tag{A.8}$$

which gives the desired kinetic energy term. The mass m' is completely arbitrary, and will not affect the average $\langle A\rangle_n$. When using the ring-polymer Hamiltonian to calculate dynamical properties, we will choose to use the physical mass m, as discussed in Sec. 2.3, and so will use this mass here for the sake of consistency.

Since the partition function Z is currently also a quantum-mechanical trace, we must replace it with Z_n calculated in exactly the same extended ring-polymer phase space. Finally we have,

$$\langle A\rangle_n = \frac{1}{Z_n}\int \mathrm{d}\boldsymbol{q} \int \mathrm{d}\boldsymbol{p}\, A(q_1) e^{-\beta_n \mathcal{H}_n(\boldsymbol{q},\boldsymbol{p})}, \tag{A.9}$$

where $\boldsymbol{q} = (q_1, \cdots, q_n)$, $\boldsymbol{p} = (p_q, \cdots, p_n)$, and $\mathcal{H}_n(\boldsymbol{q},\boldsymbol{p})$ is the ring-polymer Hamiltonian,

$$\mathcal{H}_n(\boldsymbol{q},\boldsymbol{p}) = \sum_{k=1}^{n}\frac{p_k^2}{2m} + \sum_{k=1}^{n}\mathcal{V}(q_k) + \sum_{k=1}^{n}\frac{1}{2}m\omega_n^2\left(q_k - q_{k+1}\right)^2. \tag{A.10}$$

The generalization of this argument to multiple dimensions gives the result shown in Eqn. (2.10).

It is also worth noting that the integrand of Eqn. (A.9) contains $A(q_1)$. The cyclic symmetry of a trace operation means that in Eqn. (A.3) we can permute the factors of $e^{-\beta_n \hat{V}/2} e^{-\beta_n \hat{T}} e^{-\beta_n \hat{V}/2}$, giving as many of these factors on the left-hand side of the $\hat{A}$ as we desire,

$$\begin{aligned} \langle A \rangle_n &= \frac{1}{Z} \int \mathrm{d}q_1 \, \langle q_1 | A(\hat{q}) \left(e^{-\beta_n \hat{V}/2} e^{-\beta_n \hat{T}} e^{-\beta_n \hat{V}/2} \right)^n | q_1 \rangle \\ &= \frac{1}{Z} \int \mathrm{d}q_1 \, \langle q_1 | \left(e^{-\beta_n \hat{V}/2} e^{-\beta_n \hat{T}} e^{-\beta_n \hat{V}/2} \right)^l A(\hat{q}) \left(e^{-\beta_n \hat{V}/2} e^{-\beta_n \hat{T}} e^{-\beta_n \hat{V}/2} \right)^{n-l} | q_1 \rangle, \end{aligned} \tag{A.11}$$

with $l \leq n$. Depending on the value chosen for l, $A(\hat{q})$ will operate on a different position eigenstate when the complete sets of their eigenstates are inserted. Thus, we could replace $A(q_1)$ with $A(q_2), \cdots, A(q_n)$ in Eqn. (A.3) and obtain the same result. In terms of statistics the best choice is to take the average of all of these possibilities, denoted $A_n(\boldsymbol{q})$ as in Eqn. (2.12). The exact equilibrium average of A is then,

$$\langle A \rangle = \lim_{n \to \infty} \langle A \rangle_n \, . \tag{A.12}$$

Lastly, we note that A must be a configurational property in order to derive this isomorphism. If this variable depends on p, then we will not in general be able to carry out the integration of Eqn. (A.6), from which the harmonic spring potential energies are derived. We cannot use Eqn. (A.9) to find the average of a momentum-dependent quantity. To find the average of such a quantitity $B(p)$, we must instead use an estimator, which is a configuration-dependent property $A(q)$ whose average is the same as that of $B(p)$. An example, which we consider in Sec. 2.4, is the centroid

virial estimator for the kinetic energy [119, 120].

Appendix B

Orientational Averaging

In Eqn. (5.15) we have the average,

$$\left\langle \beta_{\mathrm{OII}}^{m} e^{+\mu_0 E(\boldsymbol{r}_m)\cos\theta_m/k_{\mathrm{B}}T} \right\rangle_0 , \tag{B.1}$$

where $\langle\cdots\rangle_0$ represents an average over all possible orientations of molecule m relative to a coordinate system fixed in the laboratory.

Let $\{\boldsymbol{e}_i\}$ $(i = 1, 2, 3)$ be an orthonormal set of vectors defined relative to the molecule, with $\boldsymbol{e}_3$ parallel to the molecular dipole moment. We will also take $\{\boldsymbol{u}_J\}$ $(J = X, Y, Z)$ to be an orthonormal set of vectors defined relative to the laboratory. If $\boldsymbol{u}_Z$ ($\equiv \boldsymbol{u}_{\mathrm{IN}}$ in Chapter 5) is parallel to the polarization of the incoming electric field then there are two possible cases:

1. The outgoing electric field is also polarized in this direction ($\boldsymbol{u}_{\mathrm{OUT}} = \boldsymbol{u}_Z$), in which case,

$$\beta_{\mathrm{OII}} = \beta_{ZZZ} = \sum_{i,j,k} \beta_{ijk} \left(\boldsymbol{u}_Z \cdot \boldsymbol{e}_i\right)\left(\boldsymbol{u}_Z \cdot \boldsymbol{e}_j\right)\left(\boldsymbol{u}_Z \cdot \boldsymbol{e}_k\right). \tag{B.2}$$

2. The outgoing field is polarized perpendicular to this direction (without loss of

generality, we can take $\boldsymbol{u}_{\mathrm{OUT}} = \boldsymbol{u}_X$), whence,

$$\beta_{\mathrm{OII}} = \beta_{XZZ} = \sum_{i,j,k} \beta_{ijk} \left(\boldsymbol{u}_X \cdot \boldsymbol{e}_i\right) \left(\boldsymbol{u}_Z \cdot \boldsymbol{e}_j\right) \left(\boldsymbol{u}_Z \cdot \boldsymbol{e}_k\right). \tag{B.3}$$

Assuming that the temperature is high enough that $\mu_0 E(\boldsymbol{r}_m) \ll k_{\mathrm{B}}T$, we can use the approximation $e^{+\mu_0 E(\boldsymbol{r}_m)\cos\theta_m / k_{\mathrm{B}}T} \simeq 1 + \mu_0 E(\boldsymbol{r}_m)\cos\theta_m / k_{\mathrm{B}}T$. Since,

$$\mu_0 E(\boldsymbol{r}_m)\cos\theta_m = \mu_0 \boldsymbol{e}_3 \cdot \boldsymbol{E}(\boldsymbol{r}_m), \tag{B.4}$$

we now have a sum of two averages,

$$\sum_{i,j,k} \beta_{ijk} \left\langle \left(\boldsymbol{u}_{\mathrm{OUT}} \cdot \boldsymbol{e}_i\right) \left(\boldsymbol{u}_Z \cdot \boldsymbol{e}_j\right) \left(\boldsymbol{u}_Z \cdot \boldsymbol{e}_k\right) \right\rangle_0 + \frac{\mu}{k_{\mathrm{B}}T} \sum_{i,j,k} \beta_{ijk} \left\langle \left(\boldsymbol{u}_{\mathrm{OUT}} \cdot \boldsymbol{e}_i\right) \left(\boldsymbol{u}_Z \cdot \boldsymbol{e}_j\right) \left(\boldsymbol{u}_Z \cdot \boldsymbol{e}_k\right) \boldsymbol{e}_3 \cdot \boldsymbol{E}(\boldsymbol{r}) \right\rangle_0, \tag{B.5}$$

where $\boldsymbol{u}_{\mathrm{OUT}} = \boldsymbol{u}_Z$ in case 1 above and $\boldsymbol{u}_{\mathrm{OUT}} = \boldsymbol{u}_X$ in case 2. Both of these averages are over all orientations of the molecule.

To carry out these averages, an integration is performed over the Euler angles (θ, ϕ, χ) that define the rotation which transforms the $(\boldsymbol{u}_X, \boldsymbol{u}_Y, \boldsymbol{u}_Z)$ axes into the $(\boldsymbol{e}_1, \boldsymbol{e}_2, \boldsymbol{e}_3)$ axes; excellent descriptions of how to evaluate these integrals are given by Andrews [342] and by Cyvin *et al.* [343].

The first term in Eqn. (B.5) is zero. In order for an average over Euler angles to be nonzero, it must contain terms in which no scalar product is raised to an odd power [342], and when the sums are expanded there will be no terms for which this is the case. There will be three types of average,

- those such as $\left\langle \left(\boldsymbol{u}_X \cdot \boldsymbol{e}_1\right) \left(\boldsymbol{u}_Z \cdot \boldsymbol{e}_2\right) \left(\boldsymbol{u}_Z \cdot \boldsymbol{e}_3\right) \right\rangle_0$, in which all terms are different,
- those like $\left\langle \left(\boldsymbol{u}_Z \cdot \boldsymbol{e}_1\right) \left(\boldsymbol{u}_Z \cdot \boldsymbol{e}_1\right) \left(\boldsymbol{u}_Z \cdot \boldsymbol{e}_2\right) \right\rangle_0$ in which two terms are equal,

- and those like $\langle (\boldsymbol{u}_Z \cdot \boldsymbol{e}_1)(\boldsymbol{u}_Z \cdot \boldsymbol{e}_1)(\boldsymbol{u}_Z \cdot \boldsymbol{e}_1)\rangle_0$ in which all three terms are equal,

all of which have at least one scalar product raised to an odd power.

For the second term of Eqn. (B.5) we write,

$$\boldsymbol{e}_3 \cdot \boldsymbol{E}(\boldsymbol{r}_m) = \sum_J (\boldsymbol{e}_3 \cdot \boldsymbol{u}_J)\, \boldsymbol{u}_J \cdot \boldsymbol{E}(\boldsymbol{r}_m), \tag{B.6}$$

such that the average becomes,

$$\frac{\mu}{k_\mathrm{B}T} \sum_{i,j,k} \sum_J \beta_{ijk} \boldsymbol{u}_J \cdot \boldsymbol{E}(\boldsymbol{r}_m) \left\langle (\boldsymbol{u}_\mathrm{OUT} \cdot \boldsymbol{e}_i)(\boldsymbol{u}_Z \cdot \boldsymbol{e}_j)(\boldsymbol{u}_Z \cdot \boldsymbol{e}_k)(\boldsymbol{u}_J \cdot \boldsymbol{e}_3)\right\rangle_0 . \tag{B.7}$$

If $\boldsymbol{u}_J \neq \boldsymbol{u}_\mathrm{OUT}$ then there will be no terms without scalar products raised to an odd power; the only terms that will survive are those with $\boldsymbol{u}_J = \boldsymbol{u}_\mathrm{OUT}$ and we will have,

$$\frac{\mu}{k_\mathrm{B}T} \boldsymbol{u}_\mathrm{OUT} \cdot \boldsymbol{E}(\boldsymbol{r}_m) \sum_{i,j,k} \beta_{ijk} \left\langle (\boldsymbol{u}_\mathrm{OUT} \cdot \boldsymbol{e}_i)(\boldsymbol{u}_Z \cdot \boldsymbol{e}_j)(\boldsymbol{u}_Z \cdot \boldsymbol{e}_k)(\boldsymbol{u}_\mathrm{OUT} \cdot \boldsymbol{e}_3)\right\rangle_0 . \tag{B.8}$$

The individual terms in this sum can be read from the tables of Ref. [343], or calculated following the scheme of Ref. [342]. Depending on whether $\boldsymbol{u}_\mathrm{OUT}$ is parallel or perpendicular to $\boldsymbol{u}_3$ ($\equiv \boldsymbol{u}_\mathrm{IN}$), there are two possible results for this sum [282],

$$\frac{\mu_0 \beta_\parallel}{3k_\mathrm{B}T} (\boldsymbol{u}_\mathrm{OUT} \cdot \boldsymbol{E}(\boldsymbol{r})), \qquad \boldsymbol{u}_\mathrm{OUT} \cdot \boldsymbol{u}_\mathrm{IN} = 1, \tag{B.9a}$$

$$\frac{\mu_0 \beta_\perp}{3k_\mathrm{B}T} (\boldsymbol{u}_\mathrm{OUT} \cdot \boldsymbol{E}(\boldsymbol{r})), \qquad \boldsymbol{u}_\mathrm{OUT} \cdot \boldsymbol{u}_\mathrm{IN} = 0, \tag{B.9b}$$

with $\beta_\parallel$ and $\beta_\perp$ defined,

$$\beta_\parallel = \frac{1}{5} \sum_j (\beta_{3jj} + 2\beta_{jj3}), \tag{B.10a}$$

$$\beta_\perp = \frac{1}{5} \sum_j (2\beta_{3jj} - \beta_{jj3}). \tag{B.10b}$$

Appendix C

Spatial Correlations of Dipoles in an Electric Field

C.1 $\langle \cos\theta \rangle (r)$

Firstly, we look at the mean orientation of a dipole in the electric field of an ion. That is, if $\boldsymbol{\mu}$ is the direction of the dipole moment and $\boldsymbol{E}(r)$ the electric field at the position of the molecule, then we wish to calculate,

$$\langle \cos\theta \rangle (r) = \left\langle \hat{\boldsymbol{\mu}} \cdot \hat{\boldsymbol{E}}(r) \right\rangle, \tag{C.1}$$

with $\hat{\boldsymbol{v}}$ the unit vector in the direction of vector $\boldsymbol{v}$.

The result we derive in this Section is standard [344], but we will carry out the derivation in order to refer to it in Section C.2. The energy of this dipole is $-\boldsymbol{\mu} \cdot \boldsymbol{E}(r)$, and so $\langle \cos\theta \rangle (r)$ can be written,

$$\begin{aligned}
\langle \cos\theta \rangle (r) &= \frac{\int_0^\pi \hat{\boldsymbol{\mu}} \cdot \hat{\boldsymbol{E}}(r) e^{+\boldsymbol{\mu}\cdot\boldsymbol{E}(r)/k_\mathrm{B}T} \sin\theta \, \mathrm{d}\theta}{\int_0^\pi e^{+\boldsymbol{\mu}\cdot\boldsymbol{E}(r)/k_\mathrm{B}T} \sin\theta \, \mathrm{d}\theta}, \\
&= \frac{\int_0^\pi \cos\theta e^{+\mu E(r)\cos\theta/k_\mathrm{B}T} \sin\theta \, \mathrm{d}\theta}{\int_0^\pi e^{+\mu E(r)\cos\theta/k_\mathrm{B}T} \sin\theta \, \mathrm{d}\theta}, \\
&= \coth\left(\mu E(r)/k_\mathrm{B}T\right) - \frac{k_\mathrm{B}T}{\mu E(r)}.
\end{aligned} \tag{C.2}$$

Here, μ is the magnitude of the dipole moment and $E(r)$ the magnitude of the electric field at its position. This can be written in terms of the Langevin function $\mathcal{L}[x] = \coth(x) - 1/x$ as,

$$\langle \cos\theta \rangle\,(r) = \mathcal{L}\left[\mu E(r)/k_{\mathrm{B}}T\right]. \tag{C.3}$$

For small x, we can make use of the Taylor expansion $\mathcal{L}[x] \simeq x/3$ to give,

$$\langle \cos\theta \rangle\,(r) \simeq \frac{\mu E(r)}{3k_{\mathrm{B}}T}. \tag{C.4}$$

So long as the electric field at the position of the dipole is not too large, we would expect this approximation to be quite good. In practice, we have found that for the ions we are considering, it is a good approximation outside of the hard sphere radius of the ion, and will use it in this thesis.

C.2 $\langle \mathrm{COS}\,\psi \rangle\,(r)$

We now wish to calculate the average degree of mutual orientation of water molecules separated by a given distance. If $\boldsymbol{\mu}(0)$ is the dipole moment of a molecule at the origin of a coordinate system and $\boldsymbol{\mu}(r)$ is the dipole moment of a molecule at a distance r from the origin then we define,

$$\begin{aligned} \langle \cos\psi \rangle\,(r) &= \langle \hat{\boldsymbol{\mu}}(0) \cdot \hat{\boldsymbol{\mu}}(r) \rangle\,, \\ &= \langle \langle \hat{\boldsymbol{\mu}}(0) \cdot \hat{\boldsymbol{\mu}}(r) \rangle_{\mathrm{or}} \rangle_{\mathrm{ion}}\,. \end{aligned} \tag{C.5}$$

The average is written in terms of averages over molecular orientations and averages over ionic positions. Because the two molecules do not interact with each

other, their total energy is the sum of the interaction energies of each dipole with its local electric field, $-\left(\boldsymbol{\mu}(0)\cdot\boldsymbol{E}(0)+\boldsymbol{\mu}(r)\cdot\boldsymbol{E}(r)\right)$. We can write the average of Eqn. (C.5) in terms of integrals over $\boldsymbol{\Omega}_0$ and $\boldsymbol{\Omega}_r$, the orientations of the two dipoles, where $\boldsymbol{\Omega}_r = (\cos\vartheta(r), \phi(r))$,

$$\begin{aligned}\langle \cos\psi \rangle\,(r) &= \left\langle \frac{\int \mathrm{d}\boldsymbol{\Omega}_0 \int \mathrm{d}\boldsymbol{\Omega}_r\, \hat{\boldsymbol{\mu}}(0)\cdot\hat{\boldsymbol{\mu}}(r) e^{+(\boldsymbol{\mu}(0)\cdot\boldsymbol{E}(0)+\boldsymbol{\mu}(r)\cdot\boldsymbol{E}(r))/k_\mathrm{B}T}}{\int \mathrm{d}\boldsymbol{\Omega}_0 \int \mathrm{d}\boldsymbol{\Omega}_r\, e^{+(\boldsymbol{\mu}(0)\cdot\boldsymbol{E}(0)+\boldsymbol{\mu}(r)\cdot\boldsymbol{E}(r))/k_\mathrm{B}T}} \right\rangle_{\mathrm{ion}}, \\ &= \left\langle \frac{\int \mathrm{d}\boldsymbol{\Omega}_0 \int \mathrm{d}\boldsymbol{\Omega}_r\, \hat{\boldsymbol{\mu}}(0)\cdot\hat{\boldsymbol{\mu}}(r) e^{+(\boldsymbol{\mu}(0)\cdot\boldsymbol{E}(0)+\boldsymbol{\mu}(r)\cdot\boldsymbol{E}(r))/k_\mathrm{B}T}}{Z(0)Z(r)} \right\rangle_{\mathrm{ion}}, \end{aligned} \tag{C.6}$$

with $Z(r)$ given by,

$$\begin{aligned} Z(r) &= \int \mathrm{d}\vartheta \int \mathrm{d}\phi \sin\vartheta e^{+\mu E(r)\cos\vartheta/k_\mathrm{B}T}, \\ &= 4\pi \frac{\sinh\left(\mu E(r)/k_\mathrm{B}T\right)}{\mu E(r)/k_\mathrm{B}T}., \end{aligned} \tag{C.7}$$

Eqn. (C.6) can be split into an average of a scalar product of two vectors,

$$\left\langle \left(\frac{1}{Z(0)}\int \mathrm{d}\boldsymbol{\Omega}_0\, \hat{\boldsymbol{\mu}}(0) e^{+\boldsymbol{\mu}(0)\cdot\boldsymbol{E}(0)/k_\mathrm{B}T}\right)\cdot\left(\frac{1}{Z(r)}\int \mathrm{d}\boldsymbol{\Omega}_r\, \hat{\boldsymbol{\mu}}(r) e^{+\boldsymbol{\mu}(r)\cdot\boldsymbol{E}(r)/k_\mathrm{B}T}\right)\right\rangle_{\mathrm{ion}}, \tag{C.8}$$

and since both of these integrals have the same form, we need calculate only one of them.

Focusing on,

$$\frac{1}{Z(r)}\int \mathrm{d}\boldsymbol{\Omega}_r\, \hat{\boldsymbol{\mu}}(r) e^{+\boldsymbol{\mu}(r)\cdot\boldsymbol{E}(r)/k_\mathrm{B}T}, \tag{C.9}$$

the vector $\hat{\boldsymbol{\mu}}(r)$ will have three components: one in the direction of the electric field $\boldsymbol{E}(r)$ and two that are orthogonal to the field. Only the first of these components, $\boldsymbol{e}(r)\,(\hat{\boldsymbol{\mu}}(r)\cdot\boldsymbol{e}(r))$, where $\boldsymbol{e}(r)$ is the unit vector in the direction of $\boldsymbol{E}(r)$, will give a

nonzero integral,

$$\boldsymbol{e}(r)\frac{1}{Z(r)}\int \mathrm{d}\boldsymbol{\Omega}_r\, \hat{\boldsymbol{\mu}}(r)\cdot\boldsymbol{e}(r)e^{+\boldsymbol{\mu}(r)\cdot\boldsymbol{E}(r)/k_\mathrm{B}T} = \boldsymbol{e}(r)\int \mathrm{d}\vartheta \int \mathrm{d}\phi \sin\vartheta\cos\vartheta e^{+\mu(r)E(r)\cos\vartheta/k_\mathrm{B}T},$$
$$= \boldsymbol{e}(r)\mathcal{L}\left[\mu E(r)/k_\mathrm{B}T\right], \tag{C.10}$$

where we have chosen the polar axis once again to be parallel to $\boldsymbol{E}(r)$, so that ϑ is the angle between $\hat{\boldsymbol{\mu}}(r)$ and $\boldsymbol{e}(r)$. We thus find,

$$\langle\cos\psi\rangle(r) = \langle\mathcal{L}\left[\mu E(0)/k_\mathrm{B}T\right]\boldsymbol{e}(0)\cdot\boldsymbol{e}(r)\mathcal{L}\left[\mu E(r)/k_\mathrm{B}T\right]\rangle_\mathrm{ion}. \tag{C.11}$$

This form is inconvenient for further calculations, and so we use the high-temperature approximation $\mathcal{L}[x]\simeq x/3$ to obtain a result correct to second order in $1/T$,

$$\langle\cos\psi\rangle(r) \simeq \left(\frac{\mu}{3k_\mathrm{B}T}\right)^2\langle E(0)\boldsymbol{e}(0)\cdot\boldsymbol{e}(r)E(r)\rangle_\mathrm{ion},$$
$$= \left(\frac{\mu}{3k_\mathrm{B}T}\right)^2\langle\boldsymbol{E}(0)\cdot\boldsymbol{E}(r)\rangle_\mathrm{ion}. \tag{C.12}$$

C.3 Fourier Transform of Coulomb Field

Consider the vector field,

$$\boldsymbol{\varepsilon}(\boldsymbol{r}) = \frac{\boldsymbol{r}}{r^3}, \tag{C.13}$$

whose Fourier transform into reciprocal space is,

$$\boldsymbol{\varepsilon}(\boldsymbol{K}) = \int \boldsymbol{\varepsilon}(\boldsymbol{r})e^{-i\boldsymbol{K}\cdot\boldsymbol{r}}\,\mathrm{d}^3\boldsymbol{r}. \tag{C.14}$$

As in Sec. 5.2.2 we can introduce $\boldsymbol{\nabla}_K$, the gradient operator with respect to the

$\boldsymbol{K}$ vector. This allows us to write,

$$\begin{aligned}\boldsymbol{\varepsilon}(\boldsymbol{K}) &= \int \frac{\boldsymbol{r}}{r^3} e^{-i\boldsymbol{K}\cdot\boldsymbol{r}}\,\mathrm{d}^3\boldsymbol{r}, \\ &= i\boldsymbol{\nabla}_K \int \frac{1}{r^3} e^{-i\boldsymbol{K}\cdot\boldsymbol{r}}\,\mathrm{d}^3\boldsymbol{r}. \end{aligned} \tag{C.15}$$

Carrying out the integral in polar coordinates,

$$\begin{aligned}\boldsymbol{\varepsilon}(\boldsymbol{K}) &= 2\pi i\boldsymbol{\nabla}_K \int_0^\pi \mathrm{d}\theta \int_0^\infty \mathrm{d}r\, \frac{\sin\theta}{r} e^{-iKr\cos\theta}, \\ &= 4\pi i\boldsymbol{\nabla}_K \int_0^\infty \frac{\sin(Kr)}{Kr^2}\,\mathrm{d}r, \\ &= 4\pi i\boldsymbol{e}_K \frac{\partial}{\partial K} \int_0^\infty \frac{\sin(Kr)}{Kr^2}\,\mathrm{d}r, \\ &= 4\pi i\boldsymbol{e}_K \int_0^\infty \left[\frac{\cos(Kr)}{Kr} - \frac{\sin(Kr)}{K^2r^2}\right]\,\mathrm{d}r, \\ &= -4\pi i\boldsymbol{e}_K/K. \end{aligned} \tag{C.16}$$

C.4 $\langle \cos\psi \rangle\,(r)$ With Excluded Volume

We wish to evaluate Eqn. (5.63) to derive an expression for $\langle \cos\psi \rangle\,(r)$ appropriate to a solution in which no water molecules are found within a distance a of any ions. We begin by rewriting the integrand,

$$\begin{aligned}\langle \cos\psi \rangle_{\mathrm{HS}}\,(r) = \frac{\rho}{4}\left(\frac{\mu_0 Q f(0)}{3\pi\epsilon k_{\mathrm{B}}T}\right)^2 \frac{1}{a^2 r} \times \\ \int_0^\infty \frac{\left[2\sin(Kr) - \sin(2Ka + Kr) + \sin(2Ka - Kr)\right]}{K\left(K^2 + \kappa_{\mathrm{D}}^2\right)}\,\mathrm{d}K. \end{aligned} \tag{C.17}$$

We use contour integration to evaluate this expression. There are three terms, each of the form,

$$c\int_0^\infty \frac{\sin(Kx)}{K\left(K^2 + \kappa_{\mathrm{D}}^2\right)}\,\mathrm{d}K. \tag{C.18}$$

For the first two terms of Eqn. (C.17), x is always positive and we integrate $e^{iKx}/2iK\left(K^2+\kappa_{\mathrm{D}}^2\right)$ over the contour of Fig. C.1 for $y \to 0$ and $R \to \infty$. In these limits the integral over the semicircle of radius R vanishes and the integral over the smaller semicircle becomes $-\frac{c\pi}{2\kappa_{\mathrm{D}}^2}$ so that,

$$c\int_0^\infty \frac{\sin(Kx)}{K\left(K^2+\kappa_{\mathrm{D}}^2\right)}\,\mathrm{d}K = \frac{c\pi}{2\kappa_{\mathrm{D}}^2} + 2\pi i \operatorname*{Res}_{K=i\kappa_{\mathrm{D}}} \left\{ \frac{ce^{iKx}/2i}{K\left(K^2+\kappa_{\mathrm{D}}^2\right)} \right\}$$
$$= \frac{c\pi}{2\kappa_{\mathrm{D}}^2}\left[1-e^{-\kappa_{\mathrm{D}}x}\right]. \tag{C.19}$$

For the third term, if $2a > r$ then x is positive and we obtain the same result. However, if $2a < r$ then we must integrate over the contour of Fig. C.2 with $y \to 0$ and $R \to \infty$ in order that the integrals over the large semicircle vanishes. In this case the integral over the small semicircle is $\frac{c\pi}{2\kappa_{\mathrm{D}}^2}$ and we find,

$$c\int_0^\infty \frac{\sin(Kx)}{K\left(K^2+\kappa_{\mathrm{D}}^2\right)}\,\mathrm{d}K = -\frac{c\pi}{2\kappa_{\mathrm{D}}^2} - 2\pi i \operatorname*{Res}_{K=-i\kappa_{\mathrm{D}}} \left\{ \frac{ce^{iKx}/2i}{K\left(K^2+\kappa_{\mathrm{D}}^2\right)} \right\}$$
$$= \frac{c\pi}{2\kappa_{\mathrm{D}}^2}\left[-1+e^{+\kappa_{\mathrm{D}}x}\right]. \tag{C.20}$$

The integral of Eqn. (C.17) is thus defined piecewise depending on the value of r relative to $2a$. The result is,

$$\langle \cos\psi \rangle_{\mathrm{HS}}(r) = \rho\left(\frac{\mu_0 Q f(0)}{3a\varepsilon\kappa_{\mathrm{D}}k_{\mathrm{B}}T}\right)^2 \frac{1}{8\pi r}\times$$
$$\left(1-2e^{-\kappa_{\mathrm{D}}r}+e^{-\kappa_{\mathrm{D}}(2a+r)}-\mathrm{sgn}\left[2a-r\right]\left\{e^{-\kappa_{\mathrm{D}}|2a-r|}-1\right\}\right), \tag{C.21}$$

as in the text.

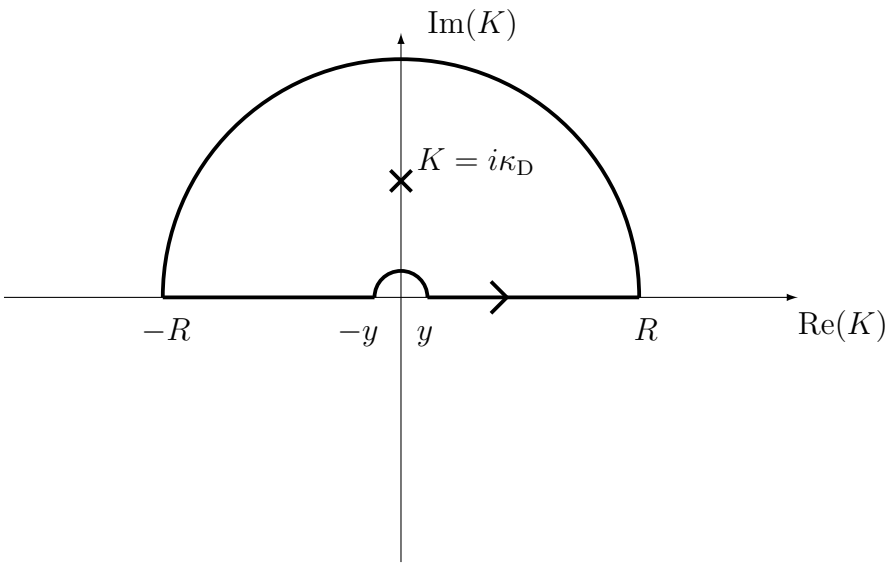

Figure C.1: Contour used for evaluating the first two terms of Eqn. (C.17) and for evaluating the third term when $2a > r$.

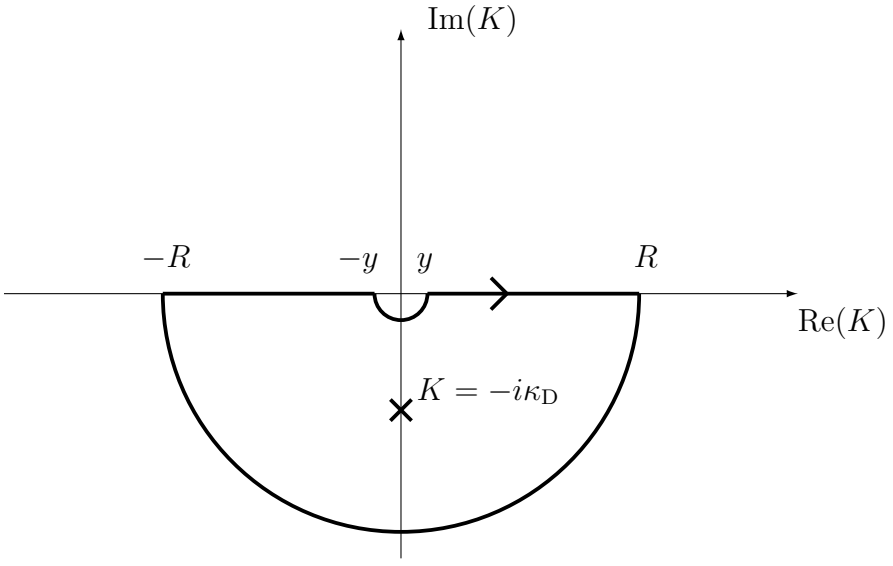

Figure C.2: Contour used for evaluating the third term of Eqn. (C.17) when $2a < r$.

Appendix D

l^{th}-Order Relaxation Times in Debye Reorientation

Consider a vector of fixed length, whose orientation in space is specified by the polar angles θ and ϕ. The polar angle is defined to be parallel to the initial orientation of this vector, so that θ is the angle between the initial vector and its current orientation.

Let $f(\theta, t)$ be the orientational probability distribution function such that,

$$f(\theta, t) \sin\theta \, \mathrm{d}\theta \tag{D.1}$$

is the probability that the molecule has an orientation within the interval $[\theta, \theta + \mathrm{d}\theta]$ at time t.

By analogy with translational diffusion, $f(\theta, t)$ can be shown to obey the diffusion equation [330],

$$\begin{aligned} \frac{1}{D_r}\frac{\partial f}{\partial t} &= \nabla^2 f \\ &= \frac{1}{\sin\theta}\frac{\partial}{\partial\theta}\left(\sin\theta\frac{\partial f}{\partial\theta}\right), \end{aligned} \tag{D.2}$$

where D_{R} is a rotational diffusion constant.

The distribution can be expanded as,

$$f(\theta,t)=\sum_{m=0}^{\infty}P_m\left[\cos\theta\right]g_m(t), \tag{D.3}$$

with $P_m\left[x\right]$ the m^{th} Legendre polynomial in x and $g_m(t)$ an expansion function. Inserting this expansion into Eqn. (D.2) gives,

$$\sum_{m=0}^{\infty}P_m\left[\cos\theta\right]g'_m(t)=D_{\text{R}}\sum_{m=0}^{\infty}\frac{1}{\sin\theta}\frac{\partial}{\partial\theta}\left(\sin\theta\frac{\partial P_m\left[\cos\theta\right]}{\partial\theta}\right)g_m(t). \tag{D.4}$$

Using the identity [303],

$$\frac{1}{\sin\theta}\frac{\partial}{\partial\theta}\left(\sin\theta\frac{\partial P_m\left[\cos\theta\right]}{\partial\theta}\right)=-m(m+1)P_l\left[\cos\theta\right], \tag{D.5}$$

the diffusion equation becomes,

$$\sum_{m=0}^{\infty}P_m\left[\cos\theta\right]\left\{g'_m(t)+D_{\text{R}}m(m+1)g_m(t)\right\}=0. \tag{D.6}$$

The orthogonality of the Legendre polynomials,

$$\int_0^{\pi}P_l\left[\cos\theta\right]P_m\left[\cos\theta\right]\sin\theta\,\mathrm{d}\theta=\frac{1}{l+1/2}\delta_{lm}, \tag{D.7}$$

means that multiplying Eqn. (D.6) by $P_l\left[\cos\theta\right]\sin\theta$ and integrating over θ gives the differential equation,

$$g'_m(t)=-D_{\text{R}}m(m+1)g_m(t). \tag{D.8}$$

The solution of this equation is $g_m(t)=A_me^{-D_{\text{R}}m(m+1)t}$. The probability distribution function $f(\theta,t)$ is then,

$$f(\theta,t)=\sum_{m=0}^{\infty}A_mP_m\left[\cos\theta\right]e^{-D_{\text{R}}m(m+1)t}, \tag{D.9}$$

with,

$$A_m=(m+1/2)\int_0^{\pi}f(\theta,0)P_m\left[\cos\theta\right]\sin\theta\,\mathrm{d}\theta. \tag{D.10}$$

Initially, $\cos\theta = 1$, so that $f(\theta, 0) = \delta_+(\cos\theta - 1)$, where $\delta_+(x)$ is the one-sided delta function, defined for $x \geq 0$ such that $\int_0^\infty \delta_+(x)\,\mathrm{d}x = 1$. Then,

$$\begin{aligned} A_m &= (m + 1/2) \int_0^\pi \delta_+ \left(\cos\theta - 1\right) P_m \left[\cos\theta\right] \,\mathrm{d}\left(\cos\theta\right), \\ &= (m + 1/2) \int_{-1}^1 \delta_+ \left(x - 1\right) P_l \left[x\right] \,\mathrm{d}x, \\ &= (m + 1/2)\, P_l \left[1\right], \\ &= (m + 1/2). \end{aligned} \tag{D.11}$$

$f(\theta, t)$ can now be used to find an expression for the time correlation function $C_l(t)$,

$$\begin{aligned} C_l(t) &= \langle P_l \left[\cos\theta(t)\right] \rangle, \\ &= \int_0^\pi P_l \left[\cos\theta\right] f(\theta, t) \sin\theta \mathrm{d}\theta, \\ &= \sum_{m=0}^{\infty} (m + 1/2)\, e^{-D_{\mathrm{R}} m(m+1)t} \int_0^\pi P_l \left[\cos\theta\right] P_m \left[\cos\theta\right] \sin\theta \mathrm{d}\theta, \\ &= e^{-D_{\mathrm{R}} l(l+1)t}, \\ &= e^{-t/\tau_l}. \end{aligned} \tag{D.12}$$

In going from the third to the fourth line, the orthogonality of Legendre polynomials has been used. Comparing the final two lines shows that the l^{th}-order relaxation time is given by,

$$\tau_l = \frac{1}{D_{\mathrm{R}} l(l+1)}. \tag{D.13}$$

Bibliography

[1] F. Franks. *Water: A Comprehensive Treatise*, volume 1. Plenum Press, New York, 1972.

[2] J. A. Barker and R. O. Watts. *Chem. Phys. Lett.*, 3:144, 1969.

[3] A. Rahman and F. Stillinger. *J. Chem. Phys.*, 55:3336, 1971.

[4] R. W. Impey, P. A. Madden, and I. R. McDonald. *J. Phys. Chem.*, 87:5071, 1983.

[5] H. Ohtaki and T. Radnai. *Chem. Rev.*, 93:1157, 1993.

[6] R. Rey and J. T. Hynes. *J. Phys. Chem.*, 100:5611, 1996.

[7] S. Koneshan, J. C. Rasaiah, R. M. Lynden-Bell, and S. H. Lee. *J. Phys. Chem. B*, 102:4193, 1998.

[8] S. Kerisit and K. M. Rosso. *J. Chem. Phys.*, 131:114512, 2009.

[9] P. Varilly and D. Chandler. *J. Phys. Chem. B*, 117:1419, 2013.

[10] N. Musolino and B. L. Trout. *J. Chem. Phys.*, 138:134707, 2013.

[11] L. X. Dang. *J. Phys. Chem. B*, 106:10388, 2002.

[12] D. E. Otten, P. R. Shaffer, P. L. Geissler, and R. J. Saykally. *Proc. Nat. Acad. Sci. USA*, 109:701, 2012.

[13] G.-J. Kroes. *Surf. Sci.*, 275:365, 1992.

[14] F. Paesani and G. A. Voth. *J. Phys. Chem. C*, 112:324, 2008.

[15] D. T. Limmer and D. Chandler. *J. Chem. Phys.*, 141:18C505, 2014.

[16] H. J. C. Berendsen, J. R. Grigera, and T. P. Straatsma. *J. Phys. Chem.*, 91:6269, 1987.

[17] W. L. Jorgensen and J. D. Madura. *Mol. Phys.*, 56:1381, 1985.

[18] G. S. Fanourgakis and S. S. Xantheas. *J. Chem. Phys.*, 128:074506, 2008.

[19] J. Zielkiewicz. *J. Chem. Phys.*, 123:104501, 2005.

[20] X. Huafeng, H. A. Stern, and B. J. Berne. *J. Phys. Chem. B*, 106:2054, 2002.

[21] K. Laasonen, M. Sprik, and M. Parrinello. *J. Chem. Phys.*, 99:9080, 1993.

[22] M. E. Tuckerman, K. Laasonen, M. Sprik, and M. Parrinello. *J. Phys. Condens. Matt.*, 6:A93, 1994.

[23] T. C. Berkelbach, H.-S. Lee, and M. E. Tuckerman. *Phys. Rev. Lett.*, 103:238302, 2009.

[24] C. B. Messner, T. S. Hofer, B. R. Randolf, and B. M. Rode. *Phys. Chem. Chem. Phys.*, 13:224, 2011.

[25] R. A. Kuharski and P. J. Rossky. *Chem. Phys. Lett.*, 103:357, 1984.

[26] A. Wallqvist and B. J. Berne. *Chem. Phys. Lett.*, 117:214, 1985.

[27] J. Lobaugh and G. A. Voth. *J. Chem. Phys.*, 106:2400, 1997.

[28] T. F. Miller and D. E. Manolopoulos. *J. Chem. Phys.*, 123:154504, 2005.

[29] L. Hernández de la Peña and P. G. Kusalik. *J. Chem. Phys.*, 121:5992, 2004.

[30] L. Hernández de la Peña and P. G. Kusalik. *J. Chem. Phys.*, 125:054512, 2006.

[31] F. Paesani, S. Iuchi, and G. A Voth. *J. Chem. Phys.*, 127:074506, 2007.

[32] S. Habershon, T. E. Markland, and D. E. Manolopoulos. *J. Chem. Phys.*, 131:024501, 2009.

[33] X.-Z. Li, B. Walker, and A. Michaelides. *Proc. Nat. Acad. Sci. USA*, 108:6369, 2011.

[34] W. M. Haynes, editor. *CRC Handbook of Chemistry and Physics*. Taylor & Francis, Boca Raton, 92nd edition, 2011.

[35] R. P. Bell. *The Tunnel Effect in Chemistry*. Springer, Cambridge, 1980.

[36] H.-H. Limbach, J. M. Lopez, and A. Kohen. *Phil. Trans. R. Soc. B*, 361:1399, 2006.

[37] M. J. Knapp and J. P. Klinman. *Eur. J. Biochem.*, 269:3113, 2002.

[38] T. Hama and N. Watanabe. *Chem. Rev.*, 113:8783, 2013.

[39] T. E. Markland and B. J. Berne. *Proc. Nat. Acad. Sci. USA*, 109:7988, 2012.

[40] W. A. Oates, R. Lässer, T. Kuji, and T. B. Flanagan. *J. Phys. Chem. Solids*, 47:429, 1986.

[41] T. B. Flanagan and W. A. Oates. *Annu Rev. Mater. Sci.*, 21:269, 1991.

[42] R. P. Feynman and A. R. Hibbs. *Quantum Mechanics and Path Integrals*. Dover, Mineola, New York, emended edition, 2010.

[43] D. Chandler. *J. Chem. Phys.*, 74:4078, 1981.

[44] M. Parrinello and A. Rahman. *J. Chem. Phys.*, 80:860, 1984.

[45] R. A. Kuharski and P. J. Rossky. *J. Chem. Phys.*, 82:5164, 1985.

[46] G. S. Del Buono, P. J. Rossky, and J. Schnitker. *J. Chem. Phys.*, 95:3728, 1991.

[47] H. A. Stern and B. J. Berne. *J. Chem. Phys.*, 115:7622, 2001.

[48] J. Cao and G. A. Voth. *J. Chem. Phys.*, 100:5106, 1994.

[49] S. Jang and G. A. Voth. *J. Chem. Phys.*, 111:2371, 1999.

[50] I. R. Craig and D. E. Manolopoulos. *J. Chem. Phys.*, 121:3368, 2004.

[51] S. Habershon, D. E. Manolopoulos, T. E. Markland, and T. F. Miller. *Annu. Rev. Phys. Chem.*, 64:387, 2013.

[52] F. Paesani, S. Yoo, H. J. Bakker, and S. S. Xantheas. *J. Phys. Chem. Lett.*, 1:2316, 2010.

[53] S. Habershon, G. S. Fanourgakis, and D. E. Manolopoulos. *J. Chem. Phys.*, 129:074501, 2008.

[54] F. Paesani, W. Zhang, D. A. Case, T. E. Cheatham, and G. A. Voth. *J. Chem. Phys.*, 125:184507, 2013.

[55] T. F. Miller and D. E. Manolopoulos. *J. Chem. Phys.*, 122:184503, 2005.

[56] V. Babin, C. Leforestier, and F. Paesani. *J. Chem. Theor. Comput.*, 9:5395, 2013.

[57] V. Babin, G. R. Medders, and F. Paesani. *J. Chem. Theor. Comput.*, 10:1599, 2014.

[58] G. R. Medders, V. Babin, and F. Paesani. *J. Chem. Theor. Comput.*, 10:2906, 2014.

[59] D. Marx and M. Parrinello. *Z. Phys. B*, 95:143, 1994.

[60] D. Marx and M. Parrinello. *J. Chem. Phys.*, 104:4077, 1996.

[61] R. N. Barnett, H.-P. Chang, H. Hakkinen, and U. Landman. *J. Phys. Chem.*, 99:7731, 1995.

[62] D. Marx, M. E. Tuckerman, and M. Parrinello. *J. Phys. Condens. Matt.*, 12:153, 2000.

[63] S. Biermann, D. Hohl, and D. Marx. *J. Low Temp. Phys.*, 110:97, 1998.

[64] T. E. Markland and D. E. Manolopoulos. *J. Chem. Phys.*, 129:024105, 2008.

[65] T. E. Markland and D. E. Manolopoulos. *Chem. Phys. Lett.*, 464:256, 2008.

[66] O. Marsalek and T. E. Markland. *J. Chem. Phys.*, 144:054112, 2016.

[67] M. Ceriotti, M. Parrinello, T. E. Markland, and D. E. Manolopoulos. *J. Chem. Phys.*, 133:124104, 2010.

[68] M. Ceriotti, D. E. Manolopoulos, and M. Parrinello. *J. Chem. Phys.*, 134:084104, 2011.

[69] M. Ceriotti and D. E. Manolopoulos. *Phys. Rev. Lett.*, 109:100604, 2012.

[70] A. P. Willard and D. Chandler. *J. Phys. Chem. B*, 114:1954, 2010.

[71] D. A. McQuarrie. *Statistical Mechanics*. University Science Books, Sausalito, 2000.

[72] A. Szabo and N. S. Ostlund. *Modern Quantum Chemistry*. Dover, Mineola, New York, 1996.

[73] M. P. Allen and D. J. Tildesley. *Computer Simulation of Liquids*. Oxford University Press, Oxford, 1987.

[74] D. Frenkel and B. Smit. *Understanding Molecular Simulation: from Algorithms to Applications*. Elsevier, San Diego, 2nd edition, 2002.

[75] R. Car and M. Parrinello. *Phys. Rev. Lett.*, 55:2471, 1985.

[76] M. E. Tuckerman, D. Marx, M. L. Klein, and M. Parrinello. *J. Chem. Phys.*, 104:5579, 2000.

[77] J. S. Tse. *Annu. Rev. Phys. Chem.*, 53:249, 2002.

[78] C. Vega, E. Sanz, and J. L. F. Abascal. *J. Chem. Phys.*, 122:114507, 2005.

[79] A. Rahman. *Phys. Rev.*, 136:A405, 1964.

[80] N. Metropolis, A. W. Rosenbluth, M. N. Rosenbluth, A. H. Teller, and E. Teller. *J. Chem. Phys.*, 21:1087, 1953.

[81] P. H. Hünenberger. Thermostat Algorithms for Molecular Dynamics Simulations. In C. Holm and K. Kremer, editors, *Adv. Polymer Sci Volume 173*, pages 105–149. Springer-Verlag, Heidelberg, 2005.

[82] M. E. Tuckerman. *Statistical Mechanics and Molecular Simulations*. Oxford University Press, Oxford, 2010.

[83] P. Turq, F. Lantelme, and H. L. Friedman. *J. Chem. Phys.*, 66:3039, 1977.

[84] T. Schneider and E. Stoll. *Phys. Rev. B*, 17:1302, 1978.

[85] G. Bussi and M. Parrinello. *Phys. Rev. E.*, 75:056707, 2007.

[86] N. Watanabe and A. Kouchi. *Prog. Surf. Sci.*, 83:439, 2008.

[87] Y. Cha, C. Murray, and J. Klinman. *Science*, 243:1325, 1989.

[88] Z. D. Nagel and J. P. Klinman. *Chem. Rev.*, 106:3095, 2006.

[89] R. P. Feynman. *Rev. Mod. Phys.*, 20:367, 1948.

[90] R. P. Feynman. *Statistical Mechanics: a Set of Lectures*. Addison-Wesley, Redwood City, 1972.

[91] R. Zwanzig. *Annu. Rev. Phys. Chem.*, 16:67, 1965.

[92] R. Kubo. *J. Phys. Soc. Jpn.*, 12:570, 1957.

[93] R Kubo. *Rep. Prog. Phys.*, 29:255, 1966.

[94] T. Yamamoto. *J. Chem. Phys.*, 33:281, 1960.

[95] W. H. Miller. *J. Chem. Phys.*, 61:1823, 1974.

[96] L. Van Hove. *Phys. Rev.*, 95:249, 1954.

[97] S. H. Glarum. *J. Chem. Phys.*, 33:1371, 1960.

[98] D. Laage and J. T. Hynes. *J. Phys. Chem. B*, 112:14230, 2008.

[99] T. J. H. Hele, M. J. Willatt, A. Muolo, and S. C. Althorpe. *J. Chem. Phys.*, 142:134103, 2015.

[100] T. J. H. Hele, M. J. Willatt, A. Muolo, and S. C. Althorpe. *J. Chem. Phys.*, 142:191101, 2015.

[101] B. J Braams and D. E. Manolopoulos. *J. Chem. Phys.*, 125:124105, 2006.

[102] S. Jang, A. V. Sinitskiy, and G. A. Voth. *J. Chem. Phys.*, 140:154103, 2014.

[103] I. R. Craig and D. E. Manolopoulos. *J. Chem. Phys.*, 122:84106, 2005.

[104] I. R. Craig and D. E. Manolopoulos. *J. Chem. Phys.*, 123:34102, 2005.

[105] J. O. Richardson and S. C. Althorpe. *J. Chem. Phys.*, 131:214106, 2009.

[106] T. J. H. Hele and S. C. Althorpe. *J. Chem. Phys.*, 138:084108, 2013.

[107] T. J. H. Hele and S. C. Althorpe. *J. Chem. Phys.*, 139:084115, 2013.

[108] T. J. H. Hele and S. C. Althorpe. *J. Chem. Phys.*, 139:084116, 2013.

[109] R. W. Hall and B. J. Berne. *J. Chem. Phys.*, 81:3641, 1984.

[110] M. Rossi, M. Ceriotti, and D. E. Manolopoulos. *J. Chem. Phys.*, 140:234116, 2014.

[111] T. D. Hone, P. J. Rossky, and G. A. Voth. *J. Chem. Phys.*, 124:154103, 2006.

[112] C. G. Swain, E. C. Stivers, J. F. Reuwer, and L. J. Schaad. *J. Am. Chem. Soc.*, 80:5885, 1958.

[113] J. Hirschi and D. A. Singleton. *J. Am. Chem. Soc.*, 127:3294, 2005.

[114] A. H. Cockett and A. Ferguson. *Phil. Mag.*, 28:685, 1939.

[115] P. E. Videla, P. J Rossky, and D. Laria. *J. Chem. Phys.*, 139:164506, 2013.

[116] C. P. Herrero and R. Ramírez. *J. Chem. Phys.*, 134:094510, 2011.

[117] C. P. Herrero and R. Ramírez. *Phys. Rev. B*, 84:224112, 2011.

[118] C. P. Herrero and R. Ramírez. *J. Chem. Phys.*, 137:104505, 2012.

[119] M. F. Herman, E. J. Bruskin, and B. J. Berne. *J. Chem. Phys.*, 76:5150, 1982.

[120] J. Cao and B. J. Berne. *J. Chem. Phys.*, 91:6359, 1989.

[121] J. Liu, R. S. Andino, C. M. Miller, X. Chen, D. M. Wilkins, M. Ceriotti, and D. E. Manolopoulos. *J. Phys. Chem. C*, 117:2944, 2013.

[122] G. Romanelli, M. Ceriotti, D. E. Manolopoulos, C. Pantalei, R. Senesi, and C. Andreani. *J. Phys. Chem. Letters*, 4:3251, 2013.

[123] W. Kabsch. *Acta Crystallog. A*, 32:922, 1976.

[124] W. Kabsch. *Acta Crystallog. A*, 34:827, 1978.

[125] J. E. Bertie and Z. Lan. *Appl. Spect.*, 50:1047, 1996.

[126] J. R. Gat. *Annu. Rev. Earth Planet. Sci.*, 24:225, 1996.

[127] C. D. Cappa, W. S. Drisdell, J. D. Smith, R. J. Saykally, and R. C. Cohen. *J. Phys. Chem. B*, 109:24391, 2005.

[128] C. D. Cappa, J. D. Smith, W. S. Drisdell, R. J. Saykally, and R. C. Cohen. *J. Phys. Chem. C*, 111:7011, 2007.

[129] B. Boehrer and M. Schultze. *Rev. Geophys.*, 46:RG2005, 2008.

[130] J. H. Hu, Q. Shi, P. Davidovits, D. R. Worsnop, M. S. Zahniser, and C. E. Kolb. *J. Phys. Chem.*, 99:8768, 1995.

[131] D. R. Hanson. *J. Phys. Chem. B*, 101:4998, 1997.

[132] G. M. Nathanson. *Annu. Rev. Phys. Chem.*, 55:231, 2004.

[133] P. Davidovits, C. E. Kolb, L. R. Williams, J. T. Jayne, and D. R. Worsnop. *Chem. Rev.*, 106:1323, 2006.

[134] Y. R. Shen. *Annu. Rev. Phys. Chem.*, 40:327, 1989.

[135] F. Vidal and A. Tadjeddine. *Rep. Prog. Phys.*, 68:1095, 2005.

[136] Y. R. Shen and V. Ostroverkhov. *Chem. Rev.*, 106:1140, 2006.

[137] J. Horita and D. J. Wesolowski. *Geochim. Cosmochim. Acta*, 58:3425, 1994.

[138] Araguás-Araguás L. S., K. Froehlich, and K. Rozanski. *Hydrolog. Proc.*, 14:1341, 2000.

[139] J. Worden, d. Noone, and K. Bowman. *Nature*, 445:528, 2007.

[140] C. Lorius, L. Merlivat, J. Jouzel, and M. Pourchet. *Nature*, 280:644, 1979.

[141] J. R. Petit, J. Jouzel, D. Raynaud, N. I. Barkov, J.-M. Barnola, I. Basile, M. Bender, J. Chappellaz, M. Davis, G. Delaygue, M. Delmotte, V. M. Kotlyakov, M. Legrand, V. Y. Lipenkov, C. Lorius, L. Pepin, C. Ritz, E. Saltzman, and M. Stievenard. *Nature*, 399:429, 1999.

[142] F. Vimeux, V. Masson, G. Delaygue, J. Jouzel, J. R. Petit, and M. Stievenard. *J. Geophys. Res. Atmos.*, 106:31863, 2001.

[143] F. Zernike and J. E. Midwinter. *Applied Nonlinear Optics*. John Wiley and Sons, New York, 1973.

[144] D. A. Long. *The Raman Effect: A Unified Treatment of the Theory of Raman Scattering by Molecules*. John Wiley and Sons, Chichester, 2002.

[145] S. H. Lin and A. A. Villaeys. *Phys. Rev. A*, 50:5134, 1994.

[146] Y. R. Shen. *Nature*, 337:519, 1989.

[147] G Richmond. *Annu. Rev. Phys. Chem.*, 52:357, 2001.

[148] Q. Du, R. Superfine, E. Freysz, and Y. Shen. *Phys. Rev. Lett.*, 70:2313, 1993.

[149] D. E. Gragson and G. L. Richmond. *J. Phys. Chem. B*, 102:366, 1998.

[150] M. J. Schultz, S. Baldelli, C. Schnitzer, and D. Simonelli. *J. Phys. Chem. B*, 106:5313, 2002.

[151] D. Liu, G. Ma, L. M. Levering, and H. C. Allen. *J. Phys. Chem. B*, 108:2252, 2004.

[152] W. Gan, D. Wu, Z. Zhang, R.-R. Feng, and H.-F. Wang. *J. Chem. Phys.*, 124:114705, 2005.

[153] M. Sovago, R. K. Campen, G. W. H. Wurpel, M. Müller, H. J. Bakker, and M. Bonn. *Phys. Rev. Lett.*, 100:173901, 2008.

[154] I. V. Stiopkin, C. Weeraman, P. A. Pieniazek, F. Y. Shalhout, J. L. Skinner, and A. V. Benderskii. *Nature*, 474:192, 2011.

[155] X. Wei, P. Miranda, and Y. Shen. *Phys. Rev. Lett.*, 86:1554, 2001.

[156] X. Wei, P. Miranda, C. Zhang, and Y. Shen. *Phys. Rev. B*, 66:085401, 2002.

[157] M. G. Brown, E. A. Raymond, H. C. Allen, L. F. Scatena, and G. L. Richmond. *J. Phys. Chem. A*, 104:10220, 2000.

[158] L. F. Scatena and G. L. Richmond. *J. Phys. Chem. B*, 105:11240, 2001.

[159] L. F. Scatena and G. L. Richmond. *Chem. Phys. Lett.*, 383:491, 2004.

[160] L. F. Scatena and G. L. Richmond. *J. Phys. Chem. B*, 108:12518, 2004.

[161] Q. Du, E. Freysz, and Y. R. Shen. *Phys. Rev. Lett.*, 72:238, 1994.

[162] M. S. Yeganeh, S. M. Dougal, and H. S. Pink. *Phys. Rev. Lett.*, 83:1179, 1999.

[163] K. A. Becraft and G. L. Richmond. *Langmuir*, 17:7721, 2001.

[164] S. Kataoka, M. C. Gurau, F. Albertorio, M. A. Holden, S.-M. Lim, R. D. Yang, and P. S. Cremer. *Langmuir*, 20:1662, 2004.

[165] W. Gan, D. Wu, Z. Zhang, R.-R. Feng, and H.-F. Wang. *J. Chem. Phys.*, 124:114705, 2006.

[166] D. F. Coker, R. E. Miller, and R. O. Watts. *J. Chem. Phys.*, 82:3554, 1985.

[167] Q. Du, E. Freysz, and Y. R. Shen. *Science*, 264:826, 1994.

[168] J. J. Kipling. *J. Colloid Sci.*, 18:502, 1963.

[169] E. A. Raymond, T. L. Tarbuck, and G. L. Richmond. *J. Phys. Chem. B*, 106:2817, 2002.

[170] E. A. Raymond, T. L. Tarbuck, M. G. Brown, and G. L. Richmond. *J. Phys. Chem. B*, 107:546, 2003.

[171] Y. Nagata, R. E. Pool, E. H. G. Backus, and M. Bonn. *Phys. Rev. Lett.*, 109:226101, 2012.

[172] I. Benjamin. *Phys. Rev. Lett.*, 73:2083, 1994.

[173] A. Morita and J. T. Hynes. *Chem. Phys.*, 258:371, 2000.

[174] A. Morita and J. T. Hynes. *J. Phys. Chem. B*, 106:673, 2002.

[175] E. C. Brown, M. Mucha, P. Jungwirth, and D. J. Tobias. *J. Phys. Chem. B*, 109:7934, 2005.

[176] S. Gopalakrishnan, P. Jungwirth, D. J. Tobias, and H. C. Allen. *J. Phys. Chem. B*, 109:8861, 2005.

[177] P. Jungwirth and Douglas J. Tobias. *Chem. Rev.*, 106:1259, 2006.

[178] B. M. Auer and J. L. Skinner. *J. Phys. Chem. B*, 113:4125, 2009.

[179] T. Imamura, T. Ishiyama, and A. Morita. *J. Phys. Chem. C*, 118:29017, 2014.

[180] T.-M. Chang and L. X. Dang. *Chem. Rev.*, 106:1305, 2006.

[181] F. P. Buff, R. A. Lovett, and F. H. Stillinger. *Phys. Rev. Lett.*, 15:621, 1965.

[182] J. D. Weeks. *J. Chem. Phys.*, 67:3106, 1977.

[183] M. Ceriotti and T. E. Markland. *J. Chem. Phys.*, 138:014112, 2013.

[184] D. M. Wilkins, D. E. Manolopoulos, and L. X. Dang. *J. Chem. Phys.*, 142:064509, 2015.

[185] S. Arrhenius. *Z. Physik. Chem.*, 1:631, 1887.

[186] K. A. Dill. *Biochem.*, 29:7133, 1990.

[187] C. Zhang and P. Carloni. *J. Phys. Condens. Matt.*, 24:124109, 2012.

[188] M. Barton and J. D. Atwood. *J. Coord. Chem.*, 24:43, 1991.

[189] W. A. Herrmann and B. Cornils. *Angew. Chem.*, 36:1048, 2003.

[190] J. W. Steed. *Chem. Soc. Rev.*, 38:506, 2009.

[191] J. R. Mor and R. Guarnaccia. *Anal. Biochem.*, 79:319, 1977.

[192] S. Park, H. Boo, and T. D. Chung. *Anal. Chim. Acta*, 556:46, 2006.

[193] A. Heller and B. Feldman. *Chem. Rev.*, 108:2482, 2008.

[194] M. D. Tissandier, K. A. Cowen, W. Y. Feng, E. Gundlach, M. H. Cohen, A. D. Earhart, J. V. Coe, and T. R. Tuttle. *J. Phys. Chem. A*, 102:7787, 1998.

[195] M. Born. *Z. Phys.*, 1:45, 1920.

[196] R. M. Fuoss. *Proc. Nat. Acad. Sci. USA*, 45:807, 1959.

[197] R. Zwanzig. *J. Chem. Phys.*, 38:1603, 1963.

[198] P. G. Wolynes. *Annu. Rev. Phys. Chem.*, 31:345, 1980.

[199] J. I. Kim. *J. Phys. Chem.*, 82:191, 1978.

[200] Y. Marcus. *J. Chem. Soc. Faraday Trans. 1*, 82:233, 1986.

[201] Y. Marcus. *J. Chem. Soc. Faraday Trans.*, 87:2995, 1991.

[202] R. Schurhammer and G. Wipff. *New J. Chem.*, 23:381, 1999.

[203] S. H. Lee and J. C. Rasaiah. *J. Phys. Chem.*, 100:1420, 1996.

[204] D. Spångberg, M. Wojcik, and K. Hermansson. *Chem. Phys. Lett.*, 276:114, 1997.

[205] K. Hermansson and M. Wojcik. *J. Phys. Chem. B*, 102:6089, 1998.

[206] D. Spångberg, R. Rey, J. T. Hynes, and K. Hermansson. *J. Phys. Chem. B*, 107:4470, 2003.

[207] A. Chandra. *J. Phys. Chem. B*, 107:3899, 2003.

[208] T. S. Hofer, H. T. Tran, C. F. Schwenk, and B. M. Rode. *J. Comp. Chem.*, 25:211, 2004.

[209] J. M. Heuft and E. J. Meijer. *J. Chem. Phys.*, 122:094501, 2005.

[210] J. R. Rustad and A. G. Stack. *J. Am. Chem. Soc.*, 128:14778, 2006.

[211] H. H. Loeffler, Y. Inada, and S. Funahashi. *J. Phys. Chem. B*, 110:5690, 2006.

[212] D. Laage and J. T. Hynes. *J. Phys. Chem. B*, 112:7697, 2008.

[213] L. X. Dang and H. V. R. Annapureddy. *J. Chem. Phys.*, 139:084506, 2013.

[214] H. V. R. Annapureddy and L. X. Dang. *J. Phys. Chem. B*, 118:7886, 2014.

[215] L. X. Dang. *J. Phys. Chem. C*, 118:29028, 2014.

[216] S. Habershon. *Phys. Chem. Chem. Phys.*, 16:9154, 2014.

[217] M. J. S. Dewar and D. M. Storch. *J. Chem. Soc. Chem. Commun.*, page 94, 1985.

[218] T. K. Udeigwe, P. N. Eze, J. M. Teboh, and M. H. Stietiya. *Environ. Int.*, 37:258, 2011.

[219] K. Modig, E. Liepinsh, G. Otting, and B. Halle. *J. Am. Chem. Soc.*, 126:102, 2004.

[220] D. Russo, R. K. Murarka, J. R. D. Copley, and T. Head-Gordon. *J. Phys. Chem. B*, 109:12966, 2005.

[221] Z. Luz and R. G. Shulman. *J. Chem. Phys.*, 43:3750, 1965.

[222] P. Yu, B. L. Phillips, and W. H. Casey. *Inorg. Chem.*, 40:4750, 2001.

[223] L. Helm. *Coord. Chem. Rev.*, 252:2346, 2008.

[224] E. Balogh and W. H. Casey. *Prog. Nuc. Mag. Res. Spect.*, 53:193, 2008.

[225] P. S. Salmon, W. S. Howells, and R. Mills. *J. Phys. C: Solid State Phys.*, 20:5727, 1987.

[226] P. S. Salmon, G. J. Herdman, J. Lindgren, M. C. Read, and M. Sandstrom. *J. Phys. Condens. Matt.*, 1:3459, 1989.

[227] P. S. Salmon, M.-C. Bellissent-Funel, and G. J. Herdman. *J. Phys. Condens. Matt.*, 2:4297, 1990.

[228] D. E. Moilanen, D. Wong, D. E. Rosenfeld, E. E. Fenn, and M. D. Fayer. *Proc. Nat. Acad. Sci. USA*, 106:375, 2009.

[229] S. Park, M. Odelius, and K. J. Gaffney. *J. Phys. Chem. B*, 113:7825, 2009.

[230] M. Ji, M. Odelius, and K. J. Gaffney. *Science*, 328:1003, 2010.

[231] C. H. Langford and H. B. Gray. *Ligand Substitution Processes*. W. A. Benjamin: New York, 1966.

[232] L. Helm and A. E. Merbach. *J. Chem. Soc. Dalton Trans.*, page 633, 2002.

[233] Y. Ducommun, K. E. Newman, and A. E. Merbach. *Inorg. Chem.*, 19:3696, 1980.

[234] L. Helm and A. E. Merbach. *Chem. Rev.*, 105:1923, 2005.

[235] C. Cossy, L. Helm, and A. E. Merbach. *Inorg. Chem.*, 27:1973, 1988.

[236] C. Cossy, L. Helm, and A. E. Merbach. *Inorg. Chem.*, 28:2699, 1989.

[237] G. Powell and D. T. Richens. *Inorg. Chem.*, 32:4021, 1993.

[238] A. Drijaca, L. Spiccia, H. R. Krouse, and T. W. Swaddle. *Inorg. Chem.*, 35:985, 1996.

[239] M. Nyman, T. M. Alam, F. Bonhomme, M. A. Rodriguez, C. S. Frazer, and M. E. Welk. *J. Cluster Sci.*, 17:197, 2006.

[240] G. D. Mahan. *Phys. Rev. A*, 22:1780, 1980.

[241] C. Hattig and B. A. Heß. *J. Chem. Phys.*, 108:3863, 1998.

[242] K. P. Jensen and W. L. Jorgensen. *J. Chem. Theor. Comput.*, 2:1499, 2006.

[243] D. E. Smith and L. X. Dang. *J. Chem. Phys.*, 100:3757, 1994.

[244] T. Peng, T.-M. Chang, X. Sun, A. V. Nguyen, and L. X. Dang. *J. Mol. Liq.*, 173:47, 2012.

[245] L. X. Dang. *J. Chem. Phys.*, 96:6970, 1992.

[246] G. Lamoureux and B. Roux. *J. Phys. Chem. B*, 110:3308, 2006.

[247] I. S. Joung and T. E. Cheatham. *J. Phys. Chem. B*, 112:9020, 2008.

[248] D. Horinek, S. I. Mamatkulov, and R. R. Netz. *J. Chem. Phys.*, 130:124507, 2009.

[249] M. Ceriotti, J. More, and D. E. Manolopoulos. *Comp. Phys. Comm.*, 185:1019, 2013.

[250] H. Yu, T. W. Whitfield, E. Harder, G. Lamoureux, I. Vorobyov, V. M. Anisimov, A. D. Mackerell, and B. Roux. *J. Chem. Theor. Comput.*, 6:774, 2010.

[251] M. Paluch. *Adv. Colloid Interface Sci.*, 84:27, 2000.

[252] P. Hunenberger and M. Reif. *Single Ion Solvation*. Cambridge University Press, Cambridge, 2011.

[253] M. A. Wilson, A. Pohorille, and L. R. Pratt. *J. Chem. Phys.*, 88:3281, 1988.

[254] Y. Marcus. *Chem. Rev.*, 88:1475, 1988.

[255] S. Varma and S. B Rempe. *Biophys. Chem.*, 124:192, 2006.

[256] C. H. Bennett. volume 46 of *ACS Symposium Series*, pages 63–97, Washington, D. C., 1977.

[257] D. Chandler. *J. Chem. Phys.*, 68:2959, 1978.

[258] R. Collepardo-Guevara, I. R. Craig, and D. E. Manolopoulos. *J. Chem. Phys.*, 128:144502, 2008.

[259] T. E. Markland, S. Habershon, and D. E. Manolopoulos. *J. Chem. Phys.*, 128:194506, 2008.

[260] Y. V. Suleimanov2011, R. Collepardo-Guevara, and D. E. Manolopoulos. *J. Chem. Phys.*, 134:044131, 2011.

[261] E. Guàrdia, R. Rey, and J. A. Padró. *Chem. Phys.*, 155:187, 1991.

[262] H. C Andersen. *J. Comp. Phys.*, 52:24, 1983.

[263] C. Dellago, P. G. Bolhuis, F. S. Csajka, and D. Chandler. *J. Chem. Phys.*, 108:1964, 1998.

[264] P. G. Bolhuis, D. Chandler, C. Dellago, and P. L. Geissler. *Annu. Rev. Phys. Chem.*, 53:291, 2002.

[265] P. Bopp, W. Dietz, and K. Heinzinger. *Z. Nat.*, 34a:1424, 1979.

[266] A. Luzar and D. Chandler. *Phys. Rev. Lett.*, 76:928, 1996.

[267] A. Luzar and D. Chandler. *Nature*, 379:55, 1996.

[268] S. H. Northrup and J. T. Hynes. *J. Chem. Phys.*, 73:2700, 1980.

[269] C. Kritayakornupong, K. Plankensteiner, and B. M. Rode. *J. Comp. Chem.*, 25:1576, 2004.

[270] Y. Chen, H. I. Okur, N. Gomopoulos, C. Macias-Romero, P. S. Cremer, P. B. Petersen, G. Tocci, D. M. Wilkins, C. Liang, M. Ceriotti, and S. Roke. *Sci. Adv.*, 2:1501891, 2016.

[271] L. D. Landau and E. M. Lifshitz. *The Classical Theory of Fields*. Pergamon Press, Oxford, 2nd edition, 1971.

[272] S. Roke and G. Gonella. *Annu. Rev. Phys. Chem.*, 63:353, 2012.

[273] D. B. Hollis. *Am. Mineralog.*, 73:701, 1988.

[274] R. Bersohn, Y. Pao, and H. L. Frisch. *J. Chem. Phys.*, 45:3184, 1966.

[275] R. Terhune, P. Maker, and C. Savage. *Phys. Rev. Lett.*, 14:681, 1965.

[276] A. G. F. de Beer, S. Roke, and J. I. Dadap. *J. Opt. Soc. Am. B*, 28:1374, 2011.

[277] D. P. Shelton. *J. Chem. Phys.*, 123:111103, 2005.

[278] D. P Shelton. *J. Chem. Phys.*, 123:084502, 2005.

[279] H. Wang, E. C. Y. Yan, Y. Liu, and K. B. Eisenthal. *J. Phys. Chem. B*, 102:4446, 1998.

[280] E. C. Y. Yan, Y. Liu, and K. B. Eisenthal. *J. Phys. Chem. B*, 102:6331, 1998.

[281] P. Maker. *Phys. Rev. A*, 1:923, 1970.

[282] D. P. Shelton. *J. Chem. Phys.*, 130:114501, 2009.

[283] R. H. C. Janssen, D. N. Theodorou, S. Raptis, and M. G. Papadopoulos. *J. Chem. Phys.*, 111:9711, 1999.

[284] M. A. Pounds and P. A. Madden. *J. Chem. Phys.*, 126:104506, 2007.

[285] M. Hidalgo Cardenuto and B. Champagne. *J. Chem. Phys.*, 141:234104, 2014.

[286] Z. Hu, J. Autschbach, and L. Jensen. *J. Chem. Phys.*, 141:124305, 2014.

[287] D. P. Shelton and J. E. Rice. *Chem. Rev.*, 94:3, 1994.

[288] J. Barrat and J. Hansen. *Basic Concepts for Simple and Complex Liquids*. Cambridge University Press, Cambridge, 2003.

[289] L. Onsager. *J. Am. Chem. Soc.*, 58:1486, 1936.

[290] P. Debye and E. Hückel. *Phys. Z.*, 24:185, 1923.

[291] R. H. Fowler. *Statistical Mechanics*. Cambridge University Press, Cambridge, 2nd edition, 1936.

[292] H. S. Frank and P. T. Thompson. *J. Chem. Phys.*, 31:1086, 1959.

[293] A. V. Gubskaya and P. G. Kusalik. *J. Chem. Phys.*, 117:5290, 2002.

[294] K. R. Srinivasan. *J. Chem. Phys.*, 60:3645, 1974.

[295] A. V. Gubskaya and P. G. Kusalik. *Mol. Phys.*, 99:1107, 2001.

[296] G. Tocci. *private communication*.

[297] Y. Marcus. *Chem. Rev.*, 109:1346, 2009.

[298] M. M. Reif and P. H. Hünenberger. *J. Chem. Phys.*, 134:144104, 2011.

[299] S. Plimpton. *J. Comp. Phys.*, 117:1, 1995.

[300] S. Nosé. *Mol. Phys.*, 52:255, 1984.

[301] W. Hoover. *Phys. Rev. A*, 31:1695, 1985.

[302] S. Winstein, E. Clippinger, A. H. Fainberg, and G. C. Robinson. *J. Am. Chem. Soc.*, 76:2597, 1954.

[303] M. L. Boas. *Mathematical Methods in the Physical Sciences*. John Wiley & Sons, Inc., New York, 2nd edition, 1983.

[304] N. Agmon. *Chem. Phys. Lett.*, 244:456, 1995.

[305] D. Marx, M. E. Tuckerman, J. Hutter, and M. Parrinello. *Nature*, 397:601, 1999.

[306] Y. Levy and J. N. Onuchic. *Annu. Rev. Biophys. Biomol. Struct.*, 35:389, 2006.

[307] A. C. Fogarty, E. Duboué-Dijon, F. Sterpone, J. T. Hynes, and D. Laage. *Chem. Soc. Rev.*, 42:5672, 2013.

[308] D. Laage and J. T. Hynes. *Science*, 311:832, 2006.

[309] A. J. Masters. *J. Chem. Phys.*, 74:2460, 1981.

[310] R. M. Lynden-Bell and I. R. McDonald. *Mol. Phys.*, 43:1429, 1981.

[311] R. Impey, P. Madden, and I. R. McDonald. *Mol. Phys.*, 46:513, 1982.

[312] A. Szabo. *J. Chem. Phys.*, 81:150, 1984.

[313] H. J. Bakker and J. L. Skinner. *Chem. Rev.*, 110:1498, 2010.

[314] G. Lipari and A. Szabo. *Biophys. J.*, 30:489, 1980.

[315] J. Teixeira, M. C. Bellissent-Funel, S. H. Chen, and A. J. Dianoux. *Phys. Rev. A*, 31:1913, 1985.

[316] J. G. Powles. *J. Chem. Phys.*, 21:633, 1953.

[317] J. T. Kindt and C. A. Schmuttenmaer. *J. Phys. Chem.*, 100:10373, 1996.

[318] R. Buchner, J. Barthel, and J. Stauber. *Chem. Phys. Lett.*, 306:57, 1999.

[319] O. Teleman, B. Jönsson, and S. Engström. *Mol. Phys.*, 60:193, 1986.

[320] R. Frattini, M. A. Ricci, G. Ruocco, and M. Sampoli. *J. Chem. Phys.*, 92:2540, 1990.

[321] A. Wallqvist and O. Teleman. *Mol. Phys.*, 74:533, 1991.

[322] D. van der Spoel, P. J. van Maaren, and H. J. C. Berendsen. *J. Chem. Phys.*, 108:10220, 1998.

[323] Gy. I. Szász, W. O. Riede, and K. Heinzinger. *Z. Natur.*, A34:1083, 1979.

[324] Gy. I. Szász and K. Heinzinger. *J. Chem. Phys.*, 79:3467, 1983.

[325] D. Laage and J. T. Hynes. *Proc. Nat. Acad. Sci. USA*, 104:11167, 2007.

[326] P. J. Rossky, J. D. Doll, and H. L. Friedman. *J. Chem. Phys.*, 69:4628, 1978.

[327] R. Abseher, H. Schreiber, and O. Steinhauser. *Proteins*, 25:366, 1996.

[328] A. R. Bizzarri and S. Cannistraro. *J. Phys. Chem. B*, 106:6617, 2002.

[329] F. Pizzitutti, M. Marchi, F. Sterpone, and P. J. Rossky. *J. Phys. Chem. B*, 111:7584, 2007.

[330] P. Debye. *Polar Molecules*. The Chemical Catalog Company, Inc., New York, 1st edition, 1929.

[331] G. Sposito. *J. Chem. Phys.*, 74:6943, 1981.

[332] K. Winkler, J. Lindner, H. Bursing, and P. Vohringer. *J. Chem. Phys.*, 113:4674, 2000.

[333] I. M. Svishchev and P. G. Kusalik. *J. Chem. Soc. Faraday Trans.*, 90:1405, 1994.

[334] D. E. O'Reilly. *J. Chem. Phys.*, 60:1607, 1974.

[335] B. Bagchi. *Chem. Rev.*, 105:3219, 2005.

[336] E. N. Ivanov. *Sov. Phys. JETP*, 18:1041, 1964.

[337] D. Laage. *J. Phys. Chem. B*, 113:2687, 2009.

[338] G. Stirnemann and D. Laage. *J. Phys. Chem. Lett.*, 1:1511, 2010.

[339] P. Gasparotto and M. Ceriotti. *J. Chem. Phys.*, 141:174110, 2014.

[340] J. Boisson, G. Stirnemann, D. Laage, and J. T. Hynes. *Phys. Chem. Chem. Phys.*, 13:19895, 2011.

[341] D. Borgis and J. T. Hynes. *Chem. Phys.*, 170:315, 1993.

[342] S. S. Andrews. *J. Chem. Ed.*, 81:877, 2004.

[343] S. J. Cyvin, J. E. Rauch, and J. C. Decius. *J. Chem. Phys.*, 43:4083, 1965.

[344] T. L. Hill. *An Introduction to Statistical Thermodynamics*. New York, 2nd edition, 1986.